Experimental studies of the properties of dust, ice, and their associations with relevance for planet formation and characterization of planetary surfaces

Inauguraldissertation
der Philosophisch-naturwissenschaftlichen Fakultät
der Universität Bern

vorgelegt von

Stefano Spadaccia

von Italien

Leiter der Arbeit:

PD. Dr. Antoine Pommerol

Physikalisches Institut, Universität Bern

Experimental studies of the properties of dust, ice, and their associations with relevance for planet formation and characterization of planetary surfaces

Inauguraldissertation
der Philosophisch-naturwissenschaftlichen Fakultät
der Universität Bern

vorgelegt von

Stefano Spadaccia

von Italien

Leiter der Arbeit:

PD. Dr. Antoine Pommerol

Von der Philosophisch-naturwissenschaftlichen Fakultät angenommen.

Bern, 17-01-2022

Der Dekan

Prof. Dr. Marco Herwegh

Aknowledgements

There are so many people to thank, that I am forced to reduce my acknowledgments to the closest ones in space and time. To all the others whose name is not in this page: don't take it wrong, I still carry you in my heart.

First and foremost, I want to thank **Antoine Pommerol**, for giving me the opportunity to join the Planetary Imaging Group. In the last four years, you let me free to invent and create my own path into research, and for this I am extremely grateful. I always knew that I could count on you for any counsel or help, which you lent with patience and optimism. As a supervisor, you definitely created the best environment for my growth, both personal and professional, making my Ph.D. an extraordinary experience. Thank you for that.

I continue with my thanks to **Pierre Beck** for agreeing to evaluate the quality of this work.

A good Swiss fondue starts always with good pieces of bread. I want to thank the current and former members of the space PIGs: **Olga, Camila, Caroline, Nico, Lea, Lucas, Miguel, Patricio, Clémence, Romain, Clément, Matt, Linus, Holly, Tatiana, Nick, Rafael, SBG, Marie, Aleks, Adam, Kristina**. Thank you for your friendship, and for the good time we spent together during the last four years. I wish you all the best for your future, hoping we will cross our paths again.

Special thanks to **Lucas**, it would not have been the same without you (for sure I would not have enjoyed so much). I am happy that what started as a normal collaboration ended up with a great friendship. We do not always choose with whom to spend most of our time, but sometimes it works perfectly. I am confident for the future!

Thanks also to **Olga, Verdiana, Alex, Willeke, María, Nikhil** for the company and the real affection. Your support and friendship means a lot to me.

Thank you, **Benedetta**, for being the most important thing in my life. Even the negative things get better with you. E se la vita è bella, è soprattutto perchè tu ne fai parte.

Abstract

Planet formation processes in protoplanetary disks are still not completely understood. We can approach this problem through the study of both the physical processes that are crucial for formation of planetesimals in the disk, and by studying the most pristine and ancient bodies of our Solar System. Recently, the water ice line has attracted the attention as a potential preferred location where planet formation and growth can be triggered. To correctly simulate planetary formation at the ice line, it is important to understand the evolution processes involving millimeter-size icy aggregates (icy pebbles) that drift inward in the disk toward the central star, and they cross the ice line. The outcome of the ice sublimation due to the rising temperatures can determine the different evolutionary path of planet formation. In this context, it is important to study the properties of ice-dust pebbles to understand their physical processes in the disk. Stepping forward in time, we need to infer the properties of the available planetesimals in the Solar System (like asteroids and comets) to gather information on how, when, and where they formed in the disk. Observing their surface characteristics, such as the presence of water ice and the type of minerals mixed together, is precious for deriving their origin and accretion processes.

In this work, I present experiments that address the evolution of icy pebbles in the protoplanetary disk, the analysis of composition and textural properties of asteroid through reflected polarimetry, and finally the spectroscopic and spectropolarimetric analysis of water ice frost forming on regolith surfaces. I created experimental models of mm-size icy pebbles, and I observed their evolution under temperature-pressure conditions relevant for protoplanetary disks. I found that pebbles do not disrupt easily under sublimation of the ice, meaning that icy pebbles produce porous mm-sized dusty aggregates when they cross the ice line. The porous dusty pebbles can then be accreted or participate in planet formation processes close to the ice line. Moreover, I performed polarimetric measurements of pulverized mineral mixtures and aggregates, to understand how the negative polarization phase curve is influenced by the surface mineralogical composition and texture of asteroids. I found that while the presence of aggregates does not change the negative polarimetric phase curve, mixing different minerals can result in a deepening and broadening of the negative polarization. This phenomenon can be important in explaining the polarimetric characteristics of some classes of asteroids (for example, F-type and L-type asteroids). Finally, I studied the possibility of detecting thin layers of water ice frost condensing on regolith surfaces both through spectropolarimetry and spectrophotometry in the visible. I discovered that water frost can be well detected by its spectral slope or negative polarization changes over time, already when it is only 10 µm thick. Our spectrophotometric data agree with the inferred frost thickness measured on 67P/Churyumov-Gerasimenko, and the spectropolarimetric data are sensitive to the deposition of the fist micrometers of frost and to its crystalline structure.

Contents

Chapter 1

Introduction

The origins of astronomical bodies in our universe is a gas and dust tale. A solar-mass star journey starts in molecular clouds, cold gaseous nebulae containing molecules (such as H_2 and CO) and small dust grains, representing only a small percentage of the whole cloud mass. Triggered by external events (e.g. supernova explosions, galactic and molecular collisions etc.), the molecular cloud undergoes gravitational collapse. As a first consequence of the collapse, the molecular cloud fragments in smaller pieces with stellar mass. Further collapse is facilitated through the dust, which increases its temperature and radiates at longer wavelengths, thus maintaining the necessary disequilibrium between the gravitational force and the inner gas pressure. The collapse slows down when the protostar is hot enough to burn deuterium while accreting the material surrounding the protostar. Finally, the temperature inside the protostar is high enough to burn hydrogen and the star is now a full main-sequence star. Already in the phase of pre-main-sequence star, the gaseous and dusty envelope around the young star starts to flatten because of the conservation of the angular momentum, creating a circumstellar disk. Here all the wonders of planet formation happen, and eventually, a whole new planetary system is formed.

Following intricate and tortuous paths, the newborn planetary system forms small icy bodies (comets), asteroids and protoplanets, and up to rocky and gaseous planets. The standard model for planet formation (called "core-accretion" model) assumes that planets are formed following a hierarchical process, where small micrometer dust grains stick together to form the first cm-size bodies ("pebbles"), which can form even bigger planetesimals up to km-size that are held together by gravity. At this point, the accretion of planetesimals and/or pebbles leads to the formation of the first proto-planets (called "planetary embryos" in case of sub-terrestrial mass or " planetary cores" otherwise). Their final planetary mass and the eventual accretion of gas from the disk to form an atmosphere depend on the position in the disk and availability of gas and planetesimals. Water ice is extremely important in all these stages, and studying its role in planet formation as well as its distribution between the newly formed bodies is of paramount importance to understand all the past and present geological processes of the planets in our Solar System. This is a complicate task, and in the

last decades new telescopes and instruments have been developed to observe protoplanetary disks, and new in-situ missions studied the surfaces of many different bodies of our Solar System, which, combined with theoretical simulations and laboratory experiments, allowed to unravel many of the physical processes happening during their formation and evolution. Since dust and/or ice are the ingredients to form astronomical objects of any size (pebbles, asteroids, comets, and planets), laboratory experimentation with ice and dust allows one to derive results that are important for many or all those objects, which are intrinsically connected by their subsequent evolution.

The purpose of this work is to provide an experimental basis for assessing different physical properties of water ice, dust, and their combinations with relevance for planet formation theory, small bodies (like asteroids and comets) and, more in general, planetary surfaces characterization. In Chapter 2, I present the general theoretical and experimental framework for the development of our experimental approach, followed by Chapter 3, where I introduce new experimental techniques and instruments that I developed. We conducted a series of experiments to answer to different questions in the aforementioned research fields:

- We studied icy pebbles evolution under low temperature and pressure conditions relevant for protoplanetary disks environments. We discovered that the sublimation of the ice hardly disrupts the pebble, leaving a porous dust aggregate after the sublimation. This has important consequences on planet formation theory close to the ice lines, indicating a preferential pebble-accretion scenario for planet growth close and inside the ice line (Chapter 4).
- We studied the negative polarization phase curve of mineral dust with relevance for astronomical observation in polarized light of small solar system bodies. We discovered that complex regolith composed by different minerals changes greatly its polarization properties, depending on the minerals used, and we apply this result to the interpretation of the surface composition of different classes of asteroids (F, L and M-classes) (Chapter 5).
- We explored the possibility to detect early stages of frost formation on regolith through spectropolarimetry and spectrophotometry. Our results indicate that both spectral slope and negative polarization are useful to detect thin frost layers (already 10 µm thick), and that spectropolarimetric measurements can distinguish the crystalline lattice of the frost (i.e. providing limits to its temperature). Our results are in agreement with the observed frost deposited on the comet 67P/Churyumov–Gerasimenko, and can be used as ground truth to interpret remote sensing data from planetary surfaces where frost deposits periodically, like Mars (Chapter 6).

This manuscript ends with chapter 7, where I summarize our findings and I discuss the future perspectives for our laboratory research in the context of the upcoming planetary missions.

The results presented in this thesis provide an exciting benchmark for future experiments that can help the theoretical description of planet formation, interpretation of the astronomical observations of small bodies, and finally the remote sensing or in-situ exploration of icy surfaces of our Solar System. It is interesting to observe that using similar methodologies

and experiments, we can produce considerably different outcomes in terms of astrophysical applications, which reflects the interconnection between the different origins and evolutionary stages of planetary bodies.

Chapter 2

Theoretical and experimental context

The purpose of this chapter is to provide a succinct overview of the theoretical framework of the experiments presented in the following chapters. Firstly, I describe the observation techniques that are used both in remote sensing, astronomy, and in our laboratory, giving basic definitions that are going to be used in all this thesis. I continue summarizing the state of the art of the relevant theoretical context of planetary formation, with specific emphasis on planetesimals and small bodies formation and evolution. Finally, I conclude describing some properties of the Solar System small bodies with relevance for the experimental works presented in chapter 5 and 6.

2.1 Observational techniques

In our laboratory, we mainly focus on the characterization of the reflected light from surfaces with different compositions. We developed a strong know-how on production of analogues for planetary surfaces, with different protocols that allow us to control a variety of physical properties: composition (ice, dust, organics, salts), mixing modes, roughness, particle size and shape, and porosity. We quantitatively characterize these properties, correlating them to the characteristics of the reflected light. We can study three wavelength-dependent properties of the emerging light from the particulate surface: its intensity, anisotropic angular distribution, and its polarization state. These properties are determined by the interaction of light with the single elements constituting the surface. I will focus on the reflectance spectrum and the polarization state of light, since these are the techniques we used to characterize the samples in our experiments.

2.1.1 Reflectance spectrum

When the Sun incident light interacts with a surface, it is either absorbed or reflected. The ratio of the amount of light reflected from a surface with respect to the total incidence light is called albedo. The albedo of a material varies from 0 (completely absorbing) to 1 (completely reflective), and it depends on the considered wavelength. The directional reflectance is the

ratio between the radiance (the optical power per unit area and solid angle) from the surface into a given direction, and the irradiance (collimated optical power received by the surface per unit area). Often, once the observation geometry is defined, the directional reflectance is just called reflectance. The observation geometry is defined by the knowledge of the incidence angle, emergence angle, and phase angle (Fig. 2.1). The incidence angle is the angle between the illumination source and the normal to the illuminated surface. The emergence angle (sometimes called emission angle) is the angle between the observer and the normal to the surface. The phase angle is the angle between the observer and the illumination surface. Note that the same phase angle can be obtained with different incidence/emergence angles. When the observer is not on the scattering plane, we introduce an azimuth angle, which is the horizontal angle between observer and illumination source. Finally, we define as scattering plane the plane containing both the incidence and the scattered light.

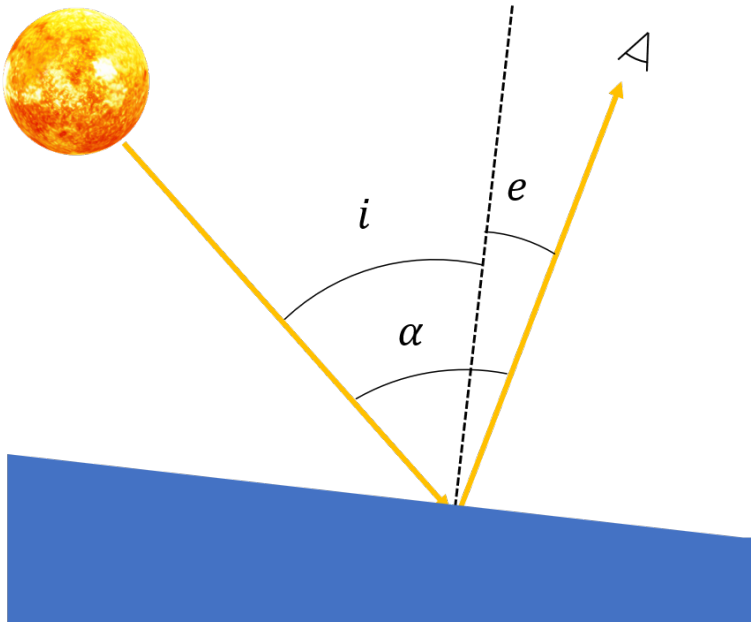

Figure 2.1: Scheme of the different angles involved in the geometry of observation. i is the incidence angle, e emergence angle, and α is phase angle.

The dependence of directional reflectance with the wavelength is called reflectance spectrum of a material or surface. The reflectance spectrum is a powerful tool that allows to detect specific compounds on the observed surface through remote sensing. Each material reflects and absorbs light in different ways depending on the wavelength, and this means that specific spectral patterns are associated to different materials composing the surface. In the UV-VIS, this is due to absorption by electronic transitions, while in the NIR by electronic transitions and vibrational overtones. differential absorption and scattering of the molecules composing the material. In the laboratory, we generally limit our measurements to the visible (VIS) and near-infrared (NIR) part of the spectrum, defined as the wavelength range $380 - 800\,\text{nm}$ and $800 - 2500\,\text{nm}$, respectively. The observation of infrared (IR) and ultraviolet (UV) parts of the spectrum requires specific instrumentation and detectors that are not implemented in

our laboratory at the moment. We are planning to increase our wavelength coverage in the near future, because these parts of the spectrum provide important information on organic molecular compounds and crystalline structure of the materials.

The spectrum of a material can be analyzed in different ways. A very common practice is to study the depth of absorption bands, which are the wavelengths where a specific material absorbs more. Many criterions have been defined to study the absorption bands, for example their centroid, depth, or integrated area. Another widely used criterion to study the reflectance spectrum is the spectral slope between two wavelengths $S_{\lambda_1-\lambda_2}$, defined as

$$S = \frac{R_{\lambda_2} - R_{\lambda_1}}{R_{\lambda_1}\,(\lambda_2 - \lambda_1)}. \tag{2.1}$$

with R_{λ_1} and R_{λ_2} being the reflectance measured at wavelengths λ_1 and λ_2, respectively (Delsanti et al., 2001; Fornasier et al., 2015).

The reflectance spectrum of a surface is extremely useful when tracking some composition or physical processes happening on the surface. The slope in the visible is used, for example, to see effects of space weathering on asteroids. Space weather produces an increase of spectral slope (reddening), but also a decrease of albedo (darkening), and a decrease of absorption band depth in S-type asteroids (Chapman, 1996). This effect is thought to be caused by solar wind bombardment that creates nanophase metallic iron on the surface, in analogy to space-weathered Moon regolith (Keller and McKay, 1997). More recently, Lantz et al. (2017) showed that samples of ions-irradiated carbonaceous chondrites showed either reddening and darkening, or blueing (lower spectral slope) and brightening in the VIS depending on their initial composition and albedo. The spectral slope in the visible is very sensitive to the presence of water frost or ice too, making it a powerful tool for its detection on planetary surfaces (see Chap. 6). Generally, the presence of ices flattens the visible spectrum, and causes a lower spectral slope than dusty surfaces.

Other parameters influence the reflectance spectrum. The grain size of the particles composing a surface influences directly the type of light scattering regime. In the Rayleigh scattering regime, the particles are much smaller than the wavelength (about 1/10 of the wavelength), and the resulting reflected intensity I varies with the wavelength λ following a power law $I \propto \lambda^{-4}$. When the particles size approaches the wavelength, the scattering regime is called Mie regime, that treats the scatterers as homogeneous spherical particles. Mie regime is very important for atmospheric and colloids science, although the theoretical application is limited to spherical particulate media. When the particles are much bigger than the wavelength, the scattering regime is described by geometrical optics. The temperature of the medium can also influence the reflectance spectrum. For example, the NIR water ice absorption bands can be sharpened and enhanced at cold temperatures, since lower temperatures decrease the range of frequencies affecting the O-H bonds. Furthermore, the roughness on the particle surfaces and their tendency to create very porous structures (fairy castles) can produce spectral slopes. This is extremely important for all solar system objects, since the spectral slope created by this microroughness is depending on the phase angle, and it usually increases with higher phase angles (it is often referred to as phase reddening).

2.1.2 Polarization

Polarization is a property arising from the wave nature of electromagnetic radiation. The polarization of light is defined by the spatial direction of the oscillation of the electrical field vector. When the electrical field oscillates in a plane perpendicular to the propagation direction of the wave, we refer to it as linearly polarized light. The plane where the electrical field lays is called plane of polarization. If a phase shift of exactly $\pm 90^\circ$ between the vertical and horizontal component is introduced, we obtain circular polarization (right-hand rotation or left-hand rotation, respectively), since the resulting electrical field will rotate in space and time along the propagation axis in the plane perpendicular with the direction of propagation of the light. For any other phase shift, the circle becomes an ellipse. An immediate way to describe the state of polarization of electromagnetic is to use the Stokes vector $\vec{S}$ containing four different parameters (the Stokes parameters), I, Q, U, and V

$$\vec{S} = \begin{pmatrix} I \\ Q \\ U \\ V \end{pmatrix} = \begin{pmatrix} E_x^2 + E_y^2 \\ E_x^2 - E_y^2 \\ 2\mathrm{Re}(E_x E_y^*) \\ -2\mathrm{Im}(E_x E_y^*) \end{pmatrix} \tag{2.2}$$

with E_x and E_y representing the decomposition of the electrical field vector on the orthogonal x and y directions. I represents the total intensity of the light, while Q and U represent the horizontal-vertical and the $\pm 45^\circ$ linear polarization, respectively. V represents the circular polarization and is positive for right-handed circular polarization and negative otherwise.

Light is said to be unpolarized when it is created by photons with random polarization states, so that there is no overall preferential polarization state ($I = 1, Q = U = V = 0$). This is the case of many artificial light sources (halogen lamps), and natural sources (for example the Sun). When unpolarized light interacts with a surface, it can induce partial polarization, resulting in non-zero Q, U, and V. The induced partial polarization (called polarizance) is used widely in astronomy, since it correlates to many properties of the illuminated medium, such as porosity, particles size and shape, albedo, mineralogy, and refractive index. In the astronomical context, circular polarization can be caused by light reflected in elongated, magnetically-aligned grains in reflection nebulae in star forming regions (Bailey, 2001), or by enantiomeric excess of organic molecules (Patty et al., 2018). Unresolved objects of our solar system observed from Earth show usually $U \ll Q$ for geometrical reasons, and since the V component is usually negligible, the most used quantity to infer the polarization of the reflected light from an object is

$$P = \frac{\sqrt{Q^2 + U^2}}{I} \simeq \frac{Q}{I}. \tag{2.3}$$

P is either called partial linear polarization, degree of linear polarization, or simply linear polarization. Note that these names are often used with different meanings in various contexts. P represents the ratio of linearly polarized light with respect to the total light reflected from an object. Linear polarization of Solar System objects focuses on the study of the linear polarized

light dependency with the phase angle of observation. The curve of the linear polarization of an object depending on the phase angle is called polarization phase curve. The polarization phase curve of regolith-covered objects has a well known peculiar shape (Fig. 2.2). For small phase angles, the polarization phase curve is negative, therefore polarization of the reflected light is mainly on the direction parallel to the scattering plane. The minimum of the negative polarization P_{min} and the phase angle at which the curve crosses the $P = 0$ (called inversion angle α_{inv}) are often used to parametrize the negative part of the phase curve. The phase curve has a maximum of polarization around 90°-100°, and then returns to null polarization at 180°.

The reflected polarization is affected by the spatial distribution of the particles. When a photon is scattered only by one particle before reaching the observer, we refer to this event as a single scattering event. On the other hand, in dense media, the light can interact with more than one particle before reaching the observer, causing a multiple scattering event. In general, multiple scattering tends to randomize the polarization axis, causing a decrease of the overall measured polarization (Fig. 2.2-C).

The physics behind the negative part and the positive maximum is of different origin. The maximum of polarization is mainly correlated to the albedo of the object, and this effect is called Umov effect. In general, objects with higher albedo show smaller polarization compared to darker objects (Umov, 1905). This relation was then investigated further by Zubko et al. (2011), who tested the relation between albedo and various particle sizes and compositions. The negative polarization arises for both regolith surfaces (multiple scattering regime) and clouds of particles (single scattering regime). The single scattering negative polarization seems related to interference phenomena between the light scattered from different parts of the particle (Muinonen et al., 2011), while multiple scattering negative polarization is produced by a complicate combination of coherent backscattering opposition effect (Mishchenko et al., 2009), interference between close particles, multiple scattering, single-scattering negative polarization, and near-field contribution of packed particles with sizes comparable to the wavelength (see Kolokolova et al. (2011)). The theoretical origin of the negative polarization by single and multiple scattering systems of particles is still a researched topic, and recent simulations are trying to involve more complexity in terms of particle shape, composition, spatial distribution, and packing density to mimic natural surfaces and complex aggregates of dust (see for instance Grynko et al. (2022)).

2.2 Protoplanetary disks and planets formation

After the formation of a new star, part of the molecular cloud which produced it starts to orbit around the star and to flatten. This mass of gas and dust is called a protoplanetary disk, out of which planets form. Rapidly, a series of physical phenomena induce fast evolution of the solid material in the disc, triggering the planet formation processes.

The inner part of the disc has higher temperatures and gas density, and both decrease with the distance from the central star. A small parcel of gas orbiting in the disk is in equilibrium between centrifugal force, gravitational force and gas pressure. The pressure force is directed outward, since the gas pressure is higher in the inner part of the disk. This extra pressure

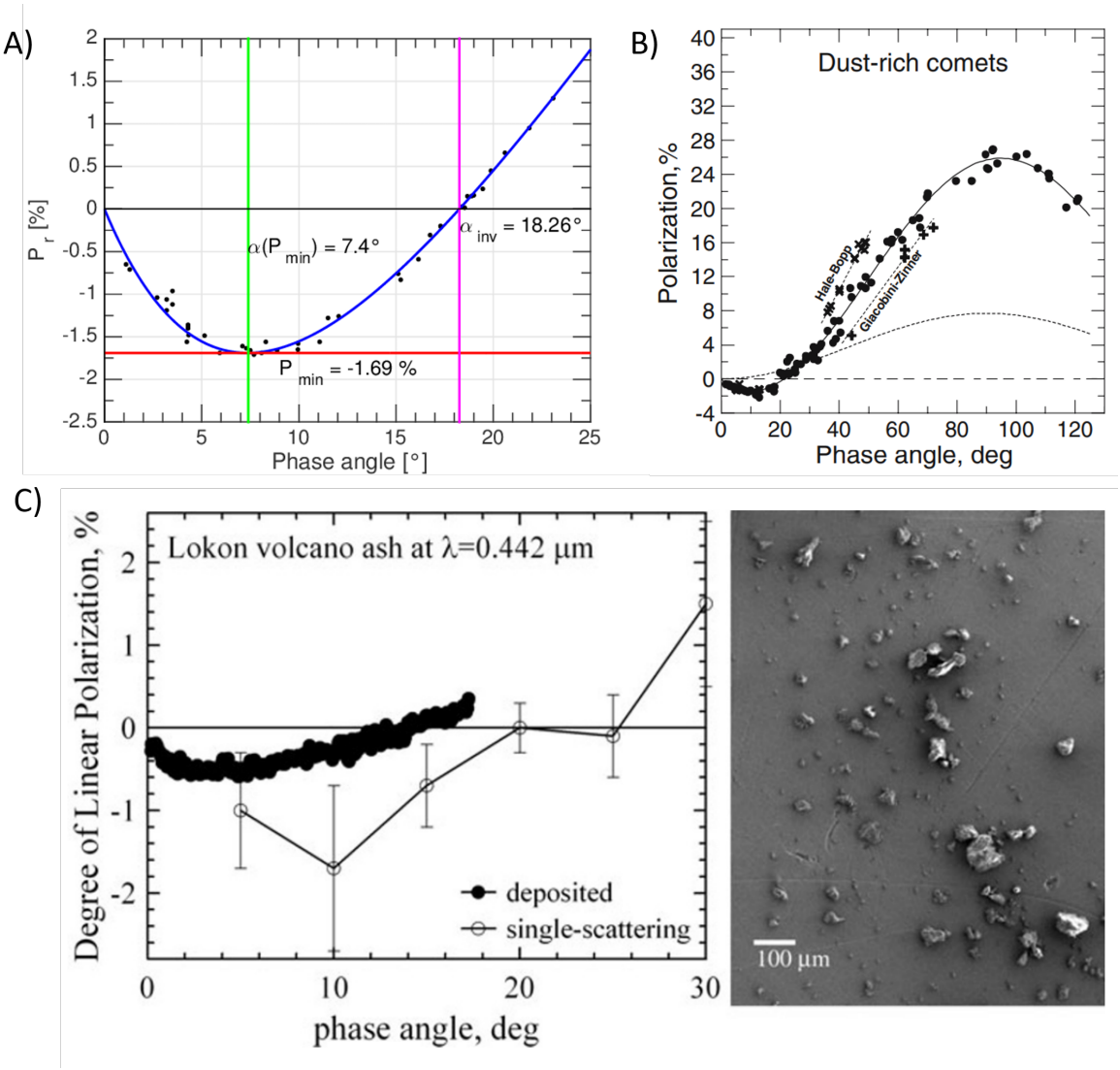

Figure 2.2: Surfaces made by small particles show a peculiar polarization phase curve. A) Typically, P is negative at small phase angles, and this negative polarization curve is often parametrized by the minimum polarization P_{min} and the inversion angle α_{inv} (figure from Devogèle et al. (2018b), Fig.1[1]). B) At higher phase angles, the curve is positive again, reaching a maximum around 90°, which maximum is inversely correlated to the albedo of the object (figure from Kiselev et al. (2005), Fig.1[2]). C) The polarization phase curve is not the same for surfaces or for clouds of sparse dust grains, since in the first case the multiple scattering scrambles the polarization signal and lowers it, while in the case of single scattering the polarization signal is stronger (figure from Zubko (2011), Fig.2).

force causes the gas to orbit at slightly sub-Keplerian velocities. On the other hand, solids are only subject to the gravitational and centrifugal force, and would tend to orbit at Keplerian velocities. Despite the small difference in velocity, the higher velocity of the dust particles

causes them to be decelerated because of the drag force F_d by the gas. The deceleration causes a loss of angular momentum, with consequential drift toward smaller distances from the central star (radial drift). The radial drift represents an important process of solid mass removal from the disk. A useful definition to quantitatively address the radial drift is the stopping time t_s, that represents the characteristic timescale for the acceleration or deceleration of the dust particles, $t_s = mv/F_d$, with mass m and speed v. Often the stopping time is used in its dimensionless form, called Stokes number $St = \Omega_k t_s$, with Ω_k the Keplerian orbital period. The drag force regime depends on the size of the dust particle compared to the local mean free path of the gas molecules. If the particle radius is much smaller than the mean free path l_{mfp}, the drag force is in the Epstein regime, while if the particle is much bigger than l_{mfp}, the drag force is in the Stokes regime (Whipple, 1972; Weidenschilling, 1977). The Stokes number of a particle with radius a and density ρ_p changes accordingly

$$St = \begin{cases} \frac{\Omega_k a \rho_{\mathrm{p}}}{c_{\mathrm{s}} \rho_{\mathrm{gas}}} & \text{for } a < \frac{9}{4} l_{mfp} \\ \\ \frac{2\Omega_k a^2 \rho_{\mathrm{p}}}{9\eta} & \text{for } a \geqslant \frac{9}{4} l_{mfp} \end{cases} \tag{2.4}$$

with c_s the speed of sound in the gas, and ρ_{gas} gas density. This mean that, in general, dense, big particles in dense gas undergo more friction and drift more quickly toward the central star, unless they grow enough to decouple from the disk gas.

The classic model of planet formation forecasts a hierarchical process where µm-sized dust particles coagulate together to form mm-size objects. Due to their increasing mass, these "pebbles" start to settle in the mid-plane of the disc, where their increase in number density allows collisional growth and the subsequent formation of the first planetesimals (km-sized body). The main mechanism used to explain the formation of mm-sized objects from µm dust particles is coagulation. The electrostatic or van der Waals forces can aggregate µm dust particles if their velocity is below a certain threshold (that depends also on their composition, see for instance Poppe et al. (2000) and Gundlach and Blum (2014b)). When the first mm-size objects start to appear, though, the classic model of planet formation fails because of the following processes:

- the radial drift becomes extremely effective in removing aggregates, suppressing further growth;
- since pebbles are more massive, their velocity increases, causing fragmentation (fragmentation barrier) or bouncing (bouncing barrier) upon collision. Furthermore, their interaction with smaller dust grains can lead to erosion of the pebble itself (erosion barrier);
- even if particles can grow to meter-size objects, their removal from the disk through radial drift would be so efficient that planetesimals could not form.

These growth barriers must be overcome by some other efficient process for planets formation, since we know that planet form relatively quickly in protoplanetary disks. There is evidence that planet forms already in $\sim 10^6$ years old disk, while the average life of proto-

planetary disks spans between $\sim 10^6 - 10^7$ years (Johns-Krull et al., 2016). Hence, several mechanisms to grow quickly planetesimals from dust and pebbles have been proposed.

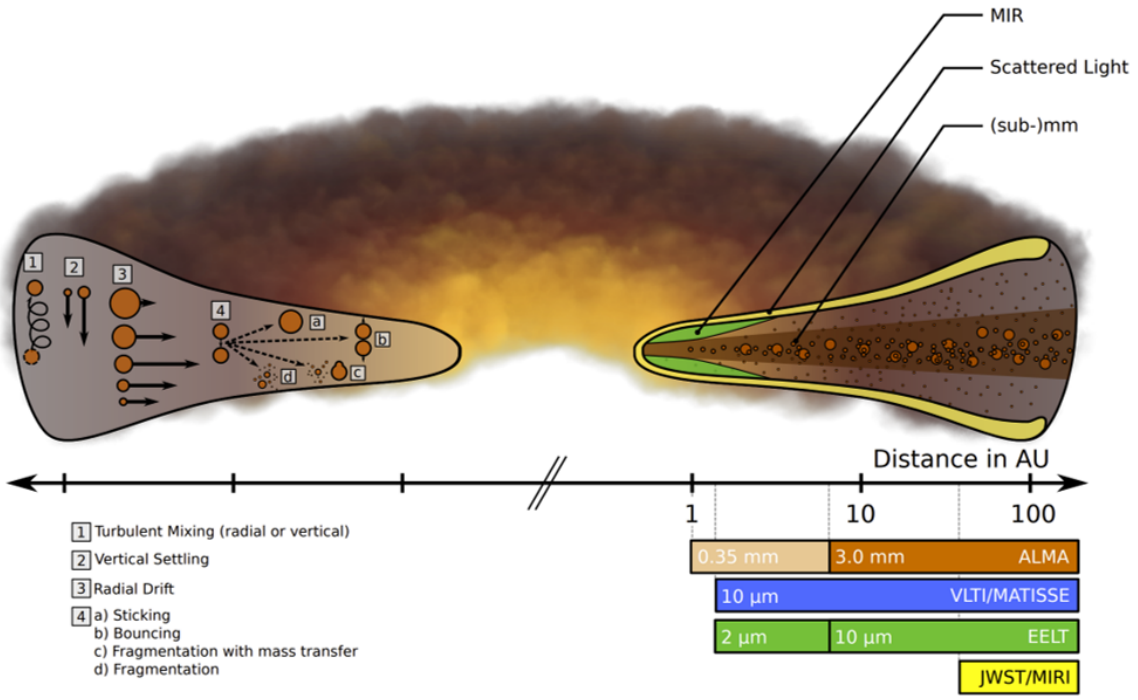

Figure 2.3: Dust in protoplanetary disks undergoes different processes that either help its growth to mm-sized bodies ("pebbles"), or inhibit it. On the right, the various observational techniques that can probe different regions of the disk are depicted. Figure from Testi et al. (2014) (Fig.1)[3].

In particular, three planetesimals formation mechanisms seem to bring advantages in terms of short time scales and size of formed planetesimals. Each of them has advantages and drawbacks, and more research is needed to address their efficiency in delivering fast planetesimals production with physical properties that are in agreement with what we observe in our Solar System and exoplanets (Blum, 2018).

1. *Streaming Instability (SI).* If a region of the disk shows a higher density of pebbles forming a cloud (for instance due to local statistical fluctuations), by mutual shielding, the pebbles in the cloud feel less headwind, and start to orbit faster and radially drift less (Youdin and Goodman, 2005a; Johansen et al., 2007). This increases the orbital velocity of the pebble cloud, capturing other pebbles along the orbit. The increase in mass of the pebble cloud can drag the surrounding gas, accelerating it and causing less friction to the cloud. Finally, the pebbles undergo less radial drift, and can collapse gravitationally and form a planetesimal. The drawback of this mechanism is that it requires high dust to gas density ratios (3%) and high Stokes numbers of the pebbles ($St = 0.1$). So, in order to invoke streaming instability, these two conditions must be achieved previously with some other processes.

2. *Collisional growth.* When mm-sized pebbles form, the bouncing barrier is efficient enough to prevent any further growth. In general, collision between pebbles with similar mass causes fragmentation, creating more small dust particles. Nonetheless, if a few cm-sized object are introduced in the system, the collision with smaller particles is translated in an efficient mass transfer growth, allowing these "lucky" pebbles to grow up to 100 meter size (Windmark et al., 2012). The problem of this scenario is that the timescale to form such bodies is increasing with the distance to the central star, and in the outer disk the growth is limited by the radial drift that becomes once again a more important effect. Furthermore, the erosion by small dust particles could inhibit the growth of objects larger than 0.1 m (Schräpler et al., 2018).

3. *Icy agglomeration.* Beyond the ice line, ice can deposit on small particles (0.1 µm-sized monomers), and this would allow them to increase their stickiness and keep their fluffy structure for longer time (Gundlach and Blum, 2014b). Their slower compaction time allows them to keep a large cross-section for longer times, that means they capture small dust grains more efficiently, while drifting more slowly than compact aggregates. The problem with this scenario is that the stickiness properties of ice are still debated (Gundlach et al., 2018; Musiolik and Wurm, 2019), and seem to depend on the temperature (the lower the temperature, the lower is its surface energy). Furthermore, erosion by small grains could still be a limiting factor in growing large (hundreds of meters) planetesimals. Laboratory experiments on icy aggregates (compact and fluffy) are missing in the literature.

4. *Ice deposition.* In the last years, a new growth mechanism has been proposed (Ros and Johansen, 2013; Ros et al., 2019). Outside the ice line, the ice can deposit on small particles, and if the partial vapor pressure is high enough, it can grow them to cm-dm size. This mechanism is efficient only where a high vapor pressure allows the heterogeneous condensation of ice on silicates (i.e. just outside the ice line), and the final growth size depends on whether the pebbles free the small silicate dust when they drift through the ice line and sublimate. Furthermore, to grow the icy pebbles to planetesimal sizes, one of the aforementioned mechanisms must be invoked. More complex simulations and laboratory work is needed to understand if this is a viable mechanism for planet formation close to the ice line.

In the last years, more complex models of planet formations studied how all these mechanisms can happen sequentially or at the same time, giving positive feedback to each other. An example is the work of Drążkowska and Alibert (2017), that shows how the ice line is a favorable place for triggering planet formation, where small dust grains in the disk drift radially less efficiently, causing a traffic-jam effect. At the same time, the sublimation of volatiles inside the ice line allows diffusion of vapor outside the ice line, causing pile-up of icy pebbles and growing their size by ice deposition. All these processes can trigger streaming instability at the proximity of the ice line.

There are two classes of sub-mm to centimeter size objects that are intensively studied in planet formation theory: Calcium Aluminum-rich Inclusions (CAIs) and chondrules. Both represent melted or partially melted droplets of condensed minerals in the innermost high-temperature regions of the disk (in many cases, these bodies experienced repeatedly heating

processes). CAIs are the oldest known solids produced in our solar system (Connelly et al. (2012) found their age to be 4567.3 ± 0.16 m.y.), and they are made of the first minerals that condense in the condensation sequence (such as oxides and silicates of calcium, aluminum, magnesium, and titanium). Their formation required very high temperatures, approximately $1400 - 1400\,\mathrm{K}$, and they are found in almost all chondritic meteorites (i.e. meteorites coming from old asteroidal parent bodies that did not undergo melting or internal differentiation after the accretion process). Chondrules were sub-millimeter droplets of molten silicates that formed around $1 - 3$ My after CAIs at high temperatures ($\sim 1600\,\mathrm{K}$). They are also found in most chondrites, although their exact formation mechanisms are still debated. Since CAIs and chondrules are found in old meteorites (and their respective asteroid parent bodies) and refractory dust grains have been found also in comets (Brownlee et al., 2006), their study is extremely important to understand the mechanism that led them to be accreted in the first planetesimals, and they can also inform us on the environment where those planetesimals formed and their subsequent evolution.

The planet formation process after the creation of many planetesimals in the disk is fairly well understood. When planetesimals with sizes larger than $\sim 100\,\mathrm{km}$ form, their further growth is assured by accretion of pebbles or boulders by gravitational deflection or gas drag (Johansen and Lacerda, 2010; Ormel and Klahr, 2010). The main problem remains to form enough localized pebbles or dust concentrations to form the planetesimals needed for planet formation.

The astronomical observation of protoplanetary disks aim at detecting some hints of the processes presented above, and giving limits to the physical properties of the growing particles (see Testi et al. (2014)). Disks are observed from UV to sub-mm wavelengths, hence probing different regions and properties of the dust (Fig. 2.3). In the UV domain it is possible to trace gas transitions lines, the VIS-IR light is scattered from the surface of the disk that hides the colder midplane where the planet formation is occurring (there, the settling of the dust increases the available mass to form planets). Observing the surface of the disk is not useless, since the uppermost layers of dust are intimately correlated to what happens in the midplane. This is due to the short timescales of vertical mixing within the disk compared to the radial drift of material. The main result from the scattered light (both in polarization and total intensity) by the disk surface is that the dust of the disk is characterized by particles of low-albedo whose vertical position in the disk is dependent on their size (with finer dust particles at the surface, and bigger particles deeper in the disk). The mid-IR probes the innermost ridge of the disk, and allows detecting the crystallinity bands of the silicates heated to temperatures $> 1000\,\mathrm{K}$. Observations at (sub-)millimeter and centimeter wavelengths can probe the pebble-size objects in the midplane. When those particles grow to sizes comparable to the wavelengths, their far IR to mm-wavelengths emission is controlled by their optical opacity k_ν. Assuming a power law dependency of the optical opacity with the frequency $k_\nu = \nu^\beta$, it is possible to correlate the opacity spectral index β to the maximum particle size, porosity, and composition (Draine, 2006). Still, the old laboratory studies on the optical opacity of aggregates are limited to minerals only, and opacities of complex aggregates made of ices, organics and minerals have never been measured in the laboratory. The main result from these observation campaigns is that mm-sized pebbles are detected in all outer protoplanetary disks, that means that some mechanisms to prevent their drift must be occurring.

Laboratory experiments provide a framework for the models of planetary formation. For instance, the properties of different types of minerals, ices, and organics at low temperatures and pressures are paramount to correctly model coagulation processes as well as growing barriers (bouncing, erosion). Furthermore, the interaction between ices and dust during the sublimation process is important to understand what is happening to dust or pebbles when they cross the ice line, or the ice line is pushed outward by the central star activity. Many laboratory works on water ice have been carried in the last years (Blum, 2018). These studies mainly focus on the mechanical properties of ice grains or icy aggregates, in order to understand if ice can help the coagulation and the collisional growth of aggregates directly to planetesimal size. Micron-size water ice particles seem to be stickier than silicate particles and their sticking-to-bouncing threshold is higer (Gundlach and Blum, 2014a), but only for temperature exceeding 200 K. This is due to a thicker diffusing layer around the icy particles above that temperature (Gärtner et al., 2017). Recently, Musiolik et al. (2016a) found that CO_2 ice has similar sticking properties of silicate dust, indicating the H_2O ice as a preferred material for enhancing the collisional growth (Musiolik et al., 2016b). Aumatell and Wurm (2011) studied the sublimation of levitated ice aggregates, and they found that those aggregates disrupt easily upon sublimation. In the literature, experimental works combining silicate dust and ice are lacking. More work is still needed to improve the experimental conditions, the fidelity of the processes happening in the disk and the type of materials involved.

2.3 Small bodies

The creation of an established planetary system composed by rocky and gaseous planets leaves behind a battlefield of planet formation remnants. The initial position and time of formation of the remnants in the protoplanetary disk determine if they contain a large fraction of ices outside the various ice lines or if they are mainly composed of refractory materials (in the inner part of the disk). Since we know that once planets are formed, they can migrate radially, these small bodies can be scattered along the disk or toward other stellar systems. Comets, asteroids, objects of the Kuiper belt and the Oort cloud are all included in the definition of small bodies, although their origins and properties can vary importantly. Our knowledge of the bodies populating the external regions of our Solar System is very limited, since only a few of them are observable from Earth or have been explored by space missions, while the vast majority has never been observed. In this section, I mainly focus on the physical properties of the surface of comets and asteroids, although some of our findings are important for other bodies as well.

2.3.1 Comets

Comets are km-sized objects composed of refractory materials (silicate dust and organics) and ices (mainly H_2O, CO_2, CO). Such types of bodies formed beyond the ice line in protoplanetary disks, and since their formation they did not undergo a significant heating. For this reason, they are thought to carry the pristine materials of the protoplanetary disk, and their study allows to better understanding the building blocks of the planets of our Solar System. Most of our knowledge of the properties and evolution of comets comes from space missions that visited different comets and analyzed them and their environment with a variety

of instruments.

Comets orbit around the Sun with elongated orbits, and when approaching the Sun, they form a tenuous atmosphere (called comae) caused by the sublimation of the ices and the lifting of small dust particles from the surface of the comet (called nucleus). Cometary nuclei have usually low densities (between 0.2 and 0.6 $\mathrm{g\,cm^{-3}}$), due to their high porosity and icy content. The exact amount of ices with respect to the refractory material, its mixing mode with the dust, and the formation of layers of the two materials are highly investigated topics, because all this information gives hints on how they formed and in which protoplanetary disk conditions. The dust particles collected from 81P/Wild 2 and 67P/Churyumov-Gerasimenko, range from tens of nanometers to tens of micrometers, and can either be quite compact irregular dust grains (Brownlee et al., 2006), or fluffy aggregates composed by $\sim 0.1\,\mu\mathrm{m}$ subunits (Mannel et al., 2019). From the mineralogical point of view, they contain unaltered minerals coming from the Solar nebula, and material that was heated and processed at high temperatures, hence coming from the innermost region of the protoplanetary disk. These results demonstrate that radial mixing of the material in the disk is indeed an important process, and the presence of fluffy aggregates is a fossilized footprint of planet formation preserved within the comet nuclei. Not only dust was accreted in the nucleus at its formation epoch, but also icy pebbles containing both ice and dust.

From the extensive analysis of *Rosetta* data of 67P/Churyumov-Gerasimenko, it has been demonstrated that the comet was formed by a gentle accretion process of icy pebbles that remained pristine within the comet, with the spaces between pebbles filled with fractal, fluffy aggregates (Blum et al., 2017). The average dust-to-ices mass ratio was also inferred to be $\delta = 8.5$, with a total porosity around $\Phi = 70\%$ (Fulle et al., 2016; Pätzold et al., 2019). The porosity was then constrained in the range 65-85% using the CONSERT instrument (Herique et al., 2019). These results assume specific volume ratios of silicates, ices, and vacuum (pores), so the extrapolation of more precise values are limited by our knowledge of the material composing the nucleus. Since comets experience sublimation of the ices when they get closer to the Sun, their surface shows a depletion of volatiles, and has a crust of dry material hiding the ice underneath. Nonetheless, there are some spots on the surface of the nuclei where patches of ice are exposed, detected by their higher albedo, bluer slope, and spectrum (Fig. 2.4). This patches of ice have been correlated to jets and outbursts of gas and dust, and in general to active regions of the surface (Fornasier et al., 2019).

It has been observed that the visible spectral slope of 67P/Churyumov-Gerasimenko becomes bluer when the comet is close to the perihelion (closest to the Sun), followed by a reddening in the outbound phase. This effect has been explained by an increase of sublimation closer to the Sun, that removes the dusty, dehydrated mantle, and reveals the icy nature of the underneath nucleus material (that has generally bluer spectral slope in the visible). However, less than 1% of the total surface, where the blue patches are localized, contribute to the overall blueing of the nucleus (Fornasier et al., 2022). Recently, Ciarniello et al. (2022) proposed a new model explaining the micro and macro distribution of ice within 67P (Fig. 2.5). They suggest the presence of meter-size water-ice enriched blocks (WEBs) below the surface of the comet, embedded in a dust-rich matrix. CO_2 sublimation increases close to perihelion, eroding the surface and revealing the WEBs (that appear as blue patches on the

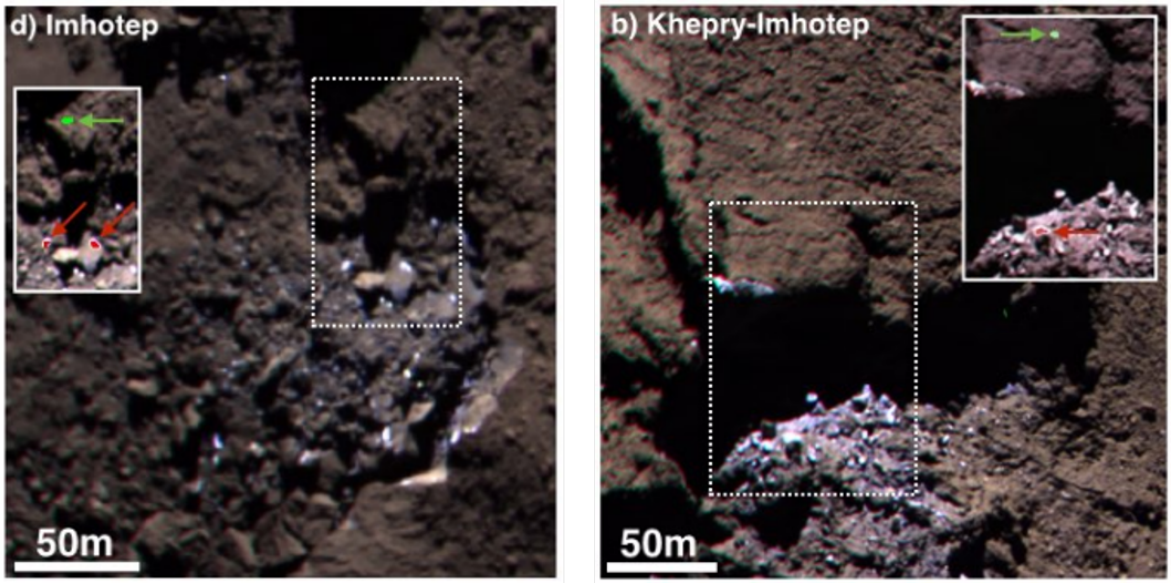

Figure 2.4: RGB color-composites images of ice patches on the surface of 67P/Churyumov-Gerasimenko using the wavelengths 882.1 nm, 649.2 nm, and 360.0 nm for the three channels. The ice patches appera as bright bluer spots compared to the dessicated regolith mantle. Image from Pommerol et al. (2015b) (Fig.8).

surface). At that point, the H_2O-driven erosion removes the WEBs from the surface, extinguishing the blue patches over time. The direct consequence of this model is the heterogeneity of the nucleus composition when it formed, made of clumps of dehydrated pebbles or ice-rich pebbles at meter scale.

Even though I do not address complex chemistry of astronomical bodies in this thesis, it is important to note the great variety of organic compounds found on 67/P and other comets (Filacchione et al., 2019). The organic compounds contain COOH and OH-groups, aliphatic, and mono- or polycyclic aromatic hydrocarbons, that contribute to a broad absorption band centered at 3.2 µm in the reflectance spectrum (together with water and salts). They are intimately mixed with silicate dust, Fe-sulfides, and possibly ammoniated salts. In this context, laboratory experiments are essential to interpret the remote sensing observation, since the optical properties of many of these compounds are not known, together with the properties of complex mixtures of organic, ices and refractory materials.

Up to now, polarization measurements of comets are limited to Earth-based, mainly disk integrated observations of their comae. Some observations in polarized light of jets and different parts of the coma exist (performed by *Giotto* spacecraft on the comet 1P/Halley) and they provide useful information on the materials populating different regions of the coma (Levasseur-Regourd et al., 1999). In general, modelling the polarization properties of different comet comae reveals the presence of low-albedo silicate aggregates, that are compact in the case of gas-rich comets and more porous for dust-rich comets (Kiselev et al., 2015). Furthermore, the only ground-based telescope observationss of reflected polarization of cometary nuclei were

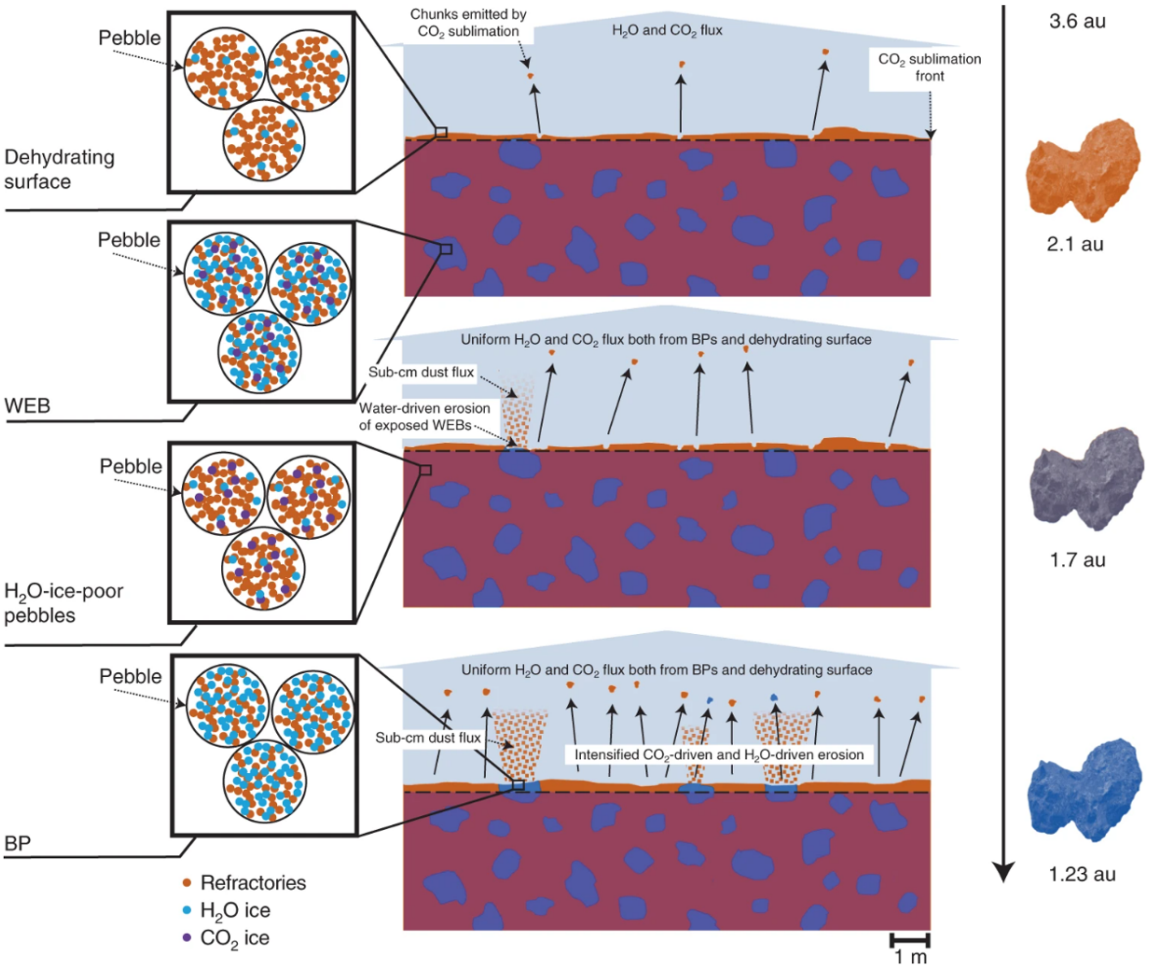

Figure 2.5: A new model of the nucleus composition proposes that the comet is heterogeneous, formed by meter-size water-ice enriched blocks (WEBs) in a dust-rich matrix. This explains the appearance of blue patches (BPs) on the surface when the comet approaches perihelion (and a general bluening of the surface), but also implies that the comet formed from heterogeneous types of pebbles. Image from Ciarniello et al. (2022) (Fig.4)[4].

performed for comet 2P/Encke (Jewitt, 2004; Boehnhardt et al., 2008) and 133/Elst-Pizarro (Bagnulo et al., 2010). In both cases, the inversion angle is smaller or comparable to F-type asteroids, although the polarization minimum of 2P/Encke nucleus appears at much smaller phase angles and has redder color compared to F-type asteroids. More studies of cometary nucleus optical properties are needed to address their similarity with some classes of asteroids, and polarization has demonstrated to be an extremely useful tool, that should have high priority with other complementary spectrometry instruments in future comet mission.

Table 2.1: Asteroid complexes and classes

Complexes	Tholen (1984)	Bus-DeMeo (2009)	Spectrum description
S	S	S, S_a, S_q, S_r, S_v	Moderate silicate absoprtion features at 1 µm (pyroxene) and 2 µm (olivine).
C	B, C, F, G	B, C, C_b, C_g, C_{gh}, C_h	Low-albedo, flat slope, subtly featured or featureless
X	E, M, P	X, X_c, X_e, X_k	Moderate slope, subtly featured or featureless. It contains both very dark and bright asteroids.
End members	T, D, O, R, V, A	T, D, Q, O, R, V, A, K, L	Distinctive spectra that are not ascribable to the other complexes.

2.3.2 Asteroids

Asteroids are $10^{-3} - 10^{3}$ km bodies thought to be the leftovers of the planetesimals which contributed to the formation of rocky planets and the cores of giant planets. In the Solar System, most of the known asteroids belong to the main belt, an asteroid belt between Mars and Jupiter about 1 au wide. The main belt total mass is estimated to be about 3% the mass of the moon (Pitjeva and Pitjev, 2018), with (1) Ceres, (4) Vesta, (2) Pallas, and (10) Hygiea accounting for most of its mass. Other orbital classes of asteroids are the trojans, namely asteroids that are orbiting around the Lagrangian points L_4 and L_5 of different planets. The most numerous family of trojan is sharing the same orbit of Jupiter. Another orbital class of asteroids is the Near-Earth asteroids (NEAs), that include all those asteroids with an orbit that crosses or gets close to Earth orbit and could be a potential hazard for humanity.

The formation process of asteroids is similar to the one of other planetesimals, and one of the scenarios discussed in section 2.2 ends up in collapsing enough dust or pebbles of various size and possibly creating a bigger planetesimal. Nonetheless, the exact formation pathways, the conditions of the environment in which they formed, and the collection of chondrules and CAIs are still topics of research. The formation history of asteroids is hand in glove related to their composition.

Many asteroid classifications and taxonomic groups based on their reflectance spectra have been proposed over the years. The most used classifications in the visible were the one by Tholen (1984) (in the range $0.33 - 1$ µm) and Bus et al. (2002) (in the range $0.35 - 0.9$ µm). In the early 2000s, new NIR spectra became available, and a new classification was created by DeMeo et al. (2009) to extend the Bus classification also in the NIR domain. Asteroid spectra are traditionally divided into three complexes, and each of the complexes is divided into individual classes or "types" (DeMeo et al., 2015). In Table 2.1 I summarize the asteroid complexes' division, their classification in different types and the general spectral properties of the complexes. Note that the F-class (referred to in chapter 5) was introduced in the Tholen classification, and it is now incorporated in the C_b and B-class in the Bus-DeMeo taxonomic system. In Fig. 2.6 the different classes of the Bus-DeMeo taxonomic system are arranged to distinguish them by spectral slope and silicates absorption band strength. Both taxonomic systems are widely used, and in this work I will use mostly the Tholen classification.

Figure 2.6: Bus-De Meo classification of asteroids. The visible-NIR spectra determines the classes of asteroids within the respective complexes. In this figure, the classes on the top have higher spectral slope, the classes on the top right have a deeper and broader pyroxene band centered at 1 µm, while the ones on the bottom right are characterized by a broader and deeper olivine absorption band centered at 2 µm. Image adapted from DeMeo et al. (2009) (Fig. 15).

The taxonomic division in classes is a great tool that allows having a common language in the asteroid community, but also it shouldn't be used as a strict labelling of asteroid compositional properties. As a matter of fact, the classes are continuously adjusted with new observations or considering new spectral ranges. Furthermore, the biggest challenge of asteroids observation is to retrieve the composition of asteroids based on their spectrum, since many are featureless. This is particularly evident in the X-complex, where the VIS and NIR spectra look similar, but the albedo difference between asteroids in this class is so different that their composition must be as well diverse. The problem lies in the fact that the spectra can change depending on a variety of processes or physical properties, such as space weathering, dust size distribution, viewing geometry, and temperature. Understanding the composition of asteroids and linking it to their classes is paramount to understand their formation process and their origin. In the last decade, also IR spectra of asteroids have been used to gather

information on some mineralogical species on the surface (for example phyllosilicates that are evidence for aqueous alteration of silicates, see Rivkin et al. (2015) and references therein). Recently, Belskaya et al. (2017) and Belskaya et al. (2022) demonstrated that the negative polarization part of the polarization phase curve can be used efficiently to separate the asteroid classes. Furthermore, they showed that the negative polarization features can be correlated to other properties such as NIR spectral slope and radio circular polarization, and proposed a differentiation in subclasses of the M-class depending on their composition. The association of polarization measurements to spectral measurements can be a useful tool to characterize and restrain the surface properties of asteroids. In this framework, more laboratory work is needed to associate the polarization and spectral properties to the physical properties of well-characterized meteorites and regolith analogues.

There is a compositional gradient with heliocentric distance in the main belt asteroids (DeMeo et al., 2015). The compositional gradient consists in the presence of higher albedo, silicate-rich asteroids in the inner main belt, while, with increasing distance, they make way to darker, organic-rich and possibly more primitive asteroids (the class progression of this gradient is S, C, P, and D). This reflects either a composition gradient of the disk when asteroids formed (and subsequently remained in the same place), or it may be due to implantation of particular families of asteroids through dynamical excitation of the whole Solar System architecture (Morbidelli et al., 2015b). A great source of uncertainty is again the real composition of these asteroid families, that would provide a better constraint to their formation history. Linking specific meteorites to asteroids families is often an extremely difficult process, and only few classes of meteorites have been solidly linked to their parent families (for instance V-type and howardite-eucrite-diogenite meteorites). The problem seems to be twofold: on one hand, the asteroid spectra sometimes are so affected by noncompositional spectral effects that it is difficult to model them; on the other hand, the lack of experimental measurements of the optical properties of different types of minerals composing meteorites limits the radiative transfer models (Reddy et al., 2015).

In the last decades, a great amount of observational data became available, allowing substantial progress in our knowledge of asteroids. Although there are still many unanswered questions, in the next future a good synergy between modelling, experimental data, in-situ space mission exploration, and ground-based observations will provide significant advance of our current knowledge. The study of planetesimals does not only give us information on our Solar System and its formation from the solar nebula, but also on what is happening in other newly discovered planetary systems, their evolution and their history.

Chapter 3

Contribution to the laboratory

This chapter describes the state of the laboratory (Laboratory for Outflow Studies of Sublimating icy material LOSSy, also called Ice Lab) at the beginning of this Ph.D. project, and my new contributions to the instrumentation in order to develop the experiments presented in this thesis. In the following pages, I describe the sample production protocols that I developed, new instruments, and improvements to the ones which we already had in the laboratory. I also provide the protocols for using the various instruments with icy samples, and the problems I encountered and how I solved them.

3.1 Ice production methods

Producing ice particles with well-defined size and shape and mixing them with other materials is a challenging process. The icy samples prepared in our laboratory must be produced and stored in liquid nitrogen or similarly cold containers to prevent sintering. The sintering process is a re-organization of the solid material to minimize the surface energy that brings the ice particles to coalesce together. Another process that is changing the shape and size of the icy particles is frost condensation. When the ice is exposed to the humidity of the air, the water vapor condenses on top of it. Firstly, it condenses as spherical sub-µm ice nuclei (nucleation), and then it grows dendritic crystals all the way up to mm-cm size, depending on the availability of humid air. Both effects should be avoided or mitigated at the ice production stage, since they could alter the physical and optical properties of the sample.

At the Ice Lab, two different types of ice particles can be produced with the Setup for Production of Icy Planetary Analogues (SPIPA). Both methods are thoroughly described in Pommerol et al. (2019a). The first setup (SPIPA-A) allows condensation of nebulized water on a cold surface. Deionized water is nebulized with ultrasound and is conducted through a pipe connected to a freezer, where it freezes in air and deposits onto the surface of a copper plate kept at liquid nitrogen temperature. This method produces spherical ice particles with a typical size of $4.5 \pm 2.5\,\mu m$. The SPIPA-A ice reacts rapidly to changes of temperature, and sintering between different particles proceeds quickly. The second method (SPIPA-B)

operates similarly: pure water is sent to an ultrasonic nebulizer that sprays the small droplet directly into a bowl filled with liquid nitrogen. With this method, it is possible to create spherical icy particles with a size range of 70 ± 30 µm.

Most of the time, we are interested in studying the physical properties of real icy planetary surfaces, and this means that ice is not pure, but it is mixed with dust particles, salts or organics (hereafter referred to generally as "dust", unless we specifically define the nature of the material mixed with ice). In the previous years, two mixing methods have been developed at the Ice Lab: inter-mixtures and intra-mixtures. Inter-mixture refers to a mixture where the dust particles are outside the ice particles, and lay between icy grains and at their surface. Inter-mixtures are created by shaking the ice particles (SPIPA-A or B) with the dust in a container at liquid nitrogen temperature, to prevent sintering. The ice is mixed in the bottom of a fridge, so that the low temperature and humidity prevents the formation of frost. The intra-mixing refers to a distribution of dust particles within the ice particles. This is achieved by suspending or dissolving the dust material in water before nebulizing it in liquid nitrogen. This method can be used only with very small particle sizes (sub-µm) or salts, that can dissolve in the liquid (see for instance Cerubini et al. (2022)).

3.1.1 Icy pebbles production

SPIPA-A and SPIPA-B ice particle models have the advantage of being well characterized in terms of shape, size, and sintering dynamics. Nonetheless, their sizes and mixing methods are hardly applicable to the simulation of icy pebbles in protoplanetary disks. Icy pebbles are aggregates of ice and dust that are formed in a protoplanetary disk beyond the ice line, and they are most probably playing an important role in the planet formation processes close to the ice line. An icy pebble is defined as an ice and dust porous aggregate of mm-size, with a variable ice-to-dust ratio. One could think to use SPIPA-A or B ice particles inter or intra-mixed with some dust to build such an aggregate like a snowball, creating a mm-aggregate. The drawback of this method is that both the porosity and the ice-dust mass ratio of the final pebble are not known.

I developed two methods to create mm to cm-size compact icy pebbles with a known ice-to-dust ratio. The ice-to-dust mass ratio provides also an estimation of the porosity of the pebble when the ice is sublimating. To preserve some continuity with the SPIPA methods, I called them Pebbles type-A (PA) and Pebbles type-B (PB).

PAs are produced with the help of a superhydrophobic surface. A superhydrophobic surface consists of a surface with hierarchical roughness, with µm-scale roughness covered by nm-scale asperities. The contact surface between this hierarchical structure and a water droplet is reduced to a point that the water tension does not let the droplet go through the asperities (capillary action). Superhydrophobic surfaces have the capability of self-cleaning: when a droplet of water rolls or impinges on the top of the surface, it can trap any contaminant that is deposited on it (Fig. 3.1). The self-cleaning of superhydrophobic surfaces is called "Lotus effect", after the known superhydrophobicity of the lotus leaves, and this property allows them to be cleaned from dust particles that decrease the photosynthesis efficiency every time it rains. Many other organisms take advantage of the Lotus effect, as a protection from fungi and algae in plants, and it is also the only way for many insects to clean their wings.

I sprayed a superhydrophobic coating on a flat glass surface with adjustable inclination. The inclination was set at 15°, and the surface was covered with the desired dust. I created the droplets with a micropipette, letting them catch the dirt and sink in a bowl filled with liquid nitrogen (see Fig. 4.3 in Sect. 4). Due to the difference of temperature between the droplet at ambient temperature and the liquid nitrogen (77 K), the nitrogen evaporates quickly around the droplet, preventing it to flash-freeze (Leiderfrost effect). The complete freezing takes a few seconds, and it proceeds from the outside to the inner part of the droplet, and when the droplet is frozen it sinks inside the bowl. This method produces compact icy spherical particles with size of about 1−5 mm, ice-to-dust mass ratio of $50 \pm 10\%$, and with the dust grains trapped within the icy pebble. The distribution of the dust within the pebble was analyzed though X-ray tomography, which revealed it to be non-homogeneously distributed in the case of big droplets. This is due to the Leidenfrost effect: when a big droplet sinks, the core of the droplet remains liquid for long enough to allow the settling of the dust under gravity within the liquid core. This causes the dust to be concentrated in one side of the pebble.

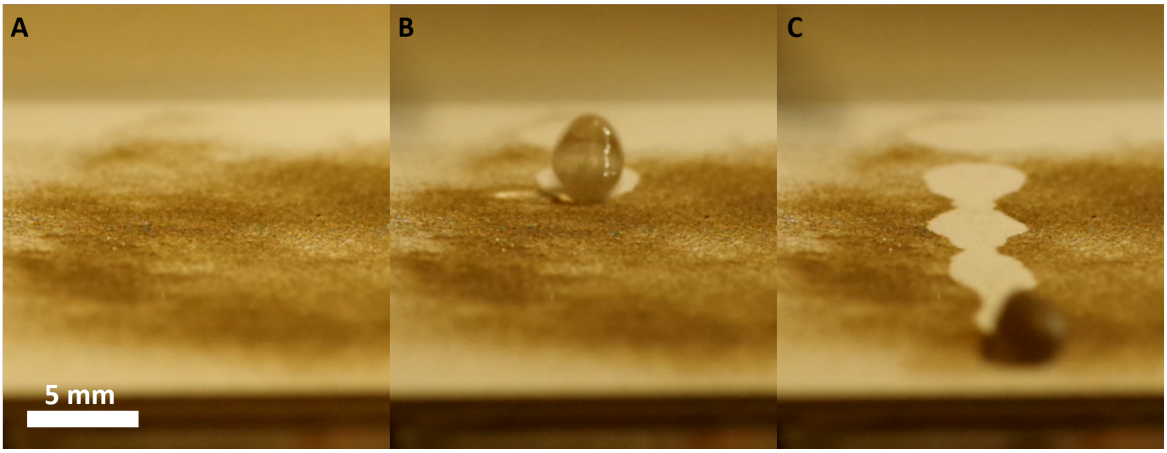

Figure 3.1: The self-cleaning process on superhydrophobic surfaces. A) A dust layer is deposited on top of an inclined superhydrophobic coating, and when a droplet impinges the surface (B), it rolls, catching up all the contaminant on the surface (C).

When a droplet impinges on the surface, it can break up and form smaller (about 1 mm) secondary droplets. These roll and catch the dust in the same way as the bigger droplet, but also they stop rolling down quickly. This is due to the fact that they catch enough dust to form a thick layer that prevents the water to touch directly the superhydrophobic surface. After that, the friction between the dust and the rough coating prevents further rolling.

PBs production is inspired by the natural phenomenon of wet aggregation. When droplets of water fall on sand, the water penetrates between the soil particles through capillarity. A thin film of water forms between each particle, and it keeps the grains together through its surface tension, acting like an inter-particle bridge. The production procedure is simple (Fig. 3.2): a micropipette is used to create mm-size droplets, that impinge a dust layer from a height of about 5 cm above the sample. The aggregate is then picked up from the dust with a spoon and sunk in liquid nitrogen, where all the water bridges freeze and create a

hard, solid aggregate with a typical size of $2 - 7$ mm. These wet aggregates are extremely stable, and they can be handled easily, paying attention to not compress them. The water content was measured before and after evaporation, and found to be approximately 15 ± 7 % of the total mass. These aggregates are more stable than PAs, probably due to the fact that the water bridges also organize the small particles at the interface between bigger grains, which contribute to higher surface energies once the water disappears. The shape of the aggregate is ellipsoidal, with a complex shape due to the different phases of grain accretion through capillary forces. The top of the aggregate is generally more hemispherical (where the droplets hit the dust surface), while the bottom part is larger and flatter (due to the capillarity expansion of water through the grains).

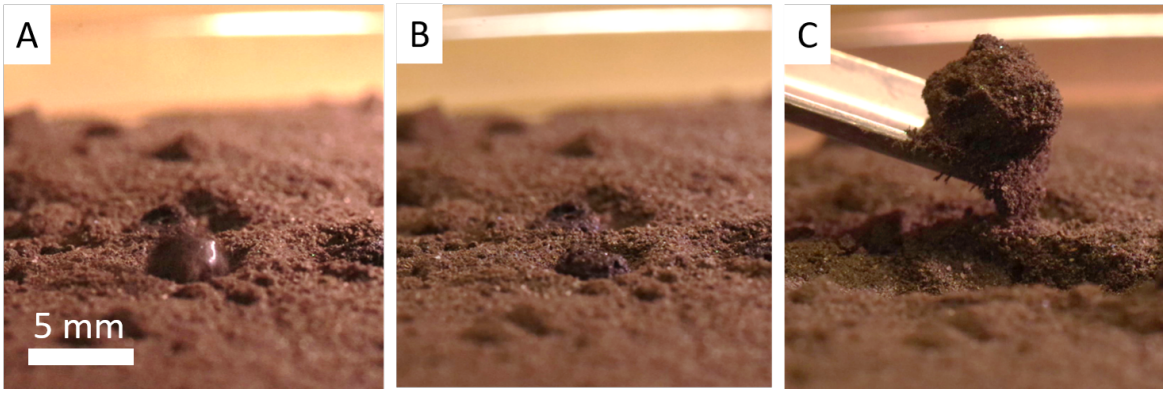

Figure 3.2: The pebbles type-B (PB) are created through wet aggregation. A) A droplet of water impacts a layer of dust at least 5 mm thick. B) After a few seconds, the water penetrates completely in the granular medium, connecting the particles with water bridges and keeping the wet aggregate together through capillarity forces. C) Finally, the aggregate is collected with a spoon and dropped in liquid nitrogen, where it loses all the dust particles not connected to others by ice films.

3.2 Simulation Chamber for Imaging Temporal Evolution of Analogous Samples (SCITEAS-2)

The Simulation Chamber for Imaging Temporal Evolution of Analogous Samples (SCITEAS-2) is a direct improvement of the SCITEAS vacuum chamber described by Pommerol et al. (2015a). The chamber has been extensively described by Cerubini (2021), and I just summarize its most important characteristics in this section. The chamber is a 77x79x58 cm enclosure (Fig. 3.3), evacuated through a primary pump (Pfeiffer ACP15) and a turbomolecular pump (Pfeiffer HiPace 300). The minimum pressure reachable is about $10^{-6} - 10^{-7}$mbar. The top of the enclosure hosts a quartz window to access the center of the chamber with optical instruments. At the center of the chamber, there is a cylindrical shroud that can be flushed with liquid nitrogen. The $\sim$ 15 cm diameter copper head of a He-cryocooler (Sumitomo CH 110) is at the bottom of the shroud, and is where we place our samples. The copper head can cool down to about 40 K (Fig. 3.4), while flowing liquid nitrogen in the shroud can isolate the sample from radiative heating. Samples are usually placed on top of specific cylinders

designed to match the copper head. Often, we use a thin layer of graphite sheet between the copper head and the sample cylinder, to ensure a good thermal contact at high vacuum.

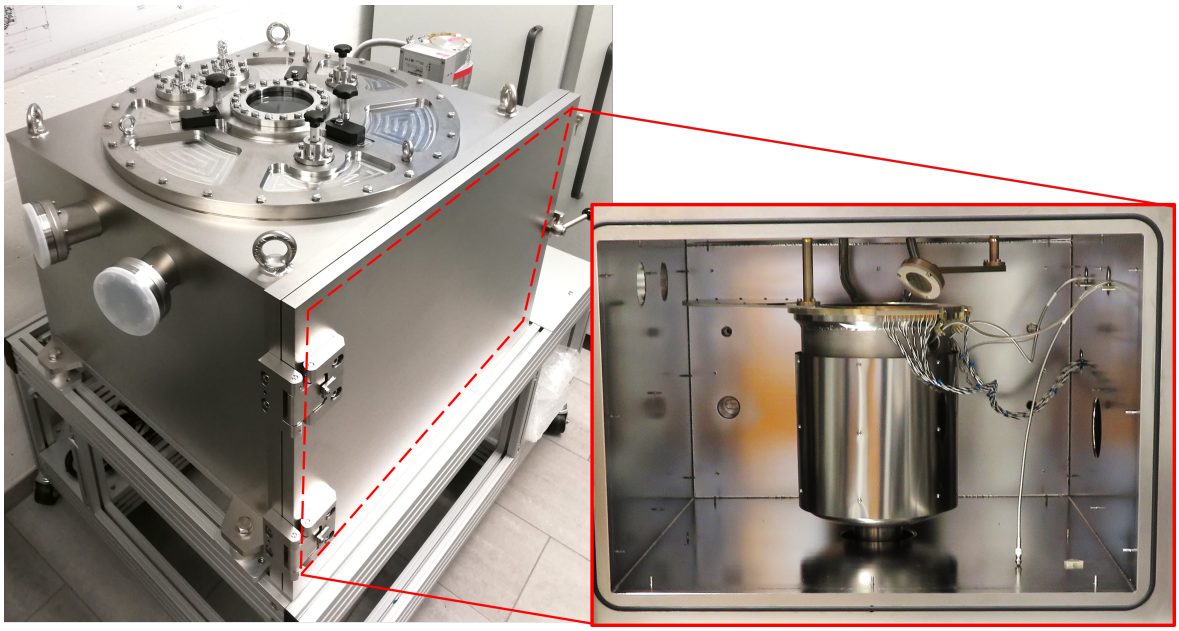

Figure 3.3: The Simulation Chamber for Imaging Temporal Evolution of Analogous Samples (SCITEAS-2) setup. The vacuum chamber has a cuboidal shape, and it has a transparent quartz window on the top, providing access for optical instruments. Inside the chamber, there is a shroud that can be flushed with liquid N_2. Inside the shroud, lies the head of the He-cryocooler, which can cool samples down to 40 K.

Since the He-cryocooler takes approximately 40 minutes to cool the cylindrical sample holder to temperatures lower than 150 K, it is necessary to pre-cool the cryocooler head before inserting the icy samples, otherwise they metamorphize or melt quickly after insertion in SCITEAS-2. If the cryocooler is turned on with air inside the chamber, it acts as a cold trap and thick layers of frost condense on it, which could slow down the evacuation through the primary pump and also act as an insulating layer between the cryocooler head and the sample holder. I tested a simple pre-cooling procedure that allows us to achieve very low starting temperature when inserting the sample, and at the same time prevents formation of large amounts of frost on the cryocooler head. Firstly, a spare cylindrical sample holder must be inserted on top of the cryocooler head, always with a graphite sheet between them. Then, I open the top window and the valve on the back of the chamber, so that air can pass through. I fill the cylinder with liquid nitrogen through a small aluminum milk pot, and I close the window on the top. At the beginning, the head is at room temperature, so the liquid nitrogen evaporates energically, but after having filled the cylinder a few times, the evaporation process is slower, and one can start preparing the samples in parallel, checking from time to time the nitrogen level inside the chamber.

When the temperature of the cryocooler head is lower than 170 K, I start the sample insertion procedure. I place the icy samples inside their cylindrical sample holder and inside

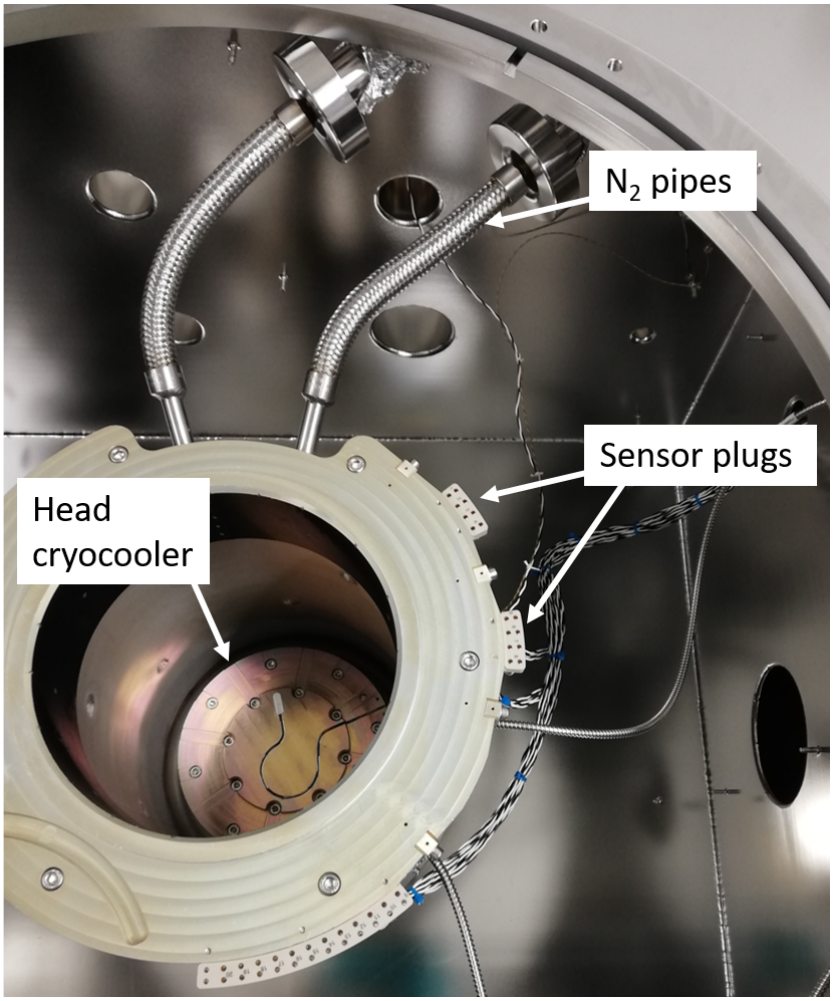

Figure 3.4: Internal view of SCITEAS-2. The shroud can be flushed with liquid N_2, and it contains the head of the He-cryocooler. The PT100 thermal sensors can be connected to the plugs on the side of the shroud and be read from the laboratory computer.

the cryogenic box previously cooled down with liquid N_2. I clear the space on top of SCITEAS-2, and I place the cryogenic box containing the samples over it. Quickly I proceed like the following:

1. I open the top window, and place it on a clean surface;
2. I remove the cylinder filled with nitrogen from inside the chamber;
3. I insert the cylindrical sample holder inside the chamber, and I connect any eventual PT100 thermal sensor to the plugs on the side of the shroud (Fig. 3.4);
4. I close the window and the flushing valve behind SCITEAS-2;
5. I start the primary pump and the He-cryocooler.

At this point, the experiment starts. It is very important to be fast and precise when performing this protocol, because if the chamber remains open too much time between the pre-cooling phase and the sample insertion, a substantial amount of air can enter inside, and condense both to the cryocooler head and the sample. Some frost formation on the sample is unavoidable, but it can be minimized by quick insertion and vacuum pumping.

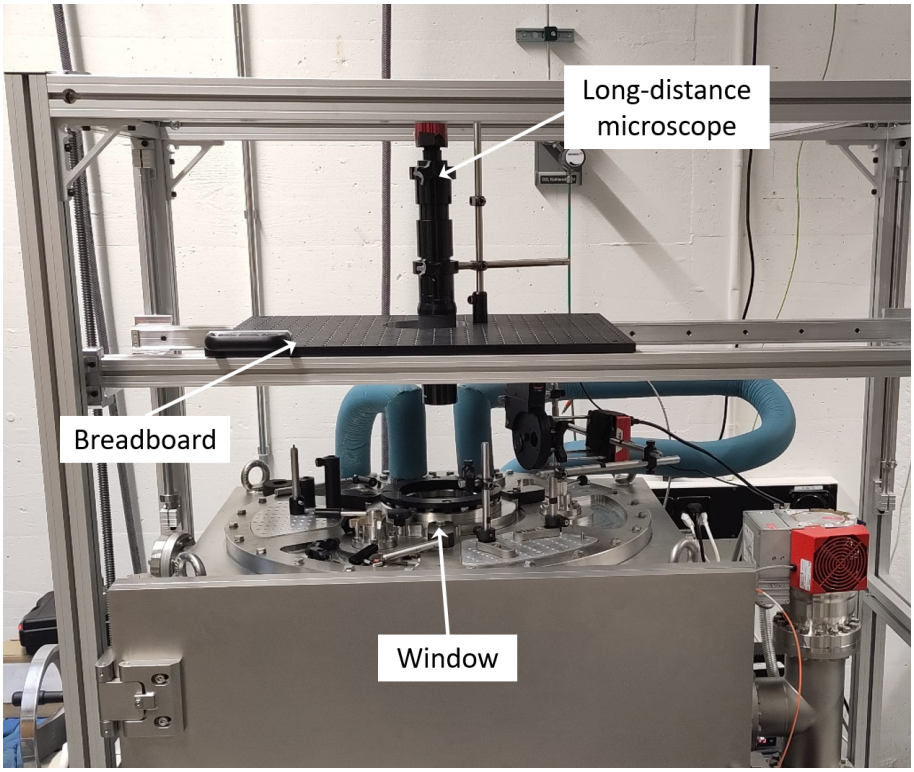

Figure 3.5: I designed a simple frame for placing a movable optical breadboard with a hole on top of the window of SCITEAS-2. The breadboard can be moved laterally, and its height from SCITEAS-2 can be adjusted through a crank. In this way, the optical system can be placed with the right setup on the breadboard beforehand, then moved up to insert the sample, and finally lowered just above the window very quickly.

Every time that we insert a sample inside SCITEAS-2, we have to close the window and place all the optics and tune the observation parameters for optimal acquisition. This process can take several minutes (if no problem arises), and it could prevent the observation of the very first evolution steps of the sample inside the chamber. I designed a simple structure that has been built by an engineer of the Physics Institute and added to SCITEAS-2 in 2022 (Fig. 3.5. One can move the breadboard from the window up to a height of 50 cm with a crank, and laterally to completely clear the space above SCITEAS-2. The breadboard has a circular hole of the same dimension as the window. This system allows to place the optics on top of the breadboard and test them before the experiment, then the breadboard can be moved up, consenting the insertion of the sample, and finally the breadboard can be lowered again above the window. Such a simple mechanism will be useful to start the acquisition process

immediately after the insertion of fast-evolving samples inside SCITEAS-2.

3.2.1 Side-View Setup (SVS) for SCITEAS-2

A drawback of the SCITEAS-2 design is that samples can be observed only from the top. While this is advantageous for certain types of measurements (for instance tracking the spectral evolution of the surface), it complicates any attempt to derive the morphological evolution of a surface, for instance due to superficial ice sublimation.

In order to observe the morphological evolution of sublimating surfaces, I designed an opto-mechanical setup to be inserted inside SCITEAS-2 that could allow a side view on the sample, the Side-View Setup (SVS) (Fig. 3.6). The instrument was built by Mathias Brändli, engineer at the University of Bern.

The philosophy behind the SVS is to have a small enclosure that can be coupled to the helium cryo-cooler head inside SCITEAS-2, with a cold bottom where to place the sample, and a reflective optical system that allows an observer from the top of SCITEAS-2 to observe the sample illuminated from behind (i.e. the silhouette of the object). the SVS is formed by three separable parts, each of them divided by an insulating material layer. The bottom part consists of a heavy copper plate carved in such a way that the sample is placed on an elevated flat surface in the middle. The copper can be plugged exactly to the cryo-cooler head, and through a thin layer of graphite sheet the thermal coupling at low pressures is assured. The middle part consists in two mirrors inclined at 45° respect with the copper plate, a 10x10cm diffusing glass and a structure for accommodating the feeding optical fiber. The optical fiber illuminates the first mirror, that sends the light through a diffusing glass, illuminates the sample on the copper surface, arrives to the second mirror at 45° and is sent back to the observer above the SVS. The diffusing glass removes eventual specular reflections from the first mirror. In this configuration, the observer looking at the second mirror will see a back-illuminated object. The back-illumination is extremely useful when one seeks the maximum contrast between object and background, for instance for measurements of the sample evolution at small scales (in particular when the observer uses a long-distance microscope). The top part is the top of the enclosure, with two holes (one for the fiber and one for observing the second mirror), and a circular ceramic heater embedded on the top enclosure. The heater can be connected to a digital controller outside the chamber, with which one can set the target temperature.

The SVS can be used in a variety of experiments in the laboratory, and if necessary the setup is easily adaptable. Both mirrors can be moved on the horizontal and vertical plane through manual screws, and the optical fiber vertical position can also be adjusted. The diffusing window is fixed with screws, so it can be changed depending on the diffusing power needed, or completely removed. Finally, one can use the SVS in SCITEAS-2 without the top part, if the heater is not needed (configuration like in Fig. 3.6 B). This is particularly useful if the sample observation is performed by an optical system with enough field of view to see both the sample from the top and the second mirror (i.e. the sample from the side). In this case, the illumination from the fiber allows seeing the topography of the sample also when seen from above, since the extremely high incidence light casts shadows in correspondence of local topographic heights. Another useful practice is to attach temperature sensors

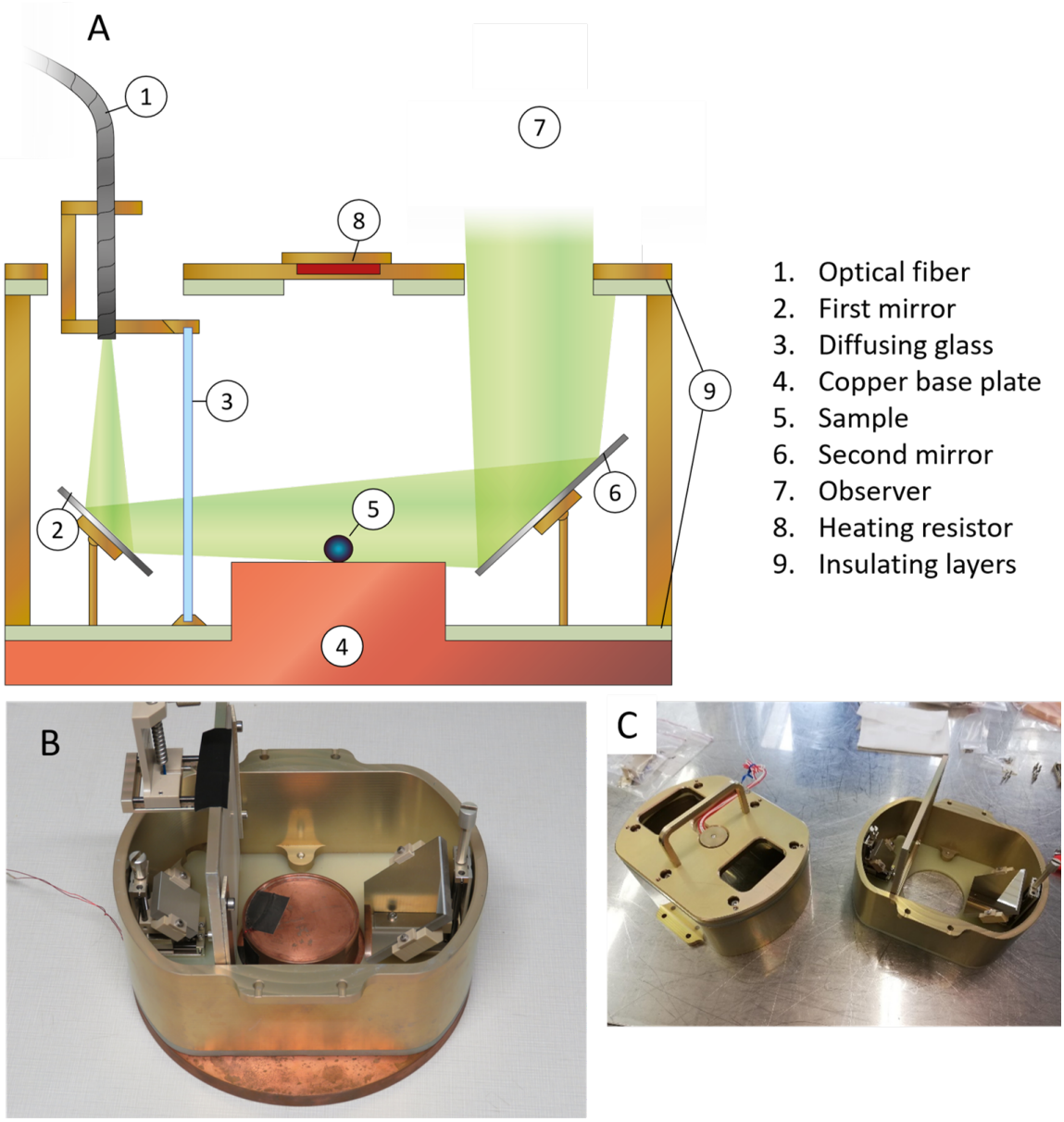

Figure 3.6: The Side-View Setup (SVS) built for SCITEAS-2. A) A scheme of the cross-section of the SVS with all the components, B) view of the SVS bottom and middle part, and C) view of the top part of SVS (left) and middle part (right). Pictures credits: Camila Cesar and Mathias Brändli.

(PT100/PT1000) to the copper base plate, to know the temperature of the surface where the sample lays, and in other parts of the setup. The thermal insulator layers between the bottom, middle, and top part, efficiently contain the thermal conduction when the bottom layer is cooled down to temperatures lower than 100 K (Fig. 3.7). The reason behind inserting insulating materials is to avoid the deposition of volatile species on the mirrors of the middle

layer, keeping them at higher temperature than the copper base plate that acts as a cold trap. Furthermore, the ceramic heater on top also should be insulated from the rest of the structure, to avoid heat conduction to the sample. The heater can then warm up the sample via thermal radiation, setting a gradient of temperature between the top of the sample and the bottom (that has the same temperature as the copper stage).

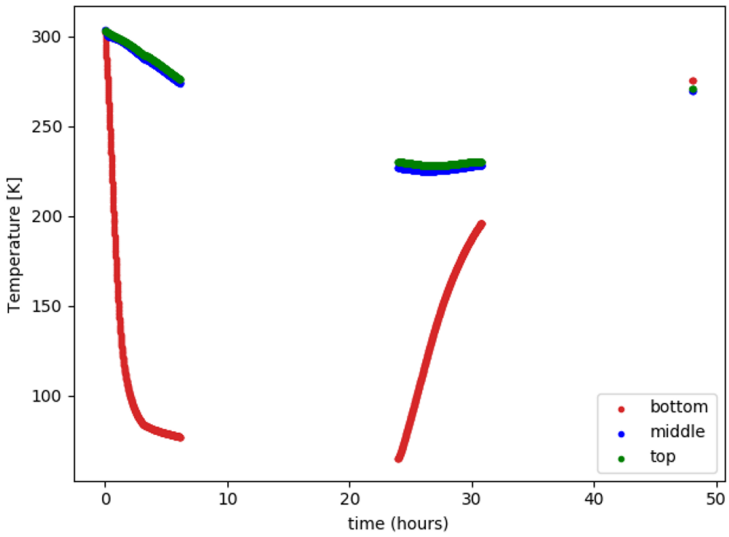

Figure 3.7: When the SVS is plugged on the SCITEAS-2 helium cryo-cooler head, the copper base plate has a good thermal contact with it, allowing to cool down the sample to temperatures lower than 100 K. The insulating layers prevent excessive cooling of the middle part (containing the mirrors) and the top part (ceramic heater). In this way, the copper base plate acts as a cold trap and deposition of frost is not possible on the mirrors, while warming up of the sample by the ceramic heater is also prevented. The measurements were interrupted at 7 and 32 hours due to a malfunctioning of the computer.

The procedure to use the SVS with cryogenic samples is straightforward, but it requires some practice. Before the start of the experiment, the copper base plate should already be placed inside SCITEAS-2 on the He cryocooler head, with a thin graphene sheet between the two. Furthermore, to track the temperature at the base of the sample, it is good practice to tape a PT100 sensor where the sample will lie, outside the field of view of the mirrors. The PT100 sensor must be already plugged to the connectors on the top of the shroud inside SCITEAS-2, possible taping the PT100 wire so that it does not impede the insertion of the rest of the SVS and the observation of the sample. If the top of SVS is needed, then one can attach to the middle part through the appropriate screws holes on the side of SVS. Finally, the light source for illuminating the sample needs to be set up beforehand. Usually, we use a LED light connected to the SCITEAS-2 optical fiber plug. Inside SCITEAS-2 there is another optical fiber with an adapter that is ready to be connected to the one attached to the SVS. Afterwards, I proceed like the following (assuming the top part is needed):

1. I close the chamber and the top window and I start cooling down the copper stage

through the He cryo-cooler. I monitor the changes in temperature of the PT100 placed on the copper plate with the lab computer.

2. In the meanwhile, I prepare the icy sample and I store it in a small aluminum bowl filled with liquid nitrogen to prevent frost formation.
3. I position the rest of the SVS on the top of SCITEAS-2 for faster insertion.
4. When the target copper temperature is reached, I take the bowl with the sample, I open the glass window on the top of SCITEAS-2, and quickly insert my sample on the top of the elevated copper area with a previously cooled spoon.
5. Immediately after, I place the rest of the SVS on top of the copper stage using the handle on the SVS top part, paying attention to not touch the sample with the bottom insulating layer of the middle part of SVS during the insertion.
6. I close the glass window on the top of SCITEAS-2, and open the side door to connect the optical fiber to the other optical fiber connected to the wall plug on SCITEAS-2.
7. I close the lateral door and start the primary vacuum pump.

In case the top part is not needed, one can put the bottom and middle part of the SVS inside the chamber before starting the experiment, cool it down and open the chamber just to put the sample on the copper stage, then close it and start the primary pump.

Since there is some dead time between the insertion of the sample and the activation of the vacuum pump, some frost might condense on the sample. This can be avoided by flushing continuously the chamber with inert gas (like N_2), although one has to pay attention to the oxygen level when opening the chamber and inserting the sample. The procedure is better carried out with the help of another person, also for safety reasons in case of low oxygen levels close to the chamber.

Unfortunately, the pandemic situation in 2020 caused some delays in the construction phase of the SVS, and I only had the chance to test its functionality, and experiment it with pebbles in 2021. For this reason, the results of these experiments have not been included in the published work of chapter 4, but I present them in Annex 4.6.

3.3 The Mobile Hyperspectral Imaging System (MoHIS)

We use the Mobile Hyperspectral Imaging System (MoHIS) to acquire hyperspectral cubes of our samples, which is particularly useful when tracking compositional changes over time (see for instance chapter 4.7). The experimental setup and its coupling to SCITEAS-2 have been thoroughly described by (Cerubini et al., 2022), while the original calibration and acquisition pipeline was developed by A. Pommerol and Z. Yoldi (Yoldi et al., 2021). Since I did not introduce any new protocol or instrumental changes to the MoHIS setup, I will briefly summarize its design and capabilities, while for a full description I redirect the reader to the works of Cerubini et al. (2022) and Yoldi et al. (2021).

The MoHIS setup is composed by a VIS (Thorlabs TSI – 1501M-GE) and a NIR (Xeva – 2.5) camera, mounted on a portable aluminum frame (Fig. 3.8). The two cameras are

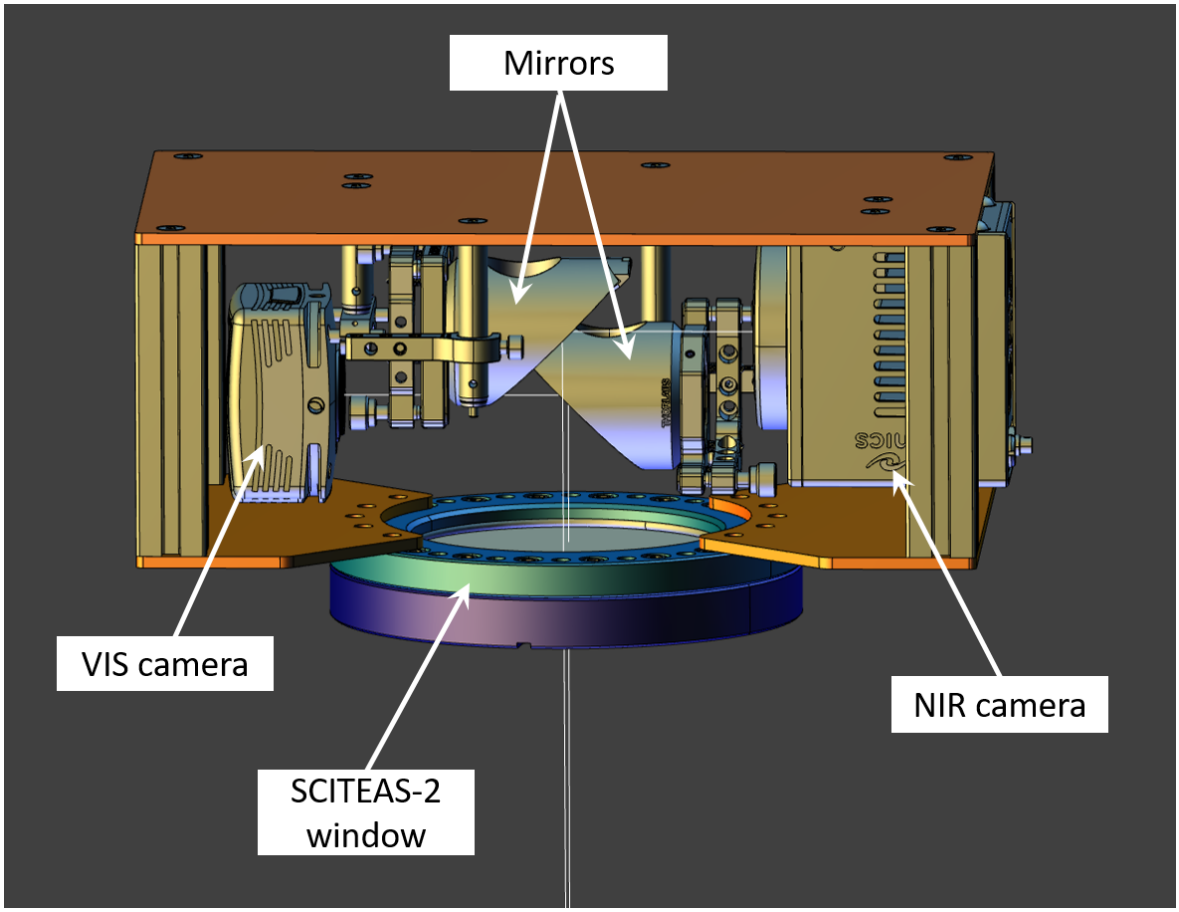

Figure 3.8: Design of the Mobile Hyperspectral Imaging System (MoHIS) setup. An aluminum structure holds a VIS and a NIR infrared camera that are horizontally aligned to two 45° mirrors, allowing them to image a sample placed approximately 50 cm below the setup, sharing the same field of view. The structure can be placed above the window of SCITEAS-2 through four fixed pins.

mounted horizontally and pointed to two flat mirrors that redirect their field of view vertically. The illumination is delivered by an optical fiber bundle (Bundle 500, CeramOptec) mounted close to the VIS camera and directed downward, allowing a small phase angle geometry. On the bottom of the aluminum frame, a perforated plate allows the correct and reproducible positioning on top of the SCITEAS-2 window trough four fixed pins. The optical fiber bundle is connected to a monochromator (previously MS 257, now Quantum Design MSH-300) fed by a light source (50 – 250 W, F2/2 FSA, QTH bulbs). The bulb output is controlled by an intensity controller from Newport Oriel. The entire setup and the computer to control the acquisition are placed on a trolley so that it can be moved in different labs, making it portable and flexible.

Before starting the hyperspectral cube acquisition, both the VIS and NIR cameras are calibrated using a large spectralon (Labsphere) covering the field of view. The calibration is

performed at 560 nm and 560 nm and 1650 nm for the VIS and NIR cameras, respectively. The exposure time is wavelength dependent, and every time the monochromator changes wavelength, a new exposure time is adopted. This means that at the end of the measurement at each wavelength, the pipeline acquires automatically the dark images too. The VIS camera acquires images every 15 nm from 380 nm to 935 nm, and at 800 nm the NIR camera starts acquiring images too, up to 2450 nm, every 6 nm. The VIS and NIR spectra are merged at 920 nm, usually adjusting the NIR spectrum to the VIS one, since the NIR camera is sensitive to temperature changes, while the VIS camera is not.

3.4 Centrifuge for Accelerated Pebbles Observation (CAPO)

After the experiments with pebbles presented in chapter 4, I discovered that pebbles disrupt (when they do) in different ways, due to a varying resistance of the aggregates made with different silicates and dust grain sizes. The Centrifuge for Accelerated Pebbles Observation (CAPO) responds to the need to measure quantitatively the resistance to disruption of a pebble. Initially, I tried using a penetrometer, but unfortunately the force needed to destroy the pebbles was lower than the sensitivity of the instrument (0.02 N). The idea behind CAPO is simple, I want to centrifuge a pebble in a small sample holder, and observe with a camera the centrifugal acceleration at which it disrupts against the wall of the sample holder.

CAPO is a cuboid enclosure with a central rotatory pillar connected to a brushless motor (Faulher DC 100W) through a transmission assy (Fig. 3.9). The pillar itself is connected to two circular plates distant 15 cm from each other. On the bottom side of the top plate, there is an aluminum cage that can host a GoPro camera (model HERO7 Black) and a commercial magnifying lens. The cage is fixed to the top plate with four screws, and the camera faces the edge of the bottom plate. On this edge, directly below the camera, there is a small space where a cubic sample holder can fit. The sample holder is a 1x1x1 cm transparent, polished, PMMA box, with a missing side to insert the pebble, produced by SwissPlex. Below the bottom plate, there is a circular stripe of LED lights (by Simplex) that illuminates the pebble from below over the whole circular movement of the plate. The final result is that, while the plates are moved together by the motor, the camera will see the shadow of the pebble while it is accelerated outward against the external wall of the cubic transparent sample holder. The acceleration felt by the pebble is measured by the GoPro itself, which has a builtin 3-directional accelerometer with an acquisition rate of 4 ms. The controller unit was built from the electronics section of the Physics Institute, and it is provided with a Raspberry Pi accessible by terminal (PuTTY). It is possible to control the maximum rpm of the motor, the speed ramp up time, and the increase of rpm during time (exponential or linear). Note that this does not correspond to the real rpm of the centrifuge, because the inertia of the transmission complex to the middle rotatory pillar does not allow maintaining stable angular speed at low rpm. Generally, I use the exponential ramp up rpm, with the maximum available rpm (2000) and a ramp up time of 10 s. The final centrifugal acceleration at the pebble position looks like the one in Fig. 3.10. The linear acceleration is creating some oscillations detected by the accelerometer, so I did not use it to avoid changes of acceleration of the pebble. The whole centrifuge is enclosed by transparent Plexiglas walls, and has a magnetic break that can stop it quickly for safety.

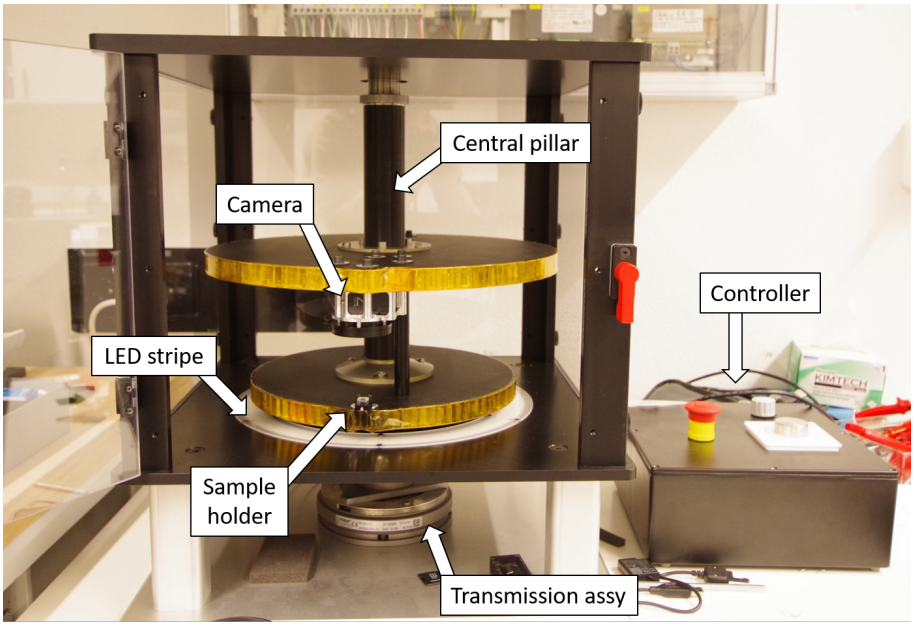

Figure 3.9: The Centrifuge for Accelerated Pebbles Observation (CAPO) setup. The camera and the sample holder are aligned and placed on two different circular plates that are accelerated by the motor underneath. A LED stripe is positioned below the pebble, so that the camera can have better contrast.

In chapter 4, I present an experiment performed with CAPO using PBs made of pyroxene with different grain size distributions. Note that crushing a pebble with the flat head of a penetrometer would cause internal failure of the aggregate due to the internal tensile forces developed when the aggregate is loaded on two sides (i.e. similar to a Brazilian test), and compression forces changing the porosity of the material. In CAPO, in the reference system of the pebble, a wall is compressing the pebble on one side, and changing its structure and porosity. In this perspective, measuring at what acceleration the pebble structure fails is a direct measurement of the compressive strength of the aggregate.

A few improvements can be done to CAPO in the future:

- The PMMA sample holders are worked in such a way that they appear very polished on the external walls to allow better visibility. This process is expensive, and while the external walls are well transmitting, the internal walls have been carved, and are not as polished as the external one, contributing to a certain blurriness of the image. Probably a better result would be achieved just by assembling together the flat PMMA sides with some glue. Another possibility is to cast some clear epoxy in a mold, and make it transparent with polishing paste.
- The imaging capability of the GoPro could be supported by a high speed camera positioned outside, possibly watching at the pebble from the side. To make this possible, we need a new design of the small cage where the sample holders are positioned, so that a side can be clear to observe the pebble.

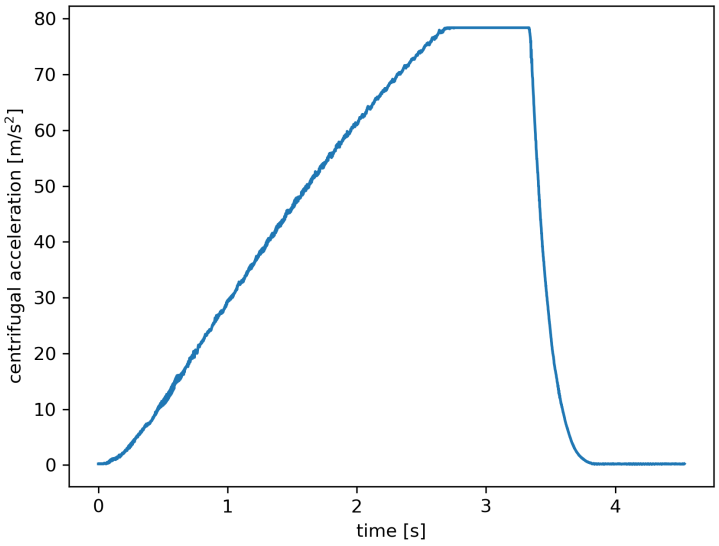

Figure 3.10: Centrifugal acceleration measured by the 3-directional accelerometer inside the GoPro. All the measurements presented in chapter 4 are performed with the same increment of acceleration over time.

- The built-in 3-directional accelerometer of the GoPro saturates at about $78\,\mathrm{m\,s^{-2}}$, so the pebbles that are disrupting at higher accelerations are not measurable. An external accelerometer, or a photodiode on the side of the bottom circular plate that measures the passage of the pebble could be a fast solution for reading higher accelerations.

3.5 The POLarimeter for ICE Samples (POLICES)

We can measure the reflected polarized light from our analogues through the POLarimeter for ICE Samples (POLICES) setup. The initial design is described by Poch et al. (2018), and it has been improved by R. Cerubini, who built a trapezoidal enclosure to better control the atmosphere for the study of icy samples. Finally, L. Patty automatized the pipeline for acquisition and calibration of the polarization data. During my Ph.D. project, L. Patty and I modified the geometrical configuration to achieve very small phase angles (0.8°) and we configured POLICES for experiments with controlled atmosphere and icy samples (chapter 5 and 6).

POLICES is a gonio-polarimeter and consists of an optical module, placed over a trapezoidal enclosure that contains a motorized arm and rotating stage (Fig. 6.1). The optical module is a 25x25x20 cm box that contains a commercial full Stokes polarimeter (Dual PEM II/FS42-47, Hinds Instruments). The light enters through an entrance at the bottom of the optical module, then it encounters two photoelastic modulators (PEMs) oriented at 45° between each other and modulated at resonance frequencies of 42 kHz and 47 kHz. After the two PEMs, the light passes through a polarizer oriented at 22.5° to the two PEMs, and finally to

a lens converging it to a photomultiplier detector (PMT Hamamatsu R928). The aperture of the optical module is about 23 mm wide, and it is aligned exactly over the sample through a hole in the ceiling of the enclosure. Inside the trapezoidal enclosure, the motorized arm holding the collimating head can travel between -30° to 75° to sample normal (i.e. the vertical axis passing through the polarimeter). This means that the inclination of the motorized arm correspond to the observation phase angle (Fig. 5.1). A fiber is connected to either a LED or the monochromator using a halogen light source (as used for MoHIS).

The fiber is attached to a component we refer to as "head" of POLICES. This is the connecting piece between the motorized arm and the optical fiber, which has the purpose of collimating the light to the sample. Originally, the head used by Poch et al. (2018) consisted only of a parabolic mirror inside a small box, with the optical fiber launcher on the side. In their experiments, they used LEDs as light source, and the LEDs intrinsic polarization coupled with the interaction with the mirror, caused a remnant linear polarization of 2.4% of the incidence light on the sample. Generally, the polarized reflected light from a surface depends on the polarization state of the incident light, so they had to calibrate the polarization surface with a spectralon. Unfortunately, there is no standardized target to correct the reflected polarized light in the literature, causing variability between different instruments.

3.5.1 Improvements to POLICES

After the experiments performed by O. Poch and R. Cerubini, POLICES has been used by L. Patty to measure the reflected circular polarization of photosynthetic organisms (Patty et al., 2022). He improved the setup by introducing a new motorized horizontal stage below the sample, which could rotate it on the azimuthal plane (Fig. 5.1). The horizontal motorized stage allows removing geometrical effects caused by sample structural alignment or by tilts or irregular surface of the sample, by averaging the linear polarization at a fixed phase angle over 8 azimuthal sample positions. Furthermore, he developed an automatized pipeline for acquiring polices data and saving them in an organized way.

To perform the experiments presented in chapter 5, I collaborated with L. Patty to improve the geometrical precision and the data analysis of POLICES. First, we modified the optical path of the incidence light to remove the remnant linear polarization (Fig. 3.11). The polarization of the light emerging from the monochromator is firstly spatially randomized by a 1" LCP Achromatic Depolarizer (Thorlabs DPP25-A). Then, the beam is focused to the fiber by a system of two converging lenses. The optical fiber is 1 m long and contributes to spatially scramble the polarization, effectively disrupting the fast-axis pattern of the depolarizer. To avoid reflective optics, the head consists of a half inch lens tube containing three lenses that collimate the final beam to the sample. The remnant polarization has been measured directly shining the light from the head to the polarimeter aperture, and is lower than 0.01%, which agrees well with the level of polarization of the Sunlight. This low level of remnant polarization is achieved through the wavelengths between 450 nm and 750 nm. Furthermore, the small diameter of the lens tube (18 mm) allows the head to get very close to the vertical axis between the sample and the polarimeter. In this way, we managed to decrease the minimum phase angle from $\sim 2^\circ$ (Poch et al., 2018) to 0.8°, that can be very useful for future studies of the opposition effect.

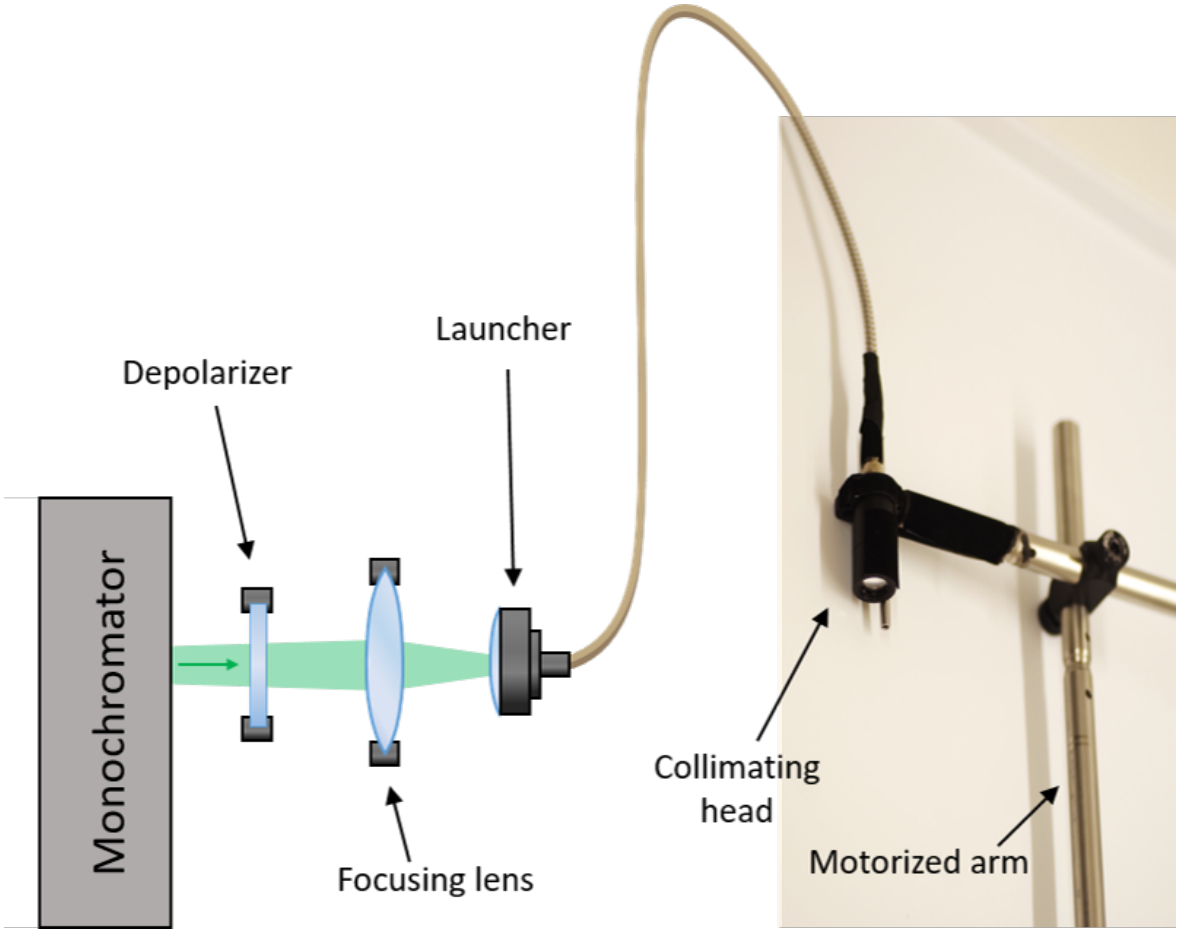

Figure 3.11: The optical path of the incident light in POLICES. A monochromator selects a wavelength from the light produced by a filament bulb. The monochromatic light emerging from the slit passes through a depolarizer, to ensure time and spatial depolarization. Then the beam it is focused by a converging lens and a launcher which feeds an optical fiber. In the optical fiber, the internal reflections contribute to the spatial depolarization. The head itself is a small tube with three lenses that collimate the light beam.

Lastly, we tested POLICES for the measurement of icy samples in controlled atmospheric conditions. There are several problems that make extremely difficult the measurements of icy samples with POLICES. First of all, the POLICES enclosure is not sealed, and air can pass through the interstitial spaces and the bottom breadboard. This means that the cryogenic sample undergoes quickly frost condensation, that can completely cover its polarization properties (see chapter 6). The second problem is that maintaining the sample at cold temperatures for long measurements was very difficult, since cooling was only possible by accessing the chamber and introduce fresh liquid nitrogen to top up the sample holder. This lead L. Patty and K. Kipfer to design a new cryogenic sample holder specifically for POLICES, which was tested by me and L. Patty. The cryogenic sample holder (called hereafter cryo-stage) consists of a copper hollow cylinder with inlet and outlet pipes, on top of which a small alu-

minum sample holder (approximately 7 cm diameter) can be placed (Fig. 3.12). The sample holder has a small lid that is used to cover the sample to avoid frost formation.

We use two nitrogen tanks to actively cool the cryo-stage. The first one is attached to the inlet pipe, and it is filled with liquid nitrogen, while the second tank is connected to the outlet pipe, and is completely empty. A gardening pipe is attached to the exhaust valve of the second tank, it passes through a box filled with hot water, and is connected to the POLICES enclosure. The enclosure has a plastic glove to manipulate the sample holder when necessary.

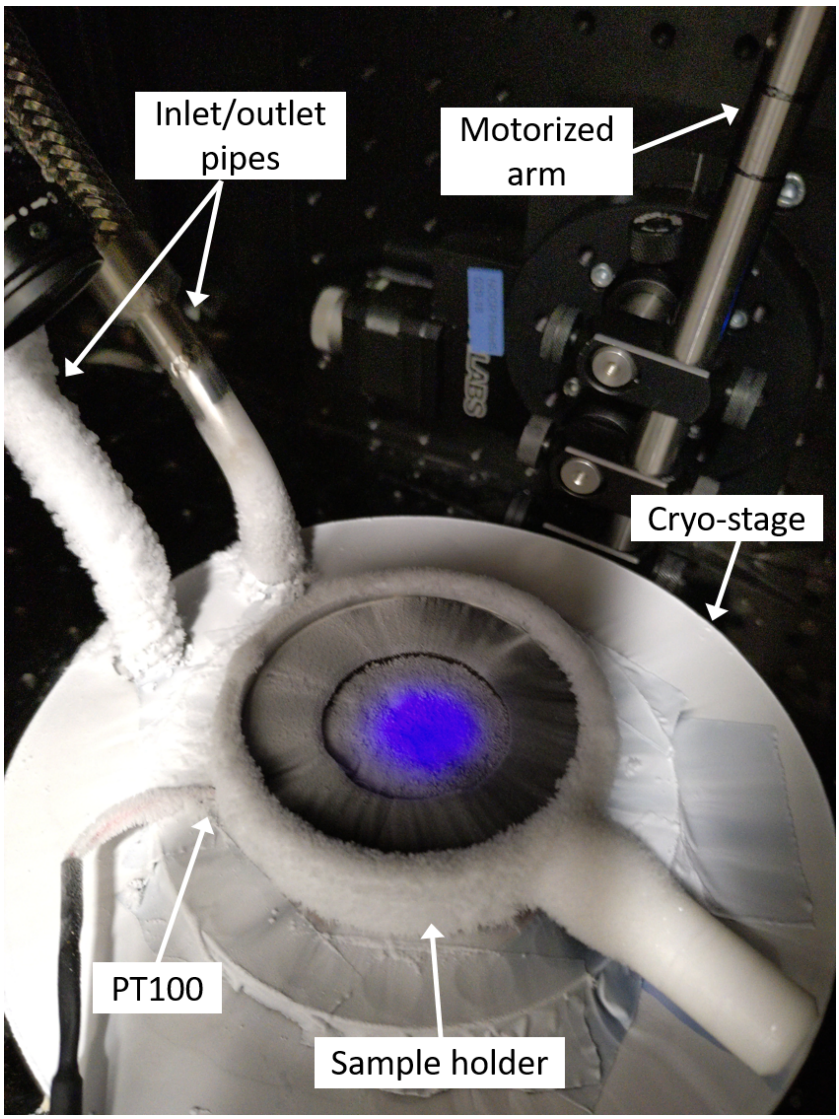

Figure 3.12: The cryo-stage for POLICES. The head held by the motorized arm sends a collimated spot of light on top of the sample, contained in a small volume carved in the sample holder. A PT100 thermal sensor is beneath the sample surface. The sample holder lies on top of the cryo-stage, that is a copper hollow cylinder in which liquid nitrogen can flow through the inlet and outlet pipes.

We created a protocol for the production of frost on top of cold dust samples. The procedure to cool down the cryo-stage, flush the chamber, and prepare the sample for the polarization measurements is the following:

1. I fully open the exhaust and inlet valve of the second tank;
2. I open the inlet valve of the first tank. Since the pressure is higher than the second tank, the nitrogen will start flowing into the cryo-stage, and back to the second tank;
3. Since the second tank is at room temperature, the nitrogen immediately evaporates and is pushed through the exhaust valve in the gardening pipe, and flows quickly to the POLICES enclosure. The temperature of the sample is continuously monitored with a Python program which reads the signal of the PT100 thermal sensor. The humidity level inside the chamber is monitored by a humidity sensor that saturates at about 5% relative humidity. Any percentage between 5 and 8% indicates that the chamber is well flushed by nitrogen;
4. When the temperature is about 25 K higher than the target temperature, I close the first tank inlet valve. The remaining nitrogen inside the cryo-stage will continue to cool the sample for about half an hour. Afer that, the temperature will increase logarithmically at slow pace (see Fig. 6.3);
5. I remove the lid from the sample holder, exposing the sample to the nitrogen atmosphere of the POLICES enclosure;
6. I start the data acquisition with POLICES to acquire the first polarization data from the pristine cold sample surface;
7. after the first measurements, I can start the frost deposition by letting the air entering the enclosure. I simply remove the gardening pipe attached to the exhaust valve of the second tank from the enclosure.

In this way, our samples remain cold for long times and can be protected from unwanted frost formation at the beginning of the experiment, when we cool the cryo-stage down. Frost formation is also dependent on the sample material, and we found that exposing the sample to the atmosphere during the cooling of the cryo-stage is more effective in preventing frost formation (see section 6.4.3).

Maintaining the sample at a fixed temperature is very difficult. When the inlet valve of the first tank is open, the nitrogen starts flowing through the cryo-stage, but we do not know the nitrogen flux, which depends on the initial pressure of the first tank, on the temperature of the second tank, and how much the valve is open. Usually, the temperature of the sample is sensitive to the flux of nitrogen, and it either increases or decreases over time, but it is never stable. Without quantitative measurements of the nitrogen flux within the cryo-stage, it is not possible to target a flux that maintains a target sample temperature over time. The only way to stabilize the temperature of the sample would be continuously opening and closing the inlet valve, alternating a decrease of temperature to an increase of temperature phase around the target temperature. Unfortunately, closing or opening the inlet valve causes an increase or decrease of frost deposition rate, respectively. We believe that when nitrogen is circulating

through the cryo-stage, the humidity of the cold air immediately over the cryo-stage is lower than when we close the valve and stop the circulation of nitrogen (i.e. the cryo-stage is warming up). This is evident from some initial measurements of frost formation, where the closing or opening the inlet valve directly cause a change of the reflectance of the sample (Fig. 3.13). This is the reason why opening and closing the inlet valve is not advisable for studying the frost. In order to achieve a good repeatability between experiments, we let the cryo-stage temperature increase over time by closing the inlet valve.

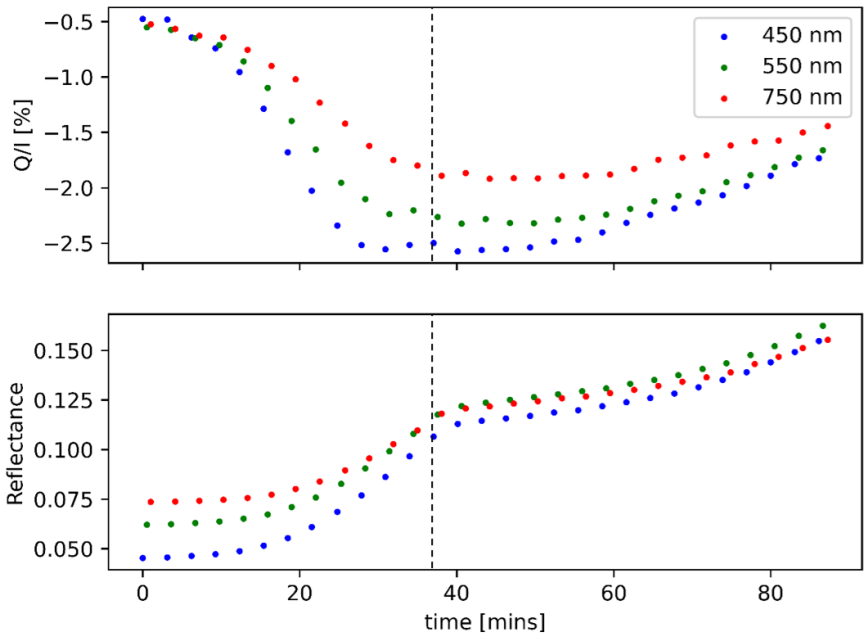

Figure 3.13: The frost deposition rate depends on the temperature of the cryo-stage. In this experiment, we let frost deposit on top of CR asteroid simulant, and we realized that the temperature was increasing more than expected, so we tried to compensate it by opening the inlet valve more at t=36 min from the beginning of the measurements (dashed line). Immediately after, the reflectance of the sample plateaued. This means that the frost deposition rate decreased importantly because we were cooling down the cryo-stage.

Chapter 4

The fate of icy pebbles undergoing sublimation in protoplanetary discs

This is a pre-copyedited, author-produced PDF of an article accepted for publication in Monthly Notices of the Royal Astronomical Society following peer review. The version of record Monthly Notices of the Royal Astronomical Society (2021), 509(2), 2825–2835 is available online at: https://doi.org/10.1093/mnras/stab3196.

Stefano Spadaccia[1], Holly L. Capelo[1], Antoine Pommerol[1], Philipp Schuetz[2], Yann Alibert[1], Katrin Ros[3] and Nicolas Thomas[1].

[1] Space Research and Planetary Sciences Division, Physikalisches Institut, University of Bern, Sidlerstrasse 5, 3012 Bern, Switzerland
[2] Lucerne University of Applied Sciences and Arts, Technikumstrasse 21, 6048 Horw, Switzerland
[3] Lund Observatory, Department of Astronomy and Theoretical Physics, Lund University, Box 43, 221 00 Lund, Sweden

Abstract

Icy pebbles may play an important role in planet formation close to the water ice line of protoplanetary discs. There, dust coagulation is more efficient and re-condensation of vapor on pebbles may enhance their growth outside the ice line. Previous theoretical studies showed that disruption of icy pebbles due to sublimation increases the growth rate of pebbles inside and outside the ice line, by freeing small silicate particles back in the dust reservoir of the disc. However, since planet accretion is dependent on the Stokes number of the accreting pebbles, the growth of planetesimals could be enhanced downstream of the ice line if pebbles are not disrupting upon sublimation. We developed two experimental models of icy pebbles using different silicate dusts, and we exposed them to low-temperature and low-pressure conditions in a vacuum chamber. Increasing the temperature inside the chamber, we studied the conditions for which pebbles are preserved through sublimation without disrupting. We find that small silicate particles ($<$50 µm) and a small quantity of ice (around 15% pebble mass) are optimal conditions for preserving pebbles through sublimation. Furthermore, pebbles with coarse dust distribution (100$-$300 µm) do not disrupt if a small percentage (10$-$20% mass) of dust grains are smaller than 50 µm. Our findings highlight how sublimation is not necessarily causing disruption, and that pebbles seem to survive fast sublimation processes effectively.

4.1 Introduction

Protoplanetary discs are collapsed clouds of gas and dust surrounding young stars. From micrometer-sized dust particles, planetary embryos form and a completely new planetary system appears eventually. The direct growth of dust up to the size of planetesimals (1$-$10 km) is inhibited. Particles bigger than mm-size tend to disrupt in collisions, and boulder-size objects interact heavily with the gas in the disc, losing angular momentum and drifting toward the central star (Weidenschilling, 1997; Blum and Wurm, 2008; Birnstiel et al., 2012). Streaming instability (Youdin and Goodman, 2005b; Johansen and Youdin, 2007) is a promising mechanism to overcome this inhibition and actually form planetesimals: mm-cm size aggregates (referred hereafter as 'pebbles'), when numerous enough, concentrate in filaments in the disc, these latter eventually collapsing to form planetesimals.

In this scenario, ice lines in the disc can play a key role in planet formation. The ice line of a certain volatile species in the disc is the location where the temperature is low enough to condensate the volatile into its solid phase (ice). Around the water ice line, the temperature is high enough ($>$170 K) that the surface energy of water ice is sufficient to allow icy particles to grow via coagulation (Gundlach and Blum, 2014b; Musiolik and Wurm, 2019). Furthermore, ice sublimation at the ice line causes vapor diffusion and re-deposition outside the ice line, enhancing pebble growth and potentially triggering streaming instability (Drążkowska and Alibert, 2017; Ros et al., 2019). Understanding the physics and chemistry of icy pebbles and the phase changes of volatiles is thus paramount for understanding planet formation processes close to the ice lines.

What is the composition of an icy pebble? We can retrieve some information about peb-

bles from comets, which are thought to be thermally unaltered objects and preserve pristine materials from the disc in their nuclei. Measurements by the *Rosetta* instrument GIADA of the dust ejected from comet 67P/Churyumov–Gerasimenko (67P hereafter) constrain the porosity of the putative pebbles composing the nucleus of the comet to $\sim 50\%$ (Fulle et al., 2016). Experiments on dust aggregates showed that a highly porous aggregate (85% porosity) can be compacted down to 60% porosity, simulating compaction by collisions between pebbles in an accretion scenario (Weidling et al., 2009; Jutzi et al., 2009). Furthermore, Blum et al. (2017) suggest that pebbles with a size range of $3 - 6$ mm are present in the nucleus of 67P and that the interstitial space between pebbles is filled with fluffy fractal aggregates. The measurements of the CONSERT instrument allowed deriving a dust-to-ice volume ratio of 67P in the range of $0.4 - 2.6$ (Kofman et al., 2015). These data depict a pebble formed outside the ice line as a mm-size porous aggregate, formed by ice and small dust grains, with a variable ice-to-dust ratio.

Although pebbles are porous aggregates of refractory and volatile materials, several studies of dust evolution in protoplanetary discs handle them more simply as compact spheres made with a specific composition of volatiles and refractory compounds (Barrière-Fouchet et al., 2005; Gonzalez et al., 2015; Drążkowska and Alibert, 2017; Schoonenberg and Ormel, 2017). This assumption may be insufficient to correctly describe coagulation processes and pebble-to-pebble collisions, but it offers a great simplicity for the purpose of modeling other dynamical processes.

The fate of icy pebbles undergoing sublimation is important to understand if the refractory materials embedded in the pebble are released back to the disc or if the sublimated pebble manages to maintain its integrity without disrupting. Many theoretical studies assume that pebbles disrupt through ice sublimation, with important consequences on planetesimals growth. Saito and Sirono (2011) and Ida et al. (2016) showed how disruption of icy pebbles drifting toward the central star through the ice line enhances the dust local density and triggers gravitational instability in the vicinity of the ice line. Schoonenberg and Ormel (2017) use a simple model of pebbles in their simulations, and find that disruption of pebbles through the ice line and ice deposition enhance pebble growth, in particular outside the ice line. Their pebbles are compact spheres made of 50% water ice and 50% silicates. In their work, they consider two mixtures of dust and water ice: one type of pebbles has a compact silicate core and a shell of ice ("single-seed model"), while the other one is a homogeneous mixture of µm-sized ice and silicates particles ("many-seeds model"). They assume two different behaviors of these pebbles once they drift through the ice line. The single-seed model sublimates the ice shell, leaving behind the compact silicate nucleus as a remnant. The many-seeds model sublimates the ice particles and releases small silicate particles. In the case of the many-seeds model, Schoonenberg and Ormel (2017) found an enhancement of dust-to-gas ratio interior to the ice line (but less than Saito and Sirono (2011) and Ida et al. (2016)) and outside the ice line, due to the fact that the released small silicate particles couple with the gas and diffuse outward, sticking to the icy pebbles outside the ice line. Interestingly, the results from Schoonenberg and Ormel (2017) do not change considering the porosity of pebbles: increasing porosity would increase the sublimation rate, but even increasing it by a factor 100 would not affect the consequent dust enhancement. Similarly, Hyodo et al. (2021) found different dust enhancement and planet formation pathways around the ice line, through

pile-up of icy pebbles outside the ice line and of small silicate grains inside the ice line. The general assumption in these works is that sublimation of ice is breaking the adhesion forces between dust grains inside the pebble, causing its disruption. Aumatell and Wurm (2011) created in the laboratory aggregates of condensed ice crystals and studied their disruption by sublimation while levitating. They found that those fluffy aggregates are easily disrupted though a fast sublimation, but they did not include dust grains in their experimental models. Understanding if icy pebbles are disrupting throughout sublimation is essential to investigate the processes that would lead quickly to the formation of planetary embryos in the proximity of ice lines.

In addition, pebble accretion in general depends strongly on their Stokes number, and therefore on their size and structure (note that a fluffy structure could lead to a drag coefficient very different from the usually assumed drag coefficient of a sphere). Understanding the disruption of pebbles at the ice line could therefore have important consequences on the formation timescale of all planets located inside the ice line. For example, Morbidelli et al. (2015a) explained the 'great dichotomy' of the Solar System (the fact that inner planets are dry and small whereas outer planets are wet and large) by the difference between the accretion rate inside the ice line and outside it, itself resulting from both the change of mass (reduction of 50% of the mass flux due to the evaporation) and of radius. Such a scenario would be put into question, at least partially, in the case where pebbles would keep their structure while crossing the ice line.

We present here new experiments on the structure of pebbles composed of water ice and silicates when they are free to sublimate in vacuum with increasing temperature. The goal of the present study is to characterize the different outcomes of sublimated icy pebbles (disruption or preservation), and understand how the environment and the composition of the pebbles determine the final outcomes of the sublimation.

The experiments aim at answering these scientific questions:

1. Are icy pebbles always disrupting due to sublimation of ice?
2. Does the dust-to-ice ratio influence pebble disruption?
3. What is the role of the dust size range in the disruption due to sublimation?

The structure of the chapter is the following. Section 4.2 presents the material used, the new pebble production methods and their features, and the experimental setup used. In section 4.3, we summarize the experimental results. Discussion of the results and future experiments are presented in section 4.4. Finally, we conclude with our main findings in section 4.5.

4.2 Material and Methods

The necessity of simulating cold planetary and space environments lead to the development of the SCITEAS-2 (Simulation Chamber for Imaging the Temporal Evolution of Analogue Samples version 2.0) vacuum chamber, which provides a low-pressure and low-temperature environment for the sublimation of icy samples, with the possibility to acquire spectral mea-

surements of the samples over time (Pommerol et al., 2015a). Two types of icy particles have been developed as analogs for icy planetary surfaces: flash-cooling of small water droplets produces two different spherical particles with size distributions peaking at 4 and 70 µm. These particles can then be mixed with dry dust in two ways (Pommerol et al., 2019a; Poch et al., 2016): through intra-mixture (i.e. dust particles embedded in icy particles) and inter-mixture (i.e. dust particles mixed externally with the icy particles). From such ice particles, it is difficult to create mm-sized aggregates. Therefore, we developed new methods for creating compact pebble-size mixtures of ice and dust.

The evolution of realistic pebbles at the ice line is a complex problem. The chemical composition of the dust, how it is mixed with ice, the dust size distribution, the presence of organics and salts, and the overall amount of water ice in the pebble are concurring to the outcome of the sublimation process.

4.2.1 Dust composition

Infrared observations of protoplanetary discs have shown an abundance of silicates, both in crystalline and amorphous form. In particular, Mg-rich endmembers of olivine and pyroxene are common (Natta et al., 2006). Alongside silicates, materials that are more refractory are produced close to the star, such as corundum, anorthite, hibonite, perovskite, and spinel. These are the first minerals formed in the protoplanetary disc, and a certain amount can diffuse in the outer disc through processes such as turbulence, meridional flows, and X-winds (Watson et al., 2009). The outward diffusion of a certain amount of highly refractory minerals is demonstrated by their presence in comets, which never left the cold outer disc since their formation (Simon et al., 2008).

A precise 'recipe' for pebble dust mineralogy is difficult to establish, since we do not know the relative abundances of the different minerals and since they are not evenly distributed within the disc and undergo different processes during the disc lifespan. In order to compare our results to previous theoretical studies of protoplanetary disc evolution, we used two different silicates as analogs for the mineral dust: olivine and pyroxene. The list of powders used in the present work is provided in Table 4.1. Different grain size ranges have been obtained by grinding the dust in a mortar and dry sieving it.

The two dust species have been analyzed through scanning electron microscopy (SEM) to check qualitatively the difference in the grain surfaces and the amount of fine material of the two silicates (Fig. 4.1). We do not see evidence for significant differences in the amount of very fine grains (<5 µm) and the surfaces of the grains appear relatively similar. The only notable difference is the sharper aspect of the edges of the olivine grains with respect to pyroxene. Unfortunately, it is not possible to derive the overall dust size distributions from the SEM images, which could explain some differences observed between the behaviours of pebbles made of olivine and pyroxene (see section 4.4.4). Following the sublimation experiments, we collected the desiccated dust and measured its near-infrared reflectance spectrum to look for possible signs of aqueous alteration (Fig. 4.2). None of the absorption features indicative of hydration and hydroxilation (around 1.4 and 1.9 µm, see Noe Dobrea et al. (2003); Pommerol and Schmitt (2008)) are visible.

Table 4.1: List of silicates used in the experiments.

Properties	Olivine	Pyroxene
Aspect	Green powder	Gray powder
Initial grain size [µm]	$0 - 3000$	$0 - 1000$
Density [$\mathrm{g\,cm^{-3}}$]	3.3	$3 - 4$
Quarry location	Norway	Brazil
Provider	Microbeads AG	UCF & Deep Space Industries

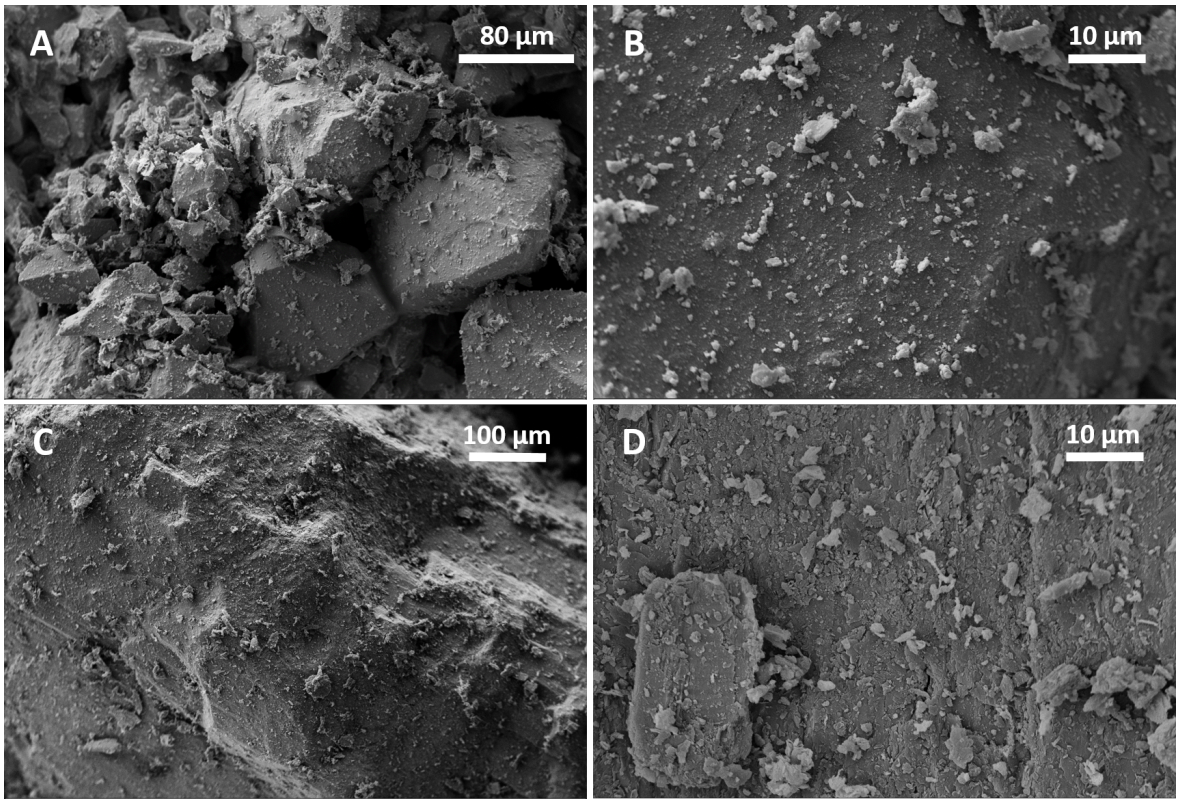

Figure 4.1: SEM images of olivine and pyroxene grains. A) and B) olivine dust at different magnifications. C) and D) pyroxene dust at different magnifications.

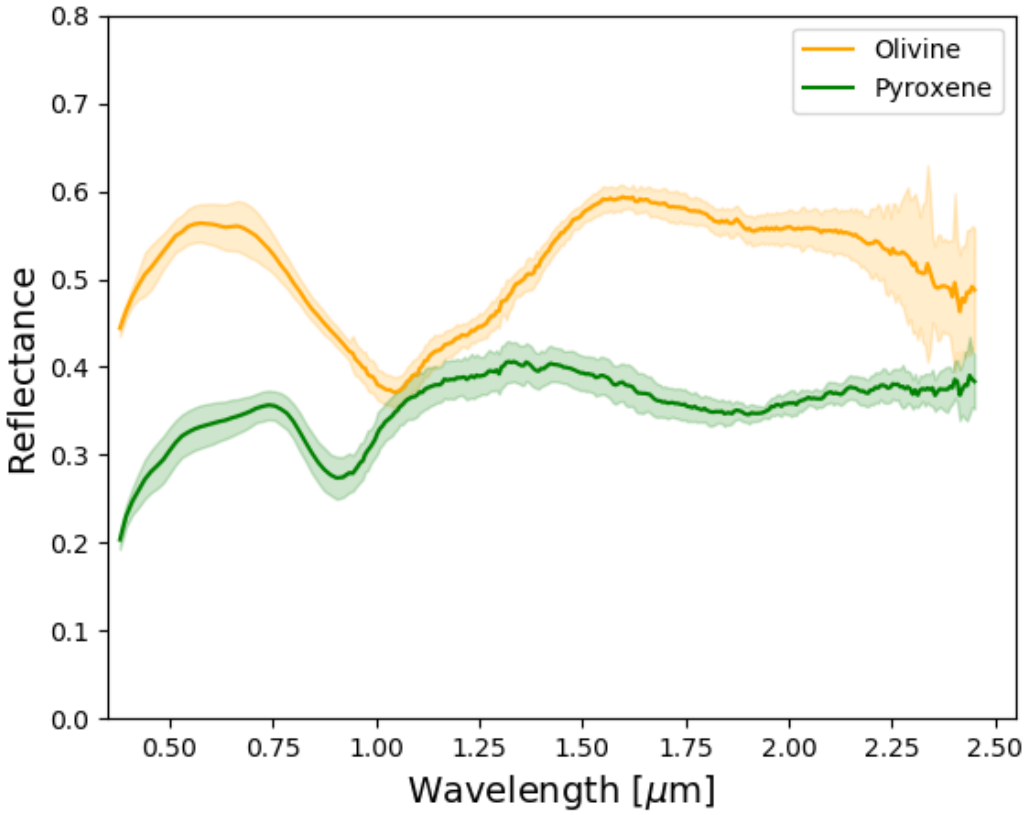

Figure 4.2: Visible and near-infrared reflectance spectra of olivine and pyroxene powders collected from the desiccated pebbles at the end of the sublimation experiments. The spectra do not show the absorption features associated with aqueous alteration at 1.4 and 1.9 µm. The shadowed region indicates the pixel variance of the reflectance in the selected region of interest defined to derive an average spectrum from hyperspectral cubes.

4.2.2 Sample preparation and analysis

In the rest of the paper, we refer to the two pebble models as pebble type-A (PA) and pebble type-B (PB). The main difference between the two production methods is the amount of water ice of the pebble and the relative ice-dust distribution inside the pebble. Both PA and PB are compact aggregates, and their initial porosity is negligible. Table 4.2 collects the main features of PA and PB pebbles.

The two types of pebbles were analyzed with X-ray computed tomography (XCT) technique, to detect the relative distribution of dust and ice inside the pebbles. The measurements have been carried on a Diondo 2 system manufactured by Diondo (Hattingen, Germany) at the Lucerne Computed tomography Imaging facility at Lucerne University of Applied Sciences and Arts. For both measurements, the microfocus tube XWT−225 TCHE+ from X-ray

Table 4.2: Summary of pebble type-A (PA) and pebble type-B (PB) main features.

	PA	PB
Shape	Spheroidal	Irregular spheroid
Ice mass content [%]	50 ± 10	15 ± 7
Typical size [mm]	$1 - 5$	$2 - 7$
Dust distribution inside the pebble	Homogeneous or in one half of the pebble	Homogeneous

WorX has been set on an acceleration voltage of 120 kV and a tube current of 80 µA and an aluminum filter with 1 mm thickness was employed. The detector VAREX 4343CT was configured with a capacity of 8 pF, and integration time of 1 s. The field of view of the detector was adjusted to match the extension of the sample with source object distance of 37 mm, and a source-detector distance of 851 mm. For the measurement of the olivine and the pyroxene sample, 1900 and 1600 projections of the object spinning around a fixed axis in equiangular steps were recorded, respectively. The recorded projections were reconstructed using the Feldkamp-Davis-Kress algorithm as integrated in the CERA suite from Siemens (Erlangen, Germany). The virtual cross-sections had a voxel size of 6.5 µm isotropically and were analyzed with Volume Graphics Studio Max 3.3 from Volume Graphics (Heidelberg, Germany) and imageJ (Schneider et al., 2012).

PA production

The PA production method takes advantage of the behavior of water on superhydrophobic surfaces. Superhydrophobic surfaces have micrometric "spikes" which, combined with the surface tension of water, allow the liquid to rest on the top of the asperities. The water flowing on the superhydrophobic surface captures any dust deposited on the top of the spikes in a process called "self-cleaning" (Marmur, 2004). An inclined plane coated with superhydrophobic paint (Cytonix WX2100 aerosol) is placed above a bowl full of liquid nitrogen (Fig. 4.3). On the surface, some dust is deposited with a spoon, distributing it on the surface as homogeneously as possible. A droplet of distilled water, created with a micropipette, rolls and captures the dust deposited on the plane, and then sinks in liquid nitrogen where the water freezes.

The droplets created with the micropipette are typically about $2 - 3$ mm in diameter, but sometimes a droplet impinging the plane can split and create secondary droplets of about 1 mm in diameter, which capture the dust in the same way as the bigger droplets.

The dust collected by the droplets on the plane would tend to remain on the surface of the droplet because of the centrifugal force and surface tension of water. On the other hand, if more dust is collected, the grains that are already embedded in water are gradually pushed toward the center of the droplet. In the limit case, if the droplet is saturated with dust, the water does not interact with the superhydrophobic plane anymore and the drop stops on the inclined plane. When a droplet sinks into liquid nitrogen, the inverse Leidenfrost effect (Thimbleby, 1989; Adda-Bedia et al., 2016) prevents the droplet to freeze instantly, and the dust captured by the droplet can move under gravity inside the liquid core of the pebble. In this way, it may happen that the frozen pebble has a heterogeneous distribution

of the dust inside it, with more dust on one half due to the gravity acting on the dust grains during the freezing process. This heterogeneity may not happen when the droplet is small (like secondary droplets): in this case, the freezing process is fast and the grains are 'trapped' homogeneously inside the pebble (Fig. 4.4). In this work, we refer by "heterogeneity" to the overall misplacement of grains with respect to the ice inside the pebble, while we make no assumption on the homogeneity of the spatial distribution of the grains with respect to each other.

The ice-dust ratio was estimated by weighing the pebble before and after the evaporation of the water. The ice mass was found to be in the range of $(50 \pm 10)\%$ of the whole pebble mass. It can happen that a droplet does not catch much dust and has a higher ice content, but since the experiments involve several pebbles in the same sample holder, an average value is more indicative.

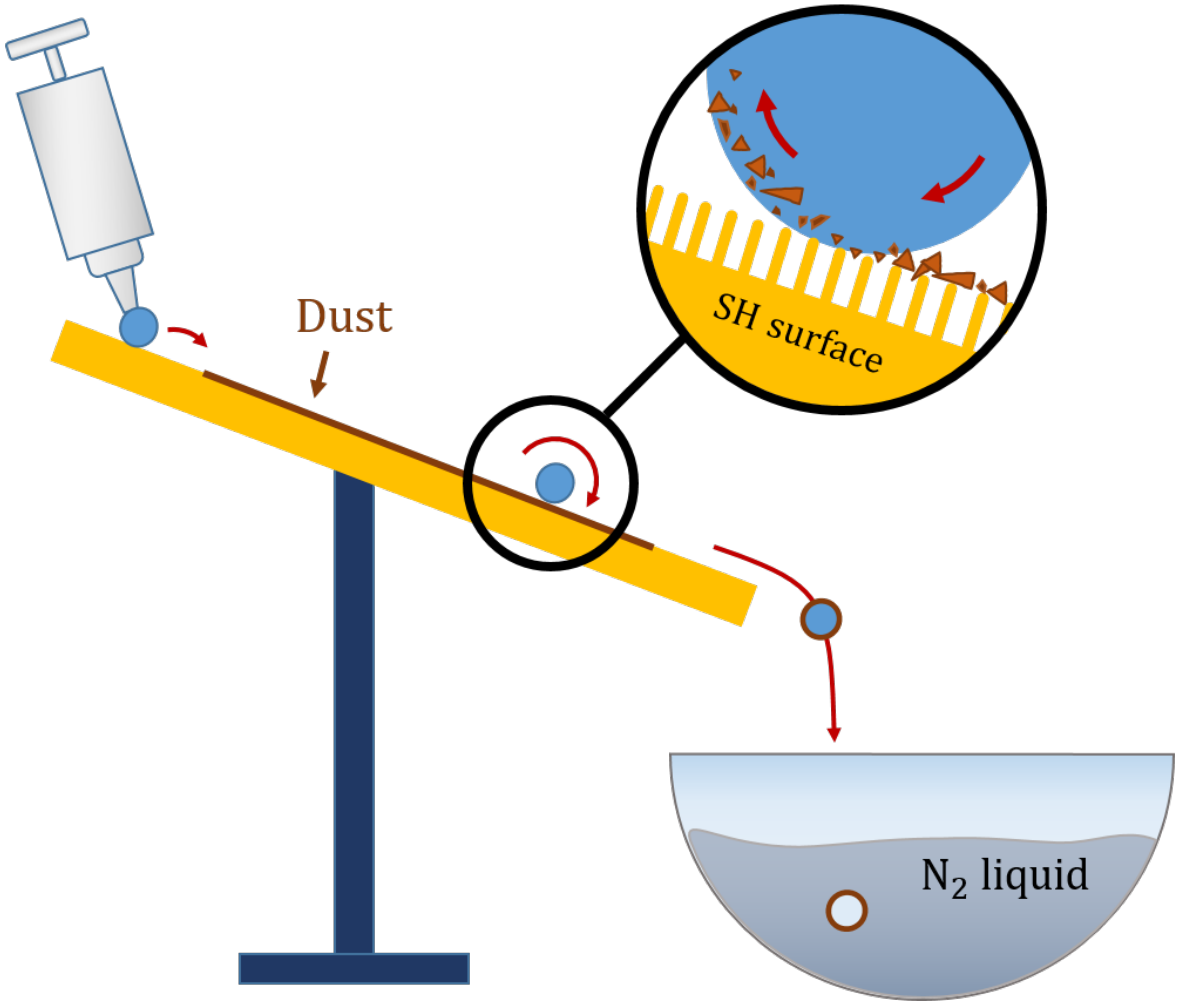

Figure 4.3: The procedure for PA production. A droplet created with a micropipette rolls over a superhydrophobic (SH) inclined plane, and it catches the dust deposited on it. Then, the droplet sinks into liquid nitrogen (N_2 liquid), where water freezes in a few seconds.

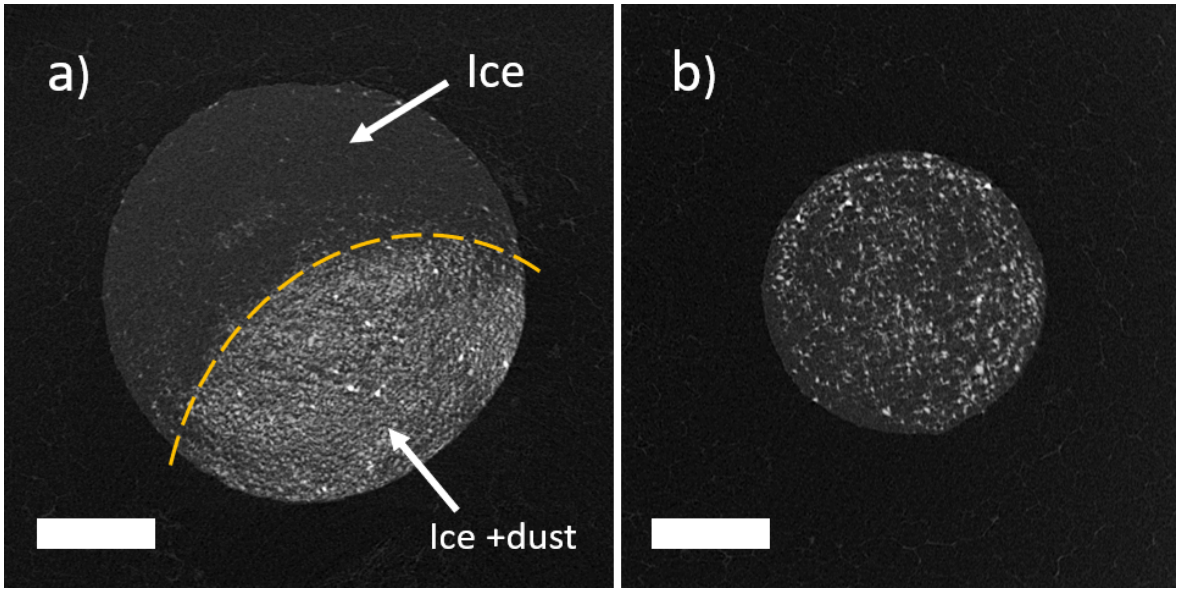

Figure 4.4: X-ray tomography of PA icy pebbles analogues made with olivine (dust size smaller than 50 µm). The circle in the center is the cross-section of an icy pebble. a) This PA clearly shows a heterogeneous spatial distribution of ice (dark gray material on the top) and dust (light gray material on the bottom), well distinguishable from each other. b) This PA contains an internally homogeneous distribution of dust grains. The scale bar for both images is 1 mm.

PB production

The second type of pebbles uses the capability of liquid water of linking small dust particles through capillary bridges, also called 'wet granulation' (Iveson et al., 2001). A 1 cm thick layer of dust is settled in a small vessel. A droplet of water is produced with a micropipette above the dust. The droplet impinges the dust layer with enough momentum to get a fast interpenetration between water and dust particles. The final wet aggregate is stable because of the capillary and viscous forces of water bridges acting on adjacent dust particles. Finally, the aggregate is carefully taken with a spoon and sunk in liquid nitrogen, where the water bridges freeze. Any dust particle that is not connected to the others through capillary bridges is lost in liquid nitrogen due to its turbulent motion at room temperature.

Weighing PBs made of different types of dust before and after the evaporation of the water resulted in an ice mass equivalent to $(15 \pm 7)\%$ of the total mass. The final shape of a PB is generally an irregular spheroid with a homogeneous distribution of dust inside the pebble (Fig. 4.5). Sometimes a wet aggregate disrupts into two or three pieces before being put into liquid nitrogen, resulting in a wider distribution of sizes of the final icy aggregates, ranging from 2 to 7 mm in diameter.

Granulation processes are intensively studied for industrial processes. The above procedure creates a compact pebble, where water is creating films on the surface of the particles and is filling the voids between particles (Iveson et al., 2001).

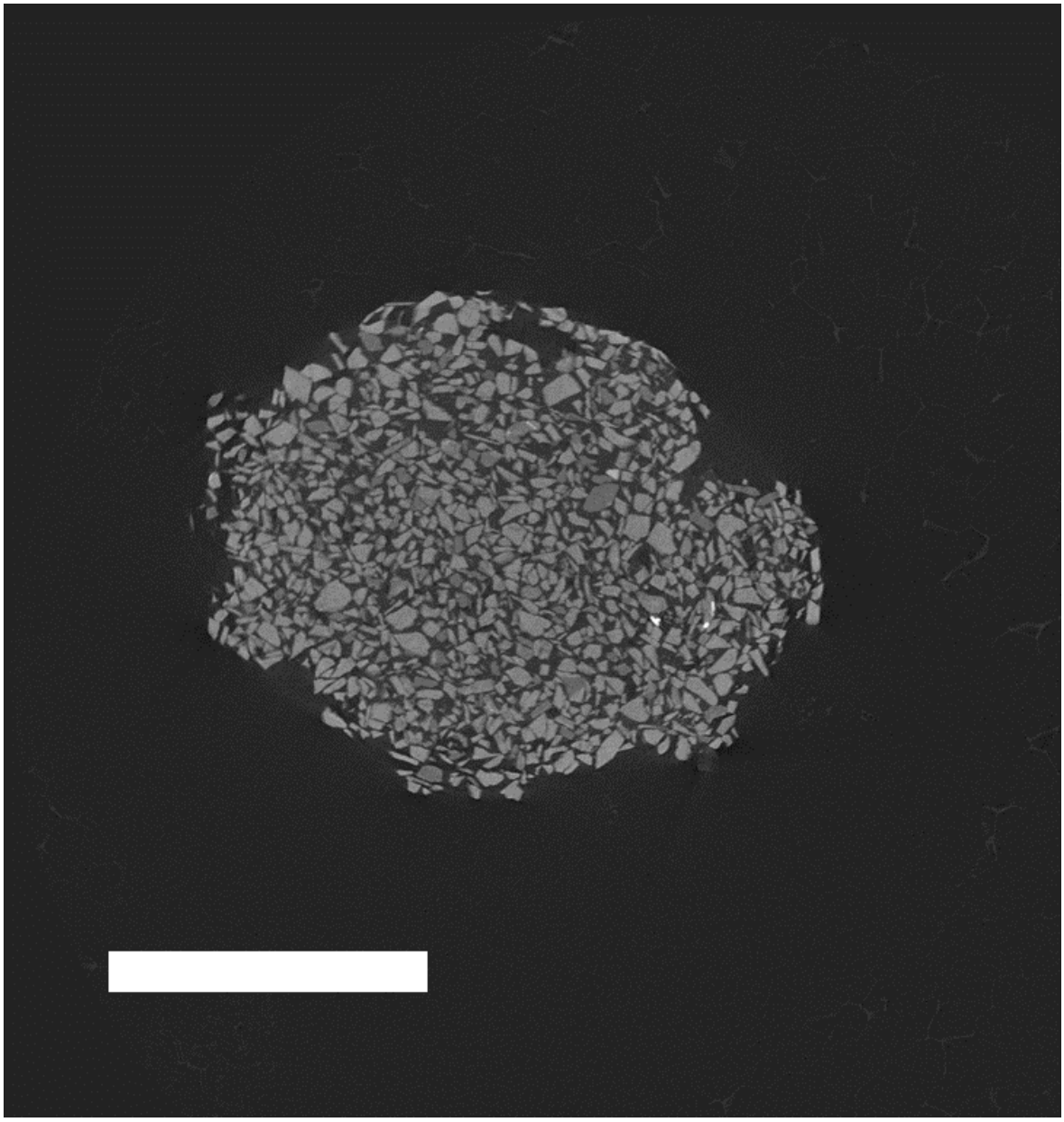

Figure 4.5: X-ray tomography of an icy PB made with pyroxene (dust size 100− 300 µm). The icy bonds keep the dust grains (bright gray) together and the dust distribution inside the pebble is homogeneous. The scale bar is 3 mm.

4.2.3 Experimental setup

We performed all the sublimation experiments with the SCITEAS-2 (Simulation Chamber for Imaging the Temporal Evolution of Analogue Samples version 2.0) vacuum chamber (Fig. 4.6). We evacuated the chamber through a primary dry vacuum pump and a turbomolecular pump, which allowed to reach a high vacuum ($\sim 10^{-7}$ mbar). At the center of the chamber, we cooled

a copper plate with a Helium cryocooler, reaching temperatures down to 40 K. The cylindrical sample holder was placed on the copper plate, and a thin sheet of graphite between the two components guaranteed good thermal contact. The icy pebbles were in contact with the sample holder, that had a higher temperature than the cooled copper plate (around 100 K at the beginning of the decompression). A PT100 thermal sensor measured the temperature at the bottom of the sample holder, recording the temperature of the surface below the icy pebbles.

During the sample production, we pre-cooled down the copper base inside SCITEAS-2 by pouring liquid nitrogen into the sample holder. Once the samples were ready, we kept them in liquid nitrogen to avoid frost formation. When the copper plate of the He cryocooler was almost at the same temperature as the liquid nitrogen, we placed the samples in the cold sample holder, which was inserted in the SCITEAS-2 chamber. Then we plugged the PT100 sensor inside the chamber and closed the upper cover. Immediately afterwards, we turned on the primary pump to quickly evacuate the chamber, and the temperature-pressure reading started. At a pressure of about 10^{-2} mbar, we turned on the turbomolecular pump, allowing to reach about 10^{-6} mbar in a few minutes. The samples rested a few hours in these conditions until we achieved an equilibrium pressure and temperature inside the chamber. We then turned off the cryocooler and the samples slowly heated up by the thermal radiation coming from the window above and the walls of the chamber. The temperature increased in about 25 hours to room temperature. At this point, we turned off the pumps to ventilate slowly the chamber. For different types of pebbles, more experiments have been carried out.

The temperature profile of the sample holder during the experiment evolves logarithmically over time, from a temperature of around 100 K to a final temperature of about 280 K. The total pressure inside the chamber settles down to 10^{-7} mbar before turning off the He-cryocooler. When the temperature starts to increase, the total pressure inside the chamber increases slowly up to $\sim 10^{-3}$ mbar due to the sublimation of ice condensed on the cold copper plate at the closure of the chamber. At around 10 hours after the beginning of the experiments, it slowly decreases down to $\sim 10^{-6}$ mbar.

Disruption measurement

After the sublimation process inside the chamber, pebbles can either keep their spheroid shape or disrupt completely or partially in piles of dust. Both gravity and sublimation participate in this disruption process (see section 4.4.3). In Fig. 4.7 we show how pebbles look like once removed from the chamber when the experiment is finished. The preserved pebbles show a clear spheroid shape, conserving overhangs and protrusions, while the disrupted pebbles are just piles of dust and lost their initial spheroidal shape.

Analyzing the pebbles outside the chamber is difficult.The vibrations caused while removing the sample holder from the vacuum chamber can disrupt weak preserved pebbles, and the re-compression of the chamber after the experiment could as well participate in the disruption of weakly preserved dust aggregates. To address this problem, we developed a method for evaluating the disruption of the aggregates directly inside the chamber, without handling the samples. To determine quantitatively the level of preservation or disruption of the pebbles, we placed a camera above the window, pointing at the sample. Two images were taken at

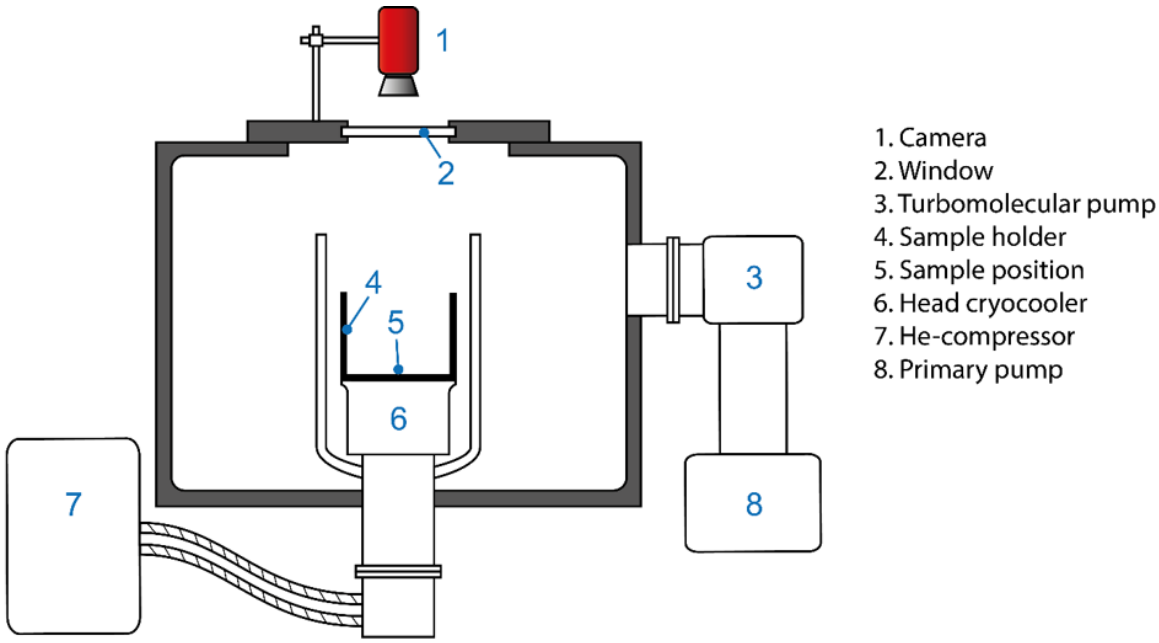

Figure 4.6: Scheme of the SCITEAS-2 setup. A camera is placed in front of a window above the vacuum chamber. The chamber is evacuated through a primary pump and a turbomolecular pump, and the sample holder is in contact with a copper head cooled down with a He-cryocooler.

the beginning and at the end of the experiment, allowing the detection of differences in the projected area of the pebbles before (A_b) and after (A_a) sublimation. For geometrical reasons, when a spheroidal aggregate disrupts into a pile of dust, its projected area increases. We define then the disruption parameter D as follows:

$$D = \frac{A_\mathrm{b}}{A_\mathrm{a}}. \tag{4.1}$$

If the ratio of the areas is close to 1, then the pebble shape did not change and the pebble survived the sublimation of the ice. If the ratio is < 1 then the projected area increased and the pebble disrupted in a pile of dust (Fig. 4.8). Disruption is measured at the end of the sublimation, before the re-compression of the chamber and its ventilation. This method allows recognizing small changes in the projected areas of disrupted pebbles, leading to a detection of disruption. For each type of pebbles and dust combination, we have run sufficient sublimation experiments to obtain a sample with good statistic relevance. The pebbles which do not disrupt during the experiment, can resist months at room temperature and ambient pressure, until some external forces stronger than gravity break the aggregates (handling, vibrations).

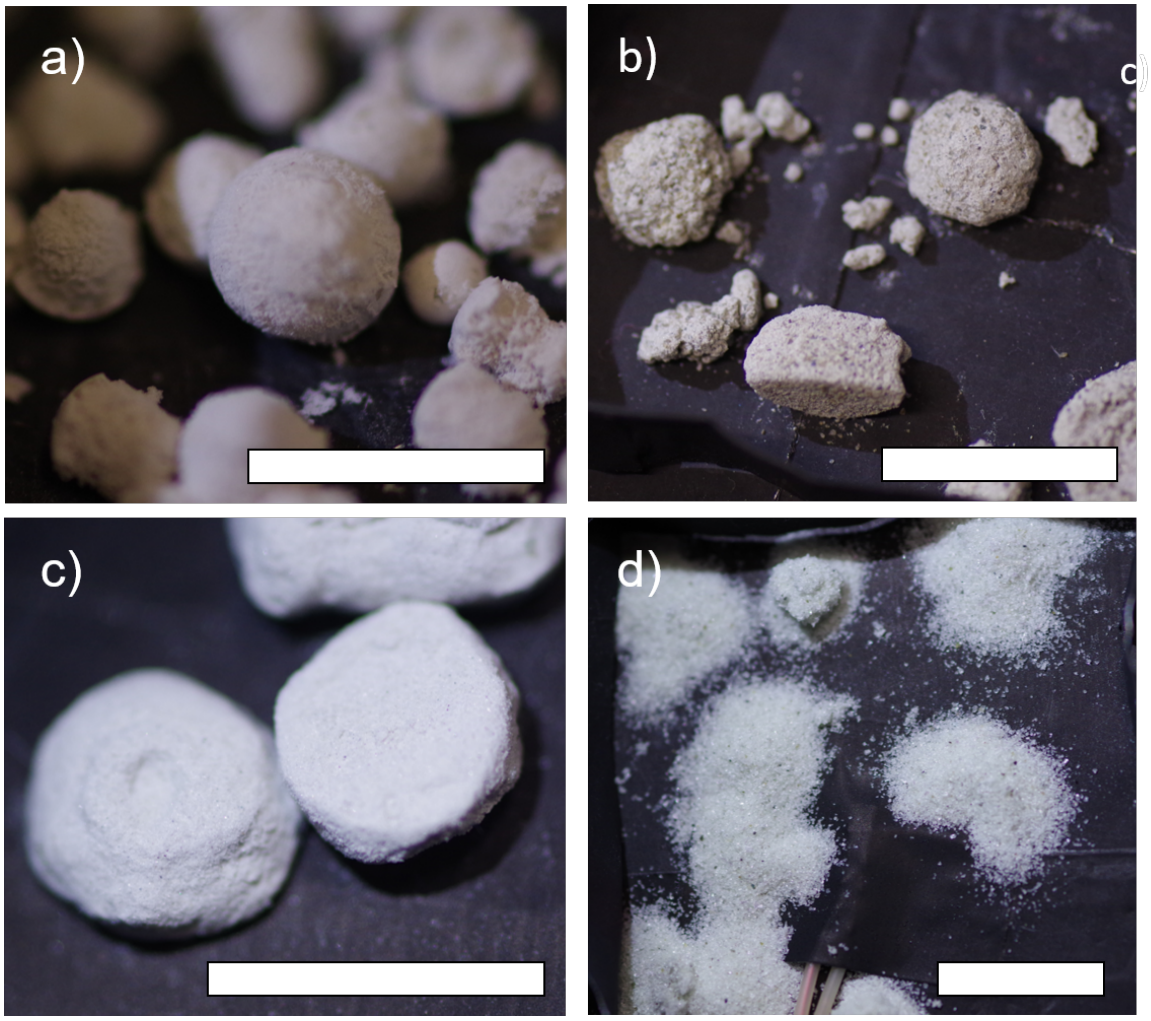

Figure 4.7: Different outcomes of the experiment: pebbles can preserve their 3D shape or disrupt in piles of dust. a) Preserved PA made of olivine with grain size range <50 µm. b) Preserved PB made with pyroxene. c) preserved PB made with olivine. d) Disrupted PB made with coarse dust of pyroxene. Note a partially disrupted pebble on the top of the image, surrounded by a halo of settled dust with a bigger projected area than the original pebble. All scale bars are adjusted to be about 1 cm.

4.3 Results

The sublimation outcome of icy pebbles depends on the grain size ranges of the dust, the ice content (i.e. PA or PB), the silicate type, and the dust-ice distribution inside the pebbles. The experiments aim at distinguishing the effects of each of these contributions to the final preservation or disruption of the pebble after sublimation.

The disruption parameter D is averaged between pebbles of the same type (PA or PB,

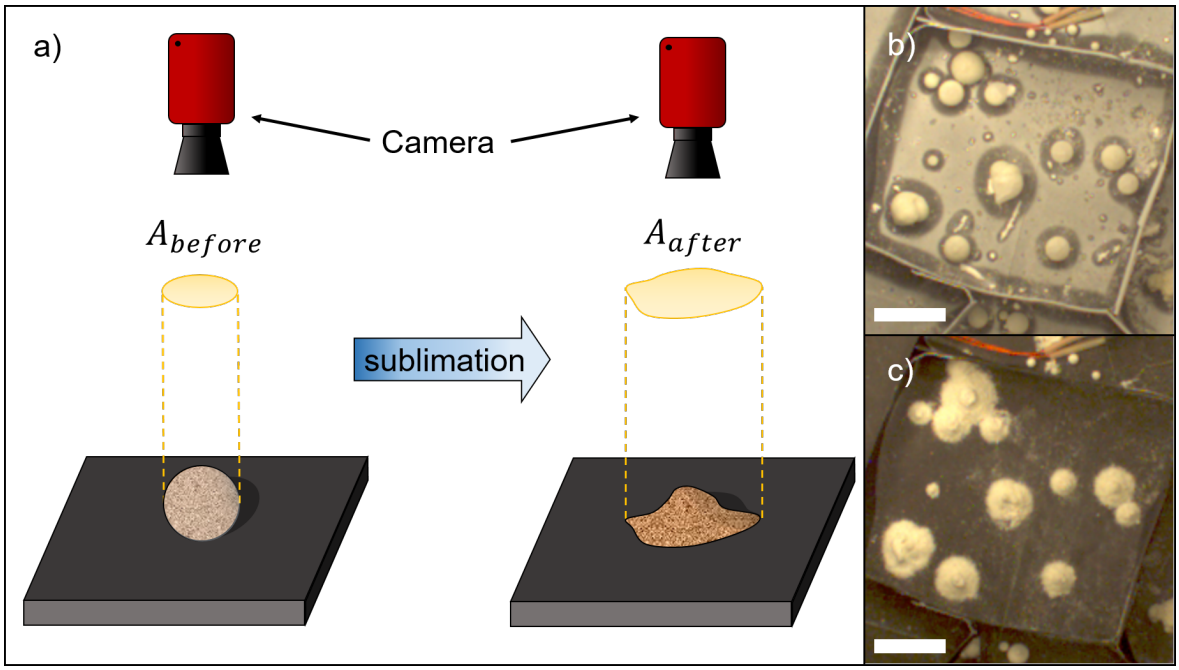

Figure 4.8: a) Setup for observation of pebble disruption. The ratio between A_{b} and A_{a} provides information on the level of disruption of the pebble. The images before and after sublimation are used to calculate the ratio between projected areas. b) PAs of olivine before sublimation. c) The same pebbles after sublimation. The disruption created piles of dust with bigger cross-sectional area. The scale bar is 1 cm.

dust type, and grain size range). The maximum error related to the average $\bar{D}$ is:

$$\Delta\bar{D} = \sqrt{{\sigma_P}^2 + 4\%\bar{D}} \tag{4.2}$$

where σ_P is the standard deviation of D between pebbles of the same type, and, assuming 2% relative error on the experimental evaluation of the pebble area on the image, the term $4\%\bar{D}$ is the absolute error of the average disruption parameter measured for pebbles of the same type. When the measurement of D with its maximum error is consistent with $D = 1$, then the pebbles are not disrupting.

4.3.1 Pebbles of olivine and pyroxene with different grain size ranges

We created the two types of pebble (PA or PB) with different grain sizes for the two dust types (olivine and pyroxene). The grain size ranges are obtained by grinding the powder in a mortar and dry sieving the dust with nylon sieves. Three ranges are used in the present work: grains smaller than 50 µm (referred to as "fine component"), 50−10 µm, and 100−300 µm (referred to as "coarse component"). Olivine pebbles made with dust grains smaller than 50 µm are not affected by sublimation (Fig. 4.9). At 50−10 µm, we already see that PAs do not maintain their integrity, while PBs are still preserved. For coarser dust, 100−300 µm, both PAs and PBs are not able to counter ice sublimation and gravity, and they disrupt. Pyroxene pebbles (Fig. 4.10), on the other hand, show complete disruption for PAs, for all the size ranges. PBs however are following the same pattern as olivine pebbles: the pebbles survive up to 100 µm, and the coarse component is disrupting under sublimation pressure and gravity.

Big error bars are usually associated to the presence, in the same sample, of both disrupted and preserved pebble (e.g. PA with olivine). This is leading to a bigger standard deviation of D within the sample.

4.3.2 Pebbles of olivine and pyroxene with two-component dust size ranges

Disruption of pebbles with 100−300 µm dust grains of olivine and pyroxene is observed for both PA and PB. Mixing a certain amount of the fine component (<50 µm) with the coarse component (100−300 µm) can change this outcome drastically (Fig. 4.11 - 4.12):

1. PBs made with olivine survive if 20% of the dust mass is the fine component;
2. PAs made with pyroxene are always disrupting, even if they are made with 100% of fine dust (see also Fig. 4.10);
3. PBs made with pyroxene do not disrupt through sublimation when at least $5 - 10\%$ mass of dust is <50 µm;
4. PAs made with olivine disrupt unless the fine dust component is up to $90 - 100\%$ of the total dust mass.

This is an indication of the capability of fine dust to cement bigger particles together after sublimation. If the icy pebbles contain a higher amount of ice (PAs), then the amount of fine dust needed to cement bigger grains increases or in extreme case sublimation disrupts the pebbles even if they are made of small grains only.

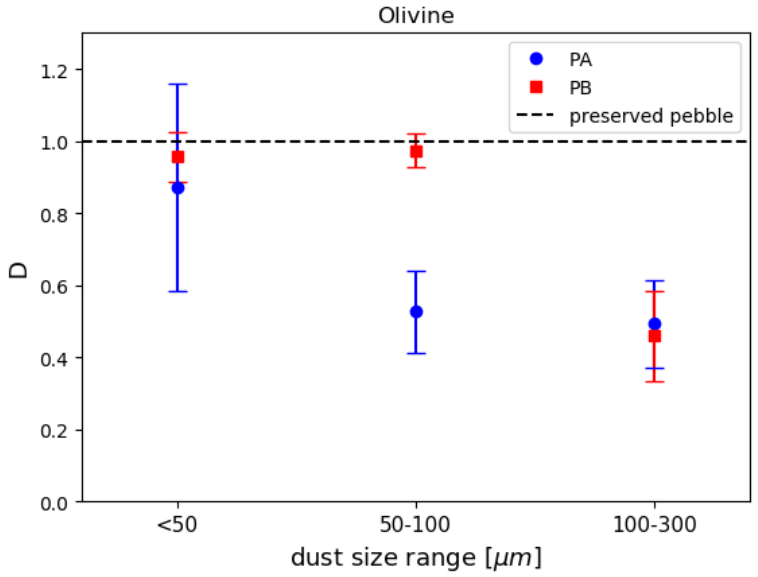

Figure 4.9: Disruption parameter depending on grain size range of olivine, for both PA and PB. When the measurement of D is consistent with 1, then the pebbles survived the sublimation process.

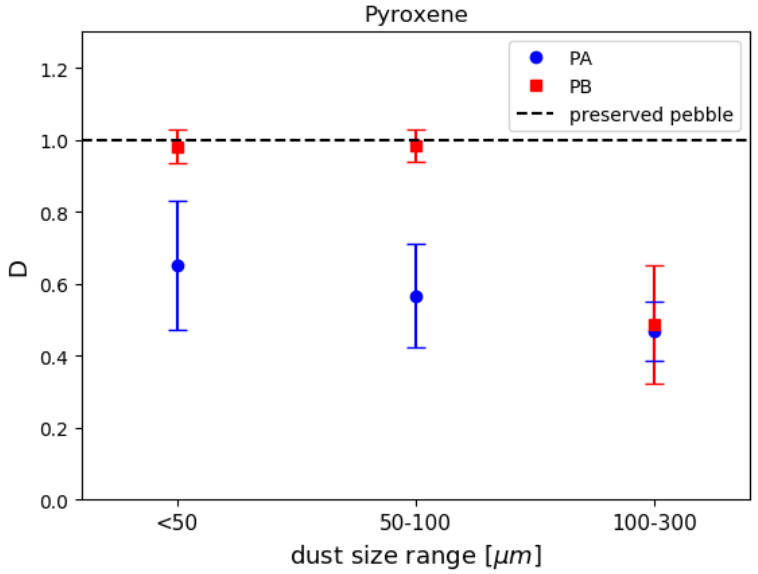

Figure 4.10: Disruption parameter depending on grain size range of pyroxene, for both PA and PB. When the measurement of D is consistent with 1, then the pebbles survived the sublimation process.

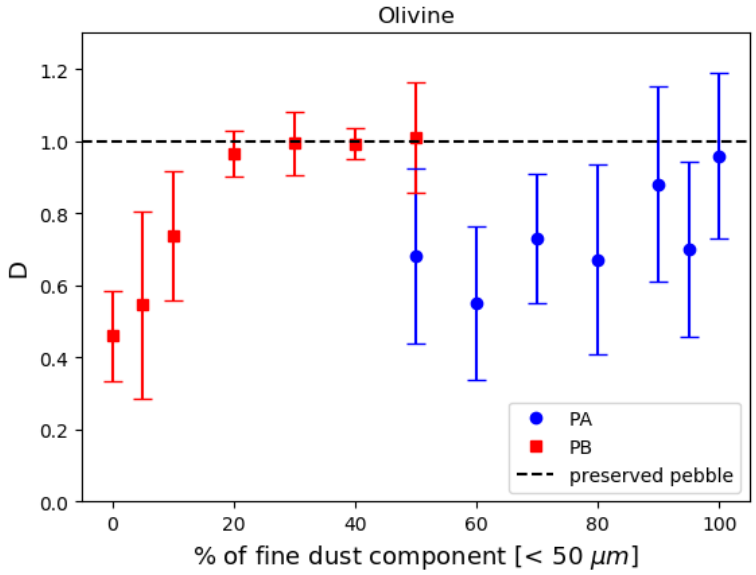

Figure 4.11: Disruption parameter depending on the amount of fine component (<50 µm) mixed with coarse component (100−300 µm) of olivine for both PA and PB. When the measurement of D is consistent with 1, the pebbles survived the sublimation process.

4.4 Discussion

In this work, we present sublimation experiments with two different icy pebble models to investigate how the initial amount of ice in the pebble, the dust type, and the dust size ranges are affecting the disruption of the icy pebble through the sublimation process. In the case of an intimate mixture of ice and dust, icy aggregates are thought to be unstable upon sublimation of the ice and undergo disruption releasing small silicate particles (Saito and Sirono, 2011; Schoonenberg and Ormel, 2017; Hyodo et al., 2021). Our experiments show that it is possible to maintain the integrity of pebbles after the complete sublimation of the ice intermixed between the dust grains.

4.4.1 Sublimation rate

Inside the vacuum chamber SCITEAS-2, the temperature below the pebbles rises from ∼120 K to 280 K in about 20 hours. The sublimation of the ice occurs during this time, although the experimental setup does not allow detecting exactly when it ends.

The mean size of PAs is about 1.5 mm in radius, with an ice volume ratio of 77%. The equivalent ice would be contained into an equivalent sphere with a radius of around 1.4 mm. The linear decrease rate of ice in the direction of the surface normal $R_{\rm ice}$, can be calculated with the Hertz-Knudsen formula (Knudsen, 1909),

$$R_{\rm ice} = \frac{V_{\rm m}(p - p_{\rm sat})}{\sqrt{2\pi\mu R_{\rm g} T}} \tag{4.3}$$

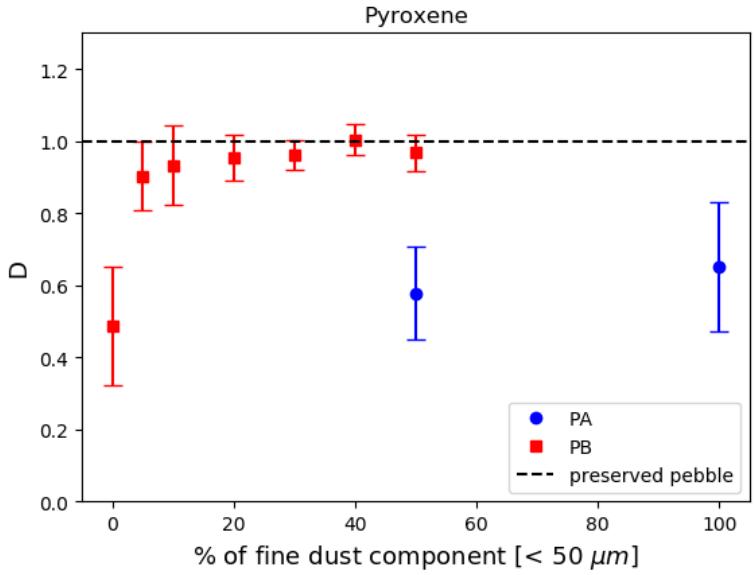

Figure 4.12: Disruption parameter depending on the amount of fine component (<50 µm) mixed with coarse component (100−300 µm) of pyroxene for both PA and PB. When the measurement of D is consistent with 1, the pebbles survived the sublimation process.

where V_{m} is the molar volume, p is the vapor pressure above the surface, p_{sat} the saturation pressure, μ is the molar mass of ice, R_{g} is the gas universal constant, and T is the temperature of the ice. The saturation pressure p_{sat} is related exponentially to the temperature T (Haynes et al., 1992)

$$p_{\mathrm{sat}} = 6.034 \cdot 10^{12} \mathrm{g\,cm^{-1}s^{-2}} \cdot \mathrm{e}^{-\frac{5938\mathrm{K}}{T}}. \tag{4.4}$$

The total pressure inside the vacuum chamber varies over time (from 10^{-7}mbar to 10^{-3}mbar), depending on the sublimation processes of the condensed gasses trapped inside. Since at the beginning of the experiment some vapor condenses inside the chamber on the cold copper plate, when the temperature increases during the experiment, the pressure increases as well, until all the condensed ice is sublimated. Assuming that the pressure inside the chamber is due to the sublimation of such ice, the vapor partial pressure p is exactly the pressure measured during the experiment inside the vacuum chamber. Once the partial vapor pressure is known, the rate of linear decrease of ice can be calculated as a function of the temperature only. Assuming that the ice of the pebbles is at the same temperature of the sample holder on which they lay and since the temperature of the sample holder is known, it is possible to calculate at what temperature the sublimation happens and how much time it requires. For our experiments, the sublimation time of a compact ice sphere with a radius of around 1.4 mm is between 4 and 6 hours and it happens on average when the temperature spans from $\sim$ 190 to 240 K. This gives a sublimation rate of about $2 \cdot 10^{-1}$ mm/hour.

At the water ice line temperature, the sublimation rate is considerably slower than in the laboratory. If we assume a protoplanetary disc with gas surface density $\Sigma(r)$ and a

temperature profile $T(r)$ described by

$$\Sigma(r) = 1000\,\mathrm{g\,cm^{-2}} \left(\frac{r}{\mathrm{au}}\right)^{-1} \tag{4.5}$$

$$T(r) = 280\,\mathrm{K} \left(\frac{r}{\mathrm{au}}\right)^{-\frac{1}{2}} \tag{4.6}$$

where r is the radial distance from the central star, and the amount of water (in both ice and vapor phases) with respect to the hydrogen and helium content of the disc is equal to $Z_{\mathrm{H_2O}} = 0.005$, it is possible to calculate the partial vapor pressure P_v from:

$$P_v = \frac{k_\mathrm{b} Z_{\mathrm{H_2O}} T(r) \Sigma(r)}{\mu_{\mathrm{H_2O}} \sqrt{2\pi} H_\mathrm{gas}(r)} \tag{4.7}$$

where k_b is the Boltzmann constant, $\mu_{\mathrm{H_2O}}$ is the weight of a molecule of water and $H_\mathrm{gas}(r)$ is the disc scale height given by

$$H_\mathrm{gas}(r) \approx 0.033\,\mathrm{au} \left(\frac{r}{\mathrm{au}}\right)^{\frac{5}{4}} \tag{4.8}$$

Given these parameters, the ice line is around 2.7 au, and the sublimation rate at 2.5 au (just inside the ice line), is about 10^{-4}mm/hour.

Considering an amount of water equal to $Z_{\mathrm{H_2O}} = 0.005$ in the disk, the water vapor pressure at the ice line is within the range of the vacuum chamber pressure (around 10^{-6} mbar), but the temperature of the sample holder increases quickly above the ice line temperature ($\sim$170 K) up to 280 K in 20 hours. This means that pebbles undergoing sublimation in the laboratory are at least three orders of magnitude faster in sublimating their ice than pebbles just inside the ice line, highlighting the fact that survivability of icy pebbles is possible at a much higher sublimation rate than the one found at the ice line. It is probable that some of the pebbles that are disrupting in our experiment could survive a sublimation process in conditions of slower sublimation rates and in the absence of gravity. Nonetheless, temperature fluctuations in protoplanetary discs could lead to faster sublimation rates than the one at the ice line (see e.g. McNally et al. (2014) and Bodénan et al. (2020)).

Previously, theoretical works have assumed that pebbles disrupt after sublimation freeing micrometer-size dust particles inside the ice line, leading to enhancement of planet formation just inside and outside the ice line. What would happen if a pebble similar to a PA (in size and porosity) passes the ice line without disrupting? If pebbles are not disrupting through sublimation, then planet formation due to pebble accretion could be enhanced inside the ice line. This is a direct effect of the change of the Stokes number of pebbles or dimensionless friction time of the pebble in the Epstein regime,

$$St = \frac{a \rho_\mathrm{p}}{H_\mathrm{gas} \rho_\mathrm{gas}} \tag{4.9}$$

with a particle radius, and ρ_p and ρ_gas being the pebble and gas density. When the ice sublimates, the pebble changes its apparent density, while maintaining the same size. The

Stokes number of a sublimated olivine pebble with 1.5 mm of radius and 77% porosity (see section 4.4.2) is about $5 \cdot 10^2$ times the Stokes number of a µm-size olivine grain. Since the effective radius for accretion onto planetesimal depends on the Stokes number of the accreting pebbles according to $r_{\text{eff}} \propto St^{\frac{1}{3}}$, their accretion efficiency would be increased inside the ice line (Lambrechts and Johansen, 2012; Morbidelli et al., 2015a). On the other hand, a higher Stokes number means a higher drift velocity toward the star, decreasing the efficiency of planet formation from pile-up of material close to the ice line. It should be noted, however, that higher velocities of pebbles could result in disruptive pebble-pebble collisions, so pile-up of fine dust material could still be possible.

4.4.2 Role of porosity

Many studies show that porosity is important for pebble evolution and for hit-and-stick growth (Dominik and Tielens, 1997; Ormel et al., 2007; Garcia and Gonzalez, 2020). For our experiments, we use two pebble models that have negligible porosity at the beginning of the sublimation experiment. At the end of the experiment however, the porosity of the preserved pebbles increases since all the ice sublimated, but they maintain their shape with insignificant changes. We can therefore calculate the final porosity of pebbles Φ_{f}:

$$\Phi_{\text{f}} = 1 - \frac{V_{\text{dust}}}{V_{\text{pebble}}} = \frac{i}{i + (1-i)\frac{\rho_{\text{ice}}}{\rho_{\text{dust}}}} \tag{4.10}$$

Where V_{dust} is the volume occupied by the dust, V_{pebble} is the total volume of the pebble, ρ_{ice} and ρ_{dust} are the ice and dust densities respectively, and i is the ice mass percentage inside the initial pebble. The final porosity of PAs is $(77 \pm 7)\%$ and the final porosity of PBs is $(37 \pm 12)\%$. PBs porosity is close to the expected porosity of pebbles in the nucleus of 67P (Fulle et al., 2016), and their initial dust-to-ice volume ratio is 1.7 ± 0.4 which is consistent with the limits found by Kofman et al. (2015).

After sublimation, preserved pebbles are porous, highlighting that such kind of dry porous aggregates would survive sublimation with an amount of ice filling the space between dust grains up to the initial mass ratio (50 and 15% mass of ice for PAs and PBs, respectively). In the limit case, the ice is filling all the space inside the dry porous pebble, but sublimation is not strong enough to push apart the dust particles.

4.4.3 Role of gravity

In the laboratory, sublimation and gravity are both concurring to the disruption of pebbles. Ice sublimation pushes the grains apart and tends to disrupt the pebble, while gravity disrupts any grain-to-grain adhesion that is weaker than the gravity force of the dust column above it inside the pebble.

Hereafter, we refer to gravity as a "disrupting" force. There are many configurations of granular materials where the dust is kept in a certain position because of gravity which acts as a "constructive force". For example, a dust pile maintains its shape because of the static friction between grains, which counters actively the tangent force of gravity and prevents the grains to slide further. On one hand, if we consider a spheroidal aggregate of dust,

the top hemisphere of the pebble is similar to a pile of dust, where friction and adhesion between particles are preventing them to slide and roll down. On the other hand, the bottom hemisphere can be seen as an upside-down pile of dust. Gravity and friction forces would tend to disrupt such configuration of dust in a pile of dust, and the weight of the top-half hemisphere of dust contributes to the disruption of the bottom-half hemisphere. This is not observed for preserved pebbles (see Fig. 4.7 a-b-c). The bottom-half of the pebble is well preserved and overhangs and protrusions are conserved in the final shape. Therefore, gravity has a disruptive role in transforming pebbles in piles of dust and preserved pebbles survived both gravity and sublimation forces during the experiment.

While it is clear that preserved pebbles survived both forces, disruption of pebbles in our experiments could be caused by both sublimation and gravity and there is a regime for which sublimation is more important than gravity. If we assume a spherical dust grain resting on an icy surface, we can compare the gravity force to the drag force of the sublimated ice acting on the small grain. The drag force F_d in Epstein regime is given by

$$F_\mathrm{d} = \frac{\pi}{3}\rho_\mathrm{vap}{R_\mathrm{p}}^2\sigma_\mathrm{th}\nu \tag{4.11}$$

with ρ_vap vapor density just above the surface of the pebble, R_p dust particle radius, σ_th thermal velocity, and ν flux velocity of the sublimating gas. The flux velocity can be retrieved applying the conservation of mass at the surface of the pebble passing from ice to vapor

$$\mu\rho_\mathrm{ice}R_\mathrm{ice} = \rho_\mathrm{vap}\nu \tag{4.12}$$

where ρ_ice is the ice density (in $\mathrm{mol\,m^{-3}}$), R_ice is the sublimation velocity (see equation 4.3) and ρ_vap is given by the ideal gas law

$$\rho_\mathrm{vap} = \frac{p_\mathrm{sat}}{RT_\mathrm{ice}} \tag{4.13}$$

with p_sat saturation pressure (see equation 4.4), and T_ice temperature of the ice. The thermal velocity σ_th is

$$\sigma_\mathrm{th} = \sqrt{\frac{8RT_\mathrm{ice}}{\pi\mu_{\mathrm{H_2O}}}} \tag{4.14}$$

If we assume that the temperature of the ice is the same of the sample holder, it is possible to calculate the drag force during the experiment and compare it to the gravity force acting on different grain sizes. Fig. 4.13 shows how the ratio between drag force and gravity force is varying depending on the temperature of the ice, for different grain diameters. In the temperature range where sublimation is important for the pebbles, gravity is the disrupting force in the case of coarse grains, while the drag force due to sublimation dominates the gravity force for small grains (up to 100 µm) above ∼225 K. This means that all the preserved pebbles with grains smaller than 100 µm overcame sublimation-driven disruption. Gravity force can be still important for preserved pebbles if inside the pebble there is a heterogeneous dust-ice distribution. In this case, if the pebble survives sublimation, it can still collapse under gravity because of a structural deficiency, like a hole left by the ice inside the core of the pebble. This is why the error on the disruption parameter for PAs is large, although the

general trend for different dust size ranges is not affected because of the presence of pebbles that are homogeneous and do not have any structural weaknesses when the ice is gone.

A detailed description of the sublimation-driven disruption process should take into consideration what happens inside the pebble, and the possible formation of over-pressure in pores of the pebbles, but this kind of model is beyond the purpose of the present work, and will be topic of future investigations.

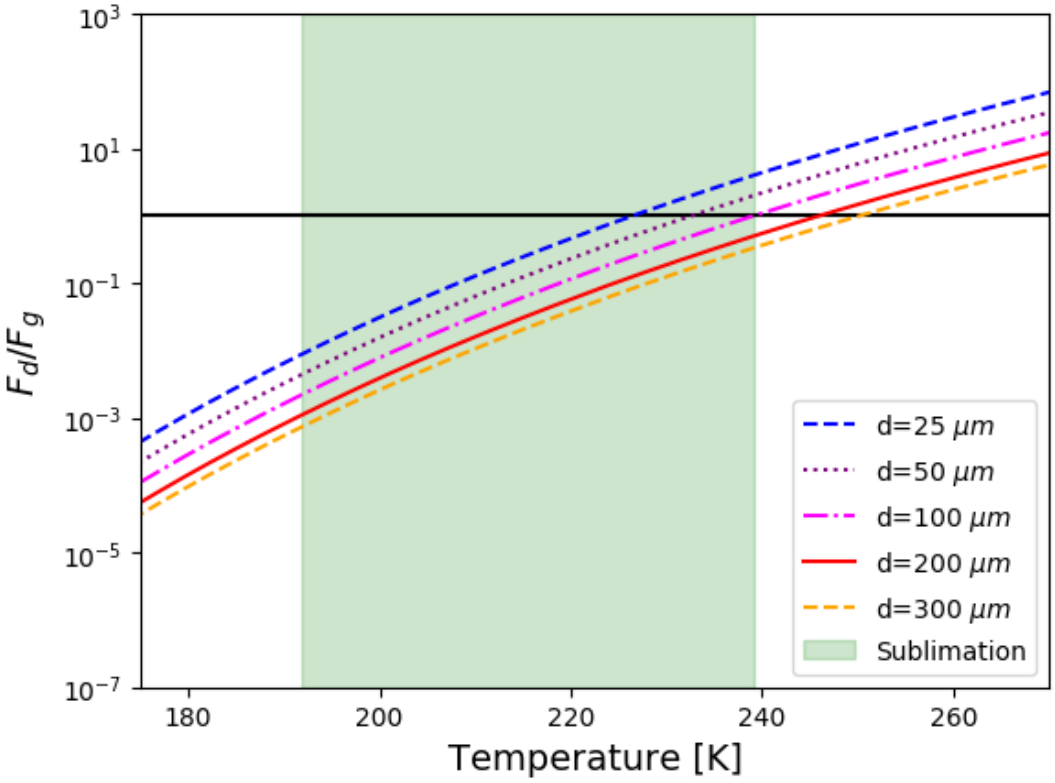

Figure 4.13: Ratio between sublimation drag force F_d and gravity force F_g acting on particles of different diameters vs. temperature of the ice. The sublimation of the pebble happens between 190 and 240 K, and in this range of temperatures, gravity is the main disruption force for coarse grains, while sublimation is important in the higher range of temperatures for grains smaller than 100 µm. The black continuous line is a reference for the case in which sublimation drag force and gravity are equal.

4.4.4 Role of grain size ranges and mineralogy

For our experiments, we used two types of silicates: olivine and pyroxene. The dust grain size ranges considered in this work span from 0 to 300 µm, divided in three categories: 'fine component' (less than 50 µm), 50−100 µm, and 'coarse component' (100−300 µm). In protoplanetary discs before growth to pebbles size, dust is mostly present as sub-µm or µm-size

covering a narrower size range than our 'fine component' (Bouwman et al., 2001; Boekel et al., 2003). Nonetheless, our experiments show that pebbles can overcome sublimation with a dust size up to 50 µm in the case of olivine PAs, and 100 µm in the case of PBs.

A pebble made with the coarse component always disrupts, but when mixed with a certain amount of fine component, it can be preserved through sublimation. The minimum amount of dust fine component needed for preservation varies with the mineral species, being higher for PB olivine (about 20% of the total dust mass) and lower for PB pyroxene (10% of the total dust mass). The pyroxene PAs are always disrupting with any percentage of fine dust, while olivine PAs increase their stability through sublimation when the fine component is between 90 and 100% of the total dust mass. Some olivine PAs do not disrupt, increasing the variability of the disruption parameter within the sample, and therefore the total error associated with the measurement. Therefore, the measurement of olivine PAs shows an increasing disruption parameter with increasing amount of fine component, but the exact minimum amount of fine component needed to avoid disruption is difficult to retrieve. In general, the introduction of fine dust mixed with coarse dust increases the pebble stability through sublimation. The small particles could act as bridges between bigger particles, increasing their adhesion capability in a way similar to the one described by Seiphoori et al. (2020). Future laboratory work should address this point, by observing the microscopic morphology of the icy pebbles and their sublimated remnants in loco.

Olivine and pyroxene pebbles have slightly different behaviors. PAs with dust size smaller than 50 µm are preserved for olivine and disrupted for pyroxene (Fig. 4.9 - 4.10). Furthermore, when fine and coarse dusts are mixed, olivine PBs seem to necessitate a higher percentage of fine component than pyroxene PBs to be preserved (Fig. 4.11 - 4.12). Explaining these differences is challenging, since several factors are governing the adhesion strength of particles. The ability of grains to aggregate and to form bonds between each other is given by properties of the material (such as surface energy, Poisson ratio and Young's modulus), grain shape characteristics (surface roughness, crystal faces) and physical and chemical state of grain surfaces (adsorption layers, chemical reactions, electric charges). Our SEM measurement do not show significant alterations of the grain surfaces before and after the experiment, and the spectra of the grains after the experiment exclude the presence of large quantity of hydroxylated material (Fig. 4.2), which could also weaken grains bonding (Quadery et al., 2017). Although the SEM images do not show clear difference in the amount of very fine material (<5 µm), a difference in particles size distribution could explain the different behaviour of olivine and pyroxene, leading to a more adhesive behaviour of pyroxene over olivine (Fig. 4.11 - 4.12). It should be noted, however, that the adhesion capability of the two species are determined also by other parameters cited above (e.g. grain roughness).

Future experiments will address the different behavior of pyroxene and olivine, and the role of ice interaction with grains of different sizes.

4.5 Conclusions

Different studies show that it is possible to enhance the growth of dust inside and outside the ice line, if icy pebbles are assumed to completely disrupt by sublimation inside the ice

line (Saito and Sirono, 2011; Schoonenberg and Ormel, 2017; Hyodo et al., 2021). We researched experimentally the outcome of two icy pebble models undergoing sublimation in low-temperature and low-pressure conditions varying the dust mineralogy, the water ice content, and the dust size range.

Our findings can be summarized as follows:

1. Icy pebbles can survive sublimation. We demonstrate that a range of combinations of dust type (olivine or pyroxene), dust size ranges and ice content lead to preserved pebbles upon sublimation of the ice.
2. Pebbles with low ice content survive sublimation better than the ones with higher ice content. Our results show that pebbles with 15% ice mass are more resistant to disruption than pebbles with 50% ice mass for different dust size ranges.
3. Icy pebbles survive better sublimation if the dust particles are smaller than 50 µm. If the pebble is made with coarse particles (100−300 µm), a minimum amount of fine dust allows it to avoid disruption. The minimum amount of fine dust increases with the amount of ice and is dependent on the silicate type.

These results are relevant for planet formation processes close to the water ice line and downstream of it, providing useful information for modeling the behavior of ice-dust aggregates in protoplanetary discs when sublimation is occurring. In particular, they provide elements for modelling the sublimation outcome of icy pebbles depending on their ice content, dust type, and dust size ranges, which play a major role in the disruption process. Verifying these results for other dust types, narrower dust size distributions, and in the presence of organics is an important future extension of this work.

Acknowledgements

This work has been carried out within the framework of the NCCR PlanetS supported by the Swiss National Science Foundation. We thank the two anonymous reviewers for the useful insights which helped to improve the manuscript.

Data Availability

All the camera images of the sublimation process are available in Figshare from https://figshare.com/articles/figure/The_fate_of_icy_pebbles_undergoing_sublimation_in_protoplanetary_disks/16912399.

4.6 Annex 1 to Chapter 4 - Imaging pebbles sublimation

This section illustrates further experiments that I did not include in the published paper, regarding the pebble sublimation process observed with a long distance microscope.

At the end of the experiments described in chapter 4, it happened that some pebbles showed a partial disruption or a thin halo of powder around them after sublimation, while other pebbles split in two and collapsed. Since the perpendicular view of the camera and its objective magnification did not allow a proper inspection of the disruption process, I used the Side View Setup (SVS) coupled with a long distance microscope to image the pebbles during the increase of temperature. With such configuration, the silhouette of the pebbles are imaged every five minutes. Unfortunately, it was not possible to track the complete evolution of the pebbles, because of some technical problems with the computer and the vibration of the chamber that changed the field of view of the microscope over time. Nonetheless, it was possible to distinguish the different phases of disruption of a PA made with olivine grain sizes in the range $50-100\,\mu m$ (Fig. 4.14).

The image A) of Fig. 4.14 is taken before turning off the He-cryocooler, and the surface of the pebble has a certain roughness given by the condensation of frost on the top of the pebble surface. The frost condensation is not avoidable, since the insertion of the sample inside SCITEAS-2 exposes it to the air, although the pre-cooling process of the cryocooler hear already removed some of it through outgassing of liquid nitrogen. In picture B), the frost is gone and the surface of the bare pebble is visible. The intensity values of each pixel are stretched so that we can see the ice transparency. Already in C) and D), the ice sublimates and retreats, and produces the first layers of porous dust mantle. While the shrinkage of the ice continues, the dust grains stick together forming porous flake that persist on the surface in the form of "fairy castles", until the gravity pulls them off the surface (E) and F)).

The formation of porous layers of dust on top of the pebbles is fascinating. The single dust grains organize in structures that are persistent over time, and they fall out from the pebble surface only when the retreating ice does not provide a good enough anchor for the mass of the dusty flake. This means that the inter-particle interactions play an important role in the stability of the pebble and that the disruption is gravity-driven. Once the gravity is out of the picture, we can imagine that the sublimation drag can remove some of the fine particles only if they do not stick together. In that case, the cohesiveness given by the adhesion between particles can overcome the sublimation strength and preserve a porous pebble through the sublimation process.

Fig. 4.15 shows the stages of sublimation compared with the temperature and pressure conditions of the experiment. The temperature is measured on the copper plate where the pebble lies, and we assumed that the pebble is in thermal equilibrium with the sample holder. The labeled letters refer to the times at which the images in Fig. 4.14 were taken. An exact overview of the sublimation stage of pebbles was not possible before acquiring images with the long-distance microscope coupled with the SVS. Now, it is possible to detect the single stages of the pebble disruption and correlate them to its temperature and the environmental pressure.

The PA sublimates its frost in the first hours after the cryocooler is turned off, and both

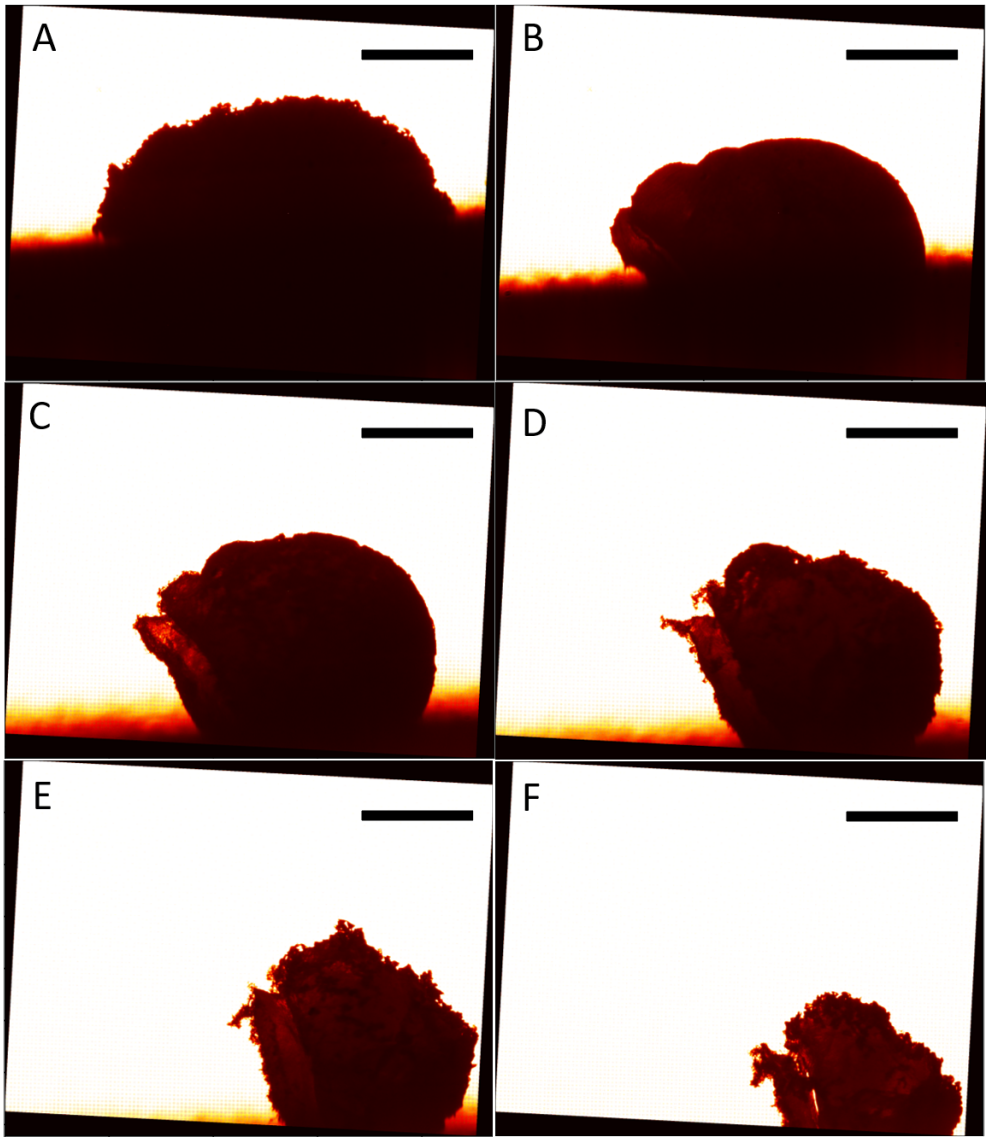

Figure 4.14: An olivine PA undergoing sublimation, observed with the Side View Setup coupled with a long-distance microscope. A) The pebble at the beginning of the experiment, that is covered by a layer of frost deposited while inserting the pebble inside the SCITEAS-2 chamber. B) the pebble loses the frost layer, showing a compact and smooth icy surface. C), D), E) and F) the ice surface retreats and leave behind a highly porous crust of dust that falls off the pebble in flakes, when they reach a sufficiently high mass (gravity driven disruption). The scale bar is approximately 1 mm.

the pressure and the temperature increase (up to 10^{-3} mbar and ~ 200 K, respectively). The increase of pressure is most probably due to the sublimation of condensed volatile species inside the chamber during its pre-cooling at nitrogen temperature. At 200 K starts already the sublimation of the PA icy core, that steadily continues up to 250 K. Compared to the

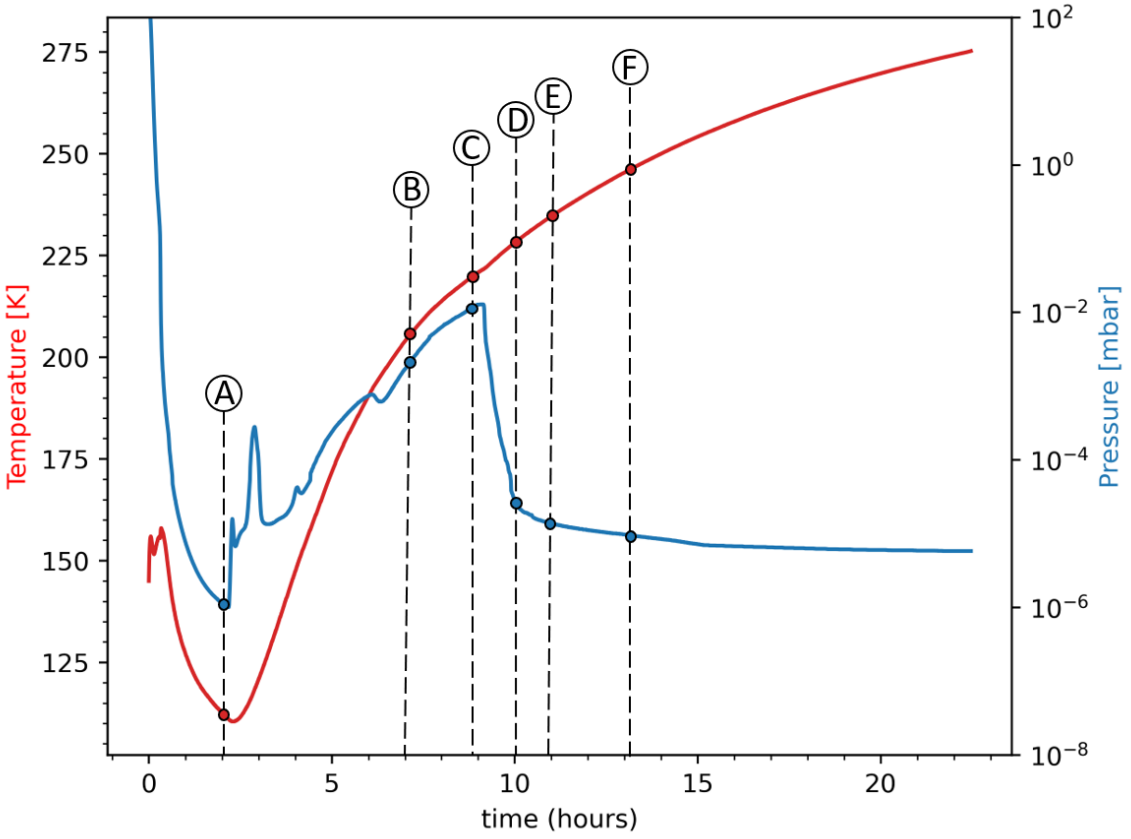

Figure 4.15: Temperature-pressure of the sublimation experiment performed with SVS and long-distance microscope. The times of the images in Fig.4.14 are labeled, for comparison with the sublimation stage.

estimation made in before this experiment (Fig. 4.13), the sublimation range was underestimated of about 10 K, that is a fairly good result, since I used first principles to determine the sublimation speed of the ice. Note that a possible cause of such discrepancy is the sublimation rate calculated with the Hertz-Knudsen formula 4.3. This formula assumes a slab of compact ice, while in our case we do not have pure ice, instead it is mixed with silicate particles. Furthermore, the partial vapor pressure was assumed to be equal to the pressure of the chamber, but this is an upper limit, since other species contribute to the total pressure. Finally, the picture is complicated by the real temperature of the ice-dust mixture, that might show gradients and not be in equilibrium with the sample holder.

The maximum resolution of the long-distance microscope (minimum observable grains sizes down to 10−15 µm) and its relatively long exposure time, does not allow the detection of small particles pushed away from the surface by the sublimation drag force. While this process is expected, the presence of dust flakes on the top of the pebble could partially prevent the small particles to leave the surface, and be trapped by the other dust particles instead. Whether the drag of dust grains is inhibited by a porous dry layer of dust, and the minimum

thickness and porosity needed to trap the particles is of interest for both comets and pebbles in protoplanetary disks.

4.7 Annex 2 to Chapter 4 - Organics, ice, and dust: morphological and spectral evolution

This section illustrates the very first experiments with the new pebble production methods that have been carried before the experiments presented in chapter 4. The experiment presented here asses the spectral and morphological evolution of PAs undergoing sublimation made with complex dust mixtures (CI asteroid simulant), and pyroxene with different grain sizes. At this stage, the laboratory experiments on PAs and PBs were still exploratory, and the choice of using CI asteroid simulant (see Britt et al. (2019) for full description) was due to its complex mixture of minerals (Mg-serpentine, magnetite, epsomite, palygorskite, olivine, vermiculite, and pyrite) and organics (sub-bituminous coal). I sieved both CI and pyroxene dust with nylon sieves, and I obtained two dust size distribution: dust smaller than 50 µm, and dust size in the range $50-1000$ µm. The method for PA production is the same as the one described in section 4.2.2. The experiment was carried out with the MoHIS setup mounted on top of the SCITEAS-2 vacuum chamber. The icy samples were organized on the bottom of a cylindrical aluminum sample holder, separated in squares made of black aluminum tape. The cylindrical sample holder is then accommodated on top of the pre-cooled head of SCITEAS-2 cryocooler. The evolution of the temperature at the bottom of the PAs and the pressure inside the vacuum chamber are displayed in Fig. 4.16. The spectra of the samples have been measured after the insertion in the chamber (Fig. 4.17-A) and every 30 mins between 16 and 42 hours after the start of the experiment (Fig. 4.17-B, C, and D are in this time range). I acquired an image of a spectralon before starting the experiment to calibrate the final spectra.

The cylindrical sample holder was in a cryogenic box filled with liquid nitrogen while I was cooling down the head of the He-cryocooler. When the He-cryocooler reached a temperature of about 150 K, I inserted the sample holder inside SCITEAS-2, connected the temperature sensors to the plugs at the top of the shroud, closed the top window, placed MoHIS on top of the window, and finally started the primary vacuum pump. During this time, the little amount of water vapor inside the chamber had a chance to deposit on the coldest point, i.e. the samples, forming a layer of frost. This is well visible both from the RGB image of the samples and their overall blue spectra (Fig. 4.17-A). I evacuated the chamber overnight, with the He-cryocooler actively cooling the sample. The day after, I turned off the cryocooler, letting the sample temperature evolve freely. At this point, the samples loosed quickly their frost and started to sublimate their ice (Fig. 4.17-B). It is interesting to observe that the fine pyroxene dust looks the darkest at this stage, when the particles on top of the pebbles are intermixed with compact ice. The absorption bands of water ice at 1.25, 1.5, and 2 µm are immediately noticeable, although the CI simulant is dark enough to efficiently hide them. After about 14 hours from the He-cryocooler shutoff, the water ice bands disappear completely from all samples (Fig. 4.17-C). We know that ice is still present inside the PAs for two reasons: the pressure is almost at 10^{-2}mbar, meaning that there is some outgassing going on, and the PAs of pyroxene have still a roundish shape, while they are expected to disrupt for both the dust size distributions. Only when the pressure lowers down to 10^{-6}mbar and the RGB images

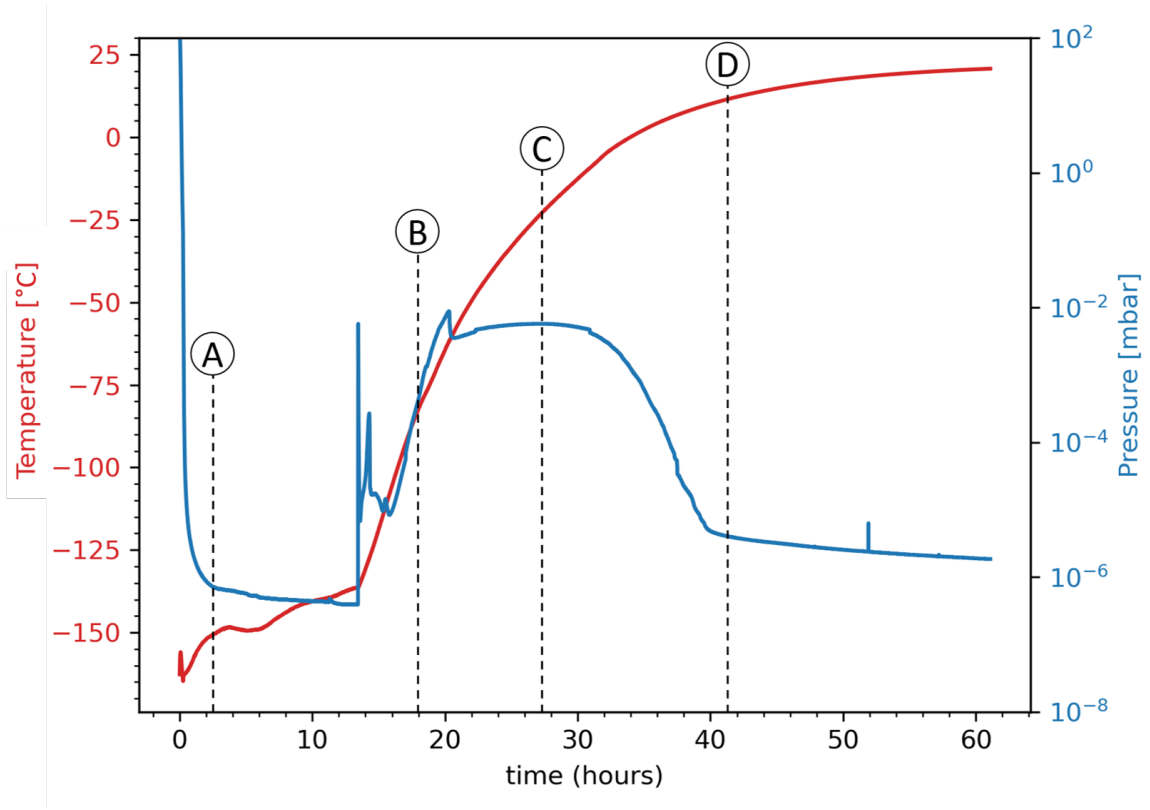

Figure 4.16: The temporal evolution of sample temperature and SCITEAS-2 pressure of the CI and pyroxene PAS experiment. The labelled letters indicate the time points at which the spectra shown in Fig. 4.17 were acquired.

show completely disrupted pyroxene pebbles, we know that the ice is completely sublimated (Fig 4.17-D). Still, the CI aggregates are strong enough to keep their roundish structure.

At the end of the experiment, I extracted the samples from SCITEAS-2 to visually inspect them (Fig. 4.18). While pyroxene pebbles seemed completely disrupted from the RGB composed images of MoHIS, at higher resolution it is possible to observe that the pyroxene pebbles made with fine dust might maintain a small aggregated shape after sublimation, although this is probably very delicate. The CI PAs are well preserved, and in particular the ones with finer dust distribution. The CI pebbles made with coarser dust show some cracks on their surface, or partial disruption. It also seems that the fine particles are creating an outer stratified shell enveloping the dust within the core of the PAs (blue star in 4.18).

I repeated the same experiment with some PBs and PAs made of humic acid mixed with pyroxene or olivine, although this time I did not measure the spectra with MoHIS. The purpose of these experiments was to investigate if the presence of organics compounds increases the resilience of pebbles undergoing sublimation. Humic acids (HAs) are complex organic molecules containing aromatic compounds with phenolic and carboxylic constituents found naturally in soils. In the past, HA has been used as astrophysical organic simulants for labo-

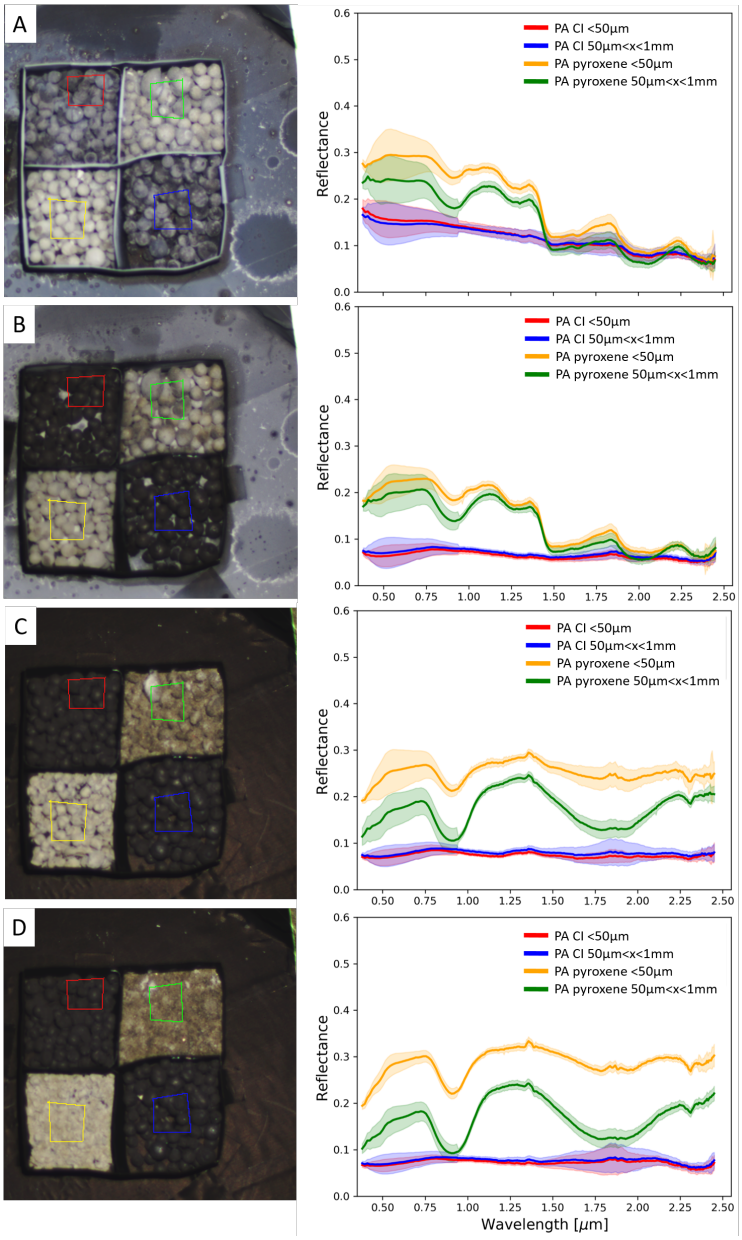

Figure 4.17: Spectral evolution of pyroxene and CI PAs with two different dust size distribution undergoing sublimation. On the left are the RGB composed images of the samples with the corresponding ROIs, while on the right the spectra are presented. The shaded line represents the variability within the ROIs. A) at the insertion of the sample inside SCITEAS-2, some frost covered the samples, creating a blue spectral slope. B) after the temperature starts increasing, the frost disappears and the ice sublimates. C) the sublimation continues inside the pebble, but the water ice absorption bands are now covered by a dust mantle. D) the sublimation is finished and there is no ice left within the pebbles. Pyroxene PAs completely disrupted. The spectral feature at 1.35 µm is an instrumental artifact.

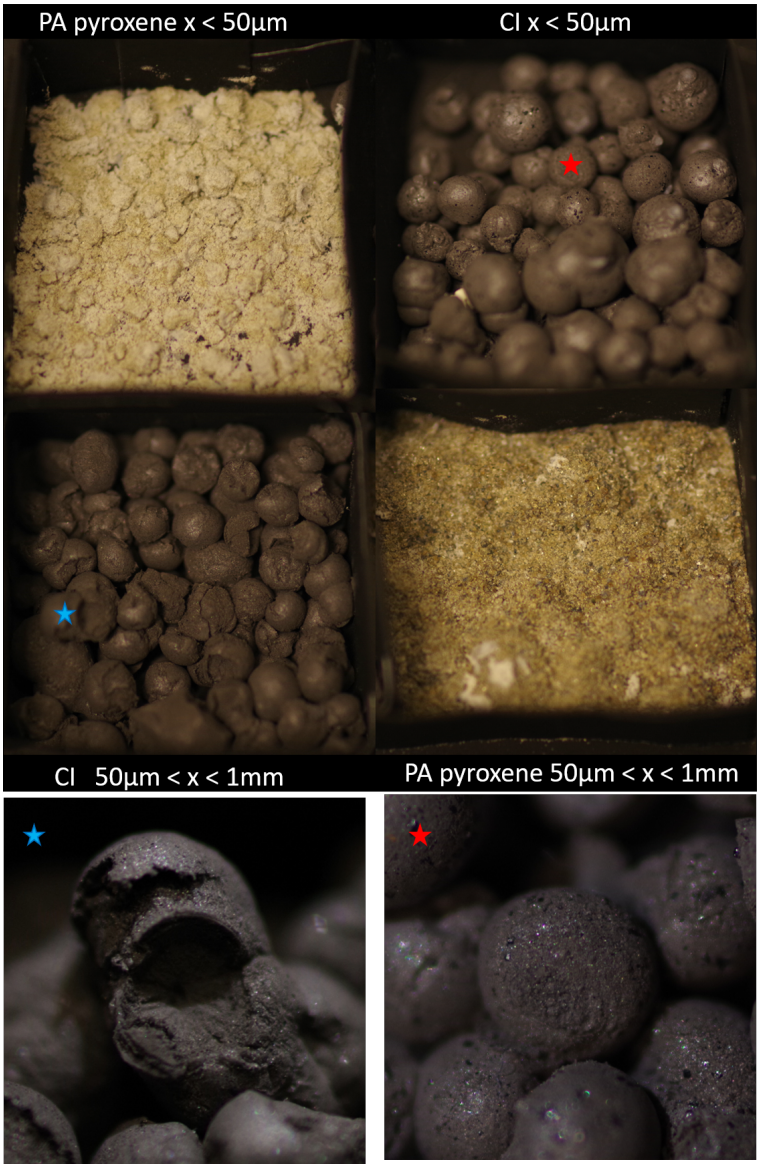

Figure 4.18: Pictures of CI and pyroxene PAs after the sublimation experiment. The sample holder has been extracted from SCITEAS-2 to take pictures with camera and a macro objective. The CI pebbles are well preserved, with the ones made of finer dust grains that keep their shape completely intact. The blue and red star indicate two pebbles captured with higher magnification (figures at the bottom).

ratory experiments (Bischoff et al., 2020; Feller et al., 2020). The HA that I used is produced by Sigma-Aldrich and appears as a brown powder with grain size smaller than 32 µm. I mixed it with different grain distributions of pyroxene and olivine in such a way that 20% of the dust mass is HA. Then I created both PAs and PBs, let them sublimate overnight inside SCITEAS-2, and finally retrieved them from the vacuum chamber to acquire some close-up

pictures (Fig. 4.19).

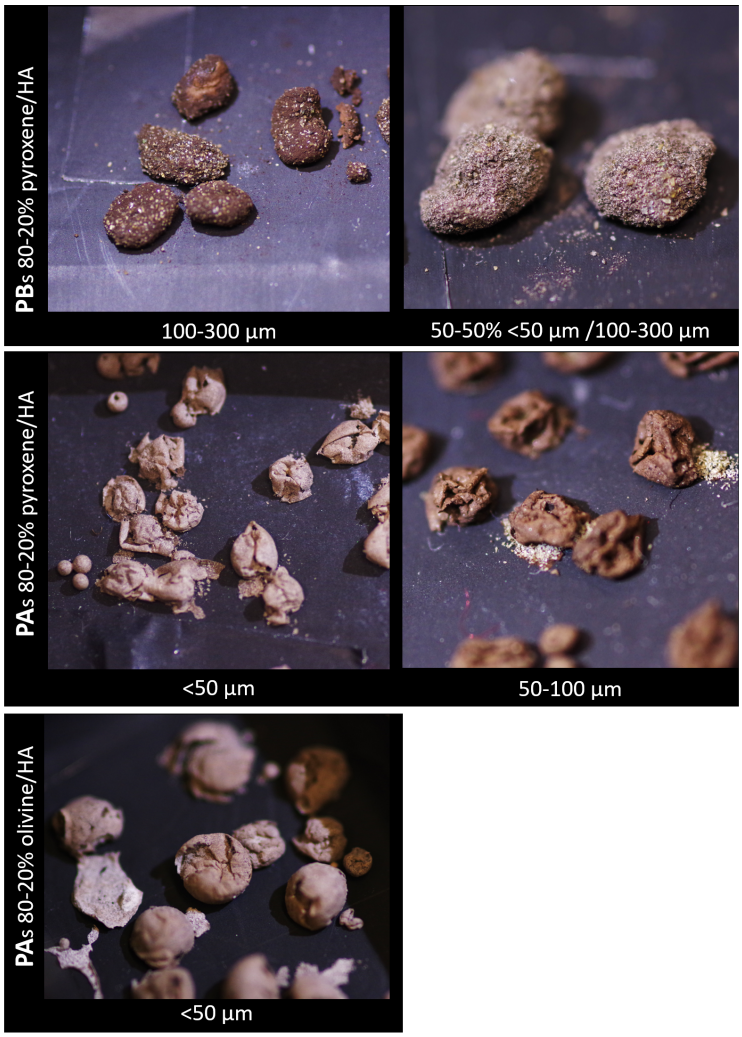

Figure 4.19: PAs and PBs made with humic acid (HA) and olivine or pyroxene. For all pebbles, 20% of the dust mass consists of HA. The dust size ranges of pyroxene or olivine are indicated on the bottom of the images. HA helps in preserving PBs made with coarse dust, while sublimated PAs show a HA-rich shell partially collapsed.

The PBs do not show any sign of disruption, and the HA seems to act as binding agent for coarse dust (pyroxene PBs made with $100-300\,\mu$m dust size should disrupt completely upon sublimation, see Fig. 4.10). In general, PAs seem to create a HA-rich crust that contains most of the dust. The crust collapses under its weight and because of the void left from the dust collapsed under its own gravity. It is still interesting to note, however, that small PAs (secondary droplets) are preserved under sublimation. The shell of HA mixed with dust is due to its partial hydrophobicity (Bischoff et al., 2020) that causes it to remain on the superficial part of pebbles, particularly evident in PAs. The segregation of HA from dust is more evident for those PBs and PAs where it was mixed with coarse dust, since the pebbles appear to have

a browner exterior.

I finally analyzed the olivine PAs HA-rich shell with scanning-electron microscope (Fig. 4.20). HA seems to have covered the single olivine grains by a solidified unstructured layer, and this means that it was partially dissolved in water before freezing the pebbles in liquid nitrogen. The partial dissolution of HA in water is expected, and it varies depending on the temperature, the HA specific molecules, and the pH of the solution (Shaban and Mikulaj, 1998). Another interesting phenomenon is the appearance of holes of different sizes on the pebble crust. The biggest holes are around 15 µm-size, and they seem to have developed between spaces left by HA and olivine grains. The smaller holes have diameters between 100 nm and 1 µm, and are characterized by more circular openings on relatively flat HA solidified layers on top of olivine grains. I interpret the presence of circular openings in the crust as a trace of the ice sublimation. The pressure developed by the sublimating ice can find a preferential path between the grains and create tunnels in the cohesive material.

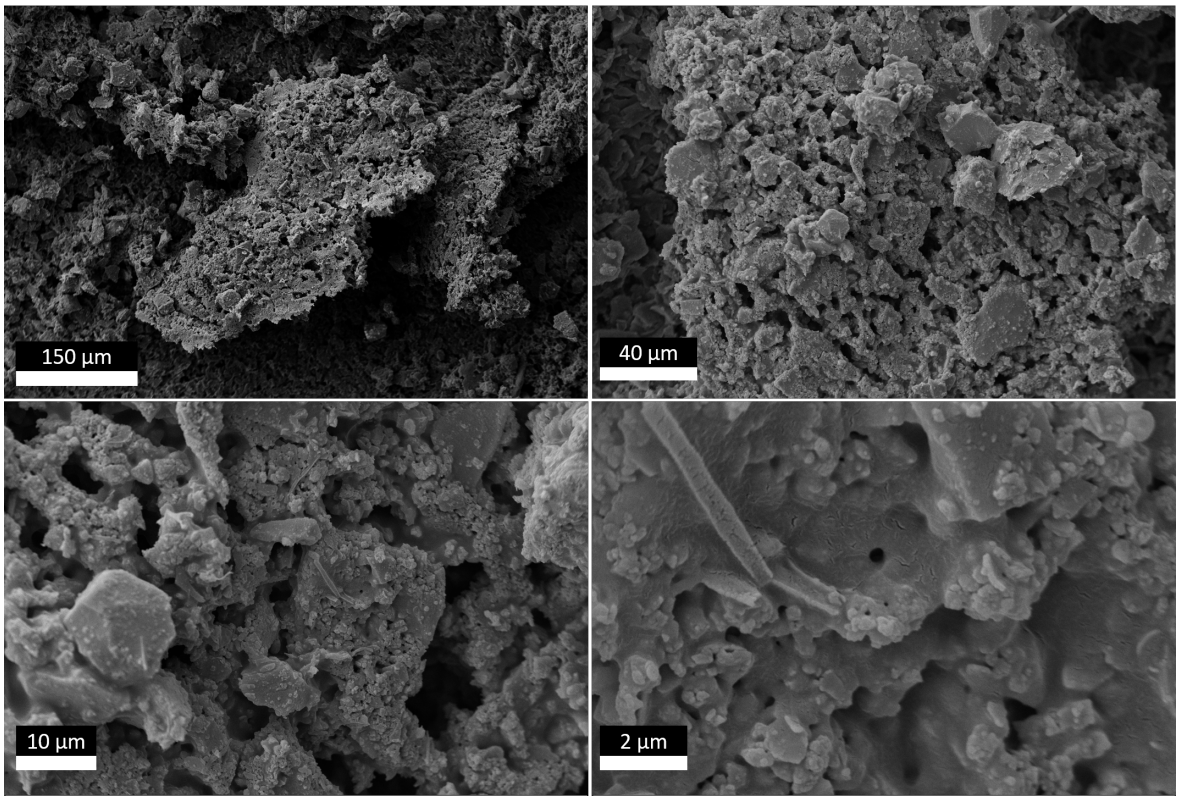

Figure 4.20: SEM images of the HA-rich crust remnant of PAs made with olivine and HA mixed together. Part of the HA has dissolved in water, since it appears that many dust particles are covered by an unstructured layer of HA (compare with clean olivine in Fig. 4.1). Furthermore, from tens of micrometers to sub-micrometers scale, the crust is covered by circular openings. I interpret this pattern due to sublimation of the ice, that moves olivine and HA grains and perforates the small HA crust on top of single olivine grains at sub-micrometer scale.

The presence of a liquid water phase during the production of PAs and PBs allows some compounds like HA to dissolve, and then solidify, creating stronger bonds between silicate grains. The presence of liquid water is not expected in pebbles in protoplanetary disks. One could argue that the strength of our pebble models containing organic material is only caused by dissolution of such organic compounds in the liquid phase, but this might be correct only for HA. Indeed, coal constitutes 5% and 2% of the CI and CR asteroid simulants, respectively, but it does not dissolve in water ((Painter et al., 2010)), and the pebbles made with these simulants show incredible stability upon disruption. Complex organic compounds have been demonstrated to have very different tensile strengths, resulting in higher (Kouchi et al., 2002) or lower (Bischoff et al., 2020) cohesiveness compared to silicate and ice grains. The stickiness of complex organic compounds have been invoked to be helpful for collisional growth of planetesimals (Kudo et al., 2002; Piani et al., 2017; Homma et al., 2019), but the physical properties of real astrophysical organic materials remain largely unknown, and as showed by Bischoff et al. (2020), wrong assumptions on the surface energy of the organic component can lead to very different tensile strengths. The main problem is a lack of knowledge of the exact composition of the organic material in comets and asteroids, and hence the difficulty in simulating the properties of such compounds both in the laboratory and from a theoretical perspective. I want to draw the attention to the fact that the most recent published works studied the properties of organic materials, ice and dust separately. To my knowledge, the experiments presented here are the first attempt to study the evolution of complex aggregates made with organic material, ice and dust together. Addressing realistic planetary formation scenarios requires an increase of complexity that could mimic the complexity of comets and asteroids in terms of chemical compounds, mineralogy, ice types, and grain sizes.

The results of the experiments shown in this section can be summarized as follows:

- when the first layer of ice sublimates, the water absorption bands are hidden by a dust mantle, masking completely the icy nature of the pebble;
- when the dust is mixed with organic compounds such as sub-bituminous coal and humic acid, the overall resilience to the sublimation process is increased;
- the sublimation of the ice through preferential paths in the dust-organic mantle creates organized holes at all scales ranging from hundreds of nanometers to tens of micrometers.

The importance of organics should be considered in future experiments aimed at understanding the physical properties of complex aggregates made of ice, silicates, and organics compounds.

4.8 Annex 3 to Chapter 4 - The strength of sublimated aggregates

This section illustrates further experiments that are not included in the published paper, regarding the strength of the sublimated pebbles after the sublimation process. To measure qualitatively the resistance of the pebbles to disruption, I used the Centrifuge for Accelerated Pebbles Observation (CAPO). This experiment is meant only to test CAPO functionality for measuring the compressive strength of dust aggregates, so I created the dusty pebbles with

a simplified procedure. Firstly, I produced only pyroxene PBs, with $100 - 300\,\mu m$ coarse dust mixed with different mass percentages of fine dust (less than $50\,\mu m$), namely 10, 20, 30, 50% of the pebble dust mass. Secondly, I did not produce icy pebbles, but only the wet aggregates. The wet aggregation creates really strong aggregates that are easy to manipulate without disruption. I put the wet aggregates inside the transparent PMMA sample holders of CAPO and I left them evaporating their water content for 24 hours before accelerating them in the centrifuge.

From the point of view of the GoPro camera, the pebbles appear like in Fig. 4.21. I define the failure of the pebble as the acceleration at which there is a visible change of the pebble shape against the external wall of the sample holder, or flakes of dust are detaching from the pebble. After the experiment, one can observe a layer of detached dust against the external wall of the sample holder, although even the weaker aggregate does not completely disrupt.

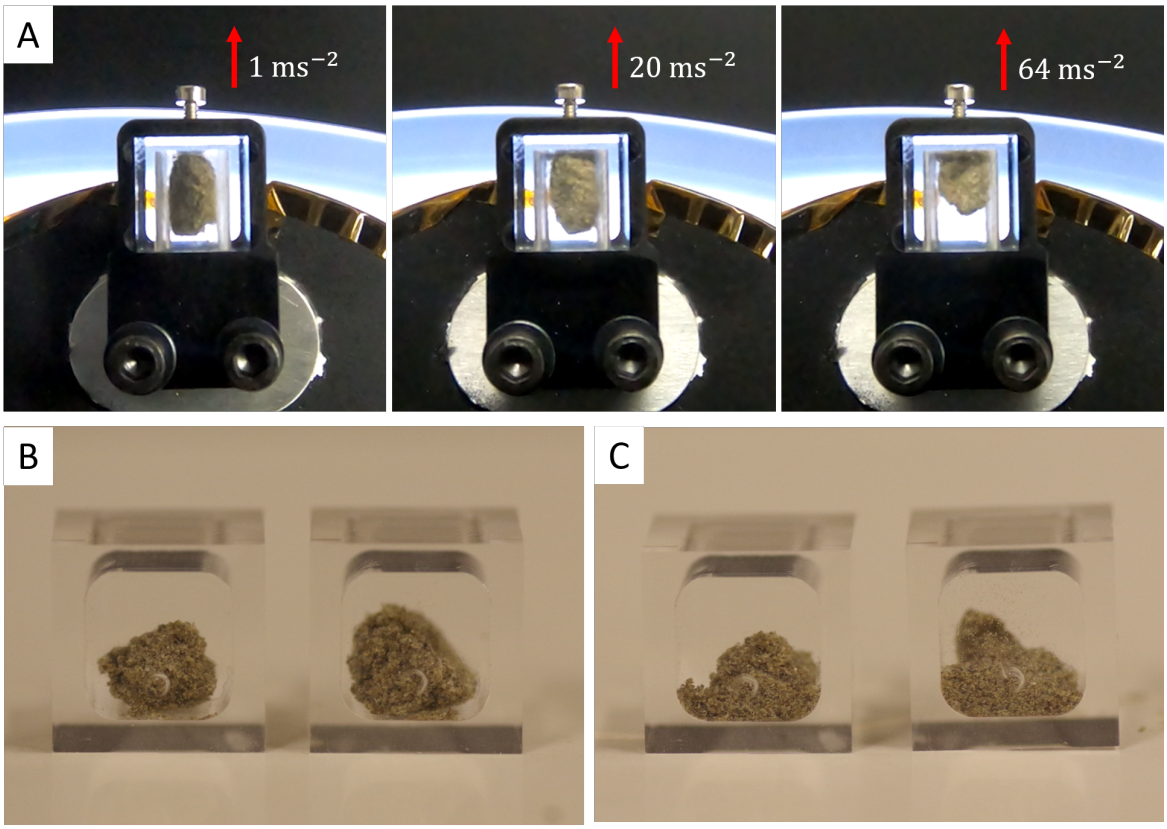

Figure 4.21: A) A series of images taken with the GoPro of the CAPO setup during the disruption of a pyroxene PB. These PBs dust is composed by 10% in mass of fine component, and 90% in mass by coarse dust grains. B) PBs before the experiment, C) after the experiment. Note that the pebble is not completely disrupted.

I created a total of four PB for each dust size distribution, and the final result is shown in Fig. 4.22. With some assumptions, we can translate the acceleration at which the pebble start to be compressed by the wall of the sample holder to a pressure indicating the uniaxial

stress σ (compressive strength) of the aggregate. Knowing an approximate aggregate porosity of 40%, and the average bulk density of pyroxene ($3.5\,\mathrm{g\,cm^{-3}}$), we can derive a mass of the aggregate of about 0.15 g. If we assume that at the moment of failure, the aggregate shares with the wall of the sample holder about $1\,\mathrm{mm}^2$, we obtain that the centrifugal acceleration a_c is linearly correlated to the failure pressure through

$$\sigma \simeq 0.15\, a_\mathrm{c}\ [\mathrm{kPa}] \tag{4.15}$$

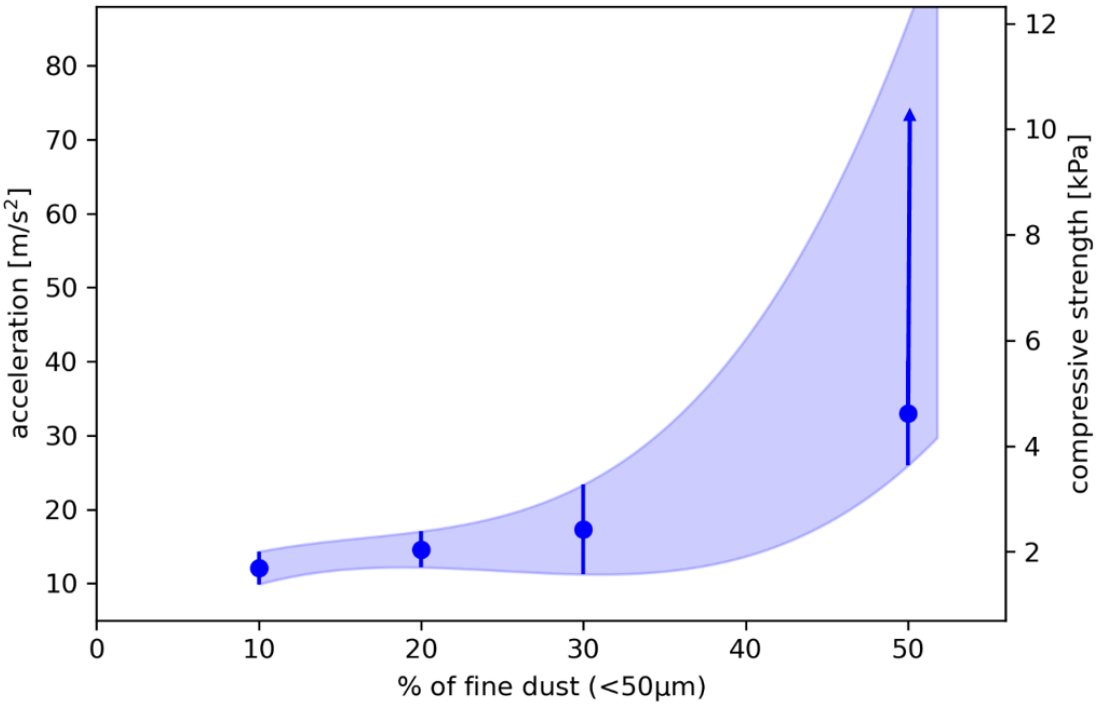

Figure 4.22: The plot shows the compressive strength of PBs created with $100-300\,\mu\mathrm{m}$ mixed with different masses of fine dust (less than $50\,\mu\mathrm{m}$). The acceleration at which the PBs start to deform is labelled on the left, while on the right the corresponding pressure is shown. The error is the standard deviation between the four PBs, except for the 50% fine component case, where two pebbles disrupted (the scatter point indicates their average), and two did not for our range of accelerations. The shadowed area indicates the area of accelerations at which PBs disrupt.

The particles with most fine (50% of the dust mass) do not disrupt easily, even when centrifuged to maximum acceleration. The disruption seen by the GoPro camera is minimal, and it seems to come not from compression of the aggregate, but from loss of some grains weakly attached to the surface of the pebble. In this case, the disruption of such dust grains is due more to some tensile strength that is pulling them apart from the bulk of the pebble. More measurement with higher magnification and macro objectives are needed to assess if

we are disrupting the pebble through compression, by tensile stress, or by a composition of the two. Our results are comparable to the one found by Meisner et al. (2012) who studied the compressive and tensile stress of cm-aggregates of silica particles (the same used in our experiment in chapter 5). They found a compressive strength in the range of $1 - 8\,\mathrm{kPa}$ and a tensile strength of $1 - 5\,\mathrm{kPa}$, with 40% porosity aggregates showing a compressive strength of about $6\,\mathrm{kPa}$. Their dust has higher amount of fines, with 80% of the dust mass less than $5\,\mu\mathrm{m}$ and maximum grain size $10\,\mu\mathrm{m}$. Different results of compressive strength could be a sign of better cohesion between particles, either because of their production method (water bridges), an increased surface energy of pyroxene, or favorable particle distribution within the pebble.

Finally, I tried to centrifuge some PBs made with bulk CR asteroid simulant (the CR simulant is better described in chapter 6). The CR asteroid simulant contains a mixture of different minerals (olivine, pyroxene, magnetite, Mg-serpentine, metallic iron, pyrite, metallic nickel), and organic material (sub-bitumunous coal), with a broad grain size distribution (Fig. 6.2). PBs made of this simulant are extremely difficult to break, and they can be manipulated by hand without disrupting them. The acceleration reached by the centrifuge is not enough to estimate their compressive strength.

Further experiments with the CAPO setup could try to derive the effective surface energy of complex aggregates made with different grain sizes and materials. If the pebble is contained in a box and glued on one side of it, the tensile strength can be measured directly, measuring the acceleration at which the aggregate detach from the wall. An approximate surface energy of the material can then be derived from the formula proposed by Blum et al. (2006), who found an upper limit to the tensile strength of an aggregate depending on the grain size r, the filling factor ϕ, and the surface energy of the material γ:

$$\sigma = \frac{9\phi\gamma}{4r} \tag{4.16}$$

The resulting surface energy of a complex aggregate formed by dust and organic material can then be compared to $\gamma = 0.07\,\mathrm{J\,m^{-2}}$ found by Bogdan et al. (2020) for aggregates with $\sim 60\%$ porosity of chondritic material under ambient conditions at room temperature. Future experiments and improvements of the current CAPO setup will provide interesting data on the strength of complex aggregates.

Chapter 5

Negative polarization properties of regolith simulants - Systematic experimental evaluation of composition effects

Astronomy & Astrophysics 665 (2022): A49
DOI: https://doi.org/10.1051/0004-6361/202243844

Stefano Spadaccia[1], Lucas Patty[1], Holly L. Capelo[1], Nicolas Thomas[1], Antoine Pommerol[1].

[1] Space Research and Planetary Sciences Division, Physikalisches Institut, University of Bern, Sidlerstrasse 5, 3012 Bern, Switzerland

Abstract

Polarization phase curves of asteroids and other small airless bodies are influenced by the compositional and physical properties of their regolith. The mixing of minerals composing the regolith influences the negative polarization at small phase angles because it changes the multiple scattering properties of the medium. This work aims to demonstrate experimentally how the mixing effect influences the polarization phase curve at small phase angles for different mineralogies relevant for asteroids, and to determine how different aggregate sizes affect the negative polarization. We prepared a set of binary and ternary mixtures with different common minerals on asteroids and one set of the same mixture with different aggregate sizes. We measured their reflected light at 530 nm with full Stokes polarimetry at phase angles ranging from 0.8° to 30°. The mixing effect of the mixtures with both bright and dark minerals significantly changes the behavior of the phase curves in terms of minimum polarization, phase angle of the minimum, and inversion angle with respect to the mineral components that are mixed together. The changes in phase curve could explain the polarization observation of particular classes of asteroids (F and L class) and other asteroids with peculiar polarization curves or photometric properties. Furthermore, we demonstrate that the negative polarization is invariant to the presence of dust aggregates up to centimeter sizes.

5.1 Introduction

Polarimetry is a powerful tool for studying the properties of many objects in our Solar System and beyond. The induced linear polarization in the light reflected from a surface can provide valuable information about the porosity, multiple scattering, shape of the grains, and their indices of refraction. The challenge lies in disentangling this intricately interwoven mass of information when the polarization of astronomical objects is measured.

One of the most commonly used methods is the analysis of the relation between the linear polarization P and the phase angle (α, i.e., the angle between the reflected light and the light source in the scattering plane). P is given by

$$P = \frac{I_\perp - I_\parallel}{I_\perp + I_\parallel}, \tag{5.1}$$

where $I_\perp$ and $I_\parallel$ are the intensities of the reflected light with the polarization axis normal and parallel to the plane of scattering, respectively. We note that $P = Q/I$ using the Stokes formalism.

Irregular particles of many bodies in the Solar System show similar features in their polarization phase curve. At very small α ($<3°$), the coherent backscattering opposition effect (CBOE) occurs and the reflected light increases nonlinearly (Shkuratov, 1989; Muinonen, 1990; Hapke, 1993). The CBOE causes a surge in reflected circular polarization and a decrease in reflected linear polarization when the object is illuminated with circular and linear polarized light, respectively (Nelson et al., 1998). For unpolarized incident light, the linear polirization at small α (i.e., smaller than $15-25°$) is negative and thus is in the backscattering regime $I_\perp < I_\parallel$. The part of the phase curve that is dominated by negative polarization is commonly referred to as the negative polarization branch, and the minimum of polarization

$|P_{min}|$ usually falls at phase angles $\alpha_{min} = 8-15^{\circ}$. The phase angle at which the polarization is zero is called inversion angle α_{inv}. At higher α (between 30 and $90-100^{\circ}$), the polarization increases and reaches a maximum. Generally, the maximum linear polarization is inversely correlated to the albedo of the surface by the so-called Umov effect (Umov, 1905; Zubko, 2011).

The negative polarization feature of asteroids, comets, and other bodies has been studied extensively both theoretically and experimentally, in order to understand its origin and its possible use as a proxy for retrieving small-particle properties through remote sensing (see Cellino et al. (2015b) and Levasseur-Regourd et al. (2018b) for a complete review). Within this framework, the relation between different parameters that control the shape of the phase curve has been analyzed.

Minor bodies such as comets and asteroids are covered by regolith, that is, by a loose deposit of fine dust and rock pieces developed by space weather and meteroid impacts. The shape of the polarization phase curve of dust depends on the number of interactions the incident radiation has with the sample, which can be one time (single scattering) or multiple times (multiple scattering). Single scattering predominantly occurs in environments with low particle density, for example, cometary comae, while regolith-like surfaces are characterized by multiple scattering. Shkuratov et al. (2004) and Zubko (2011) showed that the polarization phase curves of multiple and single-scattering environments are not identical. Multiple-scattering events effectively scramble the overall polarization signal that is reflected back to the observer, resulting in an overall weaker polarization. The single-scattering polarization phase curves are also usually characterized by higher inversion angles, higher α at the polarization minimum, and higher maximum polarization.

Many studies have been carried out with the aim to understand the origin of the negative polarization in the case of single scattering. There are indications that the negative polarization arises from the coherent backscattering effect of the particles (Zubko et al., 2008). The single-scattering negative polarization of dust grains is stronger for small particles (below 3 µm), and it also depends on their absorption properties (Zubko, 2013; Zubko et al., 2020). Interestingly, the negative polarization tends to disappear when the submicrometer particles are removed from dust simulant samples (Escobar-Cerezo et al., 2018) and from clouds of silicates (Muñoz et al., 2021). In the case of multiple scattering, the negative polarization is also dependent on the porosity of the sample, showing an increase in amplitude of the negative polarization with sample compression (thus decreasing the surface porosity) and exhibits a dependence on changing the incidence and emission angle after the phase angle is fixed (Shkuratov et al., 2002; Halder et al., 2018).

Various authors have correlated the presence of particular minerals in asteroid regolith (identified by scalar spectroscopy) to their multiple-scattering polarization properties. Cellino et al. (2015a) investigated the variation in negative polarization of asteroid (4) Vesta depending on its rotation and found a good correlation between the surface albedo variations and the polarizance. The authors, however, pointed out that a complete explanation of the polarization data needs to take variations in surface geometry and mineralogical composition into consideration. Particularly, they demonstrated that dark regions dominated by eucrite seem to show higher $|P_{min}|$. More recently, Castro-Chacón et al. (2022) observed a variation in

polarized light with the rotational curve of asteroid (16) Psyche, correlating with changes in albedo and in surface geometry. Gil-Hutton and García-Migani (2017) used the phase curve model of Muinonen et al. (2002) to calculate the refractive index of the regolith on the surface of 129 asteroids, and observed that there is a strong correlation between the refraction index and the inversion angle, and between $|P_{min}|$ and the distance between single scattering particles. A similar result was obtained by Masiero et al. (2009), who found that the refractive index plays a more important role in determining the inversion angle than the particle size.

It has been demonstrated that asteroids cluster together in the $P_{min}-\alpha_{inv}$ space depending on their class types (Belskaya et al., 2017). Generally, this indicates that asteroids in the same family share similar mineralogical compositions and physical properties. To some extent, this is also affected by the asteroid albedo. Asteroids with a high albedo in the V band (more than 0.2) have a higher P_{min} than moderate-albedo asteroids (0.1-0.2 in V), and the darkest asteroids (C, Ch, and B classes; an albedo lower than 0.1) populate the lowest P_{min} region. In this context, Cellino et al. (2015a) noted that there is some degree of mixing between moderate- and low-albedo asteroids defined in the region $P_{min} = -1.1\% - 1.4\%$ and $\alpha_{inv} = 18-21^{\circ}$ in Fig. 5.8. Dollfus et al. (1989) interpreted the fact that terrestrial rocks and lunar fines show a smaller and larger polarimetric inversion angle, respectively, than most asteroids as an indication that the surface of asteroids contains coarser material than the surface of the Moon. More recently, two new classes of rare asteroids have been identified (Belskaya et al., 2005; Cellino et al., 2006): the F-class asteroids, which show small inversion angles ($14-16^{\circ}$), and L-type asteroids ("Barbarians"), with inversion angles in the range $\alpha_{inv} = 25-30^{\circ}$. These asteroid classes are outliers with respect to the normal distribution of asteroids in the $P_{min} - \alpha_{inv}$ space.

It has been suggested that the high inversion angle of L-type asteroids is due to the presence of white spinel-bearing CAIs on the surface (Devogèle et al., 2018a; Sunshine et al., 2008), mixed in a dark matrix (Burbine et al., 1992). Nevertheless, asteroids and their corresponding meteorite classes show a wide range of mineral compositions, including olivine, pyroxene, plagioclase, spinel, and phyllosilicates (Michel et al. (2015) and references therein). While it is possible to directly observe the presence of multiple minerals on a surface through scalar spectroscopy, the effect on the polarization phase curve of such mixtures is not clear. Studies to clarify this were made by Boehnhardt et al. (2004) and Bagnulo et al. (2006), who successfully modeled the phase curve of trans-Neptunian objects at very small phase angles, under the assumption of a two-component surface medium composed of bright (ice) and dark particles.

Shkuratov (1987b) and Shkuratov et al. (1994) demonstrated that a material with a mixture of small and large albedos can show a different negative polarization phase curve and a higher $|P_{min}|$ than the endmembers of the mixture. This effect was also used by Belskaya et al. (2005) in order to explain the very small inversion angle of F-type asteroids, which are thought to share some physical properties with comets (Cellino et al., 2018). Belskaya et al. (2005) proposed that because F-class asteroids are very dark (0.03-0.07 albedo) but have a higher P_{min} than C-class asteroids, the surface regolith must be homogeneous, because any mixing effect would decrease $|P_{min}|$. A systematic study of the mixing effect, however, is lacking in the literature.

The surface roughness can also influence the linear polarizance. The irregular shape

(and/or macroscopic roughness) of an asteroid can result in nonzero polarization at $\alpha = 0$, which generally results from polarization contributions arising from different parts of the asteroids with a distribution of incidence and emission directions. The Hayabusa spacecraft observed a great variety of surface morphology on (25143) Itokawa, ranging from boulders and rough terrain to flatter terrain characterized by millimeter (mm) to centimeter (cm) gravel.

While the effect of particle size on the negative polarization at small phase angles is generally understood, there are still important effects that could influence this part of the polarization phase curve, such as the mixing of materials with different optical properties and the aggregation of small particles. The aim of this work is to systematically explore the change in polarization phase curve of relevant regolith-like minerals when the minerals are intimately mixed together in different compositions. In addition, we demonstrate the change in polarizance when the powder grains are incorporated into mm-cm size aggregates.

The remainder of this chapter is structured as follows: in section 2 we describe our method and experimental apparatus, in section 3 we present our results and summarize the findings, and section 4 provides a discussion of the results in the context of asteroid surface features. We conclude in section 5.

5.2 Materials and methods

5.2.1 Experimental Setup

The polarization measurements were carried out with the POLarimeter for ICE Samples (POLICES) at University of Bern (see also Poch et al. (2018) and Patty et al. (2022)). POLICES is a full Stokes polarimeter (Dual PEM II/FS42-47, Hinds Instruments) that allows us to measure the polarization state of the light scattered by a sample at different phase angles. It consists of an enclosure in which an arm holding a collimated light source illuminates a sample placed at the bottom of the enclosure. The scattered light is measured at the top of the enclosure in nadir direction. In this configuration, the reflection angle is approximately 0°, while the incident angle, which is thus similar to the phase angle α, can be varied.

The light source is a 530 nm LED (Thorlabs M530F2) that is depolarized and fiber-fed to a collimating head, providing an illuminated sample area with a diameter of approximately 15 mm. The remnant polarization of the incidence light at 530 nm is lower than 0.01%, which agrees well with the polarization of the global light coming from the solar disk (Clarke and Fullerton, 1996). The arm can span a wide range of phase angles (the angle formed by the incidence light and the emission direction), from -30° to 75°. The minimum rotation step of the arm is 0.1°. The sample is placed on the same plane that contains the rotation axis of the arm, and it sits on a rotation stage that can change the azimuth of the sample θ from 0° to 360° (Fig. 5.1). The polarimeter entrance pupil is approximately 50 cm away from the sample, and the fiber used to illuminate the sample is at about 44 cm from the sample. The width of the illuminated spot on the sample has a negligible effect on the estimation of the phase angle (about 0.1°).

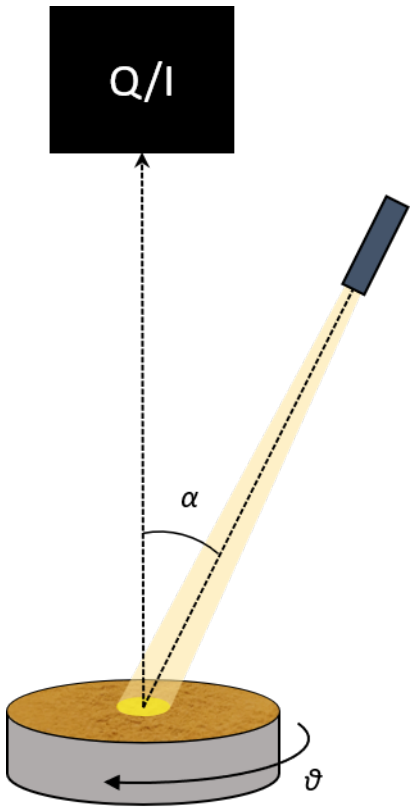

Figure 5.1: Geometry of the POLICES setup. A nearly collimated light source illuminates the sample with a phase angle α that varies between 0.8 and 30°. The sample can be turned in steps of 45° on the azimuth angle θ. The full Stokes polarimeter is is fixed perpendicular to the sample and measures Q/I at different sample angles α and θ.

5.2.2 Samples

In Table 5.1 we list the mineral powders that were used in the experiments. These include silicates (silica, forsterite, and fayalite), spinel-group minerals (magnetite, Mg-spinel) and graphite. The table also includes the reflectance R of the pure powders measured at 530 nm using an integrating sphere for homogenous illumination. In general, the samples can be divided into two groups according to their reflectance: dark powders ($R < 0.5$, magnetite, graphite, and fayalite) and bright powders ($R > 0.5$, silica, forsterite, and Mg-spinel). Table 5.2 lists the different mixtures with abbreviations measured in this work. The mass ratios of the two components mixed together (1:0, 9:1, 4:1, 7:3, 1:1, 1:3, and 0:1) are equivalent to 100-0%, 90-10%, 80-20%, 70-30%, 50-50%, and 0-100% of the total mass being first endmember and second endmember. The grain size ranges are comparable between different minerals; they are mainly about 1 µm. We acquired scanning electon microscope (SEM) images of forsterite, spinel, and fayalite, confirming that these powders are mainly composed of µm and sub-µm sized particles. We acquired SEM images of the endmembers (Fig. 5.2) and of some of the mixtures (Fig. 5.3). The grain shapes are generally irregular and within the size ranges

provided by the supplier. Forsterite and magnetite mainly have sub-µm grains, while graphite and fayalite have larger grains, although sub-µm grains are still present and the surfaces of larger grains display features at the sub-µm scale.

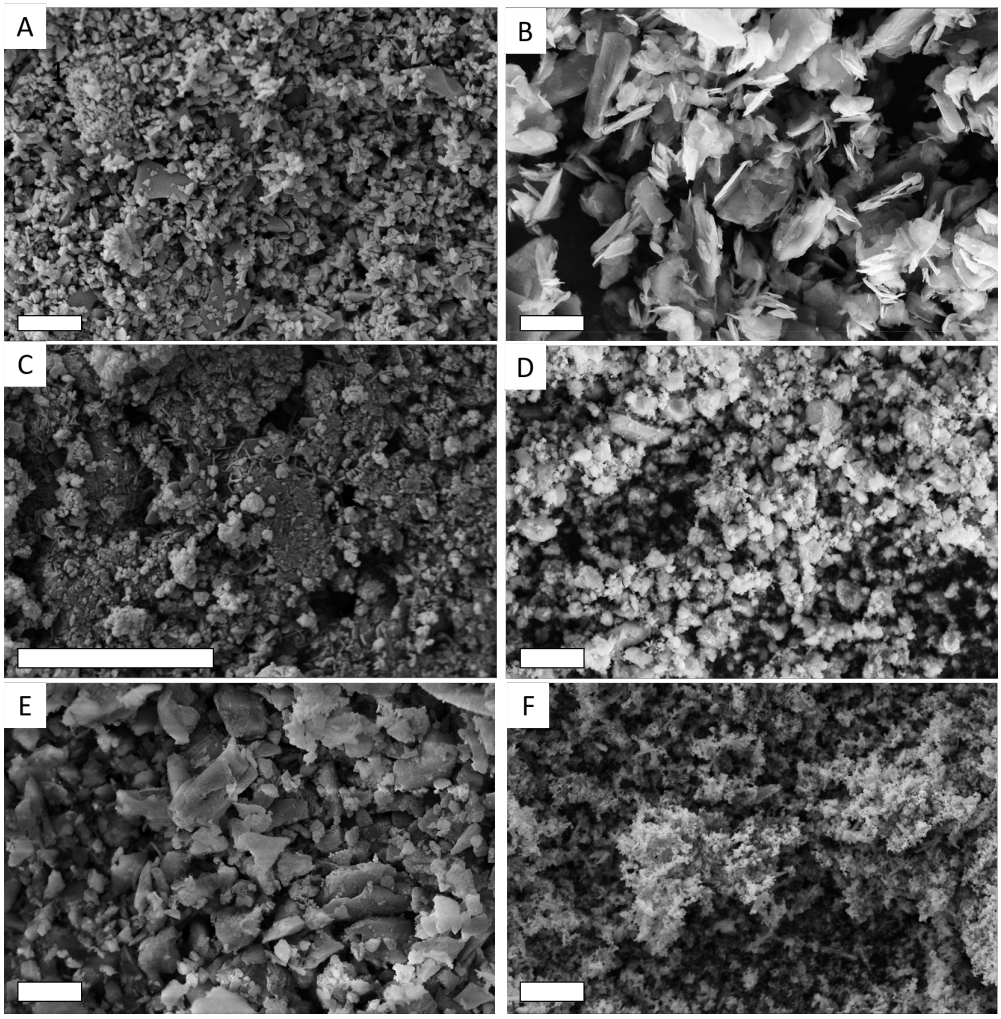

Figure 5.2: Scanning electron microscope images of the six minerals used in this study. A) Mg-spinel, B) graphite, C) forsterite, D) silica, E) fayalite, F) magnetite. All the scale bars represent 10 µm.

5.2.3 Sample preparation

In order to create binary mixtures, we weighed the two end members to the correct mass ratio. We subsequently mixed them until we obtained a homogeneous sample.

As silica can easily create aggregates of cm size (Blum et al., 2006), we used a binary

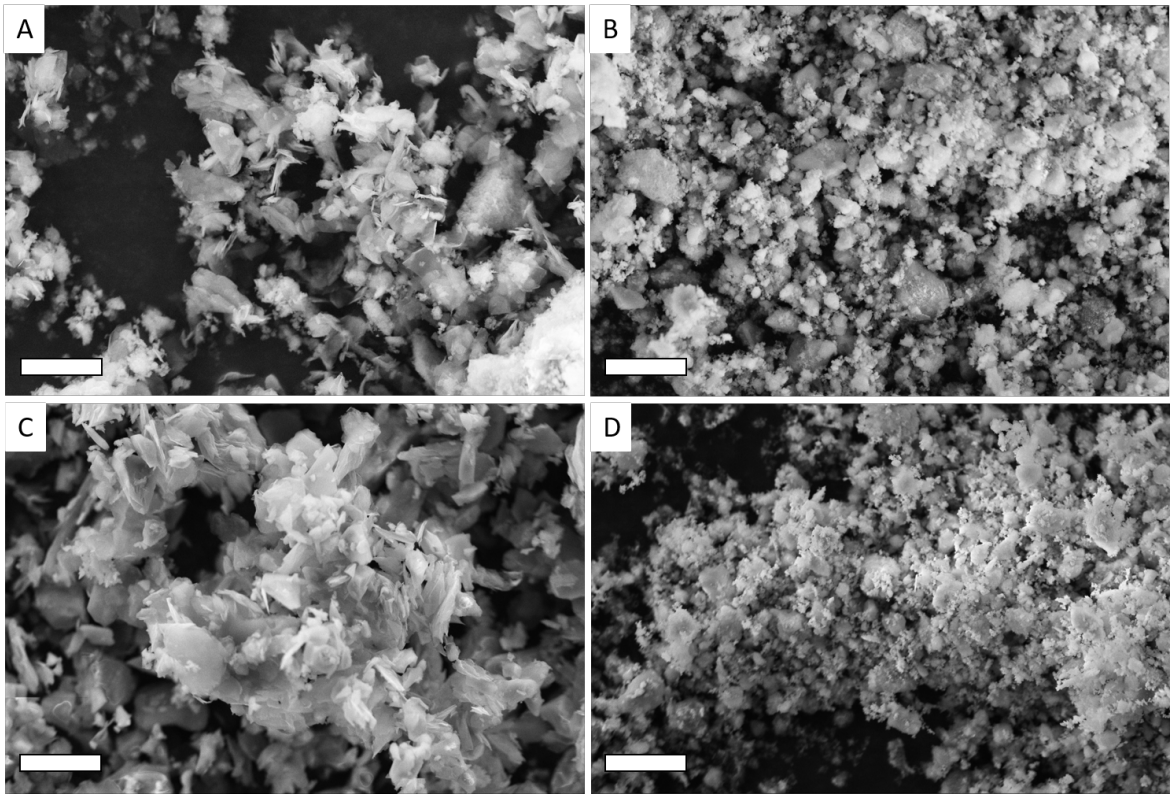

Figure 5.3: Scanning electron microscope images of four mixtures used in this study. A) Forsterite-graphite 7:3, B) silica-forsterite 7:3 , C) spinel-graphite 7:3, D) silica-magnetite 7:3. All the scale bars represent 10 µm.

mixture of silica and graphite to study the effect of aggregation on the negative polarization. After a homogeneous mixture was obtained, aggregates were created by gently moving the mixture in a bowl. Then we sieved the aggregates through a 200 µm sieve to obtain fine aggregates. Larger aggregates are easily breakable if passed through a sieve, and therefore we individually chose aggregates larger than 2 mm that were then gently placed in the sample holder. Generally, the aggregates formed with this method reach sizes up to $\sim$ 1cm.

The sample holder used for all our measurements consists of a plastic petri dish covered by black aluminum tape. The height of the sample is then adjusted in the enclosure so that the sample surface coincides with the rotation axis of the arm holding the incident light. In this way, the light spot always illuminates the center of the sample holder at the different phase angles. The sample holder is 5 mm deep and is filled with the sample in such a way that the walls and the bottom of the sample holder are completely concealed by the sample. Furthermore, the sample holder is covered by black aluminum tape to minimize the risk of polarization signal from the edges of the sample holder at large phase angles. The dust sample is gently deposited on the sample holder, without touching the surface to avoid compression of the powder.

From the SEM images of the mixtures (Fig. 5.3), it is clear that the mixing procedure is

Table 5.1: List of minerals used in the experiments.

Mineral	Ch. formula	Grain size	Reflectance (530 nm)	Supplier
Silica	SiO_2	<10 µm	0.650 ± 0.013	Honeywell Fluka
Magnetite	Fe_3O_4	<5 µm	0.010 ± 0.001	Sigma Aldrich
Graphite	C	<20 µm	0.028 ± 0.002	Sigma Aldrich
Forsterite	Mg_2SiO_4	<15 µm	0.758 ± 0.014	F.J. Brodmann & Co
Spinel	$MgAl_2O_4$	<15 µm	0.822 ± 0.013	F.J. Brodmann & Co
Fayalite	Fe_2SiO_4	<15 µm	0.158 ± 0.004	F.J. Brodmann & Co

Table 5.2: List of mixtures measured in this work.

Powder 1	Powder 2	Powder 3	Mass ratio	Abbreviation
Silica	Graphite	–	99:1, 9:1, 4:1, 7:3, 1:3	si-graph
Mg-spinel	Graphite	–	9:1, 4:1, 7:3, 1:3	spi-graph
forsterite	Graphite	–	9:1, 4:1, 7:3, 1:3	fo-graph
forsterite	Mg-spinel	–	9:1, 4:1, 7:3, 1:3	fo-spi
Magnetite	Graphite	–	9:1, 4:1, 7:3, 1:3	mt-graph
Forsterite	Fayalite	–	9:1, 4:1, 7:3, 1:3	fo-fa
Forsterite	Silica	–	9:1, 4:1, 7:3, 1:3	fo-si
Silica	Magnetite	–	9:1, 4:1, 7:3, 1:3	si-mt
Silica	Forsterite	Graphite	1:1:1, 2:9:9, 9:2:9, 9:9:2	si-fo-graph
Silica	Magnetite	Graphite	1:1:1, 2:9:9, 9:2:9, 9:9:2	si-spi-graph

effective at the particle level. Particles of different materials are well intermixed and adjacent to each other.

5.2.4 Data acquisition

The polarized light reflected by the sample was measured with $\sim$ 35 different phase angles ranging from 0.8° to 75°. At angles smaller than 30°, the sampling was smaller in order to better depict the behavior of the sample at small phase angles.

Comparing the polarization of different samples, we consider different sources that contribute to the total error. Variations resulting from the sample geometry: each phase angle curve is the result of at least five measurements in which the sample azimuth was varied by 45° incremental steps, essentially dampening the contribution of geometric effects related to nonflat samples.The presented phase curve average and standard deviation are taken over these repetitions. When the same sample is prepared different times and measured, the polarization signal is slightly different. This is due to the differences in the mixing process and in the sample preparation (i.e., geometrical effects are different for each sample). The differences between the average phase curves of the same sample mixed different times are minimal and give a standard deviation of $7 \cdot 10^{-5}$ (negligible error on the mixing). On the other hand, the standard deviation of each sample due to the azimuthal rotation is two orders of magnitude larger, depending on their different rough surfaces. This is the most important source of error when two different mixtures are compared.

From the repetition of the silica-graphite mixture (99:1 mass ratio), we estimated the maximum variation in polarization due to geometrical effects when preparing the sample to be ±0.03%. This error is to be used when the polarization of different mixtures is compared. The error on the evaluation of α_{min} is ±0.5° because all curves are sampled with 1° step around the polarization minimum. The error on the inversion angle was estimated using the maximum range of the geometrical error on the repetitions of the mixture, and it is ±0.3°.

The reflectance of the dust powders (Table 5.1) has been measured with a camera (CS126MU, Thorlabs) and through the use of an integrating sphere in combination with the 530 nm LED source for homogeneous illumination. In this configuration, the measured reflectance is a hemispherical-directional reflectance, but we refer to it as reflectance in this work. A spectralon target was used for image calibration. The errors associated with the measurements are the standard deviation of the pixel signal of the selected region of interest over the sample.

5.3 Results

We measured the polarization of different mixtures at small phase angles to understand how the polarization minimum $|P_{min}|$, the phase angle at minimum of polarization α_{min} , and the inversion angle α_{inv} change with respect to the dust endmembers of the mixture (see also Fig. 5.4). In Appendix 5.3 we present the main properties of the polarization phase curve of all the mixtures.

5.3.1 Binary dust mixtures

We prepared different mixtures and investigated the negative polarization depending on the mixing ratio of the two components (Fig. 5.4). The mixtures were silica-graphite, spinel-graphite, magnetite-graphite, forsterite-spinel, forsterite-graphite, silica-magnetite, silica-forsterite, and forsterite-fayalite (see also Table 5.2). The mixtures cover a range of contrast in reflectance between endmembers: dark-dark mixtures (magnetite-graphite), dark-bright mixtures (silica-graphite, spinel-graphite, forserite-graphite, silica-magnetite, and forsterite-fayalite), and bright-bright mixtures (forsterite-spinel and silica-forsterite). For most of the mixtures (spinel-graphite, magnetite-graphite, forsterite-spinel, silica-forsterite, and forsterite-fayalite), the phase functions of the different mixing ratios change monotonically between the phase functions of the pure endmembers. In three of the dark-bright mixtures, we observe a non-monotonic behavior of the phase function of different mixing ratios. In particular, some mixing ratios of silica-magnetite, forsterite-graphite, and silica-magnetite show higher $|P_{min}|$, α_{min} and α_{inv} than the phase curves of the endmembers.

Here we present a summary of our observations (for the mixture silica-graphite, we sieved the mixture to remove all aggregates larger than 200 µm). In some of the mixtures, the mixture behaves very differenty from the two pure minerals that were mixed (called hereafter endmembers of the mixture). We observe a deepening of $|P_{min}|$ respect with both the endmembers in the case of silica-graphite, forsterite-graphite, silica-magnetite, while the other mixtures do not show deepening of $|P_{min}|$ (within error). Of the three, the maximum of $|P_{min}|$ is found for silica-magnetite, starting at about $P_{min} = -0.5\%$ and reaching $P_{min} = -2.2\%$ when the mass ratio of the two endmembers is 1:1. The mass ratio at which $|P_{min}|$ is found

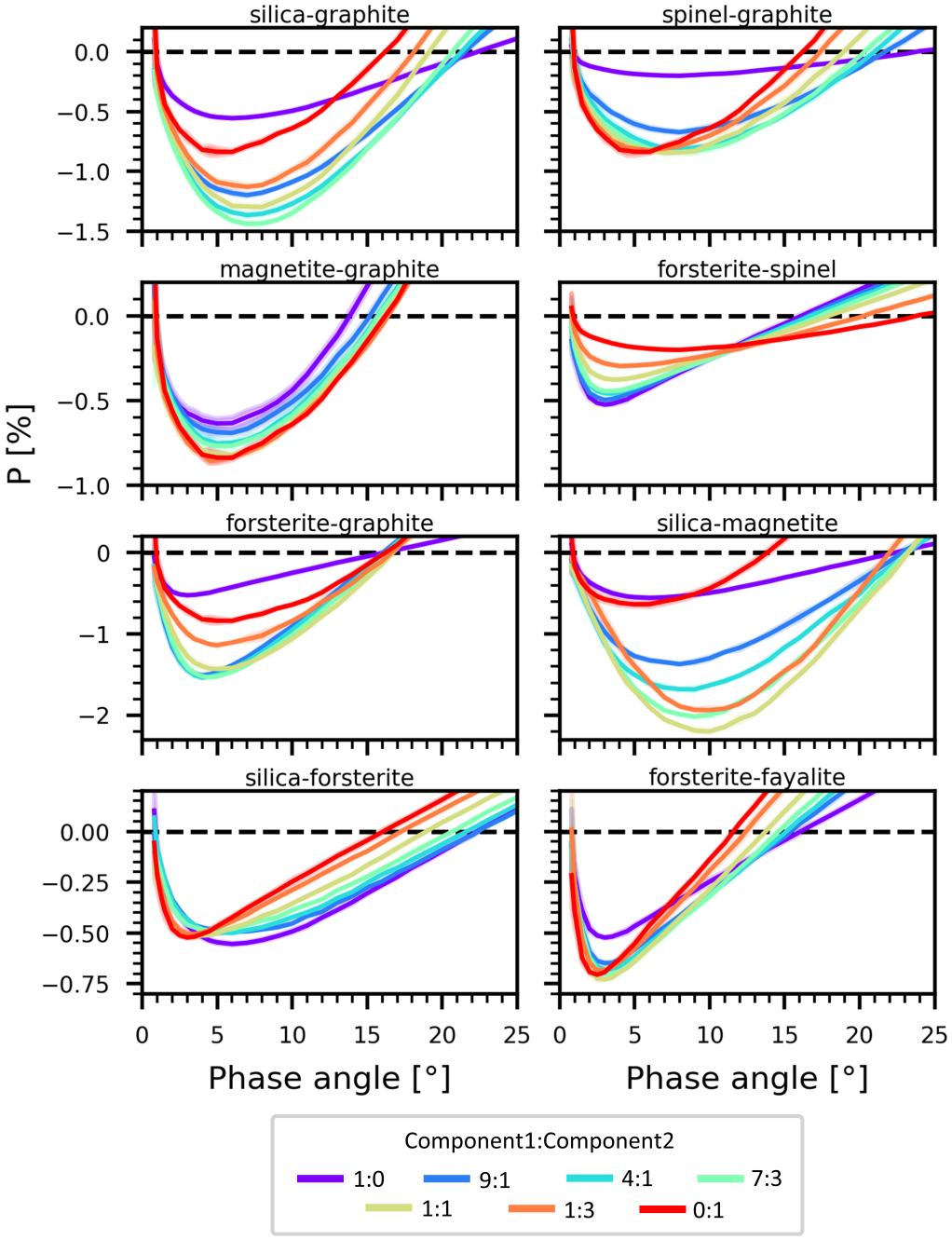

Figure 5.4: Polarization phase curves of binary mixtures. The two mineral components are mixed with mass ratios showed by different colors, with the endmembers of the mixture being purple and red. The mass ratios of the two components mixed together (1:0, 9:1, 4:1, 7:3, 1:1, 1:3, 0:1) are equivalent to have 100-0%, 90-10%, 80-20%, 70-30%, 50-50%, 25-75%, 0-100% of the total mass being first endmember and second endmember. The shaded areas around the curves denote the standard deviation, which in this figure is often smaller than the line width.

varies with the different mixtures (e.g., 7:3 for silica-graphite and 4:1 for forsterite-graphite).

Generally, the inversion angle of the mixtures varies monotonically from one of the endmembers α_{inv} to the other. There are two exceptions: forsterite-graphite and silica-magnetite. In both cases, some of their mixtures have a larger inversion angle than both endmembers (the endmembers with a larger inversion angle are forsterite and silica). In the forsterite-graphite mixture, the maximum inversion angle is reached in the 1:1 mixture with $\alpha_{inv} = 16.7 \pm 0.3^\circ$ (to be compared with the inversion angle of forsterite, $\alpha_{inv} = 16.0 \pm 0.3^\circ$). In the case of silica-magnetite, the maximum inversion angle is reached by a 1:1 mixture with $\alpha_{inv} = 23.2 \pm 0.3^\circ$ (to be compared with silica, $\alpha_{inv} = 22.3 \pm 0.3^\circ$)

The binary mixtures that show a deepening of $|P_{min}|$ also show an increase in phase angle at which the minimum polarization occurs, α_{min}. Silica-graphite, silica-magnetite, and forsterite-graphite mixtures all show a higher value of α_{min} than the endmembers α_{min}. As in the case of $|P_{min}|$, the maximum α_{min} does not occur at fixed mass ratios, but depends on the minerals that are mixed together. The highest α_{min} compared to the endmembers is given by silica-magnetite, with $\alpha_{min} = 10 \pm 0.5^\circ$ for the 1:1 mass ratio mixture (to be compared with $\alpha_{min} = 6 \pm 0.5^\circ$ of pure silica).

The change in magnitude of P_{min} with varying mixing ratios is generally nonlinear, in particular for the mixtures with a bright and a dark component. In the mixture spinel-graphite, for example, adding 10% of graphite to spinel changes P_{min} strongly, while adding more graphite results in only slight changes. Finally, if 25% of spinel is added to graphite, the changes in phase curve are practically invisible without a precise polarization measurement.

5.3.2 Ternary dust mixtures

Two ternary mixtures were prepared with silica, forsterite, and graphite (si-fo-graph) and silica, magnetite and graphite (si-mt-graph). The measured mixing ratios for the two ternary mixtures are 1:1:1, 2:9:9, 9:2:9, and 9:9:2 (corresponding to a weight percentage of the three minerals of $33.3 - 33.3 - 33.3\%$, $10 - 45 - 45\%$, $45 - 10 - 45\%$, and $45 - 45 - 10\%$). As expected, $|P_{min}|$ increases when bright and dark material are mixed together (Fig. 5.5-5.6). The inversion angles of the ternary mixtures are within the two endmembers with lower and higher inversion angle, that is, forsterite-silica for the first ternary mixture, and magnetite-silica for the second one. Another interesting result is that the phase angle of the minimum polarization is larger for the mixtures than for the single endmembers, reaching $\alpha_{min} = 8.0 \pm 0.5^\circ$ in the 9:2:9 si-fo-graph mixture and $\alpha_{min} = 9.0 \pm 0.5^\circ$ in the 9:9:2 si-mt-graph mixture.

5.3.3 Aggregates of silica-graphite

Silica can easily form cm size aggregates due to strong Van der Waals interactions between the particles (Blum et al., 2006). We measured different amounts of graphite in silica (99:1, 9:1, 4:1, 7:3, 1:1, and 1:3) with two different aggregate sizes for each mixing ratio: aggregates smaller than 200 µm, and aggregates larger than 2 mm (Fig. 5.7). As we already observed for the aggregates that are smaller than 200 µm, larger aggregates (> 2 mm) follow the same evolution pattern when the graphite mixing ratio is increased. $|P_{min}|$ increases reaching

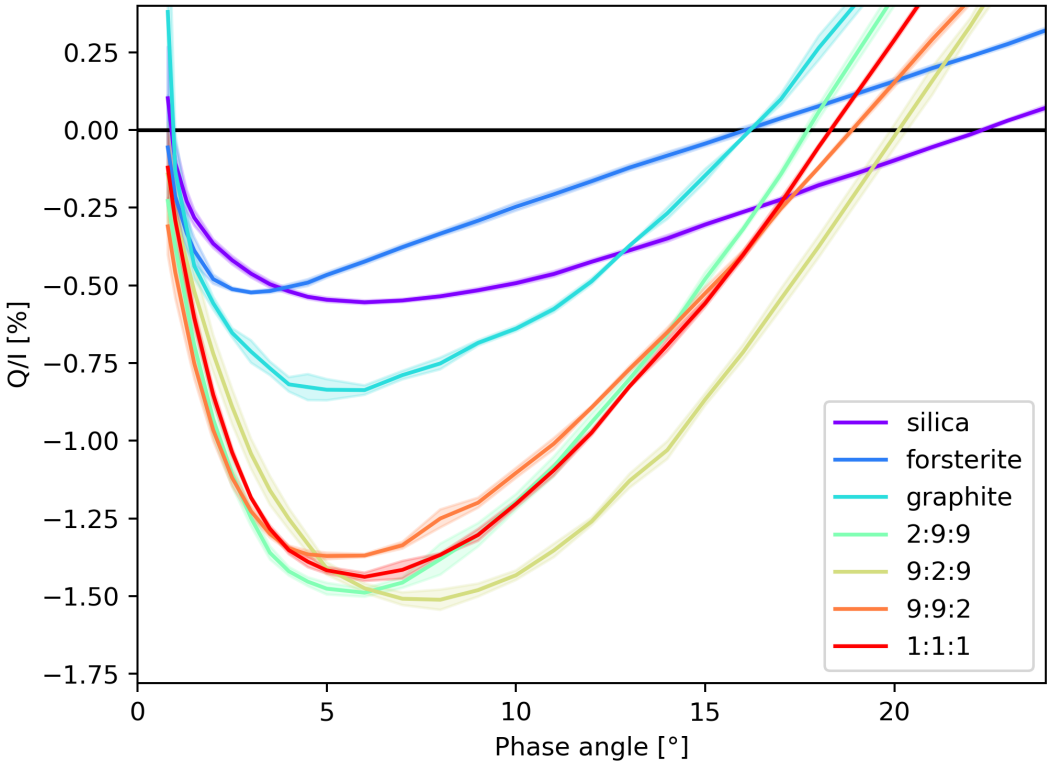

Figure 5.5: Negative polarization of the ternary mixture silica-forsterite-graphite. The three mineral components are mixed with mass ratios showed by different colors. The shaded areas denote the standard deviation.

$\simeq$ 1.5% (7:3 mass ratio silica-graphite), and the phase angle at the polarization minimum increases up to $\alpha_{min} = 7.5 \pm 0.5^\circ$, as compared to $\alpha_{min} = 6.0 \pm 0.5^\circ$ for both silica and graphite. While the inversion angle of most mixing ratios is between the inversion angles of pure silica and graphite, we observed that for the two aggregate sizes with a 99:1 silica-graphite mass ratio, the measured inversion angle exceeds the inversion angle of the pure endmembers. However, the difference was within the error range estimated for comparing different mixtures ($\alpha_{inv} = 22.6 \pm 0.3^\circ$ to the inversion angle of silica $\alpha_{inv} = 22.1 \pm 0.3^\circ$). This behavior, in which the inversion angle exceeds that of the pure endmembers, was also observed for the other binary mixtures that show a deepening of $|P_{min}|$ (silica-magnetite and forsterite-graphite).

Generally, the differences between the two aggregate sizes are very small. Most of them fall within the error on the polarization when different mixtures (and geometries) are compared. For most of the mixtures, the larger aggregate size shows a slightly lower P_{min}.

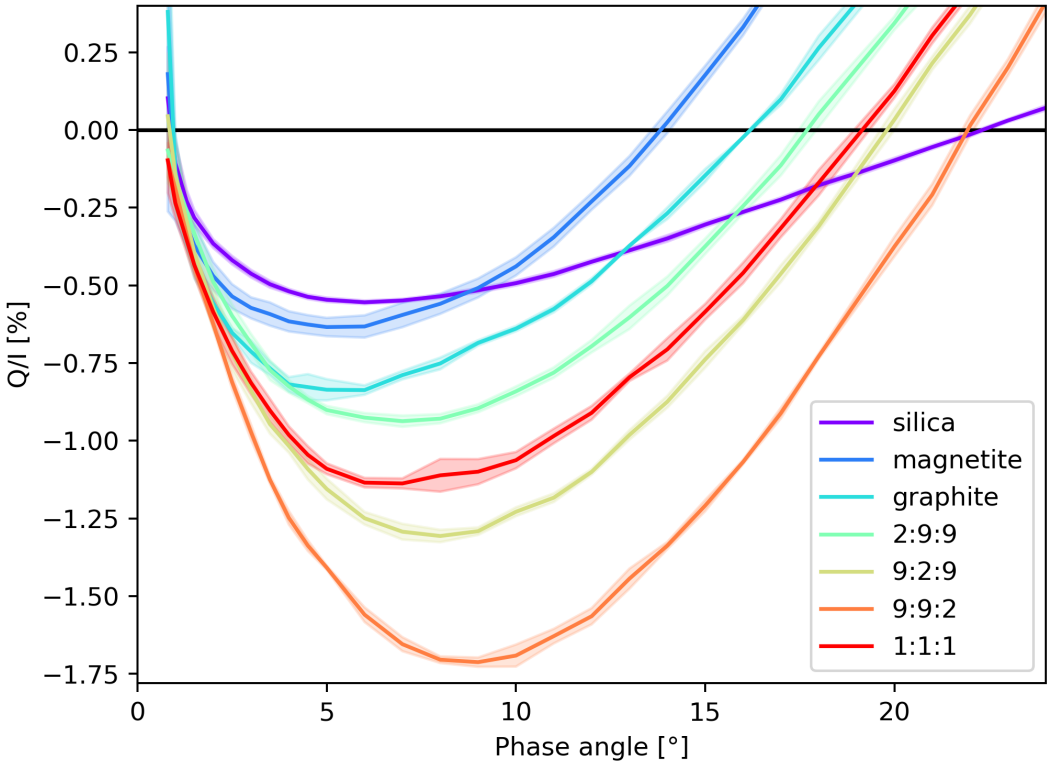

Figure 5.6: Negative polarization of ternary mixture silica-magnetite-graphite. The three mineral components are mixed with mass ratios showed by different colors. The shaded areas denote the standard deviation.

5.4 Discussion

We presented the polarization phase-angle dependence of different mineral powders, their binary and ternary mixtures, and the effects of different aggregate sizes. Our results depict a complicated but interesting picture of phase function behavior that can be used to interpret the polarimetric properties of asteroids.

5.4.1 Mixing effect

Our results indicate that mixing different mineral powders can cause a surge of P_{min}. It is possible to relate this effect to the mixing of different mineralogies, and exclude the influence of other parameters (grain shapes, grain sizes, and porosity).

All the analyzed endmembers show very irregular particles with sharp edges and different morphologies (e.g., flat for graphite, rounder for magnetite). Because the shape is so various and the polarization increases in mixtures with very different particle shapes, this parameter

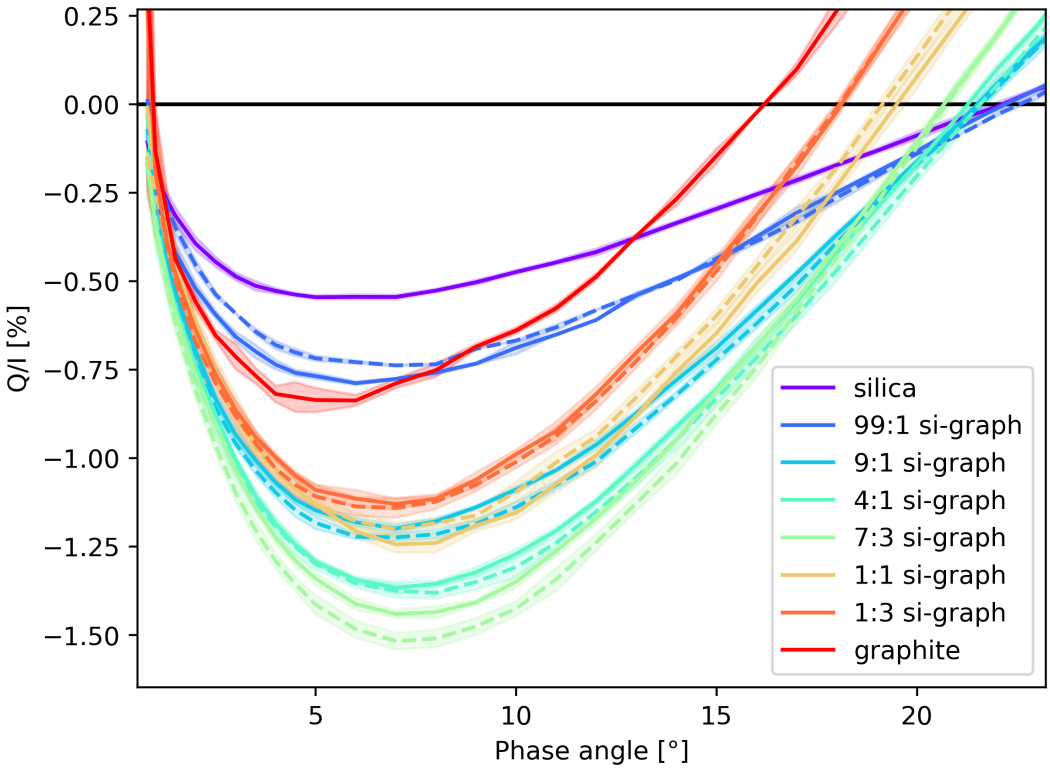

Figure 5.7: Negative polarization of a binary mixture silica-graphite. Solid lines represent aggregate size smaller than 200 µm, while dashed lines represent aggregate size bigger than 2 mm. The shaded areas around the curves are the standard deviations of the measurements when the sample is rotated along the azimuthal axis.

is apparently not responsible for the surge in negative polarization upon mixing.

Our samples also show different size distributions within the maximum grain size provided by the supplier. Forsterite and magnetite are mainly composed by small, sub-µm sized particles, while the grains of graphite and fayalite are closer to the 5−10 µm average size (Fig. 5.2). Interestingly, mixtures can have similar grains sizes and completely different phase curves. For example, the silica-forsterite 7:3 mixture and the silica-magnetite 7:3 mixture show no obvious differences in grain sizes (Fig. 5.3 B and D), but silica-magnetite shows an impressive deepening in polarization minimum upon mixing, while silica-forsterite does not. This also holds for forsterite-graphite and spinel-graphite, which both have similar particles sizes. Only the first mixture shows a deepening of the negative polarization, however. Furthermore, the presence of sub-µm sized particles in one endmember is not a sufficient condition to cause the deepening of the negative polarization when mixed with another endmember. As an example, in the case of the magnetite-graphite mixture, no deepening is observed, while graphite-forsterite mixtures show a deepening in P_{min} . These results seem to exclude that the deepening of the

negative polarization originates mainly in the particle size distribution of the mixtures.

Finally, we considered the porosity of the sample after mixing as a possible source of the observed effect. Shkuratov et al. (2002) experimentally investigated the effect of the porosity of a granular material on the shape of its polarization phase curve. They found that the minimum of polarization can deepen and shift to larger phase angles, although the analysis was limited to two very bright powders, namely MgO and SiO_2. Other theoretical works (e.g., Mishchenko et al. (2009)) indeed showed that the dust-packing density can shape the negative polarization minimum and the inversion angle. Although the samples are deposited in the sample holder without compressing their surface, the mixing of different mineral species could still change the packing density of the sample. To investigate the effect of porosity on our samples, we present in Appendix 5.7 the effect of a compression experiment on a mixture and its two end members, namely silica, magnetite and their mixture 1:1 (Fig. 5.9). Compressing the samples with a pressure of 1100 kg m^{-2} increased the minimum of polarization by approximately 0.2-0.4% in the case of silica and the mixture 1:1, but increased it by about 0.2% in the case of magnetite. The inversion angle does not show a consistent behavior upon compression either: it increases for silica, is almost the same for the silica-magnetite mixture, and decreases for compressed magnetite. In general, the decrease in P_{min} upon mixing cannot be explained by a difference in the porosity state of the sample. While compression effects are not the purpose of this work, we note that a full laboratory investigation on natural samples is lacking in the literature, and our results show that the compression of different mineral powders can change the shape of the negative polarization in opposite ways (e.g., silica vs magnetite). Future laboratory work on this topic will be an important extension of this manuscript.

We conclude that although the negative polarization of our samples is determined by the overall porosity, particle size, and particle shape, none of these parameters controls the surge in negative polarization upon mixing. In Sect. 5.4.6 we discuss the possibility that the extent of negative polarization of a mixture is given by the photometric contrast between the two endmembers.

5.4.2 Binary mixtures

It has been demonstrated that asteroids cluster together in the $P_{min} - \alpha_{inv}$ space according to their class types (Belskaya et al., 2017). Generally, this indicates that asteroids in the same family share similar mineralogical compositions and physical properties. To some extent, this is also affected by the asteroid albedo. Asteroids with a high albedo in the V band (more than 0.2) have a higher P_{min} than moderate-albedo asteroids (0.1-0.2 in V), and the darkest asteroids (C, Ch, and B classes, with an albedo lower than 0.1) populate the lowest P_{min} region. In this context, Cellino et al. (2015a) noted that there is some degree of mixing between moderate- and low-albedo asteroids defined in the region $P_{min} = -1.1\% - 1.4\%$ and $\alpha_{inv} = 18-21^\circ$ in Fig. 5.8. Dollfus et al. (1989) interpreted the fact that terrestrial rocks and lunar fines show smaller and larger polarimetric inversion angles, respectively, than most asteroids as an indication that the surface of asteroids contains coarser material than the surface of the Moon. More recently, two new classes of rare asteroids have been identified (Belskaya et al., 2005; Cellino et al., 2006): the F-class asteroids, which show small inversion angles ($14-16^\circ$), and L-type asteroids ("Barbarians"), with inversion angles larger than 25°.

These asteroid classes are outliers to the normal distribution of asteroids in the $P_{min} - \alpha_{inv}$ space.

In Fig. 5.8 we present the results of our binary mixtures and their coverage within the $P_{min} - \alpha_{min}$ space. Each line connecting the endmembers was obtained by fitting a spline through the data points of P_{min} and α_{inv} versus the concentration of one of the endmembers.

The minerals used here are not distributed in exactly the same regions as described by Dollfus et al. (1989) for terrestrial rocks. In particular, both silica and spinel show larer inversion angles than other samples. Mixing is an efficient way of exploring the $P_{min} - \alpha_{inv}$ variable space. Moreover, because two endmembers with similar size distribution are mixed, we expect that this result is free from grain size effects (the mixture size distribution is similar to that of the two endmembers). This means that P_{min} and α_{inv} are indeed related to the mineralogy of the sample. Although the endmembers are positioned in the top half of the $P_{min} - \alpha_{inv}$ space, mixing of bright and dark minerals allows the exploration of lower P_{min} values, and in some cases, also higher values of the inversion angle (e.g., as observed for silica-magnetite).

The presence of several different minerals (and organics) clearly affects the overall signal of asteroids (see 5.4.4). In addition, we did not consider other parameters that would influence the polarization signal, such as grain size and regolith porosity. However, we would like to underline that observational data and theoretical results on grain sizes, mineralogy, and surface properties of the regolith coupled to experimentally derived polarimetric phase curves could be a powerful tool for constraining these variables.

5.4.3 F-type, L-type and other asteroids

F-type asteroids have been proposed to be covered by a homogeneous dark regolith that could explain their small inversion angles and relatively small P_{min} as compared to C-type asteroids (Belskaya et al., 2005). We explored the $P_{min} - \alpha_{inv}$ space in which F-type asteroids reside through a mixture of graphite and forsterite. While this particular composition is certainly not relevant for this class of objects, we demonstrate that this region can efficiently be explored with mixtures of bright and dark material. The mixture that is closest to the F-type albedo, P_{min} and α_{inv}, is a 1:3 forsterite-graphite mixture ($R \sim 0.03 \pm 0.01$,$P_{min} = -1.14 \pm 0.03\%$, and $\alpha_{inv} = 16.6 \pm 0.3$). The polarization properties of F-type asteroids are thus still compatible with the mixing of dark material with small parts of bright minerals, and no homogeneity of the surface must be invoked.

Barbarians are positioned in a region in $P_{min} - \alpha_{inv}$ space that is not explored by our binary mixtures. Their polarimetric properties have been associated with spinel-bearing CAIs on the surface that have a high refractive index and consequently a large inversion angle (Burbine et al., 1992; Sunshine et al., 2008; Devogèle et al., 2018a). Our Mg-spinel sample has a smaller inversion angle than the Barbarians. When mixed with graphite, it shows no deepening in P_{min}, and when only 10% of graphite are added, the inversion angle decreases from $\alpha_{inv} = 23.7 \pm 0.3^\circ$ to $\alpha_{inv} = 21.7 \pm 0.3^\circ$. When spinel is mixed with graphite with a 1:3 mass ratio, the signature polarizance by spinel is completely hidden, and the total resembling pure graphite.

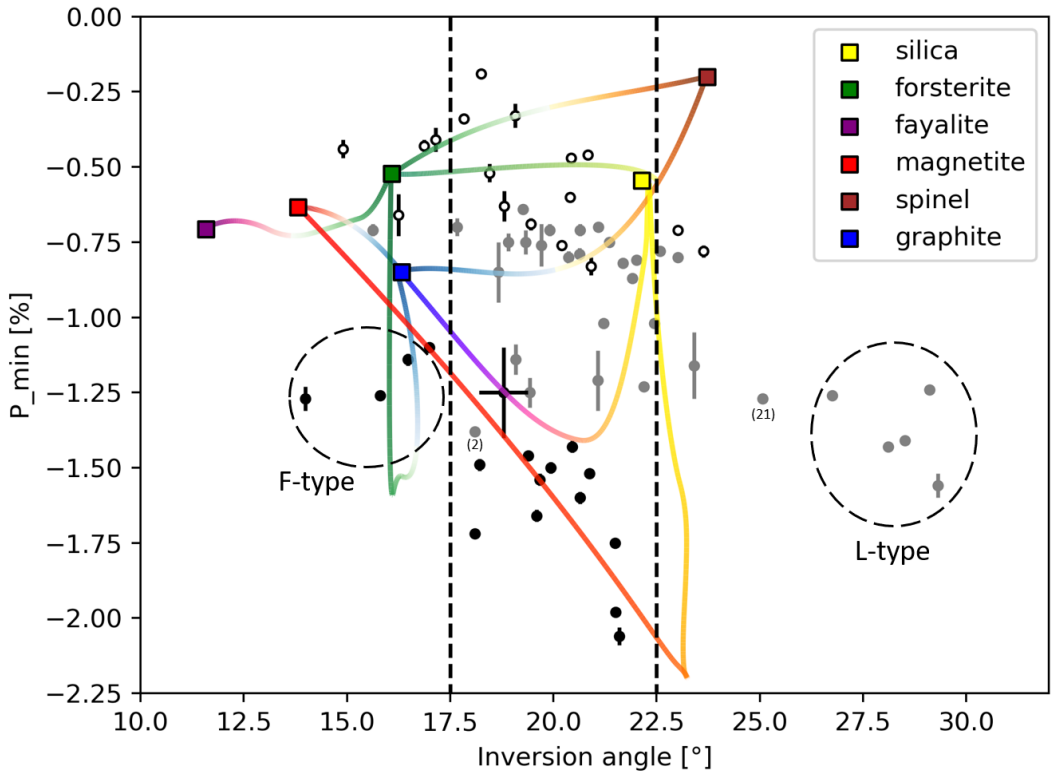

Figure 5.8: P_{min} vs α_{inv} for asteroids and laboratory measurements. The polarimetric data of asteroids is taken from Belskaya et al. (2005), Cellino et al. (2015a) and Belskaya et al. (2017). Low, moderate and high-albedo asteroids are plotted with dark, grey and white dots, respectively. The endmembers of our binary mixtures are colored squares, and the binary mixtures data fitted with a spline are represented by a line connecting two endmembers. Note that the colors of the lines are not representing the mixing ratios between the endmembers, but have only an illustrative purpose. The group of L-type asteroids ("Barbarians"), F-type asteroids, (2) Pallas and (21) Lutetia are highlighted

The polarization minima of Barbarians range from -1.2 to -1.6%, similar to C and B-type asteroids, but Barbarians also display a higher albedo (0.15-0.2 in V band). A plausible explanation for these values is the mixing of bright (CAIs) and dark material. Furthermore, another non-Barbarian asteroid, (21) Lutetia, which shares a large inversion angle (α_{inv} =25°) with Barbarians, is thought to be rich in very fine regolith (Keihm et al., 2012).

Another distinct phenomenon that we observe with our binary mixtures is the increase in inversion angle with increasing contrast of the two endmembers (pure Mg-spinel excluded). Other studies found similar results for mixing bright and dark materials: Zellner et al. (1977) found that the inversion angle increases by 3° compared to pure fine silicates when 10% of 10 nm soot were added, and Shkuratov (1987a) found that a 1:1 mixture of submicron MgO

and Fe_2O_3 shows a 9° larger inversion angle with respect to the largest inversion angle of the endmembers (MgO). In our sample, the largest increase in inversion angle is given by a 1:1 mixture of silica and magnetite, with an excess of 1° compared to the inversion angle of pure silica. We expect that mixtures of very fine dark and bright particles could increase the inversion angle even more substantially compared with the single endmembers.

We therefore propose that the polarimetric behavior of Barbarians is not merely related to the presence of a single mineral, but to a combination of very fine regolith that contains both bright and dark components that are mixed finely together. In-depth polarimetric measurement of CAIs and dark matrix from meteorites are necessary to make further progress on this question.

In addition, mixtures of bright and dark components can also explain that in the same $P_{min} - \alpha_{inv}$ region ($P_{min} = -1.1\% - 1.4\%$ and $\alpha_{inv} = 18-21°$), a certain mixing occurs between low and moderate-albedo asteroids. The asteroid (2) Pallas is a good example. While it is classified as a B-type asteroid, it has a higher albedo (0.145) than the other B-class asteroids. The reason for the higher albedo has been suggested to be the presence of salts on the surface (Marsset et al., 2020). Even if these salt spots are localized on its surface, it is plausible that the salt is mixed to some degree with the asteroid dust. This could give rise to the polarization mixing effect and thus explain why its P_{min} remains low even when albedo is higher than that of asteroids of the same class. Other M-type asteroids that have a quite low P_{min} but moderate albedo ($P_{min} = -1.1\% - 1.4\%$ and $\alpha_{inv} = 18-21°$) can have some degree of mixing on their surface, which determines their polarimetric properties. Recent observations by Belskaya et al. (2022) showed that the negative branch of M-class asteroids can be correlated to different compositions of their surface. It might be divided into sub-groups depending on their different mineral compositions (represented by different meteorite analogs, such as irons and stony irons, and enstatite and high-iron carbonaceous chondrites).

5.4.4 More complex mixtures

The mineralogical complexity of asteroids is much broader than simple binary mixtures. Our results with ternary mixtures show that a more complicate mineralogical mixture can result in different polarization phase curves. The phase curve does not only depend on the overall dark and bright materials. For instance, in the silica-forsterite-graphite mixture (Fig.5.5), the 1:9:9 and 9:1:9 mixtures have the same amount of graphite, but different amounts of silica and forsterite (10-45% of the sample mass in the first and 45-10% in the second mixture). More silica as the bright component results in an increase in inversion angle and phase angle of the polarization minimum at more or less similar P_{min}. In the silica-magnetite-graphite mixture (Fig. 5.6), the 9:1:9 and 9:9:1 have the same amount of dark and bright material, while the first has only 10% of magnetite and 45% of graphite, and the second has 45% of magnetite and 10% of graphite. The difference of the two mixtures in terms of polarimetric properties is significant: P_{min} decreases by 0.5%, the inversion angle increases by 2° and α_{min} increases by 1°.

Similar polarimetric experiments in the laboratory combined with astronomical observations could provide many important constraints on the mineralogical and physical properties

of the regolith. When the main mineral constituents that contribute to the bright and dark components of asteroid regolith are known (deduced from spectroscopy, or from the associated class of meteorites), the polarization phase curve can provide great insight into the mixing ratios, grain sizes, and porosity.

5.4.5 Aggregates

We used different mixing ratios of graphite and silica with two different aggregate sizes in order to investigate the dependence of polarization on aggregate size at small phase angles. We find that the aggregate size does not play a significant role in changing the negative polarization, at least for aggregates up to cm size. It is possible that the negative polarization might vary on those asteroids where regolith is composed of more compact aggregates of very fine material. The compaction of fine powder increases $|P_{min}|$ and can in general change the shape of the negative polarization (Shkuratov et al., 2002). For asteroids on which very fine, porous regolith is expected, the phase function at small phase angles is not sensitive to possible aggregation processes, at least up to cm size aggregates. Above this limit, compaction could play an important role in shaping the negative polarization.

5.4.6 Reflectance contrast between endmembers

One of the parameters used to evaluate the photometric homogeneity of a granular material is the contrast parameter K, which can be defined as

$$K = \frac{A_l - A_d}{A_l + A_d}, \tag{5.2}$$

where A_l and A_d are the albedos of the light and dark components of a mixture, respectively. Similarly, using our reflectance data, we can calculate a contrast parameter K_R. In the past, an increase in contrast parameter for different wavelengths has been correlated to an increase in $|P_{min}|$ and α_{inv} (Shkuratov, 1987a). The contrast parameters for the silica-graphite, forsterite-graphite, and silica-magnetite are $K_R = 0.92$, 0.93, and 0.97 respectively. While this increase correlates with the maximum decrease of P_{min} of the three mixtures (-1.44, -1.53, -2.20%, respectively), we observe no deepening in P_{min} in the mixture spinel-graphite, even though the contrast parameter is very high: $K_R = 0.93$. This indicates that the contrast between the two components alone does not determine the extent of the negative polarization of the mixture. Future experiments should aim to address this point and investigate the underlying causes for the increase in $|P_{min}|$ and α_{inv}, and their relation to the mineralogy of the mixtures.

5.5 Conclusion

We have consistently investigated the influence of mixing different minerals on their polarization phase function at small phase angles. We found that the polarization minimum, the inversion angle, and the phase angle of the minimum polarization are very sensitive to the mixing of bright and dark components. Furthermore, we observe that larger inversion angles and minimum phase angles can be reached by mixing different minerals, without changing the grain size distribution. More complex mixtures of minerals show different negative polarization properties of the endmembers, and aggregates up to cm sizes do not affect the negative

polarization. Furthermore, the mixing effect dominates the negative polarization contribution over other parameters (particle size distributions, porosity, particles shape, and albedo of the mixed minerals). We propose that this effect contributes to the polarization properties of particular classes of objects (F- and L-type asteroids) and other asteroids with unusual polarimetric features (mixing of low- and moderate-albedo asteroids in $P_{min} - \alpha_{inv}$ space).

A good synergy between modeling, observations, and laboratory experiments has the potential of strongly aiding in interpreting the surface properties of regolith when reflected polarized light is observed. Future sample-return missions and in-situ highly sensitive polarimetric observations will greatly improve our understanding of asteroid regolith properties. This will help to interpret astronomical measurements and constrain laboratory simulations to more realistic mineralogies.

Acknowledgements

This work has been carried out within the framework of the National Centre of Competence in Research (NCCR), PlanetS, supported by the Swiss National Science Foundation (SNSF). We thank the anonymous reviewer for the useful insights which helped improving the manuscript.

5.6 Appendix A: polarimetric phase curves data

Table 5.3: Polarization phase curve data

Minerals	Mass ratio	Aggregate size [mm]	P_{min} (± 0.3) %	α_{inv} (± 0.3)°	α_{min} (± 0.5)°	R [%]
silica (si)	–	< 0.2	-0.56	22.2	6.0	65.0 ± 1.0
Mg-spinel (spi)	–	–	-0.20	23.7	8.0	82.3 ± 1.3
graphite (graph)	–	–	-0.84	16.2	6.0	2.8 ± 0.2
magnetite (mt)	–	–	-0.63	13.8	5.5	1.0 ± 0.1
forsterite (fo)	–	–	-0.52	16.1	3	75.8 ± 1.4
fayalite (fa)	–	–	-0.71	11.6	2.5	15.8 ± 0.4
si-graph	99 : 1	< 0.2	-0.78	22.2	6.0	35.1 ± 4.0
si-graph	99 : 1	> 2	-0.74	22.6	7.0	–
si-graph	9 : 1	< 0.2	-1.20	21.5	7.0	15.0 ± 0.7
si-graph	9 : 1	> 2	-1.22	21.6	7.0	–
si-graph	4 : 1	< 0.2	-1.37	21.6	7.0	10.5 ± 1.6
si-graph	4 : 1	> 2	-1.38	21.3	8.0	–
si-graph	7 : 3	< 0.2	-1.44	20.7	7.0	9.3 ± 0.5
si-graph	7 : 3	> 2	-1.52	20.7	7.0	–
si-graph	1 : 1	< 0.2	-1.24	19.5	7.0	4.3 ± 0.6
si-graph	1 : 1	> 2	-1.20	19.1	7.0	–
si-graph	1 : 3	< 0.2	-1.13	18.1	7.0	3.7 ± 0.4
si-graph	1 : 3	> 2	-1.14	18.1	7.0	–
fo-spi	9 : 1	–	-0.5	16.5	3.0	77.4 ± 3.0
fo-spi	4 : 1	–	-0.46	16.7	3.5	79.9 ± 2.6
fo-spi	7 : 3	–	-0.44	17.3	3.0	71.7 ± 2.6
fo-spi	1 : 1	–	-0.37	17.9	3.5	73.0 ± 0.1
fo-spi	1 : 3	–	-0.29	20.2	4.0	69.9 ± 2.8
fo-graph	9 : 1	–	-1.51	16.0	4.0	10.1 ± 0.7
fo-graph	4 : 1	–	-1.54	16.2	4.5	7.6 ± 0.8
fo-graph	7 : 3	–	-1.53	16.4	4.5	5.7 ± 0.7
fo-graph	1 : 1	–	-1.43	16.7	5.0	3.7 ± 0.5
fo-graph	1 : 3	–	-1.14	16.6	5.0	2.8 ± 0.5
fo-fa	9 : 1	–	-0.65	15.4	3.0	45.4 ± 1.4
fo-fa	4 : 1	–	-0.68	15.1	3.5	38.7 ± 1.5
fo-fa	7 : 3	–	-0.70	14.6	3.0	32.3 ± 1.1
fo-fa	1 : 1	–	-0.73	13.7	3.0	22.8 ± 1.2
fo-fa	1 : 3	–	-0.68	12.4	2.5	17.5 ± 0.5
si-mt	9 : 1	–	-1.31	22.8	8.0	13.9 ± 1.4
si-mt	4 : 1	–	-1.68	23.2	9.5	8.6 ± 1.5
si-mt	7 : 3	–	-2.02	23.1	9.0	5.6 ± 0.6
si-mt	1 : 1	–	-2.20	23.2	10.0	3.9 ± 0.6
si-mt	1 : 3	–	-1.94	22.0	10.0	1.9 ± 0.4
si-fo	9 : 1	–	-0.50	22.4	5.0	61.4 ± 3.1
si-fo	4 : 1	–	-0.50	21.6	6.5	66.4 ± 2.8
si-fo	7 : 3	–	-0.49	20.7	5.0	64.8 ± 2.5
si-fo	1 : 1	–	-0.51	18.9	3.5	76.5 ± 1.4
si-fo	1 : 3	–	-0.51	17.3	3.5	76.1 ± 1.6
mt-graph	9 : 1	–	-0.69	15.2	6.0	1.8 ± 0.3
mt-graph	4 : 1	–	-0.75	15.7	5.0	1.9 ± 0.3
mt-graph	7 : 3	–	-0.76	15.7	5.0	2.3 ± 0.5

mt-graph	1 : 1	–	−0.82	16.1	6.0	2.2 ± 0.1
mt-graph	1 : 3	–	−0.85	16.4	4.5	2.3 ± 0.2
spi-graph	9 : 1	–	−0.67	21.7	8.0	10.3 ± 0.7
spi-graph	4 : 1	–	−0.82	21.0	8.0	6.1 ± 0.8
spi-graph	7 : 3	–	−0.84	20.3	7.0	5.9 ± 0.8
spi-graph	1 : 1	–	−0.85	18.9	7.0	5.0 ± 0.3
spi-graph	1 : 3	–	−0.82	17.4	6.5	2.4 ± 1.7
si-mt-graph	1 : 1 : 1	–	−1.14	19.2	7.0	3.1 ± 0.7
si-mt-graph	2 : 9 : 9	–	−0.94	17.7	7.0	2.5 ± 0.4
si-mt-graph	9 : 2 : 9	–	−1.31	19.8	8.0	2.4 ± 0.8
si-mt-graph	9 : 9 : 2	–	−1.71	22.0	9.0	3.9 ± 0.8
si-fo-graph	1 : 1 : 1	–	−1.44	18.3	6.0	5.8 ± 1.0
si-fo-graph	2 : 9 : 9	–	−1.49	17.7	6.0	4.6 ± 0.8
si-fo-graph	9 : 2 : 9	–	−1.51	18.9	8.0	4.6 ± 0.6
si-fo-graph	9 : 9 : 2	–	−1.37	22.0	5.0	12.7 ± 2.1

5.7 Appendix B: polarimetric phase curves of compressed samples

We present here the negative polarization of two endmembers (silica and magnetite) and their mixture 1:1 (Fig. 5.9) after compression. The samples were compressed with a hydraulic press up to a pressure of 1100 kg m^{-2}, producing a flat compacted surface. Further compression was not possible due to the fragility of the sample holder. Interestingly, the compression changed the negative polarization curves differently, depending on the material, with higher $|P_{min}|$ for silica and si-mt mixture, and lower $|P_{min}|$ for magnetite. The inversion angle after compression is larger for silica, equal for the si-mt mixture, and smaller for magnetite than in the uncompressed samples.

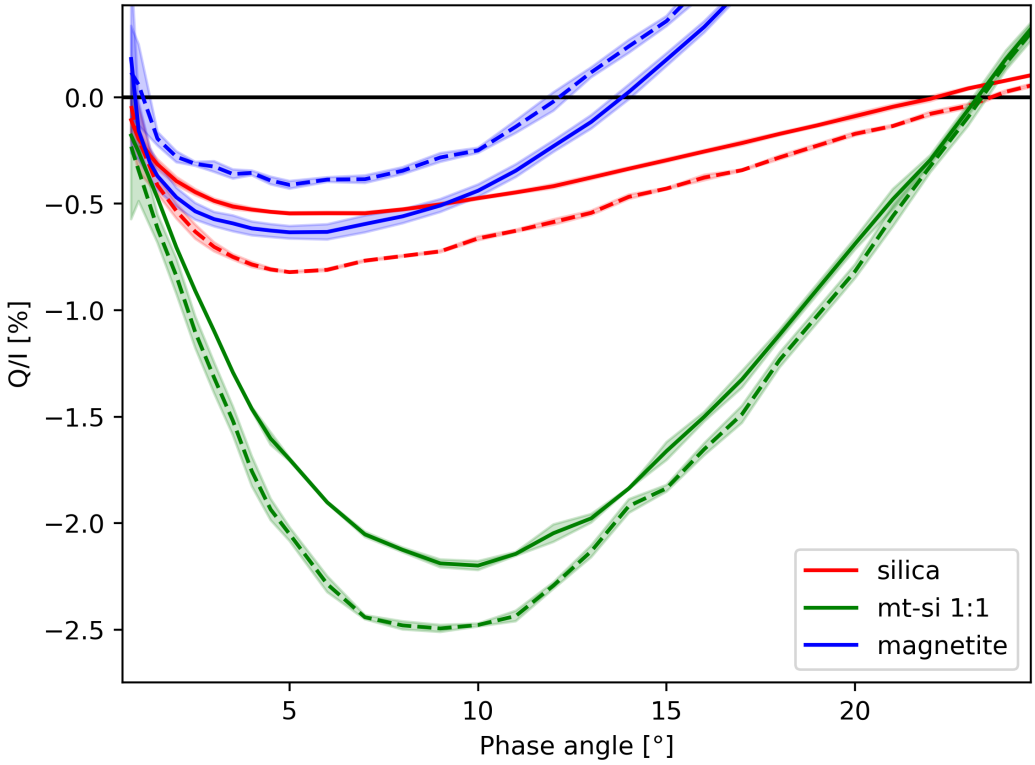

Figure 5.9: The negative polarization of silica, magnetite and their mixture 1:1 (in solid line). The same samples have been compressed and measured again (dashed line).

Chapter 6

Experimental study of frost detectability on planetary surfaces using spectrophotometry and spectropolarimetry

Submitted to Icarus in December 2022

Stefano Spadaccia[1], Lucas Patty[1], Nicolas Thomas[1], Antoine Pommerol[1].

[1] Space Research and Planetary Sciences Division, Physikalisches Institut, University of Bern, Sidlerstrasse 5, 3012 Bern, Switzerland

Abstract

Water ice is ubiquitous in our Solar System. When the temperature and pressure conditions allow it, water ice can deposit as frost on the regolith of planetary surfaces. Frost is an important indicator of the surface physical conditions, and the geological processes that might be triggered by its deposition and sublimation. In general, the detection of ice on different bodies of our Solar System is important to track their formation and evolution processes. This works aims to explore experimentally the possibility of detecting early stages of frost formation and to characterize its spectrophotometric and spectropolarimetric signatures in visible reflected light. We deposit ice on top of different regolith simulants, measuring the dust temperature, the thickness and morphology of the frost through a microscope, while measuring the reflected light at a phase angle of 50° and 61°, and the linear polarization at a phase angle of 5° and 16°, at three different wavelengths (450, 550, and 750 nm). We discover that both the spectral slope in particular between 450−550 nm), and the difference of polarization between 450 and 750 nm are an efficient method to detect frost layers with thicknesses as low as 10 to 20 µm. Furthermore, we find that the linear polarization at 16° relates to the temperature of the regolith i.e. the type of the deposited ice crystalline structure.

6.1 Introduction

Water ice is ubiquitous on many surfaces of our Solar System bodies. Ice in the Solar System can assume many configurations: enclosed in thick polar ice sheets (like on Earth and Mars), as thin frost layers on objects where the day-night temperature difference allows ice deposition, intermixed with dust and organic material (like in the case of comets), as tiny ice crystals in clouds of different planets (Earth, Mars, Jupiter), and finally it is also found in interplanetary dust particles. The observation of water ice on surfaces of the Solar System bodies allows tracing their present and past geological processes, but also understand how water ice distributed among those bodies during the Solar System formation and evolution (Blum et al., 2022). The deposition of thin layers of water ice crystals (referred in this study as "frost") on dusty surfaces is important for minor bodies and planetary surfaces. We distinguish frost from more compact, thick, sintered, slab-like icy surfaces. Monitoring the frost formation helps to understand the diurnal and seasonal water cycles of such bodies, providing important information on how the ice interacts with planetary surfaces and changes their physical properties.

The superficial water ice on Solar System bodies can be detected by the water absorption bands in the near infrared (NIR) and infrared (IR) positioned at 1.05, 1.25, 1.5, 2.0, and 3.2 µm, which are very distinctive and diagnostic of the presence of pure water ice. Nonetheless, when ice is mixed with low-albedo materials (such as the dark asteroid or comet regolith), its NIR absorption bands can become shallower, or disappear completely (Clark, 1981; Roush et al., 1990; Pommerol et al., 2019b; Raponi et al., 2016). Another way to detect ice is through color differences of the scattered light in the visible range. In general, dust in our Solar System has a higher reflectance in the red than in the blue, translating into a positive slope of its visible spectrum. Since the visible spectrum of ice is flat or slightly more reflecting in the blue (for smaller particle sizes), the spectral slope in the range ∼400 to 800 nm can

be indicative of water ice on the surface. On comets 9P/Tempel 1, 103P/Hartley 2 and 67P/Churyumov–Gerasimenko (67P hereafter), the decreases in the 400 and 800 nm range slopes have been associated to the presence of surface ice (Fornasier et al., 2015; Li et al., 2007, 2013), and the "blueing" effect of ice has been confirmed through experimental studies (Pommerol et al., 2015b). On minor bodies, both the deposition and sublimation of ice are extremely important processes, that change the morphology of the surface, its spectra and other physical properties such as porosity, compressive strength, and thermal conductivity. Ice deposition and sublimation have been observed at the surface of 67P, in shadowed regions showing an increase of albedo and higher blue slopes when illuminated, and becoming darker and redder a few minutes afterwards (De Sanctis et al., 2015a; Fornasier et al., 2016). The spectra and thermal modeling of such frost seem to indicate that the ice is inter-mixed with the dust particles and up to 15 µm thick (Fornasier et al., 2016).

The presence of permanent superficial frost on some asteroids is still debated (Yang and Jewitt, 2007). While the presence of sub-surface ice is plausible for many main-belt asteroids (Schorghofer, 2016), icy patches or frost on the surface would be rapidly lost due to the sublimation rates at that heliocentric distances. Nonetheless, recent observations of 24-Themis and 65-Cybele have revealed an absorption band at 3.1 µm that is consistent with surface water ice and organic material (Campins et al., 2010; Rivkin and Emery, 2010; Licandro et al., 2011). Jewitt and Guilbert-Lepoutre (2011) did not find any spectroscopic emission lines associated with water ice sublimation on 24-Themis and 65-Cybele, and proposed that the surface ice must have been a transient event due to impacts that blanketed these bodies with a thin layer of ice. Still, the detection of thin films of ice remains problematic.

Polarization is a powerful observational technique used to characterize the properties of the dust on the surface of different bodies in our solar system. The polarization of the solar light scattered by a planetary surface provides useful insights on the composition, size, morphology and porosity of the regolith particles. The linear polarization is defined as

$$P = \frac{I_\perp - I_\parallel}{I_\perp + I_\parallel}, \tag{6.1}$$

where $I_\perp$ and $I_\parallel$ are the intensities of the reflected light with the polarization axis normal and parallel to the plane of scattering, respectively. Note that $P = Q/I$ using the Stokes parameters. P varies depending on the angle between the observer, the observed object, and the illumination source, called phase angle α. The linear polarization of an astronomical body depending on the phase angle is called polarization phase curve. Polarization phase curves have been used intensively to investigate the properties of the Moon regolith (Dollfus, 1998), of asteroid surfaces (Belskaya et al., 2017; Cellino et al., 2015b; Belskaya et al., 2019), and comets comae (Levasseur-Regourd et al., 2018a). When unpolarized light shines on these objects for phase angles about $\alpha < 25°$, P is negative, i.e. $I_\perp < I_\parallel$. This part of the polarization phase curve is often called negative polarization branch or negative polarization (NP). The NP shape is determined by the minimum of polarization P_{min} and the phase angle at which the polarization goes back to zero, called inversion angle α_{inv}. These two parameters vary importantly depending on the scattering regime of the observed dust: in the case of single scattering (e.g. cometary comae) the inversion angle is larger and $|P_{min}|$ is higher than in the case of multiple scattering (regolith and planetary surfaces). This is due to

the fact that multiple scattering contributes to the scrambling of the polarization direction, decreasing the overall net polarization escaping the medium. The minimum of polarization can change importantly depending on the phase curve, but in general it lies in the range $P_{min} = 0.2 - 2\%$ for asteroids and cometary comae. The inversion angle can also change importantly, depending on the physical properties of the observed dust: its value lies in the range $\alpha_{inv} = 14 - 28^{\circ}$ for asteroids and about $\alpha_{inv} = 22^{\circ}$ for comets. Modelling the observed NP both experimentally and theoretically can provide important constraints on the particle size distribution, porosity, and mineralogy (Shkuratov et al., 2002; Zubko et al., 2013; Frattin et al., 2019; Spadaccia et al., 2022).

Frost and small icy particles have a distinctive polarization signal in reflected light, that makes polarization an interesting tool for detection and analysis of their properties. In the literature, a limited number of studies are available on the polarizance of frost. The first pioneering measurements of frost polarization phase curves were carried out by Dollfus (1957), who observed low polarization values and curve variability depending on the melting state of the frost. Steigmann (1993) was the first studying frost-dust associations, demonstrating that Callisto polarization phase curve at small angles (negative polarization) could be fitted by sprinkling different types of silicate dust on top of a frost layer. The crystal size of frost or snow influences the polarization signal too - snow crystals with sizes in the range up to 900 µm show low negative polarization, that is dependent to some degree on the grain size (Shkuratov and Ovcharenko, 2002; Lv and Sun, 2014). More recently, Poch et al. (2018) studied how the phase polarization curve of small spherical icy particles (SPIPA-A and SPIPA-B) and frost change over time due to sintering and frost growth. They discovered that frost deposition seems to cause oscillations to the polarization phase curve, which they attributed to the Mie scattering of the first hemispherical nucleation sites of the frost. All these works studied frost deposition either at one single wavelength or of pure ice on a metal substrate, and more comprehensive spectropolarimetry studies of frost forming on regolith simulants are lacking in the literature.

In this chapter, we explore the possibility of detecting early-formation of water frost on dusty surfaces through observation of both total and polarized reflected light in different wavelengths and phase angle configurations. Furthermore, we correlate the total reflected light and polarization variations over time with the frost thickness and physical properties. Frost is formed on two different regolith surfaces: the Martian Global Simulant MGS-1 (Cannon et al., 2019) and the CR Carbonaceous Chondrite Simulant (Britt et al., 2019). The asteroid simulant is cooled down to $-150\,^{\circ}$C (about 120-130 K), that is consistent with the surface temperature of asteroids like (1) Ceres at mid-high latitudes (Rivkin and Emery, 2010). The martian simulant was cooled either at $-130\,^{\circ}$C or $-100\,^{\circ}$C that are lower than the mean water frost point on Mars ($183 - 193$ K) and are consistent with the low temperatures of polar-facing martian slopes (Schorghofer and Edgett, 2006).

This chapter is structured as follows: in Sec. 6.2 we present our experimental methods and apparatus, in Sec. 6.3 we summarize our findings, in Sec. 6.4 we provide a discussion of the results in the context of frost detectability through total and polarized reflected light. We finally present future perspective and experiments in Sec. 6.5, and we conclude in Sec. 6.6.

6.2 Materials and methods

In this section, we describe the experimental setup used for the frost deposition, and we give details about its photopolarimetry measurement procedure.

6.2.1 Experimental setup description

We made some modifications to the POLarimeter for ICE Samples (POLICES) developed at the University of Bern (Poch et al., 2018) to allow a better control of the conditions at which the cryogenic samples were exposed. More details on the setup and its operation steps are in Chap. 3.5.1.

The POLICES setup for frost study is schematically depicted in Fig. 6.1. The POLICES full Stokes polarimeter (Dual PEM II/FS42-47, Hinds Instruments) is positioned on top of a trapezoidal enclosure, with the entrance pupil exactly above and perpendicular to the sample. A motorized arm holds an optical fiber that sends a collimated beam of light to the sample with a spot diameter of approximately 15 mm. The light source is a 250 W halogen lamp which feeds a monochromator (Quantum Design MSH-300) placed outside the enclosure. To ensure unpolarized incident light, a liquid-crystal depolarizer was placed in front of the optics converging into the fiber launcher. In this way, the incidence light on the sample has less than 10^{-4} remnant polarization at $450 - 750$ nm, which agrees well with the polarization of the global light coming from the solar disk (Kemp et al., 1987). The arm can assume any position between 2° and 70°, changing the incidence angle of the illumination, while the polarimeter measures the reflected light at 0° (in this configuration, the incidence angle has the same value as the phase angle). To measure the total reflected light, we used a monochromatic camera (Thorlabs Kiralux CMOS CS126MU) placed at 45° with respect to the sample surface, on the opposite side of the motorized arm. The regolith sample is accommodated in a cylindrical volume carved in an aluminum sample holder, with a diameter of 3.5 cm and depth of 5 mm. The aluminum sample holder is placed on top of the cryo-stage that consists of a copper cylindrical volume equipped with two pipes (inlet and outlet) connected to two liquid nitrogen tanks. The first tank is full of liquid nitrogen and thus has a higher pressure than the second one, which is empty. When the valve of the inlet pipe is open, the nitrogen flows inside the copper volume actively cooling it down, and the exhaust nitrogen flows in the second tank. The exhaust valve of the second tank is fully open and connected to a pipe that goes back in the POLICES enclosure. When the nitrogen flows in the second tank that is at ambient pressure and temperature, it evaporates and escapes from the exhaust valve in the pipe and finally into the enclosure. This allows the chamber to be flushed with gaseous nitrogen. To avoid the gaseous nitrogen to be too cold, the pipe is sunk in a warm water bath before entering the enclosure.

The experiments consist in measuring the linear polarization at two fixed phase angles sampling the minimum and the inversion angle of the negative polarization phase curve ($\alpha =$ 5° and 16°) and three wavelengths (blue channel 450 nm, green channel 550 nm, and red channel 750 nm) of the regolith simulants cooled at low temperatures. At the same time, the total light intensity in the three wavelengths is measured by the camera that is placed at 45° with respect to the sample (that means, the intensity is measured with phase angles

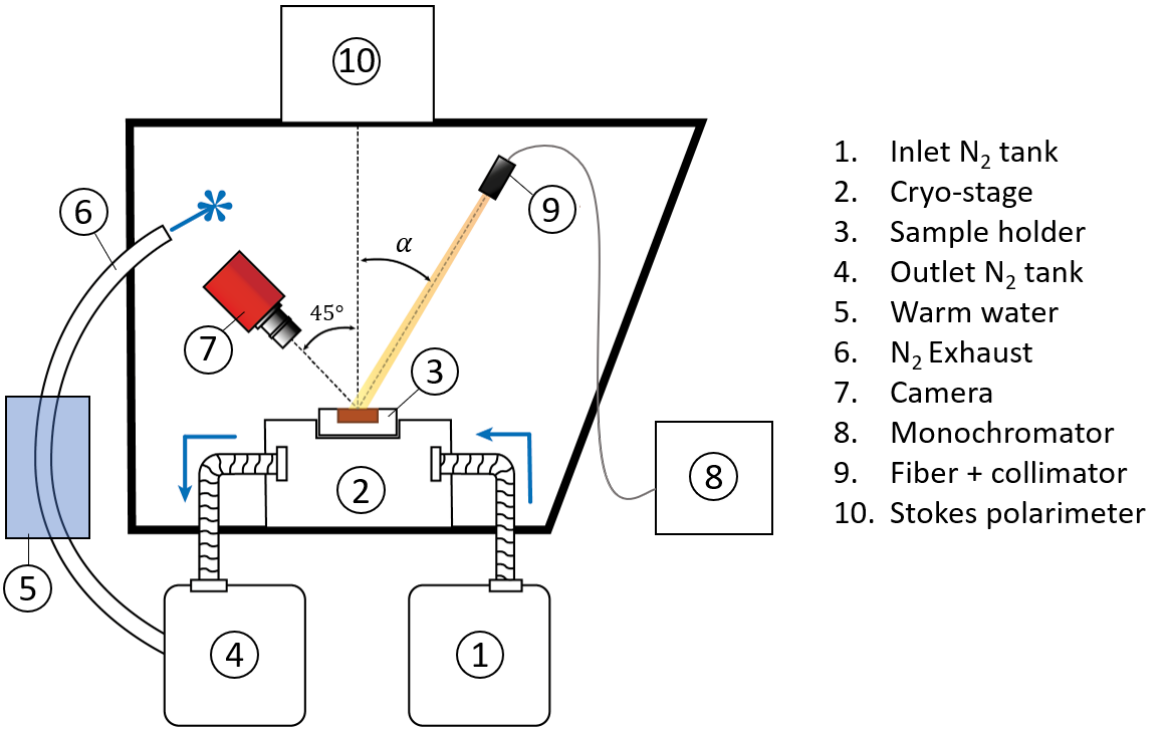

Figure 6.1: Schematics of the POLICES setup for measuring the polarization and total intensity of cryogenic samples.

50° and 61°). The intensity measurements are then calibrated using a 75% spectralon target. The camera is not focused on the target, so that the observed illuminated spot is spatially averaged, and the reflectance is then calculated over a region of interest within the light spot.

Finally, we repeated the experiment with the different regolith types (see Sec. 6.2.2) observed with a long-distance microscope (K2 DistaMax) and illuminated by broadband incident light. The images from the microscope were used to measure the frost thickness and growth.

6.2.2 Samples and experimental procedure

The two regolith simulants used in our experiment are the Martian Global Simulant MGS-1 (Cannon et al., 2019) and the CR Carbonaceous Chondrite Simulant (Britt et al., 2019). Both simulants appear quite dark in the visible: the MGS-1 reflectance is about 11% at 450 nm and reaches 24% at 750 nm, while CR is about 4% at 450 nm and about 7% at 750 nm (Fig. 6.2 A and B). The scanning electron microscope (SEM) inspection of the simulants reveals that part of their mass is composed by fine powder with grain sizes less than 5 µm (Fig. 6.2 C and D).

We sieved the simulants to remove grains and aggregates bigger than 2 mm and then we carefully placed the regolith inside the carved volume of the sample holder to obtain a flat surface without compressing the sample. A Pt100 resistance thermal sensor is placed inside the regolith layer to measure its temperature during the experiment, at approximately

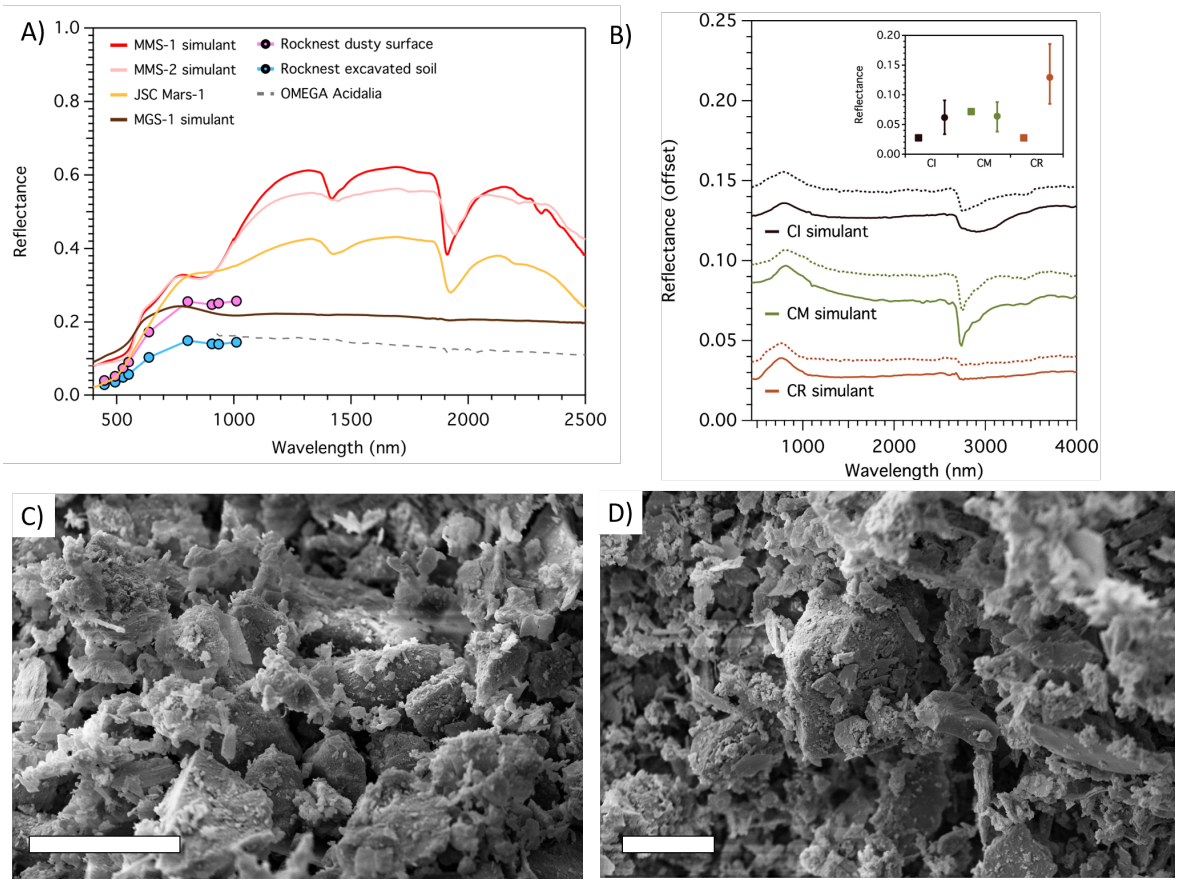

Figure 6.2: Spectra of the MGS-1 (in brown, plot A) and of the CR simulants (in brown, plot B). The spectra are from Cannon et al. (2019) (Fig.4)[5] and Britt et al. (2019) (Fig.4, ©John Wiley Sons, Inc). C) SEM image of MGS-1 and D) CR. The scale bar is 20 µm for both SEM images.

$2-3$ mm from the regolith surface. The sample holder is then placed on top of the cryo-stage at ambient temperature. A good thermal contact between the cryo-stage and the aluminum sample holder is assured by a piece of graphite sheet. Before cooling down the cryo-stage, the aluminum sample holder is covered by an aluminum lid to prevent frost depositing on the sample before the target temperature is reached. At this point, we opened the first tank inlet valve, flowing liquid nitrogen in the cryo-stage that starts cooling down. At the same time, the exhaust gaseous nitrogen flows from the second tank to the enclosure, rapidly flushing the chamber. Shortly before the regolith reached the target temperature, we removed the aluminum lid over the sample through a glove hermetically sealed on one side of the enclosure, and started the polarization and intensity measurements.

The data acquisition steps are the following. The motorized arm moves to the first target phase angle (α =5°), then the monochromator selects the 450 nm wavelength, and we measure the Stokes parameters. Afterwards, the camera acquires the image in total light. Then, the other two wavelengths (550 and 750 nm) are selected successively and the polarization and

intensity data are acquired in the same way. Finally, the motorized arm moves at α =16° and the whole procedure is repeated. The data acquisition for the two phase angles and the three wavelengths takes 3 minutes.

After the acquisition of the polarization and reflection data in all wavelengths for both phase angles, the exhaust pipe is removed from the chamber and the inlet nitrogen valve of the first is closed. The cryo-stage still contains liquid nitrogen and continues to cool down for about 10-20 minutes (depending on the final temperature reached), until the liquid nitrogen evaporates completely and goes out through the outlet towards the second tank. At this point, the temperature of the cryo-stage starts to increase. The measurements continue until a thick layer of frost has formed on the sample, usually between 80 and 140 minutes after the beginning of the experiment (depending on the final temperature).

From the reflectance data, we can derive the spectral slope in %/100 nm between two wavelengths λ_2 and λ_1 (with $\lambda_2 > \lambda_1$)

$$S = \frac{R_{\lambda_2} - R_{\lambda_1}}{R_{\lambda_1}\,(\lambda_2 - \lambda_1)}. \tag{6.2}$$

following the definition introduced by Delsanti et al. (2001), and used to interpret 67P spectrophotometric data by Fornasier et al. (2015, 2016).

6.3 Results

Here we present the averaged photometric and polarimetric results from five experiments with the CR simulant, three experiments with the MGS-1 simulant cooled down to −130 °C (hereafter called cold-case) and three experiments with the MGS-1 cooled at −100 °C (hereafter called hot-case). Furthermore, for both simulants under all temperature conditions, we performed one separate experiment with the long-distance microscope to observe the frost formation and measure its thickness.

Since the difference of the spectral slopes between phase angles $\alpha = 50°$ and $\alpha = 66°$ is within 1%, we show only the spectral slopes measured at $\alpha = 50°$. The frost thickness in the first minutes of experiment is extrapolated from the measured data through polynomial fitting.

6.3.1 Frost growth and temperature conditions

The temperatures of CR and the MGS-1 (cold and hot case) are presented in Fig. 6.3. The long-distance microscope acquired one image every three minutes, starting when the cooling of the cryo-stage is turned off and the nitrogen exhaust pipe is removed from POLICES enclosure. The images were compared to each other, and we measured the thickness of frost in different areas of the image to get an average and a standard deviation. High values of standard deviation come from the appearance of big single ice crystals localized on top of bigger dust grains.

The temperature at which the frost deposits on top of the simulant plays an important role. Counterintuitively, the MGS-1 grows frost faster when it is warmer. This effect is due

to the fact that the air on top of the cryo-stage is cooled by conduction, and the colder is the air, the less water vapor it can contain. Furthermore, there is a compositional difference between CR and MGS-1. Ice deposition is different for different materials, since the vapor partial pressure needed to trigger the nucleation of ice depends on the substrate material (Iraci et al., 2010). This is the reason why deposition of frost on CR simulant is faster than MGS-1, although its temperature is lower.

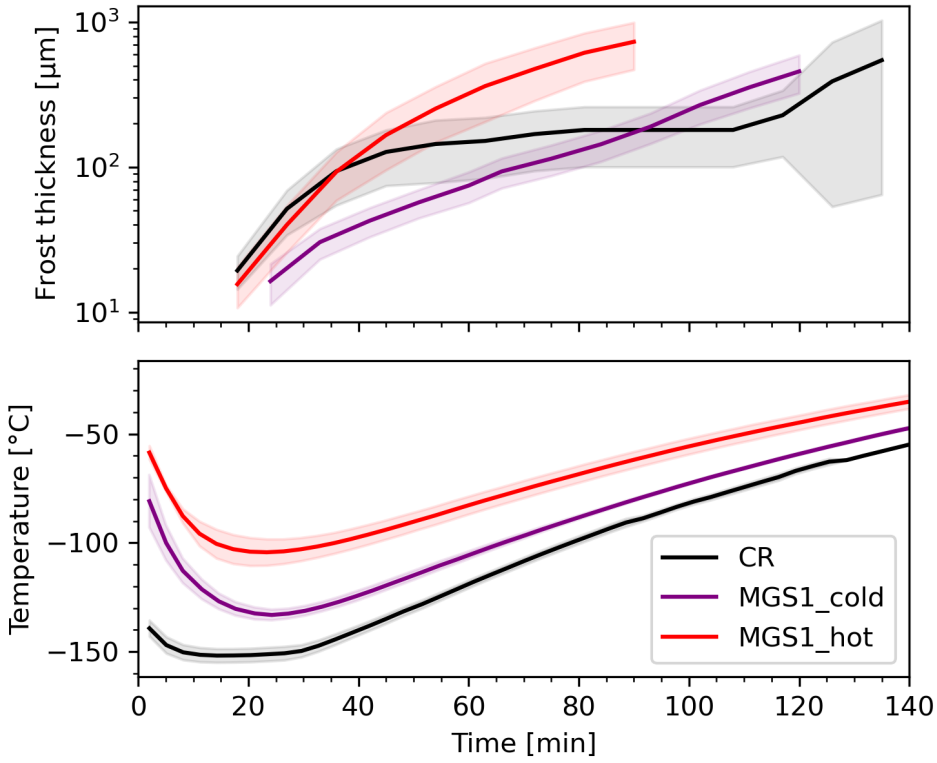

Figure 6.3: On top, result from the long-distance microscope measurements of frost thickness with CR and MGS-1 (cold and hot case). The shadowed areas around the curves indicate the standard deviation of at least ten measurements in different parts of the image. At the bottom is the average temperature of the experiments. The shadowed areas around the curves represent the standard deviation of the experiment repetitions.

6.3.2 Spectropolarimetry and spectrophotometry of frost

In this section, we present the spectropolarimetric and spectrophotometric results during the frost deposition process. The CR simulant is cooled down to T= −150 °C and during the first 10 minutes of experiment it deposits approximately 10 µm of frost. At the beginning of the experiment, the linear polarization at 5° and 16° show approximately the same value in the three wavelengths ($P = -0.6\%$ and $P = -0.2\%$, respectively). After about 10 minutes (i.e. 10 µm of frost), the P at 450 nm (P_{450}) decreases to $P_{450} = -0.85\%$ and it is well distinguished from the P in the other two wavelengths. The differentiation of P between

the three wavelengths continues until the frost become between 125 and 150 µm-thick, then the three channels return to the same P values within the uncertainties. The maximum difference between blue and red linear polarization $|P_{450} - P_{750}| = 0.4\%$ is reached at 5° when the frost thickness is $50 - 100$ µm, and at 16° when the frost thickness is 50 µm. The spectral slope diminishes over time toward negative values. Because of its definition (see Eq. 6.2), the spectral slope is higher when $\lambda_1 = 450$ nm, than when $\lambda_1 = 550$ nm. The spectral slope $S_{450-750}$ decreases by 10% already at 15 minutes, when the frost is 14 µm thick. We can observe that CR undergoes a plateau phase in the frost crystal growth when it reaches approximately 100 µm thickness (Fig. 6.3).

In the first 20 minutes, the MGS-1 cools down to T= −130 °C ("cold-case"), and then its temperature evolves slowly back to T= −90 °C 80 minutes after the beginning of the experiment (Fig. 6.3). The frost deposition rate is slower than the "hot-case" MGS-1 or CR. Since MGS-1 is more reflective in the red than in the blue, the reflectance is higher at 750 nm, and, as a direct consequence, the linear polarization at small angles is lower in the red than in the other channels (see the linear polarization at $\alpha = 5°$ in the top plot of Fig. 6.5). The linear polarization close to the negative polarization minimum (at $\alpha = 5°$) is evolving similarly as CR: $|P_{450}|$ already increases when the frost is 10 µm thick, and the maximum separation from the red channel happens at ~ 20 µm frost thickness, $|P_{450} - P_{750}| = 0.5\%$. At 16°, the three channels evolve mostly together, and it is worth noting that P_{450} and P_{550} become negative with frost thickness between 10 and 20 µm. For both phase angles, the channels converge at 50-60 minutes from the beginning of the experiment, when the frost thickness exceeds 50 µm thickness, and starts looking as a white blanket over the simulant grains. The spectral slopes between $450 - 550$ nm and $450 - 750$ nm differ of $2 - 4\%$, and they decrease by approximately 10%/100 nm during the first 20 minutes, when the frost thickness is approximately 15 µm, while the spectral slope at $550 - 750$ nm decreases by the same amount in slightly more time (24 minutes i.e. approximately 20 µm of frost).

The second experiment with MGS-1 was performed at higher temperatures ("hot-case"). The minimum temperature reached by the simulant was T= −100 °C after about 20 minutes from the beginning of the experiment. The frost deposition rate is higher compared to the cold-case throughout the whole experiment duration (Fig. 6.3, red curve). The polarimetric behavior also shows some differences compared to the MGS-1 cold-case (Fig. 6.6). At 5°, the linear polarization in the blue and in the other two channels differentiates only after 13 µm of frost, reaching a maximum $|P_{450} - P_{750}| \sim 0.5\%$ (to be compared with the difference at the beginning of the experiment, $|P_{450} - P_{750}| = 0.2\%$). At 16° linear polarization it is the same for the three wavelengths at the beginning of the experiment, but P_{450} rapidly evolves toward positive values, reaching a maximum $P_{450} = 0.45\%$ at 17 minutes. At this time, the difference between linear polarization in the red and in the blue is $|P_{450} - P_{750}| = 0.3\%$, and the frost thickness is ~ 14 µm. The spectral slope behavior is very similar to the cold-case MGS-1. The first two data points show an increase of reflectance in the green channel ($S_{450-550}$ increases by about 1.5%) and then the evolution is similar to the spectral slopes of CR and colder MGS-1. Both $S_{450-550}$ and $S_{450-750}$ decrease by 10%/100 nm when the frost thickness is 20 µm, while $S_{550-750}$ decreases by the same amount once the frost reaches approximately 30 µm thickness. Since the frost growth is faster than for CR and cold MGS-1, already at 60 minutes the frost develops its characteristic dendritic crystals with sizes ~ 250 µm. When the

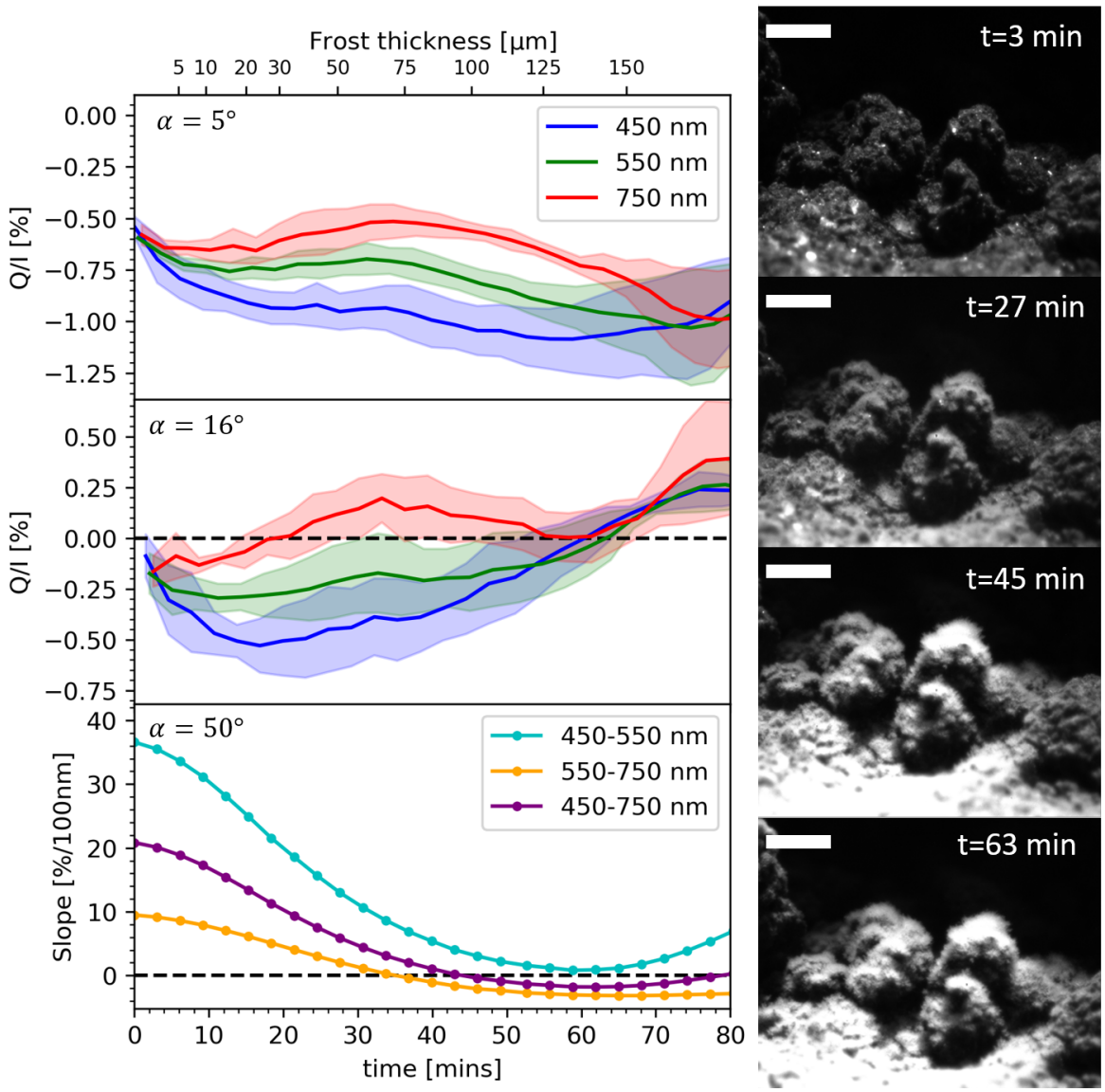

Figure 6.4: The evolution of the linear polarization at 450, 550 and 750 nm at phase angle of $\alpha = 5°$ (top graph), $\alpha = 16°$ (middle graph), spectral slope (bottom graph), and frost thickness (top bar) on CR regolith simulant. The shaded areas around the polarization measurements are the standard deviation of the four experiment repetitions. The slope is calculated using Eq. 6.2 with wavelengths 450-550, 550-750 and 450-750 nm. The images of the regolith sample show the deposition of frost on the surface at different times (right), the scale bar is 1 mm.

ice crystals grow to this size, their spectral slope is practically zero for all three wavelengths, and the polarization signal is indistinguishable in the three channels.

We can draw some general concluding remarks on the visible spectrophotometric and spectropolarimetric appearance of frost growth and evolution on different substrates:

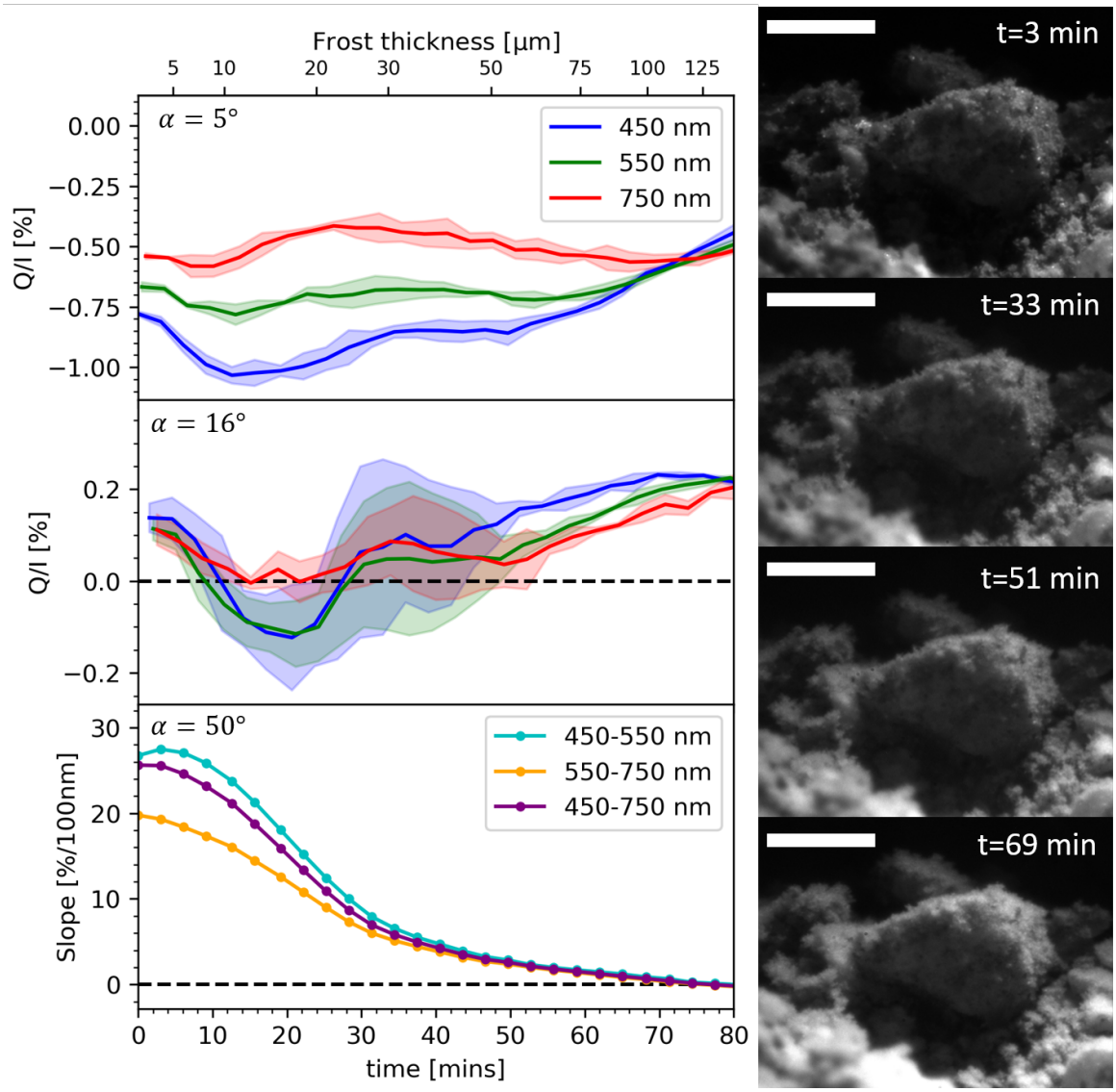

Figure 6.5: The evolution of the linear polarization at 450, 550 and 750 nm at phase angle $\alpha = 5°$ (top graph), $\alpha = 16°$ (middle graph), spectral slope (bottom graph), and frost thickness (top bar) on MGS-1 simulant in the cold case. The shaded areas around the polarization measurements are the standard deviation of the four experiment repetitions. The slope is calculated using Eq. 6.2 with wavelengths 450-550, 550-750 and 450-750 nm, the phase angle is $\alpha = 50°$. The images of the regolith sample show the deposition of frost on the surface at different times (top right). The scale bar represents 1 mm.

- When frost is observed at angles close to the minimum of the negative polarization curve (in our case 5°), the linear polarization in the blue, green and red differentiates, with the maximum difference reached by the blue and the red channels $|P_{450} - P_{750}| \sim 0.25 - 0.5\%$ when the frost thickness is $\sim 10 - 20\,\mu m$. When the frost is more mature and the ice

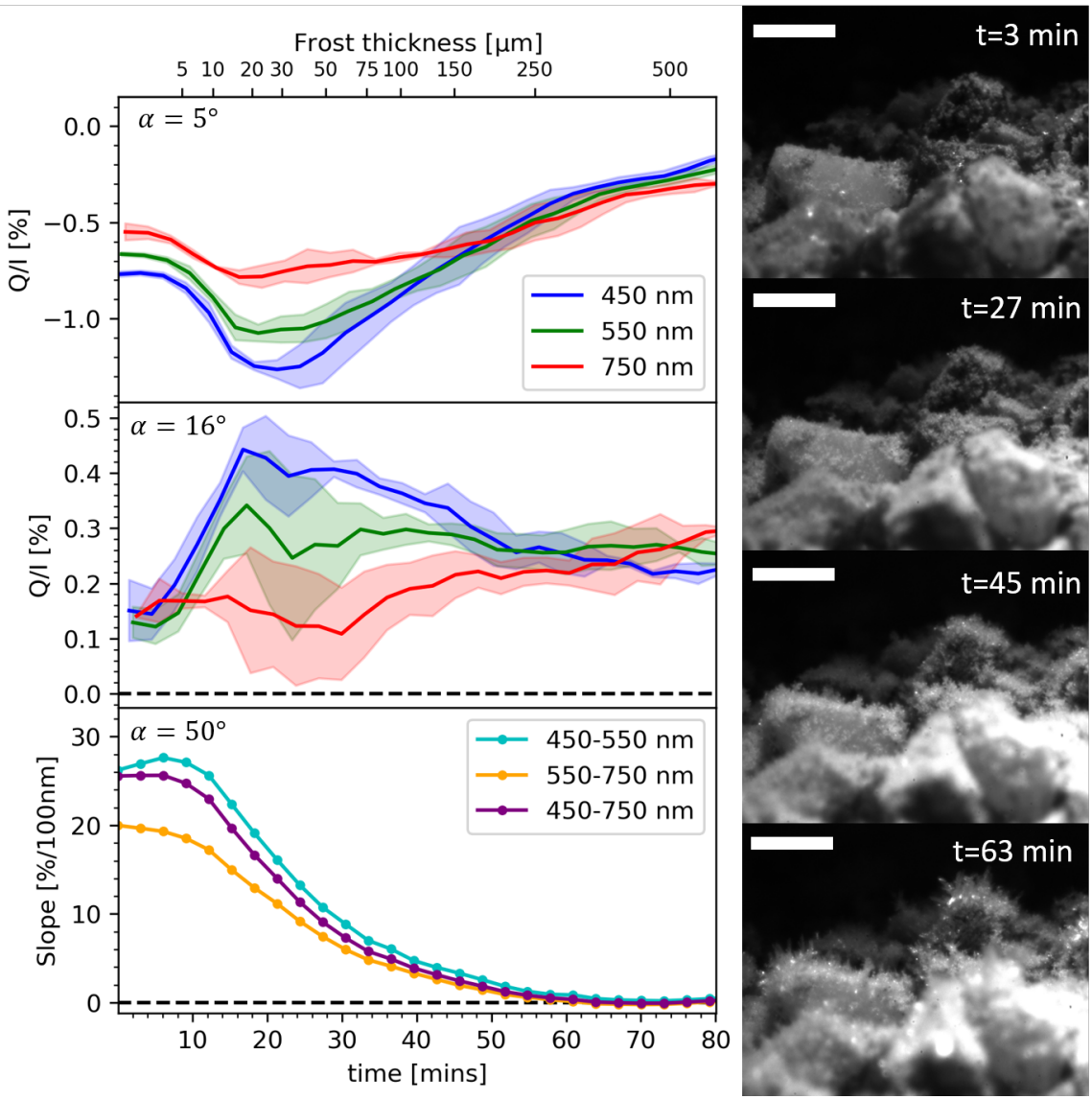

Figure 6.6: The evolution of the linear polarization at 450, 550 and 750 nm at phase angle $\alpha = 5^\circ$ (top graph), $\alpha = 16^\circ$ (middle graph), spectral slope (bottom graph), and frost thickness (top bar) on MGS-1 simulant in the hot case. The shaded areas around the polarization measurements are the standard deviation of the four experiment repetitions. The slope is calculated using Eq. 6.2 with wavelengths 450-550, 550-750 and 450-750 nm, the phase angle is $\alpha = 50^\circ$. The images of the regolith sample show the deposition of frost on the surface at different times (right), the scale bar represents 1 mm.

crystals size exceeds 100 µm, the linear polarization decreases without color differences.

- At phase angles close to the inversion angle (in our case 16°), the wavelength differentiation in linear polarization appears in the case of CR and hot MGS-1 ($|P_{450} - P_{750}| \sim$

0.4%), but it is less pronounced in the cold MGS-1 ($|P_{450} - P_{750}| \sim 0.1\%$). Interestingly, there is a strong difference between the blue linear polarization of cold MGS-1 ($P_{450} = -0.1\%$) and hot MGS-1 ($P_{450} = +0.45\%$) when frost is 15 µm thick.

- The spectral slopes decrease significantly already when the frost thickness reaches ∼ 20 µm. The spectral slope between 450 and 550 nm changes faster than the others depending on the frost size. On the contrary, the spectral slope between 550 and 750 nm shows shallower behaviours and slower changes with the frost thickness.

6.4 Discussion

We performed laboratory experiments to study the evolution of a regolith-like material when frost deposits on its surface at low temperatures, in reflected polarized and total light at different wavelengths and phase angles. Our experiments showed that a layer of frost depositing on a regolith sample can be detected already when the ice layer is tens of micrometers thick.

6.4.1 Frost thickness and spectrophotometry

The *Rosetta* mission allowed us to observe in detail the surface of 67P nucleus, and detect water ice patches (Pommerol et al., 2015b) and frost (De Sanctis et al., 2015b; Fornasier et al., 2016, 2019, 2021). Previously, bright spots of water ice had been already observed on the surface of the comet 9P/Tempel 1 (Sunshine et al., 2006) and comet Hartley 2 (A'Hearn et al., 2011). Although no spectral slope data were produced for the icy spots on these two comets, they have been correlated to water ice absorption bands and to an increase in reflectance at shorter wavelengths. Fornasier et al. (2016) detected daily color variations on the surface of 67P in the Imhotep region with 0.5% uncertainty (Fig. 6.7). These changes are due to nighttime water frost deposition that disappears shortly after illumination of the Sun. The frost fringes appear about six times brighter than the average comet reflectance, and disappear after a few minutes of illumination. The spectral slope of the fringes calculated between $535 - 882$ nm is approximately 12%/100 nm, and it increases to 16%/100 nm in about 40 minutes. From the thermal model of the surface, Fornasier et al. (2016) estimated the sublimation rate of the water ice, retrieving a $10 - 15$ µm of frost thickness. We can attempt to compare the $535 - 882$ nm color variation observed on 67P to the closest spectral slope calculated in our experiments ($550 - 750$ nm). While the albedo of 67P is closer to the reflectance values of CR, its visible spectrum is redder, with spectral slopes in the ice-free areas of approximately $S_{535-882} = 16 - 20\%/100$ nm (this value depends on the heliocentric distance, with lower values at perihelion). Such a value lies between the frost-free spectral slope of CR and MGS-1 simulants, $S_{550-750} = 10\%/100$ nm and $S_{550-750} = 20\%/100$ nm, respectively. In both cases, a decrease of $\Delta S_{550-750} = 4\%/100$ nm is equivalent to a frost thickness in the range $10 - 20$ µm. This result is in agreement with the thickness estimated by Fornasier et al. (2016) derived from the ice sublimation rate. In the Anhur region, Fornasier et al. (2019) detected long-lasting water frost in shadowed areas, with spectral slope decreasing from $S_{535-882} = 18\%/100$ nm to $S_{535-882} = 3 - 10\%/100$ nm at 87° phase angle. The phase angle of our experiment is lower (maximum 66°) than the phase angle of this observation, nonetheless, such small spectral slope values are in agreement with thick layers of frost (up to $75 - 150$ µm). These results

demonstrate that water frost is detectable already when it is tens of microns thick, tracking the color changes of a surface. The observation of color changes at shorter wavelengths should provide an advantage in detecting thinner layers of frost, due to the sensitive response of the blue color to water ice deposition.

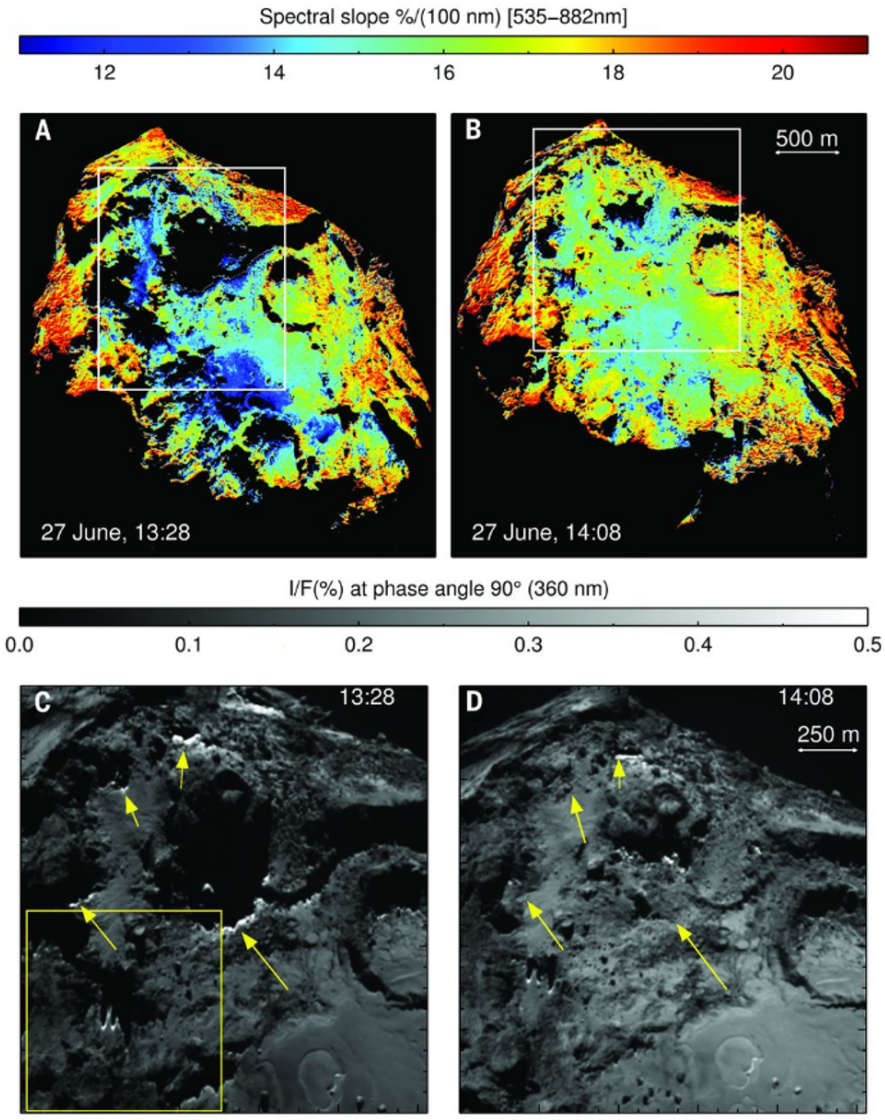

Figure 6.7: Water frost deposits at nighttime on the surface of 67P, and their disappearance at daytime. At dawn, the retreating shadow leaves a frost layer behind that sublimates quickly after being illuminated. In these regions, the spectral slope changes approximately from 12%/ 100 nm to 16%/100 nm. Image from Fornasier et al. (2016) (Fig.3)[6].

There are only a few observations of water frost on Mars. In 1977, *Viking 2* detected H_2O forming at nighttime at 48°N and disappearing a few minutes after sunrise (Jones et al., 1979; Svitek and Murray, 1990). In 2008, the space probe *Phoenix* excavated some trenches

in the Mars soil at 68°N and found a consolidated slab of subsurface water ice and more porous, pure underground patches of ice. Later on, it detected frost forming at nighttime on the landing site surface (Smith et al., 2009). Carrozzo et al. (2009) used the OMEGA imaging spectrometer near-infrared data on board of *Mars Express* and successfully detected water frost on shadowed slopes at low latitudes (between 30°S and 12°N). In the northern hemisphere (between 12°S and 30°N), frost was not detected even where the thermal model predicted its formation. The lack of detection of water frost on the slopes of the northern hemisphere remains unclear.

Unfortunately, there are no available quantitative data on water frost causing color changes on Mars, or sensitive polarization measurements of its surface. Nonetheless, some laboratory works have been carried out in the last years on frost deposition on Mars soil simulants observed in the visible spectrum. Pommerol et al. (2013) studied how frost deposited on top of JSC Mars-1 soil simulant affected its bidirectional reflectance at 650 nm. They found that a thin layer of frost increases the overall reflectance and enhances the forward scattering of the soil sample, although the experiment was limited to a single wavelength and incidence angle because of the rapid sublimation of the frost layer. Recently, Yoldi et al. (2021) carried out a spectral analysis of JSC Mars-1 soil simulant and dark basalt in association of different types of water ice, included frost. They observed that already 100 µm of frost is enough to completely flatten the spectrum, making it indistinguishable from pure ice. This result agrees with our spectral slopes on MGS-1, which approach zero when the frost thickness approaches $100 - 150$ µm (depending on the temperature of the regolith).

We note that frost growing on regolith samples does not change their reflectance spectrum in the same way as an intimate mixture of ice and regolith particles. Our data show an increase of reflectance in the blue when the frost is tens of microns thick, while an intimate mixture of spherical transparent ice particles and regolith produces the same effect only when larger quantities of ice are mixed within the dust (Yoldi et al., 2021). This is particularly important when the ice content is extrapolated by observational data - if the type of ice-dust association is unclear, the amount of ice could vary greatly depending on the mixing model. Furthermore, the surge of reflected blue light when a thin layer of frost forms on regolith grants a powerful advantage for recognizing it from other ice-dust associations.

The frost thickness or equivalent ice thickness retrieved from spectrophotometric data is a criterion that should be used carefully. In Fig. 6.8, we present the frost thickness measurements compared to the reflectance in the blue (R_{450}). At the beginning of our experiments, the frost thickness is increasing, since the frost dendrites expand outward from the regolith grain facelets. In this phase, to the increase of thickness corresponds an increase in reflectance too, and the frost thickness can be used effectively to track the reflectance changes that vary with the substrates and the frost deposition rate (i.e. the temperature of the sample for MGS-1). When the frost crystals grow up to approximately 100 µm, the frost on CR undergoes a stationary growth phase. The frost stops expanding outward from the grain surfaces, and grows between the preexisting ice crystals, increasing the density of the ice layer. This density increase of the frost layer corresponds to an increase in R_{450}. After this phase, large frost crystals ($200 - 400$ µm long) start to form on top of the regolith grains, and we stop measuring the thickness since they evolve and collapse quickly under their weight, making it

difficult to measure them precisely. The growth of large crystals corresponds to a decrease of reflectance at all wavelengths. The large ice crystals show a regular, transparent, elongated shape and the increase in transmissivity allows the photons to be absorbed in deeper layers of frost or to reach the dark substrate. This means that, at this stage, the visible reflectance does not correlate anymore with the frost thickness or the crystal size.

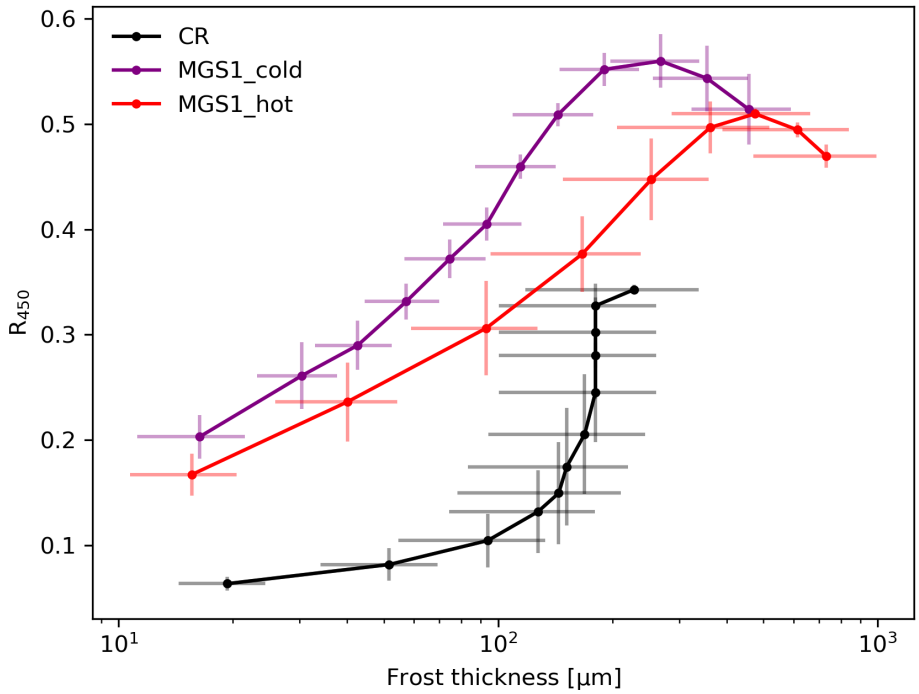

Figure 6.8: The reflectance is the blue (R_{450}) plotted versus the frost thickness measured with the long-distance microscope for the different substrates.

There is an important difference between our laboratory experiments and the frost depositing on Mars or on a cometary nucleus. In the first case, the cooling process happens from the bottom of the regolith sample, and the air above the sample has higher temperature than the sample itself, while in the second case the air temperature is lower than the regolith temperature. Since the growth of ice crystals is limited by their efficiency to disperse the latent heat of deposition, the heat transfer efficiency plays an important role in the crystal growth (Kieffer, 1968). In the case of cooling below the sample, the ice crystals lose heat more efficiently through conduction to the cold regolith. This means that they tend to increase their width to maximize the contact with the cold regolith grains. In the case of an atmosphere colder than the surface, the deposited ice loses heat through radiation. This process is more efficient if the ice crystals are thin and elongated, to maximize their surface through which the heat is radiated to the atmosphere. This means that incident photons find more scatterers than in the case of wide shorter crystal, changing the overall spectrophotometric properties. Since it is not possible to reproduce the second case in our laboratory, we have to restrict

our research to Earth-like frost, and knowing the differences with the extra-terrestrial frost, extrapolate the expected spectral and polarimetric behaviour. For the same frost thickness, the scattering within frost crystals in our experiments increases (i.e. the number density of the crystals on the regolith increases), we expect the regolith surface to become brighter more quickly, especially at shorter wavelengths. This means that the spectral slope would rapidly decrease as soon as the frost deposits, making it more detectable with spectral slopes calculated with $\lambda_1 = 450\,\mathrm{nm}$.

Often, the ice content on the substrates or intermixed with it is extrapolated by creating a synthetic spectrum from areal/intimate mixing of ice with the regolith dust. To obtain such a spectrum, the reflectance or single scattering albedo of ice and dust are linearly combined, and the ice amount is increased to fit the observed spectrum. From our data (Fig. 6.8), it is clear that this method can fail in reproducing a correct amount of ice whenever this is constituted by bigger translucent ice grains. On the other hand, a spectral linear mixing effectively detects an increase of amount of ice when the frost layer becomes denser (like in the case of CR in Fig. 6.8), since the reflectance increases too.

6.4.2 Spectropolarimetry of growing frost

Only a few attempts at studying the linearly polarized reflected light from ice-dust associations have been made. This is mainly due to the scarcity of polarization instruments for planetary observations and to the difficulty to interpret the polarimetric data that are sensitive to many different parameters (hence also carrying a rich quantity of information). The linear polarization of deposited dust at small phase angles is dominated by multiple scattering within the grains composing the regolith. When the ice nucleation sites start to alter the multiple scattering on the surface, the polarization phase curve changes its shape. In general, frost forming on a black substratum moves the minimum of the negative polarization to lower phase angles, while the inversion angle α_{inv} also decreases (see e.g. Poch et al. (2018)). In the first stages of frost deposition, an increase of $|P_{min}|$ has also been observed for different icy samples containing salts (Cerubini, 2021).

During the frost deposition process, we measured the linear polarization signal at 5° and 16° because these values are close to the phase angle of the minimum polarization α_{min} and to the inversion angle of CR and MGS-1 (Fig. 6.9). Generally, if the linear polarization $|P_{5^\circ}|$, increases, it means that $|P_{min}|$ is increasing, while its decrease means that the minimum polarization is moving toward smaller phase angles or the negative polarization becomes shallower. The measurement of the polarization at 16°, is used as a proxy to determine the position of the inversion angle α_{inv}. Since the polarization phase function is monotonically increasing between α_{min} and α_{max} (usually around $90 - 100^\circ$ that is dependent on the Umov law), $P_{16^\circ} > 0$ implies $\alpha_{inv} < 16^\circ$, and $P_{16^\circ} < 0$ means that the inversion angle moved to values $\alpha_{inv} > 16^\circ$.

All our samples show a wavelength-dependent decrease of P_{5° when the first tens of micrometers of frost forms. At 5°, P_{450} shows the biggest decrease of the order of $0.25 - 0.5\%$), while P_{750} undergoes smaller changes of the order of 0.2%. When the first frost crystals are forming on the sample, the blue light is Rayleigh scattered more efficiently, which increases the coherent backscattering opposition effect (CBOE). The CBOE is responsible for the surge

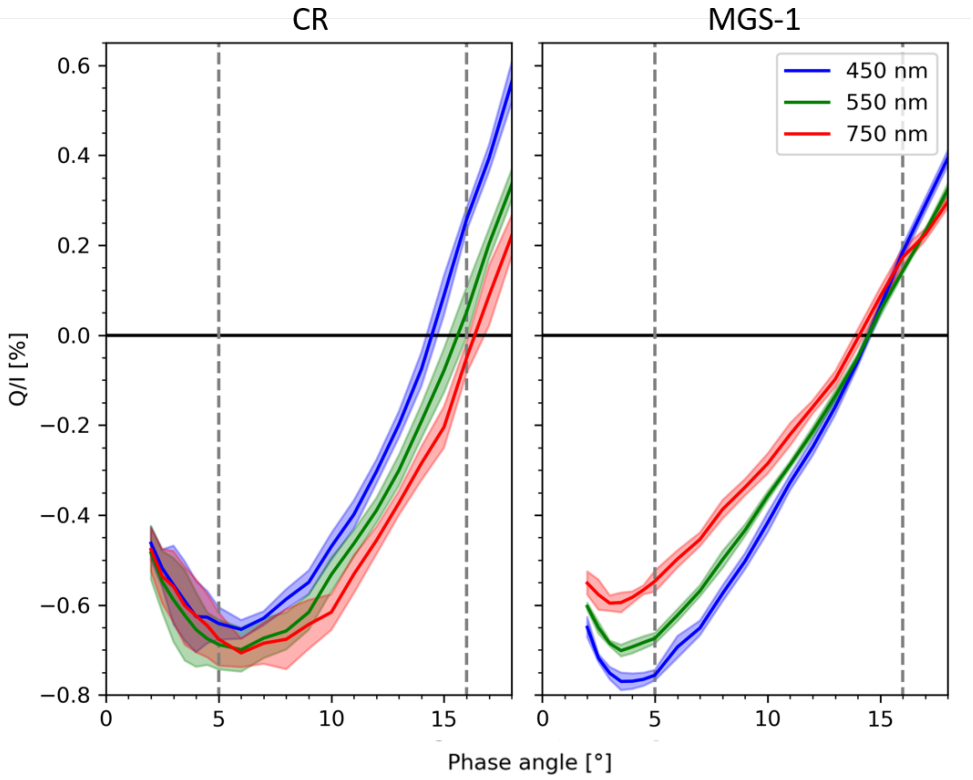

Figure 6.9: Polarization phase curves of CR and MGS-1 simulants. The phase angles observed in our experiments are indicated with vertical dashed lines.

of reflected negative polarization at small phase angles from regolith surfaces containing particles smaller than the observed wavelength (see Dlugach and Mishchenko (2013) and references therein). When small ice particles are introduced on the regolith, the second order scattering between ice and regolith dust increases, thus increasing the probability of CBOE. The CBOE is more effective for second order scattering than higher order scattering, and there is a point when the surface is covered by sufficient ice particles to produce higher order multiple scattering across the surface, scrambling enough the linear polarization and decreasing its overall averaged signal. This is the reason why, when the frost becomes thick enough and it hides the regolith beneath, the linear polarization decreases to zero without any wavelength dependence. Note that the minimum of P_{450} is reached when the frost is tens of microns thick. This means that such a thickness of small crystals is still allowing an efficient second order scattering between ice and dust grains.

At 16°, the linear polarization is also wavelength dependent, although it depends on the sample and its temperature. CR shows an interesting α_{inv} behaviour. When the frost is approximately $30 - 50\,\mu$m thick, P_{750} becomes positive, while P_{450} reaches its minimum at $P_{450} \sim -0.5\%$. This means that the 450 nm polarization phase curve increases its α_{inv} by several degrees, while the 750 nm polarization phase curve decreases its inversion angle. This is very different from the starting inversion angles of the starting pure CR (see Fig. 6.9 left).

The polarization phase curve of the dry MGS-1 soil simulant does not show a particular dependence of α_{inv} on wavelength (see Fig. 6.9 right). For the cold case MGS-1 ($T_{min} = -130\,^{\circ}C$), P_{450} and P_{550} show a certain degree of variability between experiments, and a clear distinction between the wavelengths is not possible. However, both P_{450} and P_{550} shift from positive to negative values when the frost is $10-20\,\mu m$ thick, meaning that the inversion angle slightly increases. The hot MGS-1 ($T_{min} = -100\,^{\circ}C$) shows a completely different evolution at 16°. P is positive at all wavelengths for the entire experiment duration. While P_{750} slightly increases over time, P_{450} increases sharply from $P_{450} = 0.15\%$ to $P_{450} = 0.45\%$ when frost thickness is approximately $20\,\mu m$. Note that the P_{450} surge does not correspond necessarily to a decrease of inversion angle, P_{min} of MGS-1 can deepen maintaining the same inversion angle (approximately $\alpha_{inv} = 14°$) and causing the increase of P at 16°.

Since the only difference between the two experiments with MGS-1 is the regolith temperature, this effect must be related to some temperature dependent property of the frost. The two temperatures chosen for the experiments are close to the crystalline structure transitions for ice at ambient pressure (Kumai, 1968). At $T_{=} - 130\,^{\circ}C$ to $-100\,^{\circ}C$ both cubic and hexagonal ice can form, but as soon as the temperature rises above $-100\,^{\circ}C$ only hexagonal ice can form. The reflectance of the two types of frost are different in the blue, with higher reflectance for the frost formed at $T= -130\,^{\circ}C$ to $-100\,^{\circ}C$ (Fig. 6.8). The scattering properties of the ice can be a result of its type of crystalline macrostructures (like the shape of dentrites growing on the regolith) or the single cubic or hexagonal ice crystals, that have different single-scattering properties (Riikonen et al., 2000). At the present time, there are no studies on the polarizance of ice with different crystalline structures. The negative polarization phase curve of MGS-1 at 450 nm seems to widen and deepen slightly when the first tens of micrometers of deposited frost has a mixed cubic/hexagonal structure, while for only hexagonal ice frost a greater decrease of P_{min} with no α_{inv} increase is observed.

6.4.3 Effect of the first micrometers of frost

In Fig. 6.9 we can see that the expected CR polarization in the blue at 16° is $P_{450} = 0.25\%$. This is not the measured polarization when we start our frost deposition experiment (Fig. 6.4), that is $P_{450} = -0.1\%$. There has been a decrease of polarization between the start of the experiment and when we start to acquire the data. To some extent, this is true also for the polarization at 550 nm, although the difference is almost within the uncertainty. This effect can be explained by a thin frost film formed before acquiring the measurement. In our experiments, we insert an aluminum lid over the sample before starting to cool down the cryo-stage, when the POLICES enclosure still contains ambient air. Some of that air remains trapped between the sample and the lid and might deposit over the sample as soon as it becomes cold enough and before acquiring the first polarization data. To prove that this effect is due to some frost deposition, we repeated an experiment with CR without placing the lid at the beginning of the cooling phase (Fig. 6.10). The experiment was performed only at 450 nm since this wavelength is mostly affected. It takes about 10 minutes to lower the temperature of the regolith from room temperature to $0\,^{\circ}C$, and in the meanwhile the enclosure is completely flushed with nitrogen. When the regolith temperature decreases below the freezing point, the air is virtually absent in the chamber, and frost cannot form. In Fig. 6.10 we can see that the regolith sample not covered by the lid maintains a constant reflected polarized and total

light even when the temperature drops to −100 °C. After 25 minutes, the nitrogen flushing is stopped. In about seven minutes, the polarization drops from $P_{450} = 0.25\%$ to negative values, and the reflectance starts increasing by approximately 0.2%. This is a clear sign of frost deposition happening on the sample.

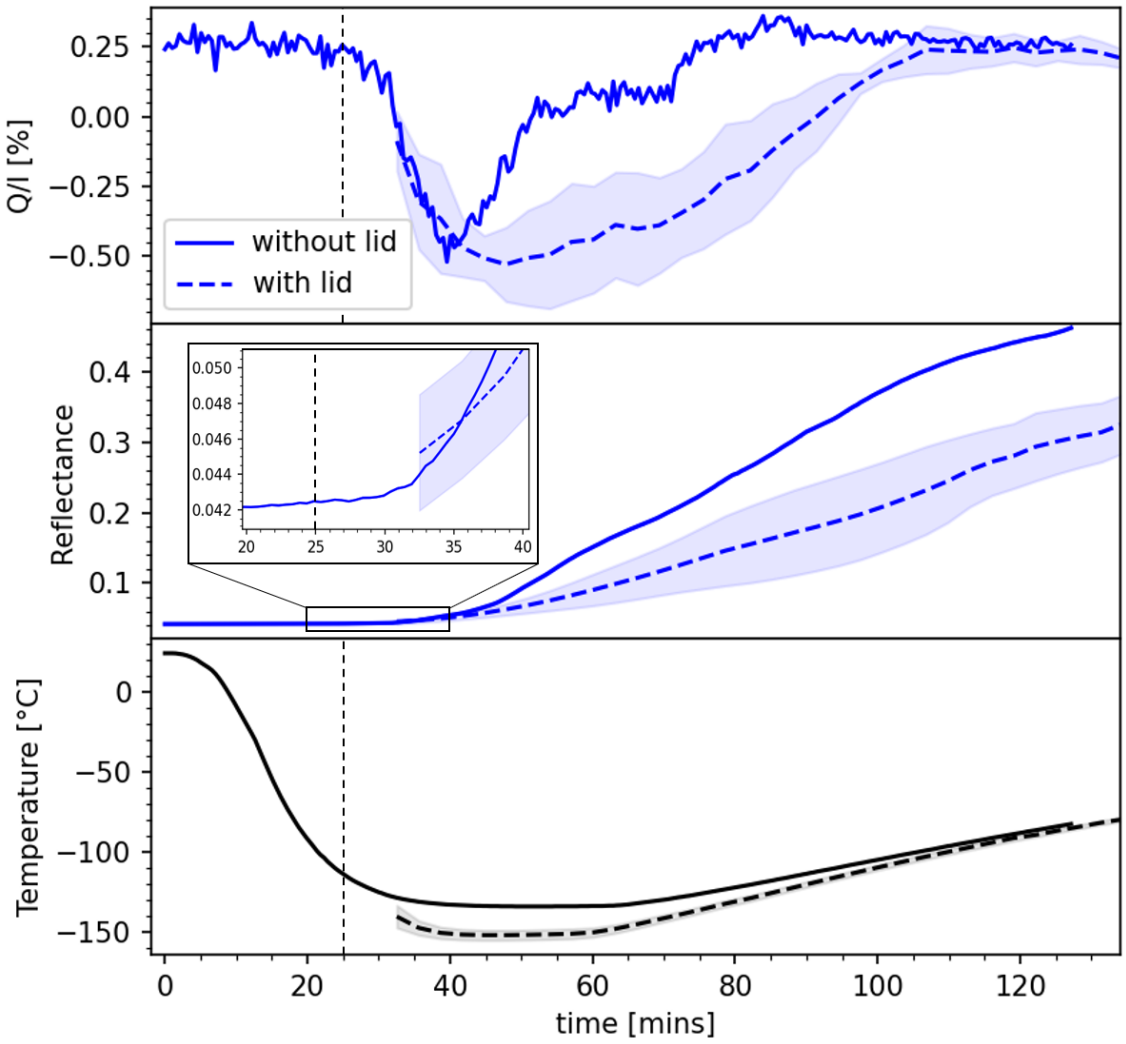

Figure 6.10: The linear polarization and reflectance of CR at 450 nm and $\alpha = 16°$. The continuous line represents one experiment without the lid over the sample, while the blue dashed line represents the average of the experiments conducted with the lid over the sample during the cooling phase (see Fig. 6.4). The black vertical dashed line represents the time at which the nitrogen flushing is stopped. On the bottom, the temperatures of the sample in the case with and without lid are plotted versus time.

It is difficult to measure directly the thickness of this first frost deposition, since there is no difference between the images taken with the microscope before starting the experiment

and when we start measuring the reflected light (i.e. after the cooling phase). A rough lower limit of frost thickness can be calculated from the amount of moisture that is trapped above the sample. Since the relative humidity in the laboratory is usually approximately 40% and knowing the volume of air trapped over the sample, if we assume that all the water deposits as ice on the sample, the thickness should be $\sim 1\,\mu m$. This supports the fact that a thin layer of frost is forming on the sample and interacts with the blue light, giving rise to a change of polarization and a slight increase in reflectance. The polarization phase curves of MGS-1 are in good agreement with the linear polarization measured at the beginning of the experiments at 5° and 16°. This means that either we do not form any thin ice film, or the ice film is not optically thick in the blue. Since frost deposits slower on MGS-1 than on CR, it might be that the vapor pressure needed to start the ice nucleation is higher than just the saturation pressure at that temperature, causing a delay in the formation of such a thin layer, which forms more rapidly as soon as ambient air is allowed to enter the enclosure.

6.5 Perspectives for remote sensing and future experiments

Our experiments are limited to very specific geometries, with the linear polarization measured at phase angles 5° or 16°, and the reflected total intensity at 50° and 66°. In the right conditions of water vapor pressure and temperature, frost forms on planetary surfaces, and these conditions are often met in shadowed areas (at terminator, or close to cliffs and on crater slopes). For instance, in the case of 67P the observation of ice patches in the Anhur/Bes regions occurred at phase angles $\alpha = 61° - 75°$ that are very similar to our experimental conditions for the total light measurements. The uncertainty related to the spectral slope measurements on 67P is enough to detect the small changes due to tens of microns of deposited frost, showing that *Rosetta* Optical, Spectroscopic, and Infrared Remote Imaging System (OSIRIS) design can be applied successfully to other missions for frost and ice detection.

The shadowed regions are in that case caused by the irregular topography of the region and the presence of cliffs and steep scarps. On mars, nighttime frost is often observed in crater shadows, that are best observed at larger phase angles. Conversely, the negative polarization must be observed with phase angles that are within the inversion angle of the observed regolith (in the range $\alpha_{inv} = 15° - 25°$ for most planetary surfaces). This means that to observe shadow-rich regions like the terminator, both the light incidence angle and the emission angle (where the observer is) must be large, which requires that either the telescope or the spacecraft specifically maneuver to target those areas (Fig. 6.11). On the other hand, if we observe frost on shadowed slopes or cliffs, the emission angle constraint can be relaxed, depending on the slope angle and the incidence of the sunlight.

Since it was demonstrated that the negative polarization can determine the compositional properties, porosity, grain shape and grain size of regolith-like materials (see for instance Shkuratov and Ovcharenko (2002); Escobar-Cerezo et al. (2018); Frattin et al. (2019); Spadaccia et al. (2022)), polarimeters should be considered a very useful addition to onboard imaging instrumentation of future planetary missions. Polarimeters could be exploited also on rovers and landers, that have more freedom in observing at high emission angles, and in-situ frost formation and evolution 6.11. Furthermore, having polarization cameras on rovers or landers is of great interest for studying the properties of aerosols and atmospheric dust and clouds.

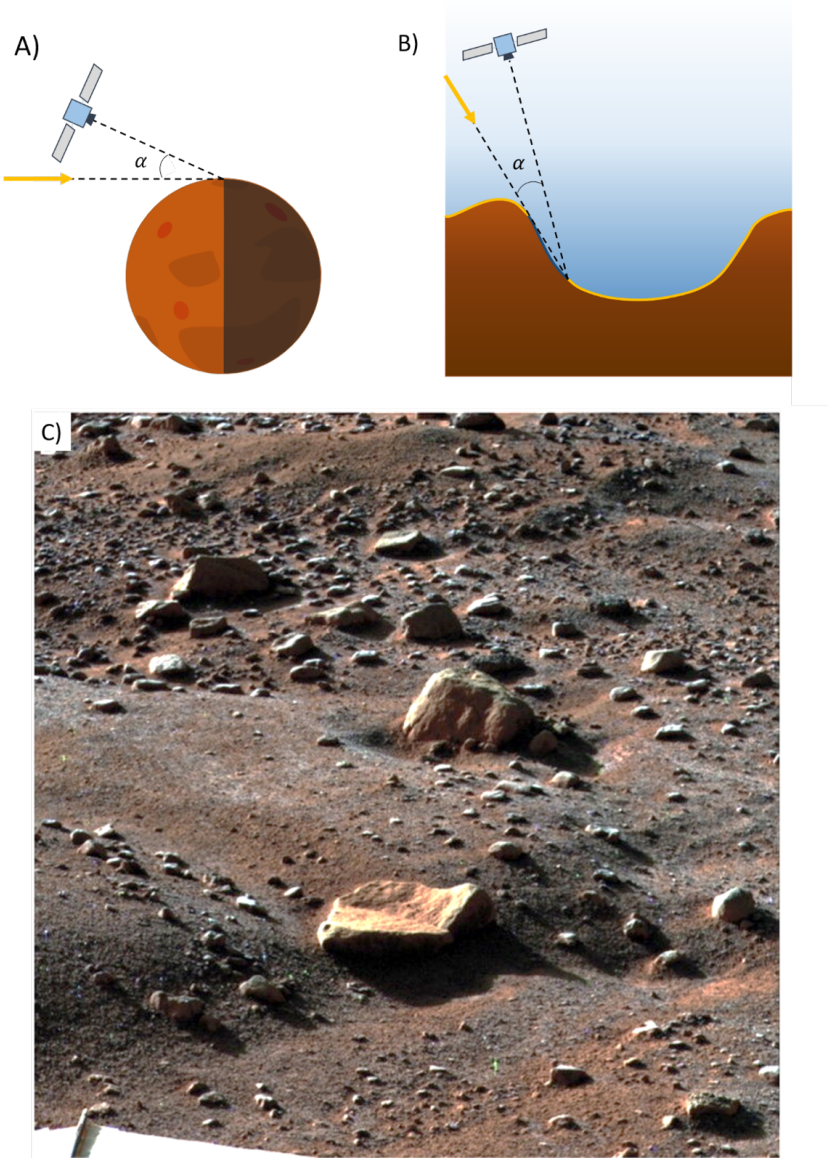

Figure 6.11: Possible geometries to measure negative polarization of frost though remote sensing. A) the terminator is rich in shadows and is the perfect area where to search for frost, but this requires high observation angles to remain at small phase angles. B) Craters and local topographic features allow relaxing the observation angle of the spacecraft, always remaining at small phase angles to observe the reflected negative polarization in shadowed areas (indicated with a blue line on the left crater wall). C) morning frost observed by the *Phoenix* lander, image from Smith et al. (2009) (Fig.3)[7].

The main limitation for frost and ice detection through polarimetry is the current lack of high-precision instruments considered for planetary missions. Many past planetary mission carried polarimeters of different types used to image other Solar System bodies. The first

missions to have polarimeters were the *Pioneer* 10 and 11 spacecrafts, launched in 1972 and 1973, respectively. Their imaging photopolarimeters (IPP) provided the first in situ polarization images of Jupiter and Titan (Coffeen, 1974; Baker et al., 1975; Tomasko and Smith, 1982). In 1977, *Voyager* 1 and 2 were launched, carrying both a photopolarimeter subsystem (PPS). Only *Voyager* 2 managed to acquire polarization data though, since the PPS of *Voyager* 1 experienced a quick degradation due to the harsh space environment. IPP polarization uncertainty was $\pm 0.5\%$ and allowed the first polarization observation of the equatorial zone of Saturn polarization at 264 nm and 750 nm (West et al., 1983). In 1986 and 1990 the *Giotto*'s optical probe experiment (OPE) measured successfully the linear polarization signal of comet 1P/Halley (Levasseur-Regourd et al., 1985) and of comet Grigg-Skjellerup (Levasseur-Regourd et al., 1993) comae with a sensitivity of $0.5 - 1\%$. In the meanwhile, the *Galileo* spacecraft was launched in 1989 and its Photopolarimeter/Radiometer (PPR) experiment (Russell et al., 1992) started to acquire linear polarization data of Jupiter and its moons with uncertainties down to $\pm 0.3\%$ (Braak et al., 2002). More recently, the Imaging Science Subsystem (ISS) of *Cassini* acquired polarization images of Saturn and its moons using a narrow angle camera (NAC) and a wide angle camera (WAC) equipped with different filters in the range $350 - 1100$ nm (Porco et al., 2004). The two cameras have two filter wheels in front of their main aperture, allowing a coupling of pass-band filters and NIR and VIS polarizers. Unfortunately, there are not published works on the polarization data of ISS, although the sensitivity of the instrument is expected to be $\pm 0.5\%$ in linear polarization (Porco et al., 2004).

The linear polarization uncertainty of the aforementioned instruments hides the most fine features of the negative polarization of regolith surfaces that requires uncertainties down to the order of 0.1%. Although previous planetary mission polarization instruments do not meet this requirement and there are no other planned polarimeters in the near-future planetary missions, some high-accuracy spectropolarimeter designs for Earth observation already exist. For instance, the Aerosol Polarimetry Sensor (APS) on board of NASA Glory satellite was designed for observing Earth atmosphere degree of polarization with uncertainties of about 0.2%, but unfortunately the Glory mission failed during the launch phase in 2011 (Knobelspiesse et al., 2012). More recently, the Lunar Observatory for Unresolved Polarimetry of the Earth (LOUPE) concept targets polarization uncertainties lower than 0.1%, to observe Earth as an exoplanet from the Moon (Klindžić et al., 2021). Future Earth observation missions will demonstrate the feasibility and usefulness of high-accuracy polarimetric data, possibly paving the way toward future polarimetry mission for exploring our Solar System.

Future experiments should include different types of deposited ices (CO_2, SO_2) commonly found in our Solar system, together with other regolith simulants and organics. While the NIR and IR spectral behaviours of different types of water ice and dust associations have already been investigated (Pommerol et al., 2013; Yoldi et al., 2021)), the NIR negative polarization is poorly studied. The reflected negative polarization in correspondence to the ice NIR absorption bands is particularly interesting, since the reflectance of frost drops importantly, and this can lead to an increase of negative polarization when mixed with higher albedo dust (the mixing effect described in Shkuratov (1989) and Spadaccia et al. (2022)).

6.6 Conclusions

We have experimentally investigated the reflected polarized and total light of water frost forming on regolith simulant at different visible wavelengths, correlating the spectral slope and the linear polarization to the measured properties of the frost (thickness, temperature and crystal shape). We found that early frost formation changes rapidly the reflected blue light and the multiple scattering within the surface grains, causing a surge in negative polarization and an increase of reflected light. The spectral slope calculated between $450 - 550$ nm is more sensitive in detecting thin frost layers, together with the difference between the negative polarization at small phase angles at 450 nm and 750 nm. This makes frost detection possible already when the frost is only $10 - 20$ µm thick. The polarization measured close to the inversion phase angle shows different behaviours with respect to the temperature of the regolith simulant, and it seems correlated to the phase transition from cubic to hexagonal ice crystal structure. Finally, our measured frost thickness agrees with the frost thickness derived by thermal modelling on some regions of 67P. We can compare the efficiency of spectral slope and negative polarization observation of frost deposited on regolith as follows:

- the visible spectral slope varies quicker to frost deposition when calculated using $\lambda = 450$ nm as smaller wavelength. After the first $30 - 50$ µm of deposited frost, the spectral slope evolves at more slowly pace, when ice crystals grow bigger. While spectral slope can provide good measurements of frost depositing on dark regolith, its variation over time is not sensitive to the temperature of the regolith;
- negative polarization measured at phase angle close to the minimum of polarization and inversion angle, with a blue ($\lambda = 450$ nm) and red filter ($\lambda = 750$ nm) provide very good sensitivity to the first microns of frost formed on the substrate, but requires high precision (down to 0.1% measurement error). Furthermore, polarization measurements are sensitive to the temperature at which the frost is deposited, that we interpret as a sensitivity to its crystalline structure (cubic or hexagonal).

In conclusion, both techniques provide useful and precise information on frost thickness over time, and negative polarization can add information on the crystal structure of ice at the cost of high required sensitivity. These results are of paramount importance to extrapolate water frost physical properties from remote-sensing data, giving a better insight on ice deposition and evolution processes on surfaces of Solar System bodies. This data set will be extended for other ices, regolith substrates, and observed wavelengths with future experiments in the Icelab at the University of Bern.

Acknowledgements

This work has been carried out within the framework of the National Centre of Competence in Research PlanetS supported by the Swiss National Science Foundation under grants 51NF40_182901 and 51NF40_205606. The authors acknowledge the financial support of the SNSF.

Chapter 7

Summary and outlook

In this chapter, I summarize the main results of my work and their implications, as well as the perspectives in the bigger picture of the undergoing research in the different fields. It comes natural to divide this chapter in sections corresponding to my experiments (chapter 4, 5, 6), but since planet formation theories, pebbles characterization, and surfaces of small bodies of our Solar System are highly interrelated topics, many results and future perspectives can actually be relevant for all these subjects.

7.1 Icy pebbles as building blocks for planet formation

Among the main research questions in the field of planet formation, there is one that particularly challenges the researchers: "What are the mechanisms to form quickly planets in protoplanetary disks?". To address this question, it is important to study the first steps toward planet formation, i.e. the processes involving small refractory and icy grains that form cm-size aggregates ("pebbles"). In the last years, it has been proposed that rapid planet formation could be triggered by the presence of ice lines in protoplanetary disks. This can be due to the discontinuity of the environmental conditions through the ice line: outside of it, vapor deposits as ice on refractory material (forming icy pebbles), while inside of it, the ice sublimates (the local pressure increases) and changes the physical properties of the pebbles. While different models can simulate the disk changes happening close to the ice line, they rely heavily on the physical and chemical properties of the pebbles in the disk. In this framework, I present the first experimental work studying the evolution of complex ice-dust pebbles under conditions comparable to the ones in protoplanetary disks (chapter 4).

I created two new protocols to produce ice-dust compact aggregates with well-defined properties (PAs and PBs), and I studied their evolution under low temperature and pressure conditions. The two new protocols allow the production of compact mm-size icy aggregates: PAs have a dust-to-ice mass ratio of 1, while PBs dust-to-ice mass ratio is 5.6. When the temperature increases, the ice starts to sublimate, and I found that the icy aggregates are mostly preserved when the ice sublimate, especially the pebbles which have high dust-to-

ice ratios and finer dust distribution. Previously, many works in the literature assumed the disruption of pebbles drifting through the ice line and undergoing sublimation of the ice. The main conclusion from my experiment is that the sublimation of the ice through the ice line does not seem to disrupt the dusty pebbles, and leaves them available for pebble accretion processes in the inner disk (hence rocky planetesimals could form faster inside the ice line). The outcome is important to correctly track the icy aggregates evolution close to the ice line in simulations, and should be accounted in models of planetary formation in this region of the disk.

Is the preservation of pebbles through the ice line enough to boost the pebble accretion inside the inner disk and form quickly rocky planets? To answer this question, other processes should be taken in account. In particular, the high Stokes number of sublimated pebbles would increase their speed, diminishing the chances for collisional growth, and increasing the erosion effect by small grains. To avoid the disruption of the dusty, porous pebbles, they should be captured early after sublimation of the ice by planetesimals in the inner disk, or they should pile up fast enough to trigger streaming instability and form a planetesimal. Then, to address the question of pebble growth efficiency, the models of planet formation should adopt the preservation of pebbles as an input (together with their increase in porosity), and study their interaction with the small dust grains, the gas, and the already present planetesimals in the inner disk.

The detection of organic matter in molecular clouds, protoplanetary disks, pebbles, comets, asteroids and meteorites suggests that organics are ubiquitous and could play an important role in the formation of planetesimals. Many experimental works on organics focus on their formation as mantles covering small icy silicate grains in molecular clouds (see for instance the review of Sandford et al. (2020)), but only a few studies on the interaction of refractory grains and organics have been conducted so far (Kudo et al., 2002; Flynn et al., 2013; Piani et al., 2017; Bischoff et al., 2020), none of them treating the association of silicate grains, organics, and ice at the same time. In Annex 4.7 I show that organics can change the sublimation outcome dramatically. Sub-bituminous coal and humic acid were my first attempts to introduce an organic component into my pebble models. Currently, our capacity of creating better analogs is constrained by our knowledge on the composition of real organics on comets and asteroids. The most accurate organics analog has been proposed and used by Kudo et al. (2002) and Nakano et al. (2003), produced by UV-irradiation of ice samples (H_2O, CO, NH_3) at high vacuum and low temperatures (10 K). I can envision future experiments with pebbles made of silicate grains, H_2O ice, and some organics used by Nakano et al. (2003), forming a more realistic “complex pebble" model. The study of such complex pebbles could focus on their reflectance changes over sublimation (SCITEAS-2 experiment in Annex 4.7) and on their mechanical strength after the ice sublimation (CAPO experiment in Annex 4.8). Organic material will be a major protagonist of the research on planet formation in the next future, in particular after the sample-return missions from asteroids (Hayabusa2, Yada et al. (2022)) and possibly future cryogenic sample-return missions from comets (Bockelée-Morvan et al., 2021).

The presence of fairy castles on top of the icy sublimating pebbles (Annex 4.6) and the directional pores in the presence of organics (Annex 4.7) are fascinating. I expect that the

changes in porosity on top of icy aggregates can change both their mechanical and optical properties, and it is worth to investigate these structures more in detail with the instruments that we have in the Icelab (spectrophotometry, spectropolarimetry, and mechanical properties) or in other facilities (cryoSEM). Unfortunately, the proposed *Origo* ESA M-class mission (Marschall et al., 2022), which objective was to land on a comet and study in situ the composition of the pristine icy pebbles on its surface, was not retained in the selection process. However, it demonstrates a large interest from the scientific community on the characterization of the icy building blocks of our solar system, which is extremely important for modeling, observing, and characterizing planet formation processes and minor bodies of our solar system.

Due to the intrinsic complexity of proposed cryogenic sample-return missions (Küppers et al., 2009; Bockelée-Morvan et al., 2021), such missions might not find fertile ground in the upcoming decades. Hence, awaiting future missions which will observe cometary nuclei with the same intensity of *Rosetta* with 67P, we have to find better ways to determine through remote sensing the presence, composition, and distribution of small pristine pebble-size sub-units. In this context, it is of vital importance to continue laboratory research on icy aggregates and complex pebbles, to address the origin and formation processes of planetesimals.

7.2 Spectropolarimetry and spectrophotometry as tools to characterize small bodies surfaces

Our capability to infer the history of small bodies of our solar system depends on how well we can determine their composition and how this evolves over time. Their composition reflects the processes that lead to their formation in the protoplanetary disk, and the environment where they accreted. In this sense, characterizing the presence of particular minerals, different ices, and organics on the surface of the Solar System's small bodies is also studying how they formed in the first place. Spectropolarimetry and sectrophotometry of Solar System's small bodies have been largely used with this purpose, both through ground-based and space-based instruments.

7.2.1 Polarimetry for investigating the composition of airless body surfaces

The analysis of the reflected induced polarized light from regolith surfaces can retrieve important information on the dust grain size distribution, albedo, refractive index, and composition of the regolith material. In the past decades, ground-based surveys of asteroids and comets have used the linear polarization phase curves to retrieve the albedo and some physical properties of the regolith. The linear polarization at small phase angles assumes negative values (negative branch of the polarization phase curve), and it is parametrized by the minimum of polarization P_{min} and the inversion angle α_{inv}. These two parameters have been shown to be sensitive to the surface composition of asteroids, allowing to refine their taxonomic classes through only the polarizance (Belskaya et al., 2017).

To correctly interpret the polarizance of airless bodies, laboratory studies are needed to understand how the reflected negative polarization can change depending on composition.

The first extensive experiments on this topic were pioneered by Dollfus (Dollfus, 1957; Dollfus et al., 1989) and continued by Shkuratov and colleagues (Shkuratov, 1987b; Shkuratov et al., 1994, 2002). An important discovery from these studies is that the mixtures of bright and dark powders can have a much deeper and broader negative polarization than the single powders measured separately ("mixing effect"). This result has been used for example to explain the polarizance at small phase angles of F-type asteroids, believed to be similar to cometary nuclei (Belskaya et al., 2005).

Since the mixing effect has been demonstrated only for a few powder samples, I extended the previous experimental works with a broad dataset of high-precision polarization phase curve measurements of six mineral commonly found in asteroids (chapter 5). I consistently created binary and ternary mixtures of these six pulverized minerals and evaluated their distribution in the $P_{min} - \alpha_{inv}$ space. I discovered that the albedo contrast of the mixed powders is a necessary but insufficient condition to give rise to the mixing effect, and that the deepening of the negative polarization is accompanied by an increase in α_{inv}. These results indicate that many asteroids polarization behavior can be linked to the presence of mineral mixtures on the surface. For example, the negative polarization phase curve of L-class asteroids ("Barbarians") that show very high inversion angles, can be better explained by the presence of very fine mineral dust with inhomogeneous albedo, than by the optical properties of a specific mineral (Sunshine et al. (2008) and Devogèle et al. (2018b) explained their high inversion angle by the presence of spinel in the CAIs on the surface, which has high index of refraction). Our ternary mixtures show that the extrapolation of the mineral composition of asteroids is more complex than just accounting for the high- and low-albedo materials, but it changes depending on the different minerals composing the dark and bright components. Furthermore, I created dust aggregates of different sizes with graphite and silica, and I found that the aggregates with different sizes ($< 200\,\mu m$ and $> 2\,mm$) do not play an important role in shaping the overall negative polarization phase curve of the surface. A direct consequence is that the negative polarization is not sensitive to the presence of porous pebbles on the dusty surface of asteroids, while it seems to be highly sensitive to their mineralogical composition.

There are still open questions that should be addressed by future experiments on this topic. For example, we do not understand why our Mg-spinel (reflectance $R = 0.82$ measured at 530 nm) mixed with graphite ($R = 0.03$) is not producing any deepening of the negative polarization. A naive unsatisfactory explanation for the deepening of the negative polarization, is that the chances of second-order multiple scattering increase when a bright material in inserted in a dark matrix, enhancing the CBOE. From our experiments, it is clear that this interpretation is not always correct and should be deepened with realistic models of multiple scattering layers composed by many irregular particles with different optical properties (e.g., Grynko et al. (2022)). Another interesting phenomenon that is not well explained or discussed in the literature, is the increase in inversion angle whenever the negative polarization is deepened by the mixing effect. The increase in inversion angle in mixtures seems to be enhanced by the presence of very fine powder (1 µm or less). A future extension of the experiments presented in chapter 5 is to measure the negative polarization phase curve of mineral mixtures with different size distributions, to quantify how further the inversion angle can be enhanced by the mixing effect combined with particle size effect, possibly exploring the area in the $P_{min} - \alpha_{inv}$ space where the Barbarians lie (see Fig.8, chapter 5).

In the Icelab we conserve a piece of the Allende meteorite which contains visible chondrules and CAIs (Fig. 7.1). To investigate the role of CAIs on the polarization properties of the regolith material, we could separate them from the meteorite and pulverize them. If they contain spinel, their polarization phase curve measurement could solve the Barbarians high inversion angle dilemma.

Figure 7.1: Allende meteorite sample of the Icelab at University of Bern. The chondrules are well distinguishable as gray circular bodies, while CAIs are the whiter circular or irregular inclusions in the dark matrix.

Retrieving important physical parameters of the regolith covering airless bodies exclusively from the polarization phase curve can be non-trivial, due to the many factors that can influence the polarizance of a surface. This is why I believe that future ground-base observations or in-situ missions should focus on implementing spectropolarimetry and spectrophotometry measurements as complementary tools. Polarimetry studies of fine contrasting powders together with VIS-NIR-MIR spectra have already demonstrated their complementary approach as a way to gather more information on asteroid superficial physical properties (Sultana et al. 2022, submitted).

7.2.2 Spectropolarimetry and spectrophotometry of frosty surfaces

Many small bodies of our Solar System retain H_2O under the form of ices beneath or on their surfaces. The presence of water ice in the interior and surface of planetesimals is directly correlated to their genesis and evolution (see Fig. 7.2 from Blum et al. (2022)), along with being very interesting for the origin of life in our Solar System. Retrieving the quantity of water ice, its superficial and internal distribution, and how they changed over time in comets and other planetesimals is then one of the most important goals of the scientific community.

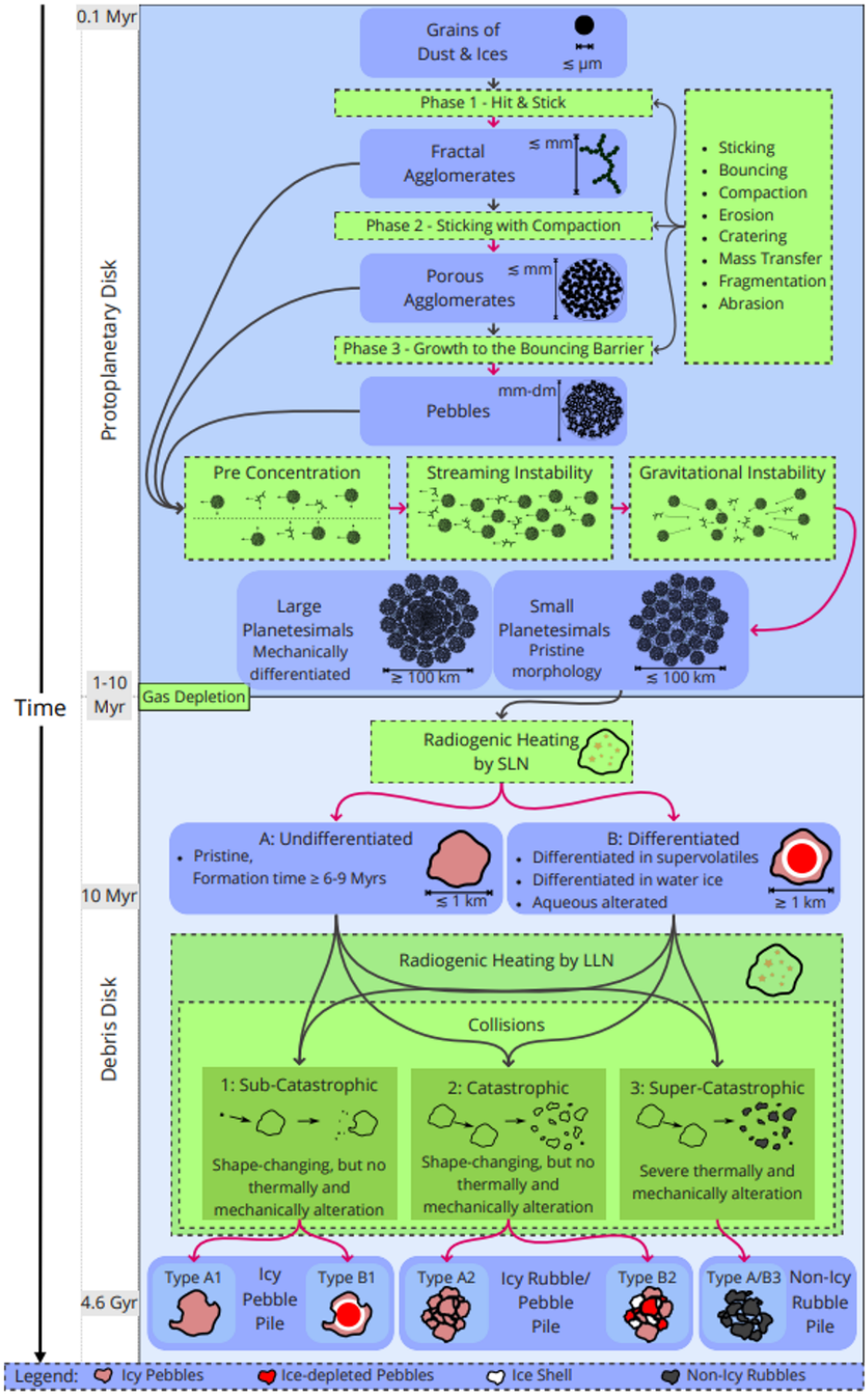

Figure 7.2: Formation and evolution of icy planetesimals formed beyond the snowline, scheme by Blum et al. (2022) (Fig.1).

Ice can be buried underneath the superficial regolith layer of comets and asteroids, and its sublimation can cause disruption of the regolith and particle ejection. The tenuous atmosphere of water vapor can then re-condense on top of the regolith as thin layers of ice (frost deposition). In chapter 6, I presented the first experimental study on the simultaneous measurement of the linear polarization and intensity of the reflected light from frost depositing on regolith analogs, at different wavelengths and observational geometries. The observation of the polarized light (at phase angles $\alpha = 5^\circ$ and $\alpha = 16^\circ$) and the reflected intensity (at phase angles $\alpha = 50^\circ$ and $\alpha = 61^\circ$) were done at three wavelengths (blue channel 450 nm, green channel 550 nm, and red channel 750 nm). I used two regolith simulants: CR asteroids simulant, and Martian Global Simulant MGS-1. The first one was measured at T= $-150\,^\circ$C, while the second regolith analog was measured at T= $-130\,^\circ$C and T= $-100\,^\circ$C. Furthermore, I measured the evolution of the frost thickness and morphology over time, correlating it to its spectrophotometric and spectropolarimetric signal. I discovered that frost can be detected at very early stages (when it is about 10 µm-thick) from both the comparison of the blue and red polarization signal, and from the spectral slope calculated between blue and green, or blue and red channels. The linear polarization evolution close to the inversion angle is sensitive to the temperature of the regolith, and we interpret this result as a sensitivity to the crystal structure of the deposited frost. Moreover, linear polarization can detect a few microns of frost, if the total measurement error is below 0.1%. I compared my spectrophotometric results to the spectral slope of frosty regions on 67P (Fornasier et al., 2016), obtaining very good agreement on the equivalent frost thickness. The measurement of the frost thickness and the morphology of its crystals is going to be very valuable for the retrieval of the water quantity in 67P's icy patches and frosty layers, and for the future missions visiting small bodies with comet-like activity. These results are also important for frost detection on Mars or Earth, expanding our capabilities of studying the frost properties on larger scales.

In 2021, NASA mission *Lucy* was launched, with the objective of studying seven Jupiter trojans. It carries a Multispectral Visible Imaging Camera (MVIC), that will take images of the trojans surfaces, on which small amount of water ice could be present (Yang and Jewitt, 2007; Brown, 2016; Sharkey et al., 2019). The JAXA mission *DESTINY+* will be launched in 2024, and will visit the active asteroid (3200) Phateon in 2028. The scientific payload includes a Multiband Camera for Phaethon (MCAP), which will observe the surface with filters in the visible between 390 and 850 nm. Finally, the CoCa (COmet CAmera) instrument onboard of the future *Comet Interceptor mission* (ESA and JAXA) will acquire high-resolution images of the comet nucleus at different wavelengths. If these instruments measure spectral slope variations on the surface of these planetesimals due to the presence of superficial ice, it will be possible to compare them to the spectral slope variations measured in chapter 6 and retrieve a first estimation of the minimum amount of water deposited on top of the regolith surface. Unfortunately, there are no polarization instruments in scientific payloads of future planned missions, preventing the exploitation and retrieval of other physical parameters such as porosity, crystal structure of the ice, grain size, and mineralogical mixing. I therefore want to emphasize the importance of developing new high-precision, dedicated polarimetric instruments for remote sensing, and raise awarness of their effectiveness in detecting several important physical parameters, especially when flanking other remote sensing instruments.

Interpretation of observational data will further benefit by future experiments on frost and

ice-dust associations. After deposition, frost can be retained for a long time on the surface, depending on the environmental conditions. (e.g. Mars seasonal frost). Over time, the frost crystals can change shape through sintering and a repeated sublimation/re-deposition cycles. The reflected linear polarization is sensitive to the particle size changes, so it can be the optimal tool to understand how frost changes when undergoing sintering or sublimation processes. Another important step is to extend this analysis to other type of ices (starting with CO_2) and substrates (compact or porous ice, organics), relevant for other bodies in our Solar System.

7.3 Final remarks

I believe that our work in the Icelab at the University of Bern shows that the experimental approach is a keystone for interpreting correctly the astronomical data and for providing inputs to simulations of complex phenomena. The work I have done within this Ph.D. project was applied to new topics, hence expanding the use of our techniques to interesting astronomical objects, where experimental data may lack or necessitate update. I suspect that the Icelab will remain at the cutting edge of astrophysics experimental research in the next decades, because since its creation, an incredible amount of experience and laboratory know-how was generated. I hope to have substantially contributed to this cumulative knowledge, and that the next generation of students and researchers who will work in the Icelab will find it of inspiration for expanding even more our knowledge boundaries.

List of Figures

Acronyms

CAIs Calcium-Aluminum Inclusions 12

CAPO Centrifuge for Accelerated Pebbes Observation 33

LOSSy Laboratory for Outflow Studies of Sublimating icy material 21

MoHIS Mobile Hyperspectral Imaging System 31

NIR Near-infrared light 5

PA Pebble type-A 22

PB Pebble type-B 22

POLICES POLarimeter for ICE Samples 35

SCITEAS-2 The Simulation Chamber for Imaging Temporal Evolution of Analogous Samples 24

SPIPA Setup for Production of Icy Planetary Analogues 21

SVS Side-View Setup 28

VIS Visible light 5

Bibliography

M. Adda-Bedia, S. Kumar, F. Lechenault, S. Moulinet, M. Schillaci, and D. Vella. Inverse Leidenfrost Effect: Levitating Drops on Liquid Nitrogen. *Langmuir*, 32(17):4179–4188, May 2016. ISSN 0743-7463. doi: 10.1021/acs.langmuir.6b00574. URL https://doi.org/10.1021/acs.langmuir.6b00574. Publisher: American Chemical Society.

Guillem Aumatell and Gerhard Wurm. Breaking the ice: planetesimal formation at the snowline. *MNRAS*, 418:L1–L5, November 2011. ISSN 0035-8711. doi: 10.1111/j.1745-3933.2011.01126.x. URL http://adsabs.harvard.edu/abs/2011MNRAS.418L...1A.

Michael F A'Hearn, Michael JS Belton, W Alan Delamere, Lori M Feaga, Donald Hampton, Jochen Kissel, Kenneth P Klaasen, Lucy A McFadden, Karen J Meech, H Jay Melosh, et al. Epoxi at comet hartley 2. *Science*, 332(6036):1396–1400, 2011.

S. Bagnulo, H. Boehnhardt, K. Muinonen, L. Kolokolova, I. Belskaya, and M. A. Barucci. Exploring the surface properties of transneptunian objects and Centaurs with polarimetric FORS1/VLT observations. *A&A*, 450(3):1239–1248, May 2006. ISSN 0004-6361, 1432-0746. doi: 10.1051/0004-6361:20054518. URL https://www.aanda.org/articles/aa/abs/2006/18/aa4518-05/aa4518-05.html. Number: 3 Publisher: EDP Sciences.

Stefano Bagnulo, Gian Paolo Tozzi, Hermann Boehnhardt, J-B Vincent, and Karri Muinonen. Polarimetry and photometry of the peculiar main-belt object 7968= 133p/elst-pizarro. *Astronomy & Astrophysics*, 514:A99, 2010.

Jeremy Bailey. Astronomical sources of circularly polarized light and the origin of homochirality. *Origins of Life and Evolution of the Biosphere*, 31(1):167–183, 2001.

AoL Baker, LR Baker, E Beshore, C Blenman, ND Castillo, Y-P Chen, LR Doose, JP Elston, JW Fountain, T Gehrels, et al. The imaging photopolarimeter experiment on pioneer 11. *Science*, 188(4187):468–472, 1975.

L. Barrière-Fouchet, J.-F. Gonzalez, J. R. Murray, R. J. Humble, and S. T. Maddison. Dust distribution in protoplanetary disks: Vertical settling and radial migration. *A&A*, 443(1):185–194, November 2005. ISSN 0004-6361, 1432-0746. doi: 10.1051/0004-6361:20042249. URL http://www.aanda.org/10.1051/0004-6361:20042249.

I Belskaya, A Berdyugin, Yu Krugly, Z Donchev, A Sergeyev, R Gil-Hutton, S Mykhailova,

T Bonev, V Piirola, S Berdyugina, et al. Polarimetry of m-type asteroids in the context of their surface composition. *arXiv preprint arXiv:2204.04929*, 2022.

I. N. Belskaya, Yu. G. Shkuratov, Yu. S. Efimov, N. M. Shakhovskoy, R. Gil-Hutton, A. Cellino, E. S. Zubko, A. A. Ovcharenko, S. Yu. Bondarenko, V. G. Shevchenko, S. Fornasier, and C. Barbieri. The F-type asteroids with small inversion angles of polarization. *Icarus*, 178(1):213–221, November 2005. ISSN 0019-1035. doi: 10.1016/j.icarus.2005.04.015. URL https://www.sciencedirect.com/science/article/pii/S0019103505001818.

IN Belskaya, S Fornasier, GP Tozzi, R Gil-Hutton, Alberto Cellino, K Antonyuk, Yu N Krugly, AN Dovgopol, and S Faggi. Refining the asteroid taxonomy by polarimetric observations. *Icarus*, 284:30–42, 2017.

Irina Belskaya, Alberto Cellino, Anny-Chantal Levasseur-Regourd, and Stefano Bagnulo. Optical Polarimetry of Small Solar System Bodies: From Asteroids to Debris Disks. In Roberto Mignani, Andrew Shearer, Agnieszka Słowikowska, and Silvia Zane, editors, *Astronomical Polarisation from the Infrared to Gamma Rays*, Astrophysics and Space Science Library, pages 223–246. Springer International Publishing, Cham, 2019. ISBN 978-3-030-19715-5. doi: 10.1007/978-3-030-19715-5_9. URL https://doi.org/10.1007/978-3-030-19715-5_9.

T. Birnstiel, H. Klahr, and B. Ercolano. A simple model for the evolution of the dust population in protoplanetary disks. *A&A*, 539:A148, March 2012. ISSN 0004-6361, 1432-0746. doi: 10.1051/0004-6361/201118136. URL http://arxiv.org/abs/1201.5781. arXiv: 1201.5781.

Dorothea Bischoff, Christopher Kreuzig, David Haack, Bastian Gundlach, and Jürgen Blum. Sticky or not sticky? measurements of the tensile strength of microgranular organic materials. *Monthly Notices of the Royal Astronomical Society*, 497(3):2517–2528, 2020.

Jürgen Blum. Dust evolution in protoplanetary discs and the formation of planetesimals. *Space Science Reviews*, 214(2):1–19, 2018.

Jürgen Blum, Rainer Schräpler, Björn JR Davidsson, and Josep M Trigo-Rodriguez. The physics of protoplanetesimal dust agglomerates. i. mechanical properties and relations to primitive bodies in the solar system. *The Astrophysical Journal*, 652(2):1768, 2006.

Jürgen Blum, Dorothea Bischoff, and Bastian Gundlach. Formation of comets. *Universe*, 8 (7):381, 2022.

Jürgen Blum and Gerhard Wurm. The Growth Mechanisms of Macroscopic Bodies in Protoplanetary Disks. , 46(1):21–56, 2008. doi: 10.1146/annurev.astro.46.060407.145152. URL https://doi.org/10.1146/annurev.astro.46.060407.145152.

Jürgen Blum, Bastian Gundlach, Maya Krause, Marco Fulle, Anders Johansen, Jessica Agarwal, Ingo von Borstel, Xian Shi, Xuanyu Hu, Mark S. Bentley, Fabrizio Capaccioni, Luigi Colangeli, Vincenzo Della Corte, Nicolas Fougere, Simon F. Green, Stavro Ivanovski, Thurid Mannel, Sihane Merouane, Alessandra Migliorini, Alessandra Rotundi, Roland Schmied, and Colin Snodgrass. Evidence for the formation of comet 67P/Churyumov-Gerasimenko through gravitational collapse of a bound clump of pebbles. *MNRAS*, 469(Suppl_2):

S755–S773, July 2017. ISSN 0035-8711. doi: 10.1093/mnras/stx2741. URL https://academic.oup.com/mnras/article/469/Suppl_2/S755/4564447. Publisher: Oxford Academic.

D Bockelée-Morvan, Gianrico Filacchione, Kathrin Altwegg, Eleonora Bianchi, Martin Bizzarro, Jürgen Blum, Lydie Bonal, Fabrizio Capaccioni, Mathieu Choukroun, Claudio Codella, et al. Ambition–comet nucleus cryogenic sample return. *Experimental astronomy*, pages 1–52, 2021.

Jean-David Bodénan, Clément Surville, Judit Szulágyi, Lucio Mayer, and Maria Schönbächler. Can chondrules be produced by the interaction of Jupiter with the protosolar disk? *ApJ*, 901(1):60, September 2020. ISSN 1538-4357. doi: 10.3847/1538-4357/abaef2. URL http://arxiv.org/abs/1912.09732. arXiv: 1912.09732.

H. Boehnhardt, S. Bagnulo, K. Muinonen, M. A. Barucci, L. Kolokolova, E. Dotto, and G. P. Tozzi. Surface characterization of 28978 Ixion (2001 KX). *A&A*, 415(2):L21–L25, February 2004. ISSN 0004-6361, 1432-0746. doi: 10.1051/0004-6361:20040005. URL https://www.aanda.org/articles/aa/abs/2004/08/aafk211/aafk211.html. Number: 2 Publisher: EDP Sciences.

H Boehnhardt, GP Tozzi, S Bagnulo, Karri Muinonen, A Nathues, and L Kolokolova. Photometry and polarimetry of the nucleus of comet 2p/encke. *Astronomy & Astrophysics*, 489 (3):1337–1343, 2008.

R. van Boekel, L. B. F. M. Waters, C. Dominik, J. Bouwman, A. de Koter, C. P. Dullemond, and F. Paresce. Grain growth in the inner regions of Herbig Ae/Be star disks. *A&A*, 400(3): L21–L24, March 2003. ISSN 0004-6361, 1432-0746. doi: 10.1051/0004-6361:20030141. URL https://www.aanda.org/articles/aa/abs/2003/12/aaei191/aaei191.html. Number: 3 Publisher: EDP Sciences.

T Bogdan, C Pillich, J Landers, H Wende, and G Wurm. Drifting inwards in protoplanetary discs i sticking of chondritic dust at increasing temperatures. *Astronomy & Astrophysics*, 638:A151, 2020.

J. Bouwman, G. Meeus, A. de Koter, S. Hony, C. Dominik, and L. B. F. M. Waters. Processing of silicate dust grains in Herbig Ae/Be systems. *A&A*, 375(3):950–962, September 2001. ISSN 0004-6361, 1432-0746. doi: 10.1051/0004-6361:20010878. URL https://www.aanda.org/articles/aa/abs/2001/33/aah2674/aah2674.html. Number: 3 Publisher: EDP Sciences.

CJ Braak, JF De Haan, JW Hovenier, and LD Travis. Galileo photopolarimetry of jupiter at 678.5 nm. *Icarus*, 157(2):401–418, 2002.

Daniel T Britt, Kevin M Cannon, Kerri Donaldson Hanna, Joanna Hogancamp, Olivier Poch, Pierre Beck, Dayl Martin, Jolantha Escrig, Lydie Bonal, and Philip T Metzger. Simulated asteroid materials based on carbonaceous chondrite mineralogies. *Meteoritics & Planetary Science*, 54(9):2067–2082, 2019.

Michael E Brown. The 3–4 μm spectra of jupiter trojan asteroids. *The Astronomical Journal*, 152(6):159, 2016.

Don Brownlee, Peter Tsou, Jérôme Aléon, Conel M O'D Alexander, Tohru Araki, Sasa Bajt, Giuseppe A Baratta, Ron Bastien, Phil Bland, Pierre Bleuet, et al. Comet 81p/wild 2 under a microscope. *science*, 314(5806):1711–1716, 2006.

Thomas H Burbine, Michael J Gaffey, and Jeffrey F Bell. S-asteroids 387 aquitania and 980 anacostia: Possible fragments of the breakup of a spinel-bearing parent body with c03/cv3 affinities. *Meteoritics*, 27(4):424–434, 1992.

Schelte J Bus, Faith Vilas, and M Antonietta Barucci. Visible-wavelength spectroscopy of asteroids. *Asteroids III*, 1:169–182, 2002.

Humberto Campins, Kelsey Hargrove, Noemi Pinilla-Alonso, Ellen S Howell, Michael S Kelley, Javier Licandro, T Mothé-Diniz, Y Fernández, and Julie Ziffer. Water ice and organics on the surface of the asteroid 24 themis. *Nature*, 464(7293):1320–1321, 2010.

Kevin M Cannon, Daniel T Britt, Trent M Smith, Ralph F Fritsche, and Daniel Batcheldor. Mars global simulant mgs-1: A rocknest-based open standard for basaltic martian regolith simulants. *Icarus*, 317:470–478, 2019.

FG Carrozzo, G Bellucci, F Altieri, E D'aversa, and J-P Bibring. Mapping of water frost and ice at low latitudes on mars. *Icarus*, 203(2):406–420, 2009.

JH Castro-Chacón, R Gil-Hutton, J Ramírez Vélez, and M Reyes-Ruiz. Polarimetric rotational curve of m-type asteroid (16) psyche. *Planetary and Space Science*, 213:105428, 2022.

A Cellino, IN Belskaya, Ph Bendjoya, M Di Martino, R Gil-Hutton, Karri Muinonen, and EF Tedesco. The strange polarimetric behavior of asteroid (234) barbara. *Icarus*, 180(2): 565–567, 2006.

A. Cellino, E. Ammannito, G. Magni, R. Gil-Hutton, E. F. Tedesco, I. N. Belskaya, M. C. De Sanctis, S. Schröder, F. Preusker, and A. Manara. The Dawn exploration of (4) Vesta as the 'ground truth' to interpret asteroid polarimetry. *Monthly Notices of the Royal Astronomical Society*, 456(1):248–262, 12 2015a. ISSN 0035-8711. doi: 10.1093/mnras/stv2683. URL https://doi.org/10.1093/mnras/stv2683.

Alberto Cellino, Ricardo Gil-Hutton, and Irina Belskaya. Asteroids. In Anny-Chantal Levasseur-Regourd, James Hough, and Ludmilla Kolokolova, editors, *Polarimetry of Stars and Planetary Systems*, pages 360–378. Cambridge University Press, Cambridge, 2015b. ISBN 978-1-107-04390-9. doi: 10.1017/CBO9781107358249.021. URL https://www.cambridge.org/core/books/polarimetry-of-stars-and-planetary-systems/asteroids/9EE5970462DD0D283F6A861B4DA60298.

Alberto Cellino, S Bagnulo, IN Belskaya, and AA Christou. Unusual polarimetric properties of (101955) bennu: similarities with f-class asteroids and cometary bodies. *Monthly Notices of the Royal Astronomical Society: Letters*, 481(1):L49–L53, 2018.

Romain Cerubini. *Spectrophotometry of salty ices with implications for the surfaces of icy moons*. PhD thesis, University of Bern, 2021.

Romain Cerubini, Antoine Pommerol, Zuriñe Yoldi, and Nicolas Thomas. Near-infrared reflectance spectroscopy of sublimating salty ice analogues. implications for icy moons. *Planetary and space science*, 211:105391, 2022.

Clark R Chapman. S-type asteroids, ordinary chondrites, and space weathering: The evidence from galileo's fly-bys of gaspra and ida. *Meteoritics & Planetary Science*, 31(6):699–725, 1996.

Mauro Ciarniello, Marco Fulle, Andrea Raponi, Gianrico Filacchione, Fabrizio Capaccioni, Alessandra Rotundi, Giovanna Rinaldi, Michelangelo Formisano, Gianfranco Magni, Federico Tosi, et al. Macro and micro structures of pebble-made cometary nuclei reconciled by seasonal evolution. *Nature Astronomy*, 6(5):546–553, 2022.

Roger N Clark. The spectral reflectance of water-mineral mixtures at low temperatures. *Journal of Geophysical Research: Solid Earth*, 86(B4):3074–3086, 1981.

D Clarke and SR Fullerton. The sun as a polarimetric variable star. *Astronomy and Astrophysics*, 310:331–340, 1996.

David L Coffeen. Optical polarimeters in space. In *Colloquium on the Planets, stars and nebulae studied with photopolarimetry*, 1974.

James N Connelly, Martin Bizzarro, Alexander N Krot, Åke Nordlund, Daniel Wielandt, and Marina A Ivanova. The absolute chronology and thermal processing of solids in the solar protoplanetary disk. *Science*, 338(6107):651–655, 2012.

Maria Cristina De Sanctis, FABRIZIO Capaccioni, Mauro Ciarniello, GIANRICO Filacchione, Michelangelo Formisano, S Mottola, Andrea Raponi, Federico Tosi, D Bockelée-Morvan, S Erard, et al. The diurnal cycle of water ice on comet 67p/churyumov–gerasimenko. *Nature*, 525(7570):500–503, 2015a.

Maria Cristina De Sanctis, FABRIZIO Capaccioni, Mauro Ciarniello, GIANRICO Filacchione, Michelangelo Formisano, S Mottola, Andrea Raponi, Federico Tosi, D Bockelée-Morvan, S Erard, et al. The diurnal cycle of water ice on comet 67p/churyumov–gerasimenko. *Nature*, 525(7570):500–503, 2015b.

AC Delsanti, H Boehnhardt, L Barrera, KJ Meech, T Sekiguchi, and OR Hainaut. Photometry of 27 kuiper belt objects with eso/very large telescope. *Astronomy & Astrophysics*, 380(1): 347–358, 2001.

Francesca E DeMeo, Richard P Binzel, Stephen M Slivan, and Schelte J Bus. An extension of the bus asteroid taxonomy into the near-infrared. *Icarus*, 202(1):160–180, 2009.

Francesca E. DeMeo, Conel M. O'D Alexander, Kevin J. Walsh, Clark R. Chapman, and Richard P. Binzel. The Compositional Structure of the Asteroid Belt. *arXiv:1506.04805 [astro-ph]*, 2015. doi: 10.2458/azu_uapress_9780816532131-ch002. URL http://arxiv.org/abs/1506.04805. arXiv: 1506.04805.

M. Devogèle, P. Tanga, A. Cellino, Ph Bendjoya, J.-P. Rivet, J. Surdej, D. Vernet, J. M. Sunshine, S. J. Bus, L. Abe, S. Bagnulo, G. Borisov, H. Campins, B. Carry, J. Licandro, W. McLean, and N. Pinilla-Alonso. New polarimetric and spectroscopic evidence of

anomalous enrichment in spinel-bearing Calcium-Aluminium-rich Inclusions among L-type asteroids. *Icarus*, 304:31–57, April 2018a. ISSN 00191035. doi: 10.1016/j.icarus.2017.12.026. URL http://arxiv.org/abs/1802.06975. arXiv: 1802.06975.

M. Devogèle, P. Tanga, A. Cellino, Ph. Bendjoya, J. P. Rivet, J. Surdej, D. Vernet, J. M. Sunshine, S. J. Bus, L. Abe, S. Bagnulo, G. Borisov, H. Campins, B. Carry, J. Licandro, W. McLean, and N. Pinilla-Alonso. New polarimetric and spectroscopic evidence of anomalous enrichment in spinel-bearing calcium-aluminium-rich inclusions among L-type asteroids. *Icarus*, 304:31–57, April 2018b. ISSN 0019-1035. doi: 10.1016/j.icarus.2017.12.026. URL https://www.sciencedirect.com/science/article/pii/S0019103517300271.

Zh M Dlugach and MI Mishchenko. Coherent backscattering and opposition effects observed in some atmosphereless bodies of the solar system. *Solar System Research*, 47(6):454–462, 2013.

A Dollfus, M Wolff, JE Geake, DF Lupishko, and LM Dougherty. Photopolarimetry of asteroids. *Asteroids Ii*, pages 594–616, 1989.

Audouin Dollfus. Étude des planètes par la polarisation de leur lumière. *Supplements aux Annales d'Astrophysique*, 4:3–114, 1957.

Audouin Dollfus. Lunar surface imaging polarimetry: I. roughness and grain size. *Icarus*, 136 (1):69–103, 1998.

C. Dominik and A. G. G. M. Tielens. The Physics of Dust Coagulation and the Structure of Dust Aggregates in Space. *ApJ*, 480(2):647–673, May 1997. ISSN 0004-637X, 1538-4357. doi: 10.1086/303996. URL https://iopscience.iop.org/article/10.1086/303996.

BT Draine. On the submillimeter opacity of protoplanetary disks. *The Astrophysical Journal*, 636(2):1114, 2006.

J. Drążkowska and Y. Alibert. Planetesimal formation starts at the snow line. *A&A*, 608: A92, December 2017. ISSN 0004-6361, 1432-0746. doi: 10.1051/0004-6361/201731491. URL http://www.aanda.org/10.1051/0004-6361/201731491.

J. Escobar-Cerezo, O. Muñoz, F. Moreno, D. Guirado, J. C. Gómez Martín, J. D. Goguen, E. J. Garboczi, A. N. Chiaramonti, T. Lafarge, and R. A. West. An Experimental Scattering Matrix for Lunar Regolith Simulant JSC-1A at Visible Wavelengths. *ApJS*, 235(1):19, March 2018. ISSN 0067-0049. doi: 10.3847/1538-4365/aaa6cc. URL https://doi.org/10.3847/1538-4365/aaa6cc. Publisher: American Astronomical Society.

Clement Feller, Antoine Pommerol, and Bastian Gundlach. Photometric and spectrophotometric measurements of the cophylab dust mixtures. In *European Planetary Science Congress*, pages EPSC2020–753, 2020.

Gianrico Filacchione, Olivier Groussin, Clémence Herny, David Kappel, Stefano Mottola, Nilda Oklay, Antoine Pommerol, Ian Wright, Zurine Yoldi, Mauro Ciarniello, et al. Comet 67p/cg nucleus composition and comparison to other comets. *Space science reviews*, 215 (1):1–46, 2019.

George J Flynn, Sue Wirick, and Lindsay P Keller. Organic grain coatings in primitive interplanetary dust particles: Implications for grain sticking in the solar nebula. *Earth, Planets and Space*, 65(10):1159–1166, 2013.

Sonia Fornasier, Pedro Henrique Hasselmann, MA Barucci, C Feller, S Besse, C Leyrat, L Lara, Pedro J Gutiérrez, Nilda Oklay, Cécilia Tubiana, et al. Spectrophotometric properties of the nucleus of comet 67p/churyumov-gerasimenko from the osiris instrument onboard the rosetta spacecraft. *Astronomy & Astrophysics*, 583:A30, 2015.

Sonia Fornasier, S Mottola, Horst Uwe Keller, MA Barucci, B Davidsson, Clement Feller, JDP Deshapriya, H Sierks, C Barbieri, PL Lamy, et al. Rosetta's comet 67p/churyumov-gerasimenko sheds its dusty mantle to reveal its icy nature. *Science*, 354(6319):1566–1570, 2016.

Sonia Fornasier, Clément Feller, Pedro H Hasselmann, Maria Antonella Barucci, J Sunshine, J-B Vincent, Xian Shi, Holger Sierks, Giampiero Naletto, PL Lamy, et al. Surface evolution of the anhur region on comet 67p/churyumov-gerasimenko from high-resolution osiris images. *Astronomy & Astrophysics*, 630:A13, 2019.

Sonia Fornasier, J Bourdelle de Micas, Pedro H Hasselmann, HV Hoang, Maria Antonietta Barucci, and Holger Sierks. Small lobe of comet 67p: Characterization of the wosret region with rosetta-osiris. *Astronomy & Astrophysics*, 653:A132, 2021.

Sonia Fornasier, Eric Quirico, et al. Extensive catalogue of exposures of volatiles on 67p/churyumov-gerasimenko comet nucleus revealed from the osiris cameras onboard the rosetta mission. Technical report, Copernicus Meetings, 2022.

Elisa Frattin, Olga Muñoz, Fernando Moreno, Jacopo Nava, Jesús Escobar-Cerezo, Juan Carlos Gomez Martin, Daniel Guirado, Alberto Cellino, Patrice Coll, Francois Raulin, Ivano Bertini, Gabriele Cremonese, Monica Lazzarin, Giampiero Naletto, and Fiorangela La Forgia. Experimental phase function and degree of linear polarization of cometary dust analogs. *Monthly Notices of the Royal Astronomical Society*, 484(2):2198–2211, April 2019. ISSN 0035-8711, 1365-2966. doi: 10.1093/mnras/stz129. URL http://arxiv.org/abs/1901.05975. arXiv: 1901.05975.

Marco Fulle, V. Della Corte, A. Rotundi, F. J. M. Rietmeijer, S. F. Green, P. Weissman, M. Accolla, L. Colangeli, M. Ferrari, S. Ivanovski, J. J. Lopez-Moreno, E. Mazzotta Epifani, R. Morales, J. L. Ortiz, E. Palomba, P. Palumbo, J. Rodriguez, R. Sordini, and V. Zakharov. Comet 67P/Churyumov–Gerasimenko preserved the pebbles that formed planetesimals. *MNRAS*, 462(Suppl 1):S132–S137, November 2016. ISSN 0035-8711, 1365-2966. doi: 10.1093/mnras/stw2299. URL https://academic.oup.com/mnras/article-lookup/doi/10.1093/mnras/stw2299.

Anthony J L Garcia and Jean-François Gonzalez. Evolution of porous dust grains in protoplanetary discs – I. Growing grains. *MNRAS*, 493(2):1788–1800, April 2020. ISSN 0035-8711, 1365-2966. doi: 10.1093/mnras/staa382. URL https://academic.oup.com/mnras/article/493/2/1788/5731863.

Sabrina Gärtner, Bastian Gundlach, Thomas F Headen, Judy Ratte, Joachim Oesert,

Stanislav N Gorb, Tristan GA Youngs, Daniel T Bowron, Jürgen Blum, and Helen J Fraser. Micrometer-sized water ice particles for planetary science experiments: influence of surface structure on collisional properties. *The Astrophysical Journal*, 848(2):96, 2017.

R. Gil-Hutton and E. García-Migani. Polarimetric survey of main-belt asteroids - VI. New results from the second epoch of the CASLEO survey. *A&A*, 607:A103, November 2017. ISSN 0004-6361, 1432-0746. doi: 10.1051/0004-6361/201731388. URL https://www.aanda.org/articles/aa/abs/2017/11/aa31388-17/aa31388-17.html. Publisher: EDP Sciences.

J. F. Gonzalez, G. Laibe, S. T. Maddison, C. Pinte, and F. Ménard. The accumulation and trapping of grains at planet gaps: Effects of grain growth and fragmentation. , 116: 48–56, October 2015. ISSN 0032-0633. doi: 10.1016/j.pss.2015.05.018. URL http://www.sciencedirect.com/science/article/pii/S0032063315001634.

Yevgen Grynko, Yuriy Shkuratov, Samer Alhaddad, and Jens Förstner. Negative polarization of light at backscattering from a numerical analog of planetary regoliths. *Icarus*, page 115099, 2022.

B Gundlach and J Blum. The stickiness of micrometer-sized water-ice particles. *The Astrophysical Journal*, 798(1):34, 2014a.

B. Gundlach and J. Blum. THE STICKINESS OF MICROMETER-SIZED WATER-ICE PARTICLES. *ApJ*, 798(1):34, December 2014b. ISSN 0004-637X. doi: 10.1088/0004-637X/798/1/34. URL https://doi.org/10.1088%2F0004-637x%2F798%2F1%2F34. Publisher: IOP Publishing.

B Gundlach, KP Schmidt, C Kreuzig, D Bischoff, F Rezaei, S Kothe, J Blum, B Grzesik, and E Stoll. The tensile strength of ice and dust aggregates and its dependence on particle properties. *Monthly Notices of the Royal Astronomical Society*, 479(1):1273–1277, 2018.

Prithish Halder, Parizath Deb Roy, and Himadri Sekhar Das. Dependence of light scattering properties on porosity, size and composition of dust aggregates. *Icarus*, 312:45–60, September 2018. ISSN 0019-1035. doi: 10.1016/j.icarus.2018.04.026. URL https://www.sciencedirect.com/science/article/pii/S0019103517308242.

Bruce Hapke. *Theory of Reflectance and Emittance Spectroscopy*. Topics in Remote Sensing. Cambridge University Press, Cambridge, 1993. doi: 10.1017/CBO9780511524998. URL https://www.cambridge.org/core/books/theory-of-reflectance-and-emittance-spectroscopy/4DE2B656DD8CCD9F75F12C66128D83D2.

D. R Haynes, N. J. Tro, and S. M. George. Condensation and evaporation of H2O on ice surfaces. *J. phys. chem. (1952)*, 96(21):8502–8509, 1992. ISSN 0022-3654. Place: Washington, DC Publisher: American Chemical Society.

Alain Herique, Wlodek Kofman, S Zine, J Blum, J-B Vincent, and Valérie Ciarletti. Homogeneity of 67p/churyumov-gerasimenko as seen by consert: implication on composition and formation. *Astronomy & Astrophysics*, 630:A6, 2019.

Kazuaki A Homma, Satoshi Okuzumi, Taishi Nakamoto, and Yuta Ueda. Rocky planetesimal formation aided by organics. *The Astrophysical Journal*, 877(2):128, 2019.

Ryuki Hyodo, Tristan Guillot, Shigeru Ida, Satoshi Okuzumi, and Andrew N. Youdin. Planetesimal formation around the snow line. II. Dust or pebbles? *A&A*, 646:A14, February 2021. ISSN 0004-6361, 1432-0746. doi: 10.1051/0004-6361/202039894. URL http://arxiv.org/abs/2012.06700. arXiv: 2012.06700.

S. Ida, T. Guillot, and A. Morbidelli. The radial dependence of pebble accretion rates: A source of diversity in planetary systems: I. Analytical formulation. *A&A*, 591:A72, July 2016. ISSN 0004-6361, 1432-0746. doi: 10.1051/0004-6361/201628099. URL http://www.aanda.org/10.1051/0004-6361/201628099.

Laura T Iraci, Bruce D Phebus, Bradley M Stone, and Anthony Colaprete. Water ice cloud formation on mars is more difficult than presumed: Laboratory studies of ice nucleation on surrogate materials. *Icarus*, 210(2):985–991, 2010.

Simon M. Iveson, James D. Litster, Karen Hapgood, and Bryan J. Ennis. Nucleation, growth and breakage phenomena in agitated wet granulation processes: a review. *Powder Technol.*, 117(1):3–39, June 2001. ISSN 0032-5910. doi: 10.1016/S0032-5910(01)00313-8. URL http://www.sciencedirect.com/science/article/pii/S0032591001003138.

David Jewitt. Looking through the hippo: Nucleus and dust in comet 2p/encke. *The Astronomical Journal*, 128(6):3061, 2004.

David Jewitt and Aurelie Guilbert-Lepoutre. Limits to ice on asteroids (24) themis and (65) cybele. *The Astronomical Journal*, 143(1):21, 2011.

A. Johansen and A. Youdin. Protoplanetary Disk Turbulence Driven by the Streaming Instability: Nonlinear Saturation and Particle Concentration. *ApJ*, 662(1):627–641, June 2007. ISSN 0004-637X. doi: 10.1086/516730. URL https://doi.org/10.1086%2F516730.

Anders Johansen and Pedro Lacerda. Prograde rotation of protoplanets by accretion of pebbles in a gaseous environment. *Monthly Notices of the Royal Astronomical Society*, 404(1):475–485, 2010.

Anders Johansen, Jeffrey S Oishi, Mordecai-Mark Mac Low, Hubert Klahr, Thomas Henning, and Andrew Youdin. Rapid planetesimal formation in turbulent circumstellar disks. *Nature*, 448(7157):1022–1025, 2007.

Christopher M Johns-Krull, Jacob N McLane, L Prato, Christopher J Crockett, Daniel T Jaffe, Patrick M Hartigan, Charles A Beichman, Naved I Mahmud, Wei Chen, BA Skiff, et al. A candidate young massive planet in orbit around the classical t tauri star ci tau. *The Astrophysical Journal*, 826(2):206, 2016.

Kenneth L Jones, Raymond E Arvidson, Edward A Guinness, Susan L Bragg, Stephen D Wall, Carl E Carlston, and Deborah G Pidek. One mars year: Viking lander imaging observations. *Science*, 204(4395):799–806, 1979.

Martin Jutzi, Patrick Michel, Kensuke Hiraoka, Akiko M. Nakamura, and Willy Benz. Numerical simulations of impacts involving porous bodies: Ii. comparison with labora-

tory experiments. *Icarus*, 201(2):802–813, 2009. ISSN 0019-1035. doi: https://doi.org/10.1016/j.icarus.2009.01.018. URL https://www.sciencedirect.com/science/article/pii/S0019103509000360.

S Keihm, F Tosi, L Kamp, F Capaccioni, S Gulkis, D Grassi, M Hofstadter, G Filacchione, S Lee, S Giuppi, et al. Interpretation of combined infrared, submillimeter, and millimeter thermal flux data obtained during the rosetta fly-by of asteroid (21) lutetia. *Icarus*, 221(1): 395–404, 2012.

Lindsay P Keller and David S McKay. The nature and origin of rims on lunar soil grains. *Geochimica et Cosmochimica Acta*, 61(11):2331–2341, 1997.

James C Kemp, GD Henson, CT Steiner, and ER Powell. The optical polarization of the sun measured at a sensitivity of parts in ten million. *Nature*, 326(6110):270–273, 1987.

Hugh H Kieffer. *Near infrared spectral reflectance of simulated Martian frosts*. PhD thesis, California Institute of Technology, 1968.

Nikolai Kiselev, Vera Rosenbush, Klaus Jockers, Sergey Velichko, and Sen Kikuchi. Database of comet polarimetry: analysis and some results. *Earth, Moon, and Planets*, 97(3):365–378, 2005.

Nikolai Kiselev, Vera Rosenbush, Anny-Chantal Levasseur-Regourd, and Ludmilla Kolokolova. Comets, May 2015. URL https://www.cambridge.org/core/books/polarimetry-of-stars-and-planetary-systems/comets/A17E3383B7187BBBB77D3CA876A2DA34. Pages: 379-404 Publisher: Cambridge University Press.

Dora Klindžić, Daphne M Stam, Frans Snik, CU Keller, HJ Hoeijmakers, DM van Dam, M Willebrands, T Karalidi, V Pallichadath, CN van Dijk, et al. Loupe: observing earth from the moon to prepare for detecting life on earth-like exoplanets. *Philosophical Transactions of the Royal Society A*, 379(2188):20190577, 2021.

Kirk Knobelspiesse, Brian Cairns, Michael Mishchenko, Jacek Chowdhary, Kostas Tsigaridis, Bastiaan van Diedenhoven, William Martin, Matteo Ottaviani, and Mikhail Alexandrov. Analysis of fine-mode aerosol retrieval capabilities by different passive remote sensing instrument designs. *Optics express*, 20(19):21457–21484, 2012.

Martin Knudsen. Die Gesetze der Molekularströmung und der inneren Reibungsströmung der Gase durch Röhren. *Annalen der Physik*, 333(1):75–130, 1909. ISSN 1521-3889. doi: 10.1002/andp.19093330106. URL https://onlinelibrary.wiley.com/doi/abs/10.1002/andp.19093330106. _eprint: https://onlinelibrary.wiley.com/doi/pdf/10.1002/andp.19093330106.

W. Kofman, A. Herique, Y. Barbin, J.-P. Barriot, V. Ciarletti, S. Clifford, P. Edenhofer, C. Elachi, C. Eyraud, J.-P. Goutail, E. Heggy, L. Jorda, J. Lasue, A.-C. Levasseur-Regourd, E. Nielsen, P. Pasquero, F. Preusker, P. Puget, D. Plettemeier, Y. Rogez, H. Sierks, C. Statz, H. Svedhem, I. Williams, S. Zine, and J. Van Zyl. Properties of the 67P/Churyumov-Gerasimenko interior revealed by CONSERT radar. *Science*, 349(6247):aab0639–aab0639,

July 2015. ISSN 0036-8075, 1095-9203. doi: 10.1126/science.aab0639. URL https://www.sciencemag.org/lookup/doi/10.1126/science.aab0639.

Ludmilla Kolokolova, Elena Petrova, and Hiroshi Kimura. Effects of interaction of electromagnetic waves in complex particles. *Electromagnetic waves*, pages 173–202, 2011.

Akira Kouchi, Tatsuyuki Kudo, Hideyuki Nakano, Masahiko Arakawa, Naoki Watanabe, Siniti Sirono, Michiya Higa, and Norikazu Maeno. Rapid growth of asteroids owing to very sticky interstellar organic grains. *The Astrophysical Journal*, 566(2):L121, 2002.

T Kudo, A Kouchi, M Arakawa, and H Nakano. The role of sticky interstellar organic material in the formation of asteroids. *Meteoritics & Planetary Science*, 37(12):1975–1983, 2002.

Motoi Kumai. Hexagonal and cubic ice at low temperatures. *Journal of Glaciology*, 7(49): 95–108, 1968.

Michael Küppers, Horst Uwe Keller, Ekkehard Kührt, Michael F A'Hearn, Kathrin Altwegg, Régis Bertrand, Henner Busemann, Maria Teresa Capria, Luigi Colangeli, Björn Davidsson, et al. Triple f—a comet nucleus sample return mission. *Experimental Astronomy*, 23(3): 809–847, 2009.

Michiel Lambrechts and Anders Johansen. Rapid growth of gas-giant cores by pebble accretion. *A&A*, 544:A32, August 2012. ISSN 0004-6361, 1432-0746. doi: 10.1051/0004-6361/201219127. URL http://arxiv.org/abs/1205.3030. arXiv: 1205.3030.

C Lantz, R Brunetto, MA Barucci, S Fornasier, D Baklouti, J Bourçois, and M Godard. Ion irradiation of carbonaceous chondrites: A new view of space weathering on primitive asteroids. *Icarus*, 285:43–57, 2017.

A-C Levasseur-Regourd, J-L Bertaux, JM Le Blanc, JL Weinberg, F Giovane, R Dumont, M Festou, RH Giese, P Lamy, and A Llebaria. In-situ photopolarimetric measurements of dust and gas in the coma of halley's comet. *Advances in Space Research*, 5(12):197–199, 1985.

A-Chantal Levasseur-Regourd et al. Polarization of light scattered by cometary dust particles: observations and tentative interpretations. *Space Science Reviews*, 90(1):163–168, 1999.

AC Levasseur-Regourd, B Goidet, T Le Duin, C Malique, JB Renard, and JL Bertaux. Optical probing of dust in comet grigg-skjellerup from the giotto spacecraft. *Planetary and space science*, 41(2):167–169, 1993.

Anny-Chantal Levasseur-Regourd, Jessica Agarwal, Hervé Cottin, Cécile Engrand, George Flynn, Marco Fulle, Tamas Gombosi, Yves Langevin, Jérémie Lasue, Thurid Mannel, et al. Cometary dust. *Space science reviews*, 214(3):1–56, 2018a.

Anny-Chantal Levasseur-Regourd, Jessica Agarwal, Hervé Cottin, Cécile Engrand, George Flynn, Marco Fulle, Tamas Gombosi, Yves Langevin, Jérémie Lasue, Thurid Mannel, Sihane Merouane, Olivier Poch, Nicolas Thomas, and Andrew Westphal. Cometary Dust. *Space Sci Rev*, 214(3):64, March 2018b. ISSN 1572-9672. doi: 10.1007/s11214-018-0496-3. URL https://doi.org/10.1007/s11214-018-0496-3.

Jian-Yang Li, Michael F A'Hearn, Michael JS Belton, Christopher J Crockett, Tony L Farnham, Carey M Lisse, Lucy A McFadden, Karen J Meech, Jessica M Sunshine, Peter C Thomas, et al. Deep impact photometry of comet 9p/tempel 1. *Icarus*, 187(1):41–55, 2007.

Jian-Yang Li, Sébastien Besse, Michael F A'Hearn, Michael JS Belton, Dennis Bodewits, Tony L Farnham, Kenneth P Klaasen, Carey M Lisse, Karen J Meech, Jessica M Sunshine, et al. Photometric properties of the nucleus of comet 103p/hartley 2. *Icarus*, 222(2): 559–570, 2013.

J Licandro, H Campins, GP Tozzi, J De Léon, N Pinilla-Alonso, H Boehnhardt, and OR Hainaut. Testing the comet nature of main belt comets. the spectra of 133p/elst-pizarro and 176p/linear. *Astronomy & Astrophysics*, 532:A65, 2011.

Yunfeng Lv and Zhongqiu Sun. The reflectance and negative polarization of light scattered from snow surfaces with different grain size in backward direction. *Journal of Quantitative Spectroscopy and Radiative Transfer*, 133:472–481, 2014.

Thurid Mannel, Mark Stephen Bentley, PD Boakes, Harald Jeszenszky, Pascale Ehrenfreund, Cecile Engrand, Christian Koeberl, Anny Chantal Levasseur-Regourd, Jens Romstedt, Roland Schmied, et al. Dust of comet 67p/churyumov-gerasimenko collected by rosetta/midas: classification and extension to the nanometer scale. *Astronomy & Astrophysics*, 630:A26, 2019.

Abraham Marmur. The Lotus Effect: Superhydrophobicity and Metastability. *Langmuir*, 20(9):3517–3519, April 2004. ISSN 0743-7463. doi: 10.1021/la036369u. URL https://doi.org/10.1021/la036369u. Publisher: American Chemical Society.

Raphael Marschall, Nicolas Thomas, Stephan Ulamec, Stubbe Hviid, Stefano Mottola, Jean-Baptiste Vincent, Francesca Ferri, Alain Herique, Dirk Plettemeier, Ákos Kereszturi, et al. Origo-an esa m-class mission proposal to challenge planetesimal formation theories. In *European Planetary Science Congress*, pages EPSC2022–1127, 2022.

Michaël Marsset, Miroslav Brož, Pierre Vernazza, Alexis Drouard, Julie Castillo-Rogez, Josef Hanuš, Matti Viikinkoski, Nicolas Rambaux, Benoît Carry, Laurent Jorda, et al. The violent collisional history of aqueously evolved (2) pallas. *Nature Astronomy*, 4(6):569–576, 2020.

Joseph Masiero, Christine Hartzell, and Daniel J. Scheeres. The Effect of the Dust Size Distribution on Asteroid Polarization. *The Astronomical Journal*, 138:1557–1562, December 2009. ISSN 0004-6256. doi: 10.1088/0004-6256/138/6/1557. URL https://ui.adsabs.harvard.edu/abs/2009AJ....138.1557M. ADS Bibcode: 2009AJ....138.1557M.

Colin P. McNally, Alexander Hubbard, Chao-Chin Yang, and Mordecai-Mark Mac Low. Temperature Fluctuations driven by Magnetorotational Instability in Protoplanetary Disks. *ApJ*, 791(1):62, July 2014. ISSN 0004-637X, 1538-4357. doi: 10.1088/0004-637X/791/1/62. URL http://arxiv.org/abs/1406.5195. arXiv: 1406.5195.

Thorsten Meisner, G Wurm, and J Teiser. Experiments on centimeter-sized dust aggregates and their implications for planetesimal formation. *Astronomy & Astrophysics*, 544:A138, 2012.

Patrick Michel, Francesca E DeMeo, and William F Bottke. *Asteroids iv*. University of Arizona Press, 2015.

Michael I Mishchenko, Janna M Dlugach, Li Liu, Vera K Rosenbush, Nikolai N Kiselev, and Yuri G Shkuratov. Direct solutions of the maxwell equations explain opposition phenomena observed for high-albedo solar system objects. *The Astrophysical Journal*, 705(2):L118, 2009.

A. Morbidelli, M. Lambrechts, S. Jacobson, and B. Bitsch. The great dichotomy of the Solar System: small terrestrial embryos and massive giant planet cores. *Icarus*, 258:418–429, September 2015a. ISSN 00191035. doi: 10.1016/j.icarus.2015.06.003. URL http://arxiv.org/abs/1506.01666. arXiv: 1506.01666.

Alessandro Morbidelli, Kevin J Walsh, David P O'Brien, David A Minton, and William F Bottke. The dynamical evolution of the asteroid belt. *arXiv preprint arXiv:1501.06204*, 2015b.

K Muinonen, G Videen, E Zubko, and Yu Shkuratov. Numerical techniques for backscattering by random media. In *Optics of cosmic dust*, pages 261–282. Springer, 2002.

Karri Muinonen, Jani Tyynelä, Evgenij Zubko, Hannakaisa Lindqvist, Antti Penttilä, and Gorden Videen. Polarization of light backscattered by small particles. *Journal of Quantitative Spectroscopy and Radiative Transfer*, 112(13):2193–2212, 2011.

Karri Olavi Muinonen. *Light scattering by inhomogeneous media: Backward enhancement and reversal of linear polarization.* PhD thesis, University of Helsinki, 1990.

Grzegorz Musiolik and Gerhard Wurm. Contacts of Water Ice in Protoplanetary Disks—Laboratory Experiments. *ApJ*, 873(1):58, March 2019. ISSN 1538-4357. doi: 10.3847/1538-4357/ab0428. URL http://stacks.iop.org/0004-637X/873/i=1/a=58?key=crossref.28706962f14fc8a0123b1328b0fa55c4.

Grzegorz Musiolik, Jens Teiser, Tim Jankowski, and Gerhard Wurm. Collisions of co2 ice grains in planet formation. *The Astrophysical Journal*, 818(1):16, 2016a.

Grzegorz Musiolik, Jens Teiser, Tim Jankowski, and Gerhard Wurm. Ice grain collisions in comparison: Co2, h2o, and their mixtures. *The Astrophysical Journal*, 827(1):63, 2016b.

O. Muñoz, E. Frattin, T. Jardiel, J. C. Gómez-Martín, F. Moreno, J. L. Ramos, D. Guirado, M. Peiteado, A. C. Caballero, J. Milli, and F. Ménard. Retrieving Dust Grain Sizes from Photopolarimetry: An Experimental Approach. *ApJS*, 256(1):17, September 2021. ISSN 0067-0049. doi: 10.3847/1538-4365/ac0efa. URL https://doi.org/10.3847/1538-4365/ac0efa. Publisher: American Astronomical Society.

Hideyuki Nakano, Akira Kouchi, Shogo Tachibana, and Akira Tsuchiyama. Evaporation of interstellar organic materials in the solar nebula. *The Astrophysical Journal*, 592(2):1252, 2003.

A. Natta, L. Testi, N. Calvet, Th Henning, R. Waters, and D. Wilner. Dust in Proto-Planetary Disks: Properties and Evolution. *arXiv:astro-ph/0602041*, February 2006. URL http://arxiv.org/abs/astro-ph/0602041. arXiv: astro-ph/0602041.

R.M. Nelson, B.W. Hapke, W.D. Smythe, and L.J. Horn. Phase Curves of Selected Particulate Materials: The Contribution of Coherent Backscattering to the Opposition Surge. *Icarus*, 131(1):223–230, 1998. ISSN 0019-1035. doi: 10.1006/icar.1997.5850.

E.Z Noe Dobrea, J.F Bell, M.J Wolff, and K.D Gordon. H2o- and oh-bearing minerals in the martian regolith:: analysis of 1997 observations from hst/nicmos. *Icarus*, 166(1):1–20, 2003. ISSN 0019-1035. doi: https://doi.org/10.1016/S0019-1035(03)00208-2. URL https://www.sciencedirect.com/science/article/pii/S0019103503002082.

C. W. Ormel, M. Spaans, and A. G. G. M. Tielens. Dust coagulation in protoplanetary disks: porosity matters. *A&A*, 461(1):215–232, January 2007. ISSN 0004-6361, 1432-0746. doi: 10.1051/0004-6361:20065949. URL http://www.aanda.org/10.1051/0004-6361:20065949.

CW Ormel and HH Klahr. The effect of gas drag on the growth of protoplanets-analytical expressions for the accretion of small bodies in laminar disks. *Astronomy & Astrophysics*, 520:A43, 2010.

Paul Painter, Neurxida Pulati, Ruveyda Cetiner, Maria Sobkowiak, Gareth Mitchell, and Jonathan Mathews. Dissolution and dispersion of coal in ionic liquids. *Energy & Fuels*, 24 (3):1848–1853, 2010.

C H L Patty, A Pommerol, JG Kuehn, B Demory, and N Thomas. Directional aspects of vegetation linear and circular polarization biosignatures. *Astrobiology*, 22(9), 2022. doi: 10.1089/ast.2021.0156.

CH Lucas Patty, Inge Loes Ten Kate, William B Sparks, and Frans Snik. Remote sensing of homochirality: a proxy for the detection of extraterrestrial life. In *Chiral Analysis*, pages 29–69. Elsevier, 2018.

Martin Pätzold, Thomas P Andert, Matthias Hahn, Jean-Pierre Barriot, Sami W Asmar, Bernd Häusler, Michael K Bird, Silvia Tellmann, Janusz Oschlisniok, and Kerstin Peter. The nucleus of comet 67p/churyumov–gerasimenko–part i: The global view–nucleus mass, mass-loss, porosity, and implications. *Monthly Notices of the Royal Astronomical Society*, 483(2):2337–2346, 2019.

Laurette Piani, Shogo Tachibana, Tetsuya Hama, Hidekazu Tanaka, Yukiko Endo, Iyo Sugawara, Lucile Dessimoulie, Yuki Kimura, Akira Miyake, Junya Matsuno, et al. Evolution of morphological and physical properties of laboratory interstellar organic residues with ultraviolet irradiation. *The Astrophysical Journal*, 837(1):35, 2017.

EV Pitjeva and NP Pitjev. Masses of the main asteroid belt and the kuiper belt from the motions of planets and spacecraft. *Astronomy Letters*, 44(8):554–566, 2018.

O. Poch, R. Cerubini, A. Pommerol, B. Jost, and N. Thomas. Polarimetry of water ice particles providing insights on grain size and degree of sintering on icy planetary surfaces. *Journal of Geophysical Research: Planets*, 123(10):2564–2584, Oct 2018. ISSN 2169-9097. doi: 10.1029/2018je005753. URL http://dx.doi.org/10.1029/2018JE005753.

Olivier Poch, Antoine Pommerol, Bernhard Jost, Nathalie Carrasco, Cyril Szopa, and Nicolas Thomas. Sublimation of ice–tholins mixtures: A morphological and spectro-photometric

study. *Icarus*, 266:288–305, March 2016. ISSN 0019-1035. doi: 10.1016/j.icarus.2015.11.006. URL http://www.sciencedirect.com/science/article/pii/S0019103515005163.

A. Pommerol, B. Jost, O. Poch, M. R. El-Maarry, B. Vuitel, and N. Thomas. The SCITEAS experiment: Optical characterizations of sublimating icy planetary analogues. , 109-110: 106–122, May 2015a. ISSN 0032-0633. doi: 10.1016/j.pss.2015.02.004. URL http://www.sciencedirect.com/science/article/pii/S0032063315000380.

A. Pommerol, B. Jost, O. Poch, Z. Yoldi, Y. Brouet, A. Gracia-Berná, R. Cerubini, A. Galli, P. Wurz, B. Gundlach, J. Blum, N. Carrasco, C. Szopa, and N. Thomas. Experimenting with Mixtures of Water Ice and Dust as Analogues for Icy Planetary Material. *Space Sci. Rev.*, 215(5):37, June 2019a. ISSN 1572-9672. doi: 10.1007/s11214-019-0603-0. URL https://doi.org/10.1007/s11214-019-0603-0.

Antoine Pommerol and Bernard Schmitt. Strength of the h2o near-infrared absorption bands in hydrated minerals: Effects of particle size and correlation with albedo. *Journal of Geophysical Research: Planets*, 113(E10), 2008. doi: https://doi.org/10.1029/2007JE003069. URL https://agupubs.onlinelibrary.wiley.com/doi/abs/10.1029/2007JE003069.

Antoine Pommerol, Nicolas Thomas, Bernhard Jost, P Beck, C Okubo, and AS McEwen. Photometric properties of mars soils analogs. *Journal of Geophysical Research: Planets*, 118(10):2045–2072, 2013.

Antoine Pommerol, Nicholas Thomas, Mohamed Ramy El-Maarry, Maurizio Pajola, Olivier Groussin, A-T Auger, Nilda Oklay, Sonia Fornasier, C Feller, Björn Davidsson, et al. Osiris observations of meter-sized exposures of h2o ice at the surface of 67p/churyumov-gerasimenko and interpretation using laboratory experiments. *Astronomy & Astrophysics*, 583:A25, 2015b.

Antoine Pommerol, Bernhard Jost, O Poch, Z Yoldi, Yann Brouet, A Gracia-Berná, R Cerubini, André Galli, Peter Wurz, B Gundlach, et al. Experimenting with mixtures of water ice and dust as analogues for icy planetary material. *Space science reviews*, 215(5):1–68, 2019b.

Torsten Poppe, Jürgen Blum, and Thomas Henning. Analogous experiments on the stickiness of micron-sized preplanetary dust. *The Astrophysical Journal*, 533(1):454, 2000.

Carolyn C Porco, Robert A West, Steven Squyres, Alfred McEwen, Peter Thomas, Carl D Murray, Anthony Delgenio, Andrew P Ingersoll, Torrence V Johnson, Gerhard Neukum, et al. Cassini imaging science: Instrument characteristics and anticipated scientific investigations at saturn. *Space Science Reviews*, 115(1):363–497, 2004.

Abrar H. Quadery, Baochi D. Doan, William C. Tucker, Adrienne R. Dove, and Patrick K. Schelling. Role of Surface Chemistry in Grain Adhesion and Dissipation during Collisions of Silica Nanograins. *ApJ*, 844(2):105, July 2017. ISSN 0004-637X. doi: 10.3847/1538-4357/aa7890. URL https://doi.org/10.3847/1538-4357/aa7890. Publisher: American Astronomical Society.

Andrea Raponi, Mauro Ciarniello, FABRIZIO Capaccioni, GIANRICO Filacchione, Federico Tosi, MARIA CRISTINA De Sanctis, MT Capria, MA Barucci, ANDREA Longobardo,

Ernesto Palomba, et al. The temporal evolution of exposed water ice-rich areas on the surface of 67p/churyumov–gerasimenko: Spectral analysis. *Monthly Notices of the Royal Astronomical Society*, 462(Suppl_1):S476–S490, 2016.

Vishnu Reddy, Tasha L Dunn, Cristina A Thomas, Nicholas A Moskovitz, and Thomas H Burbine. Mineralogy and surface composition of asteroids. *Asteroids IV*, (2867), 2015.

Marko Riikonen, Mika Sillanpää, Leena Virta, Daniel Sullivan, Jarmo Moilanen, and Ismo Luukkonen. Halo observations provide evidence of airborne cubic ice in the earth's atmosphere. *Applied optics*, 39(33):6080–6085, 2000.

Andrew S Rivkin and Joshua P Emery. Detection of ice and organics on an asteroidal surface. *Nature*, 464(7293):1322–1323, 2010.

Andrew S Rivkin, Humberto Campins, Joshua P Emery, Ellen S Howell, Javier Licandro, Driss Takir, and Faith Vilas. Astronomical observations of volatiles on asteroids. *Asteroids IV*, pages 65–87, 2015.

Katrin Ros and Anders Johansen. Ice condensation as a planet formation mechanism. *Astronomy & Astrophysics*, 552:A137, 2013.

Katrin Ros, Anders Johansen, Ilona Riipinen, and Daniel Schlesinger. Effect of nucleation on icy pebble growth in protoplanetary discs. *A&A*, 629:A65, September 2019. ISSN 0004-6361, 1432-0746. doi: 10.1051/0004-6361/201834331. URL http://arxiv.org/abs/1907.08471. arXiv: 1907.08471.

TL Roush, JB Pollack, FC Witteborn, JD Bregman, and JP Simpson. Ice and minerals on callisto: A reassessment of the reflectance spectra. *Icarus*, 86(2):355–382, 1990.

EE Russell, FG Brown, RA Chandos, WC Fincher, LF Kubel, AA Lacis, and LD Travis. Galileo photopolarimeter/radiometer experiment. *Space science reviews*, 60(1):531–563, 1992.

Etsuko Saito and Sin-iti Sirono. PLANETESIMAL FORMATION BY SUBLIMATION. *ApJ*, 728(1):20, February 2011. ISSN 0004-637X, 1538-4357. doi: 10.1088/0004-637X/728/1/20. URL https://iopscience.iop.org/article/10.1088/0004-637X/728/1/20.

Scott A Sandford, Michel Nuevo, Partha P Bera, and Timothy J Lee. Prebiotic astrochemistry and the formation of molecules of astrobiological interest in interstellar clouds and protostellar disks. *Chemical reviews*, 120(11):4616–4659, 2020.

Caroline A. Schneider, Wayne S. Rasband, and Kevin W. Eliceiri. NIH Image to ImageJ: 25 years of image analysis. *Nature Methods*, 9(7):671–675, July 2012. ISSN 1548-7105. doi: 10.1038/nmeth.2089. URL https://www.nature.com/articles/nmeth.2089. Number: 7 Publisher: Nature Publishing Group.

Djoeke Schoonenberg and Chris W. Ormel. Planetesimal formation near the snowline: in or out? *A&A*, 602:A21, June 2017. ISSN 0004-6361, 1432-0746. doi: 10.1051/0004-6361/201630013. URL http://arxiv.org/abs/1702.02151. arXiv: 1702.02151.

Norbert Schorghofer. Predictions of depth-to-ice on asteroids based on an asynchronous model of temperature, impact stirring, and ice loss. *Icarus*, 276:88–95, 2016.

Norbert Schorghofer and Kenneth S Edgett. Seasonal surface frost at low latitudes on mars. *Icarus*, 180(2):321–334, 2006.

Rainer Schräpler, Jürgen Blum, Sebastiaan Krijt, and Jan-Hendrik Raabe. The physics of protoplanetary dust agglomerates. x. high-velocity collisions between small and large dust agglomerates as a growth barrier. *The Astrophysical Journal*, 853(1):74, 2018.

Ali Seiphoori, Xiao-guang Ma, Paulo E. Arratia, and Douglas J. Jerolmack. Formation of stable aggregates by fluid-assembled solid bridges. *PNAS*, 117(7):3375–3381, February 2020. ISSN 0027-8424, 1091-6490. doi: 10.1073/pnas.1913855117. URL https://www.pnas.org/content/117/7/3375. Publisher: National Academy of Sciences Section: Physical Sciences.

IS Shaban and V Mikulaj. Impact of an anionic surfactant addition on solubility of humic acid in acid-alkaline solutions. *Chem. Papers*, 52:753–755, 1998.

Benjamin NL Sharkey, Vishnu Reddy, Juan A Sanchez, Matthew RM Izawa, and Joshua P Emery. Compositional constraints for lucy mission trojan asteroids via near-infrared spectroscopy. *The Astronomical Journal*, 158(5):204, 2019.

Iu G Shkuratov. A new mechanism for the negative polarization of light scattered by the solid surfaces of cosmic bodies. *Astronomicheskii vestnik*, 23:176–180, 1989.

Yu. Shkuratov, A. Ovcharenko, E. Zubko, O. Miloslavskaya, K. Muinonen, J. Piironen, R. Nelson, W. Smythe, V. Rosenbush, and P. Helfenstein. The Opposition Effect and Negative Polarization of Structural Analogs for Planetary Regoliths. *Icarus*, 159(2): 396–416, October 2002. ISSN 0019-1035. doi: 10.1006/icar.2002.6923. URL https://www.sciencedirect.com/science/article/pii/S001910350296923X.

Yu. Shkuratov, A. Ovcharenko, E. Zubko, H. Volten, O. Muñoz, and G. Videen. The negative polarization of light scattered from particulate surfaces and of independently scattering particles. *Journal of Quantitative Spectroscopy and Radiative Transfer*, 88(1): 267–284, 2004. ISSN 0022-4073. doi: https://doi.org/10.1016/j.jqsrt.2004.03.029. URL https://www.sciencedirect.com/science/article/pii/S0022407304001463. Photopolarimetry in remote sensing.

Yu G Shkuratov. Negative polarization of sunlight scattered from celestial bodies-interpretation of the wavelength dependence. *Soviet Astronomy Letters*, 13:182, 1987a.

Yu G Shkuratov. Negative polarization of sunlight scattered from celestial bodies-interpretation of the wavelength dependence. *Soviet Astronomy Letters*, 13:182, 1987b.

Yu G Shkuratov and AA Ovcharenko. Polarization of light scattered by surfaces with complex microstructure at phase angles 0.1–3.5. *Solar System Research*, 36(1):62–67, 2002.

Yu G Shkuratov, K Muinonen, E Bowell, K Lumme, JI Peltoniemi, MA Kreslavsky, DG Stankevich, VP Tishkovetz, NV Opanasenko, and L Ya Melkumova. A critical review of theoretical models of negatively polarized light scattered by atmosphereless solar system bodies. *Earth, Moon, and Planets*, 65(3):201–246, 1994.

S. B. Simon, D. J. Joswiak, H. A. Ishii, J. P. Bradley, M. Chi, L. Grossman, J. Aléon, D. E. Brownlee, S. Fallon, I. D. Hutcheon, G. Matrajt, and K. D. McKEEGAN. A refractory inclusion returned by Stardust from comet 81P/Wild 2. *Meteoritics & Planet. Sci.*, 43(11): 1861–1877, 2008. ISSN 1945-5100. doi: 10.1111/j.1945-5100.2008.tb00648.x. URL https://onlinelibrary.wiley.com/doi/abs/10.1111/j.1945-5100.2008.tb00648.x. _eprint: https://onlinelibrary.wiley.com/doi/pdf/10.1111/j.1945-5100.2008.tb00648.x.

Peter Hollingsworth Smith, LK Tamppari, RE Arvidson, D Bass, D Blaney, William V Boynton, A Carswell, DC Catling, BC Clark, T Duck, et al. H2o at the phoenix landing site. *Science*, 325(5936):58–61, 2009.

Stefano Spadaccia, CH Patty, Holly L Capelo, Nicolas Thomas, and Antoine Pommerol. Negative polarization properties of regolith simulants–systematic experimental evaluation of composition effects. *arXiv preprint arXiv:2207.08767*, 2022.

GA Steigmann. The two faces of callisto. *The Observatory*, 113:70–74, 1993.

J. M. Sunshine, H. C. Connolly, T. J. McCoy, S. J. Bus, and L. M. La Croix. Ancient Asteroids Enriched in Refractory Inclusions. *Science*, 320(5875):514–517, April 2008. doi: 10.1126/science.1154340. URL https://www.science.org/doi/10.1126/science.1154340. Publisher: American Association for the Advancement of Science.

JM Sunshine, MF A'hearn, O Groussin, J-Y Li, MJS Belton, WA Delamere, J Kissel, KP Klaasen, LA McFadden, KJ Meech, et al. Exposed water ice deposits on the surface of comet 9p/tempel 1. *Science*, 311(5766):1453–1455, 2006.

Thomas Svitek and Bruce Murray. Winter frost at viking lander 2 site. *Journal of Geophysical Research: Solid Earth*, 95(B2):1495–1510, 1990.

Leonardo Testi, Tilman Birnstiel, Luca Ricci, Sean Andrews, Jürgen Blum, John Carpenter, Carsten Dominik, Andrea Isella, Antonella Natta, Jonathan P Williams, et al. Dust evolution in protoplanetary disks. *Protostars and Planets VI*, 914:339–61, 2014.

Harold Thimbleby. The Leidenfrost phenomenon. *Phys. Educ.*, 24(5):300–303, September 1989. ISSN 0031-9120. doi: 10.1088/0031-9120/24/5/312. URL https://doi.org/10.1088%2F0031-9120%2F24%2F5%2F312. Publisher: IOP Publishing.

David James Tholen. *Asteroid taxonomy from cluster analysis of photometry*. The University of Arizona, 1984.

Martin G Tomasko and Peter H Smith. Photometry and polarimetry of titan: Pioneer 11 observations and their implications for aerosol properties. *Icarus*, 51(1):65–95, 1982.

N. Umov. Chromatische Depolarisation durch Lichtzerstreuung. *Phys. Z.*, 6:674–676, 1905.

Dan M. Watson, Jarron M. Leisenring, Elise Furlan, C. J. Bohac, B. Sargent, W. J. Forrest, Nuria Calvet, Lee Hartmann, Jason T Nordhaus, Joel D. Green, K. H. Kim, G. C. Sloan, C. H. Chen, L. D. Keller, Paola d'Alessio, J. Najita, Keven I. Uchida, and J. R. Houck. CRYSTALLINE SILICATES AND DUST PROCESSING IN THE PROTOPLANETARY DISKS OF THE TAURUS YOUNG CLUSTER. *ApJS*, 180(1):84–101, January 2009. ISSN

0067-0049, 1538-4365. doi: 10.1088/0067-0049/180/1/84. URL https://iopscience.iop.org/article/10.1088/0067-0049/180/1/84.

S. J. Weidenschilling. The Origin of Comets in the Solar Nebula: A Unified Model. *Icarus*, 127(2):290–306, June 1997. ISSN 0019-1035. doi: 10.1006/icar.1997.5712. URL http://www.sciencedirect.com/science/article/pii/S0019103597957122.

SJ Weidenschilling. Aerodynamics of solid bodies in the solar nebula. *Monthly Notices of the Royal Astronomical Society*, 180(2):57–70, 1977.

René Weidling, Carsten Güttler, Jürgen Blum, and Frithjof Brauer. THE PHYSICS OF PROTOPLANETESIMAL DUST AGGLOMERATES. III. COMPACTION IN MULTIPLE COLLISIONS. *ApJ*, 696(2):2036–2043, May 2009. ISSN 0004-637X, 1538-4357. doi: 10.1088/0004-637X/696/2/2036. URL https://iopscience.iop.org/article/10.1088/0004-637X/696/2/2036.

RA West, M Sato, H Hart, AL Lane, CW Hord, KE Simmons, LW Esposito, DL Coffeen, and RB Pomphrey. Photometry and polarimetry of saturn at 2640 and 7500 å. *Journal of Geophysical Research: Space Physics*, 88(A11):8679–8697, 1983.

Fred L. Whipple. On certain aerodynamic processes for asteroids and comets. *From plasmas to planet*, page 221, 1972. URL http://adsabs.harvard.edu/full/1972fpp..conf..211W.

Fredrik Windmark, Til Birnstiel, Carsten Güttler, Jürgen Blum, Cornelis P Dullemond, and Th Henning. Planetesimal formation by sweep-up: how the bouncing barrier can be beneficial to growth. *Astronomy & Astrophysics*, 540:A73, 2012.

Toru Yada, Masanao Abe, Tatsuaki Okada, Aiko Nakato, Kasumi Yogata, Akiko Miyazaki, Kentaro Hatakeda, Kazuya Kumagai, Masahiro Nishimura, Yuya Hitomi, et al. Preliminary analysis of the hayabusa2 samples returned from c-type asteroid ryugu. *Nature Astronomy*, 6(2):214–220, 2022.

Bin Yang and David Jewitt. Spectroscopic search for water ice on jovian trojan asteroids. *The Astronomical Journal*, 134(1):223, 2007.

Zuriñe Yoldi, Antoine Pommerol, Olivier Poch, and Nicolas Thomas. Reflectance study of ice and mars soil simulant associations–i. h2o ice. *Icarus*, 358:114169, 2021.

Andrew N Youdin and Jeremy Goodman. Streaming instabilities in protoplanetary disks. *The Astrophysical Journal*, 620(1):459, 2005a.

Andrew N. Youdin and Jeremy Goodman. Streaming Instabilities in Protoplanetary Disks. *ApJ*, 620(1):459–469, February 2005b. ISSN 0004-637X. doi: 10.1086/426895. URL https://doi.org/10.1086%2F426895.

B Zellner, T Lebertre, and K Day. The asteroid albedo scale. ii-laboratory polarimetry of dark carbon-bearing silicates. In *Lunar and Planetary Science Conference Proceedings*, volume 8, pages 1111–1117, 1977.

Evgenij Zubko. Interpretation of similarity in the negative polarization of comets and C-type asteroids in terms of common properties of asteroidal and cometary dust. *Earth*

Planet Sp, 63(10):1077–1085, October 2011. ISSN 1880-5981. doi: 10.5047/eps.2011.03.005. URL https://earth-planets-space.springeropen.com/articles/10.5047/eps.2011.03.005. Number: 10 Publisher: SpringerOpen.

Evgenij Zubko. Light scattering by cometary dust: Large-particle contribution. *Earth Planet Sp*, 65(3):139–148, March 2013. ISSN 1880-5981. doi: 10.5047/eps.2012.02.003. URL https://earth-planets-space.springeropen.com/articles/10.5047/eps.2012.02.003. Number: 3 Publisher: SpringerOpen.

Evgenij Zubko, Yuriy Shkuratov, Michael Mishchenko, and Gorden Videen. Light scattering in a finite multi-particle system. *Journal of Quantitative Spectroscopy and Radiative Transfer*, 109(12):2195–2206, August 2008. ISSN 0022-4073. doi: 10.1016/j.jqsrt.2008.03.007. URL https://www.sciencedirect.com/science/article/pii/S0022407308000733.

Evgenij Zubko, Gorden Videen, Yuriy Shkuratov, Karri Muinonen, and Tetsuo Yamamoto. The Umov effect for single irregularly shaped particles with sizes comparable with wavelength. *Icarus*, 212(1):403–415, March 2011. ISSN 0019-1035. doi: 10.1016/j.icarus.2010.12.012. URL https://www.sciencedirect.com/science/article/pii/S001910351000480X.

Evgenij Zubko, Karri Muinonen, Olga Muñoz, Timo Nousiainen, Yuriy Shkuratov, Wenbo Sun, and Gorden Videen. Light scattering by feldspar particles: Comparison of model agglomerate debris particles with laboratory samples. *Journal of Quantitative Spectroscopy and Radiative Transfer*, 131:175–187, December 2013. ISSN 0022-4073. doi: 10.1016/j.jqsrt.2013.01.017. URL https://www.sciencedirect.com/science/article/pii/S0022407313000368.

Evgenij Zubko, Gorden Videen, Jessica A. Arnold, Benjamin MacCall, Alycia J. Weinberger, and Sungsoo S. Kim. On the Small Contribution of Supermicron Dust Particles to Light Scattering by Comets. *ApJ*, 895(2):110, June 2020. ISSN 0004-637X. doi: 10.3847/1538-4357/ab8ae4. URL https://doi.org/10.3847/1538-4357/ab8ae4. Publisher: American Astronomical Society.

1. Reprinted from Icarus, 304, Devogèle et al., New polarimetric and spectroscopic evidence of anomalous enrichment in spinel-bearing calcium-aluminium-rich inclusions among L-type asteroids, 31-57, Copyright (2018), with permission from Elsevier.
2. Reproduced with permission from Springer Nature.
3. From *Protostars and Planets VI* by Henrik Beuther et al. ©2014 The Arizona Board of Regents. Reprinted by permission of the University of Arizona Press.
4. Reproduced with permission from Springer Nature.
5. Reprinted from Icarus, 317, K. M. Cannon et al., Mars global simulant MGS-1: A Rocknest-based open standard for basaltic martian regolith simulants, 470-478, Copyright (2019), with permission from Elsevier.
6. From Fornasier et al. (2016). Reprinted with permission from AAAS.
7. From Smith et al. (2009). Reprinted with permission from AAAS.